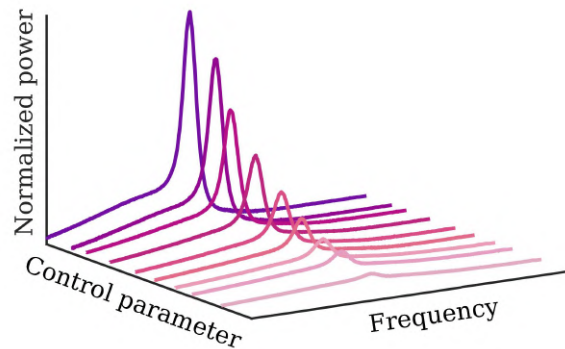




DEPARTMENT OF PHYSICS,
DEPARTMENT OF AEROSPACE
ENGINEERING
INDIAN INSTITUTE OF TECHNOLOGY
MADRAS
CHENNAI - 600036

Critical transitions in diverse physical systems: scaling and early warning signals



A Thesis

Submitted by

INDUJA P

For the award of the degree

Of

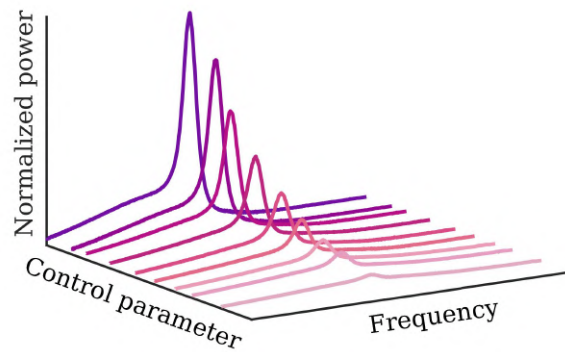
DOCTOR OF PHILOSOPHY

Feb, 2022



DEPARTMENT OF PHYSICS,
DEPARTMENT OF AEROSPACE
ENGINEERING
INDIAN INSTITUTE OF TECHNOLOGY
MADRAS
CHENNAI - 600036

Critical transitions in diverse physical systems: scaling and early warning signals



A Thesis

Submitted by

INDUJA P

For the award of the degree

Of

DOCTOR OF PHILOSOPHY

Feb, 2022

QUOTATIONS

*Science never solves a problem
without creating ten more.*

-George Bernard Shaw

DEDICATION

Dedicated to my parents and sister.

THESIS CERTIFICATE

This is to undertake that the Thesis (or Project report) titled **CRITICAL TRANSITIONS IN DIVERSE PHYSICAL SYSTEMS: SCALING AND EARLY WARNING SIGNALS**, submitted by me to the Indian Institute of Technology Madras, for the award of Ph.D., is a bona fide record of the research work done by me under the supervision of Prof. C. Vijayan and Prof. R. I. Sujith. The contents of this Thesis, in full or in parts, have not been submitted to any other Institute or University for the award of any degree or diploma.

In order to effectively convey the idea presented in this thesis, the following work of other authors was reprinted in the thesis with their permission.

- Figure. 1.1, page 2: Reproduced with permission from Scheffer, M., Carpenter, S., Foley, J.A., Folke, C. and Walker, B., 2001. Catastrophic shifts in ecosystems. Nature, 413(6856), pp.591-596.
- Figure. 2.2, page 23: Reproduced with permission from Gopalakrishnan, E.A. and Sujith, R.I., 2014. Influence of system parameters on the hysteresis characteristics of a horizontal Rijke tube. International journal of spray and combustion dynamics, 6(3), pp.293-316.
- Figure 2.9, page 38: Reproduced with permission from Murugesan, M. and Sujith, R.I., 2016. Detecting the onset of an impending thermoacoustic instability using complex networks. Journal of Propulsion and Power, 32(3), pp.707-712.

Place: Chennai 600 036

Date: 24th Feb, 2022

Induja P

Research Scholar

Prof. C. Vijayan

Research Guide

Prof. R. I. Sujith

Research Guide

LIST OF PUBLICATIONS

I. REFEREED JOURNALS BASED ON THE THESIS

1. **Pavithran Induja, Unni, V. R., Varghese, A. J., Sujith, R. I., Saha, A., Marwan, N., and Kurths, J.** (2020). Universality in the emergence of oscillatory instabilities in turbulent flows. *EPL (Europhysics Letters)*, **129(2)**, 24004. doi.org/10.1209/0295-5075/129/24004
2. **Pavithran Induja, Unni, V. R., Varghese, A. J., Premraj, D., Sujith, R. I., Vijayan, C., Saha, A., Marwan, N., and Kurths, J.** (2020). Universality in spectral condensation. *Scientific Reports*, **10(1)**, 1-8. doi.org/10.1038/s41598-020-73956-7
3. **Pavithran Induja, and Sujith, R. I.** (2021). Effect of rate of change of parameter on early warning signals for critical transitions. *Chaos: An Interdisciplinary Journal of Nonlinear Science*, **31(1)**, 013116. doi.org/10.1063/5.0025533
4. **Pavithran Induja, Unni, V. R., Saha, A., Varghese, A. J., Sujith, R. I., Marwan, N., and Kurths, J.** (2021). Predicting the Amplitude of Thermoacoustic Instability Using Universal Scaling Behavior. *Journal of Engineering for Gas Turbines and Power*, **143(12)**, 121005. doi.org/10.1115/1.4052059
5. **Pavithran Induja, Unni, V. R., and Sujith, R. I.** (2021). Critical transitions and their early warning signals in thermoacoustic systems. *The European Physical Journal Special Topics*, **230(16)**, 3411-3432. doi.org/10.1140/epjs/s11734-021-00214-w

II. REFEREED JOURNALS (Others)

1. **Pavithran, I., and Sujith R. I.** (2022). Extreme COVID-19 waves reveal hyperexponential growth and finite-time singularity. *Chaos*, **32(4)**.
2. **Kraemer, K. H., Gelbrecht, M., Pavithran, I., Sujith, R. I., and Marwan, N.** (2022). . Optimal state space reconstruction via Monte Carlo decision tree search. *Nonlinear Dyn*, **108**.
3. **Bury, T.M., Sujith R. I., Pavithran I., Scheffer M., Lenton T. M., Anand M. and Bauch C. T.** (2021). Deep learning for early warning signals of tipping points. *Proceedings of the National Academy of Sciences*, **118(39)**.
4. **Ruiz, E.A., Unni V. R., Pavithran I., R. I. Sujith and Saha A.** (2021). Convolutional neural networks to predict the onset of oscillatory instabilities in turbulent systems. *Chaos*, **31(9)**, 093131.
5. **Kasthuri, P., Pavithran I., Pawar S. A., Sujith R. I., Gejji, R. and Anderson W. E.** (2019). Dynamical systems approach to study thermoacoustic transitions in a liquid rocket combustor. *Chaos*, **29(10)**, 103115.

6. **Kasthuri, P., Pavithran I., A. Krishnan, S. A. Pawar, Sujith R. I., Gejji R., Anderson W. E., Marwan N., and Kurths J.** (2020). Recurrence analysis of slow-fast systems. *Chaos*, **30(6)**, 063152.
7. **Seshadri, A., Pavithran I., Unni V.R., and Sujith R. I.** (2018). Predicting the amplitude of limit-cycle oscillations in thermoacoustic systems with vortex shedding. *AIAA Journal*, **56(9)**, 3507-3514.

ACKNOWLEDGEMENTS

I would like to thank, first and foremost, my advisors Prof. C. Vijayan and Prof. R.I. Sujith, for their guidance and support over the past years. I am grateful to both of them for giving me the opportunity to do collaborative and interdisciplinary work. I thank Prof. C. Vijayan for showing me an open path to express myself and being a constant resource of inspiration and motivation. I particularly thank Prof. Sujith for his intuition, ideas, criticism, and belief in me. I am always indebted to him for teaching many technical and non-technical aspects, especially for working with me as a team. Apart from the two faculty members, I was closely mentored by Vishnu R. Unni during my initial years of Ph.D. I am ever grateful for the clear and reliable insight and explanations to all my questions.

Watching other seniors Samadhan, Abin and Nitin in Sujith's lab helped me learn how to work together through discussing and interacting with others. Thanks to the seniors at the Photonics Lab, Dileep, Siva and Radhika. Their experiments inspired my interest to pursue research. There are many people without whom this work would have been impossible. I would like to thank the people I approach to discuss all my ideas or results - Praveen, Alan, Veda Sri (during the first two years). Thanks to Manikandan, whom I ask for solutions when the experiments do not work. Also, I thank Midhun, Anand, Thilagraj, Reeja, Dileesh and Gayathri for all the help with the experiments. I acknowledge Krishna, Akshay, Syam, and Jabasteena for all the help they have provided. I wish to thank all my current labmates, Amitesh, ShriVignesh, Ankan, Jayesh, Abhishek, Samarjeet, Ankit, Shruti, Shanmugapriya, and all the new members of the group. Thanks to Ramesh, Siva and Thonti for correcting the chapters of my thesis. I have been fortunate to have collaborators beyond IIT Madras. I would like to sincerely thank Prof. Juergen Kurths, Dr. Norbert Marwan and Prof. Abhishek Saha. Also, I like to thank Prof. Vineeth, Prof. Gopalakrishnan and Prof. Arul Lakshminarayan for the discussions we had.

I would like to acknowledge the research assistantship from the Ministry of Human Resources and Development (MHRD), Govt. of India. I also wish to thank my doctoral committee. Thanks to my friends inside and outside IITM for their invaluable support during these years and for times well spent. I am thankful to my parents and my sister for their love and support. Thank you to all my friends and family for always being there for me.

ABSTRACT

KEYWORDS: Critical transitions; Early warning signals; Power law scaling; Tipping; Rate-induced tipping.

Critical transitions are ubiquitous in natural, economic, and social systems, manifesting in the form of sudden changes to the state of the system when the system parameters are varied past a critical point. They often result in dangerous and catastrophic outcomes such as the collapse of ecosystems, epileptic seizures, melting of arctic sea ice, and oscillatory instability in fluid mechanical systems. Whereas, critical transitions are desirable in some instances, such as the onset of coherent lasing. This thesis aims to study critical transitions and universal behaviour of diverse systems close to transition.

The critical transition to oscillatory instabilities in turbulent fluid mechanical systems is observed to follow a unique route. During this transition, we uncover the existence of an inverse square law scaling between the Hurst exponent (H) of a fluctuating state variable and its spectral amplitude. Interestingly, we observe the same power law exponent near -2 across various turbulent fluid mechanical systems such as aeroacoustic, thermoacoustic and aeroelastic systems. The energy distributed over a broadband of frequencies in the power spectrum gets condensed into a dominant mode during the transition to an ordered dynamics. We call this phenomenon spectral condensation and define a set of spectral measures to quantify it. These spectral measures follow an inverse power law relation with the power corresponding to the dominant peak in the spectrum, and is observed across fluid mechanical systems, random laser and Chua's circuit. The spectral measures and H vary gradually during the transition to oscillatory instabilities and forewarn impending critical transitions well before their onset. The power law scaling of these precursors with the spectral amplitude can be used to predict the amplitude of oscillations expected after the transition. Predicting the amplitude of the oscillations helps devise strategies to mitigate

the ruinously high-amplitude oscillations, which can lead to catastrophic failures in real-world systems.

The second part of this thesis focuses on the effects of continuous variation of parameters on critical transitions. By performing experiments on a laminar thermoacoustic system exhibiting subcritical Hopf bifurcation, we compare the efficacy of various early warning signals. Lag-1 autocorrelation (AC) and H are found to be suitable measures to predict the transition well-before its occurrence. The warning time, obtained using AC and H , reduces following an inverse power law with the rate of change of the control parameter. Further, experiments in a turbulent thermoacoustic system showed critical transition only for fast variations of the parameter. Such transitions during a quick variation of parameters are called rate-induced tipping (R-tipping). We demonstrate a mechanism of R-tipping where another parameter, which is not in our control, varies simultaneously at a different rate, and the competition between the two variables determines the dynamics.

TABLE OF CONTENTS

	Page
ACKNOWLEDGEMENTS	i
ABSTRACT	iii
LIST OF TABLES	x
LIST OF FIGURES	xxi
GLOSSARY	xxii
ABBREVIATIONS	xxiii
NOTATION	xxiv
CHAPTER 1: INTRODUCTION	1
1.1 Critical transitions	1
1.2 Mechanisms of critical transitions	2
1.3 Early warning signals for critical transitions	5
1.3.1 Conventional EWS based on critical slowing down	6
1.3.2 Possibilities and limitations of critical slowing down based early warning signals	7
1.4 Scaling during critical transitions	9
1.4.1 Universality and data collapse	10
1.4.2 Equilibrium phase transitions	11
1.4.3 Non-equilibrium phase transitions	12
1.5 The current scenario and motivation	14
1.6 Objectives of the current thesis	17
1.7 Overview and scope of the thesis	17

CHAPTER 2: Critical transitions to oscillatory instability and their early warning signals in thermoacoustic systems	19
2.1 Transitions in laminar systems	22
2.2 Transitions in turbulent systems	25
2.3 EWS for critical transitions	28
2.3.1 Critical slowing down based EWS	28
2.3.2 Fractal and multifractal measures	30
2.3.3 Recurrence quantification analysis	33
2.3.4 Complex networks	36
2.3.5 Symbolic time series analysis	39
2.3.6 Machine learning-based precursors	41
2.4 Models to study critical transitions in thermoacoustic systems	45
2.4.1 Forced acoustic oscillator type models	45
2.4.2 Synchronisation based models	46
2.5 Continuous variation of control parameters	48
2.6 Spatiotemporal dynamics of thermoacoustic systems	49
2.7 Summary	52
CHAPTER 3: Universality during critical transitions to oscillatory instabilities in turbulent flows	54
3.1 Self-organization leading to oscillatory instabilities	54
3.2 Details of the experiments and data used	57
3.2.1 Experiments on Thermoacoustic system	57
3.2.2 Experiments on Aeroacoustic system	60
3.2.3 Experiments on Aeroelastic system	61
3.3 Transition from chaos to limit cycle oscillations via intermittency	61
3.4 Fractal characteristics and Hurst exponent	63
3.4.1 Estimation of Hurst exponent	64
3.5 Scaling of Hurst exponent with the amplitude of oscillations	66

3.6	Summary	69
CHAPTER 4: Universality in spectral condensation		71
4.1	Transitions to an ordered state (pattern formation) in fluid mechanical, optical, and electronic systems	71
4.2	Experiments	73
4.2.1	Optical system	74
4.2.2	Electronic circuit	74
4.3	Mathematical models	75
4.3.1	Kicked oscillator model describing the thermoacoustic system	75
4.3.2	Noisy Hopf bifurcation model	76
4.4	Spectral condensation: Sharpening of the power spectrum during pattern formation	77
4.4.1	Spectral measures	79
4.5	Inverse power-law scaling of spectral measures with the peak power	80
4.5.1	Functional form for the power spectrum	82
4.5.2	Power law exponents for a set of spectral measures	82
4.6	Summary	83
CHAPTER 5: Predicting the amplitude of oscillatory instabilities using the scaling		85
5.1	Transition to thermoacoustic instability: Hurst exponent and spectral measures	88
5.2	Fractal characteristics and universal scaling	90
5.3	Spectral measures to estimate the amplitude of individual modes of oscillations	93
5.4	Procedure to estimate the amplitude of limit cycle oscillations	95
5.5	Illustration of efficacy of the estimation procedure	98
5.5.1	Estimating the amplitude of multiple modes of oscillations	100
5.6	Summary	103

CHAPTER 6: Effect of rate of change parameter on early warning signals for critical transitions.	105
6.1 Experiments	108
6.2 Rate-dependent tipping-delay in a thermoacoustic system	110
6.3 EWS for critical transitions	112
6.4 Variation of warning time with rate	120
6.5 Quantification of the performance of early warning signals	125
6.6 Model for noisy Hopf bifurcation with continuous variation of parameter	126
6.7 Relation between lag-1 autocorrelation and variance close to the tipping point	131
6.7.1 Autocorrelation for turbulent systems	132
6.8 Summary	136
CHAPTER 7: Rate-dependent transitions in complex systems	137
7.1 Introduction	137
7.2 Experiments	140
7.3 R-tipping in a turbulent thermoacoustic system	144
7.4 The mechanism of R-tipping	146
7.4.1 Measuring damping at high temperatures	148
7.4.2 The effect of wall temperature on acoustic damping	149
7.5 R-tipping in a noisy Hopf bifurcation model	151
7.6 Summary	154
CHAPTER 8: Conclusions and future prospects	157
APPENDIX A: Test for scaling during transitions from chaos to limit cycle via other types of intermittency	162
A.1 Type I intermittency	162
A.2 Type II intermittency	163

A.3	Type III intermittency	165
APPENDIX B: Selection of threshold for Hurst exponent and spectral		
	measures	168
B.1	Lower limit for the measures	168
B.2	Upper limit for the measures	169
APPENDIX C: Robustness of EWS with the threshold and test for false		
	warnings	171
C.1	Robustness of EWS with the threshold	171
C.2	Analysis to check false warnings	171
	REFERENCES	194

LIST OF TABLES

Table	Title	Page
2.1	Early warning signals for critical transitions in thermoacoustic systems	44
5.1	Estimated amplitude of limit-cycle oscillations using the scaling relation of H and FFT peak from the time series acquired during the stable operation. The first row in the table shows the results from only one time series. The second row shows the results using the first and the second time series, and so on.	99
5.2	Estimated amplitude of limit-cycle oscillations using the scaling relation of spectral measure and FFT peak from the time series acquired during the stable operation.	99
5.3	Estimation results for data with multiple modes	102

LIST OF FIGURES

Figure	Title	Page
1.1	Gradual and abrupt transitions in ecosystems. In (a) and (b), only one possible dynamical state exists for each condition. While the transition in (a) is more gradual, (b) looks like a sigmoid. Whereas, three equilibria exist for a given condition in (c) and the transition between alternative stable states on the upper and lower branches involve sudden jumps. The arrows indicate the direction of change and the dashed line represent unstable attractor (c). Adapted from (Scheffer <i>et al.</i> , 2001).	2
2.1	A schematic representation of the feedback mechanism between the subsystems during thermoacoustic instability. The coupling between the acoustic field in the combustor and the unsteady heat release rate fluctuations drives self-sustained oscillations.	22
2.2	(a) Supercritical bifurcation and (b) Subcritical bifurcation plots representing transitions in laminar systems. The filled and the empty circles denote the stable and unstable solutions of the the normal form equations of Hopf bifurcation, respectively. Supercritical bifurcation has a continuous transition, whereas subcritical bifurcation has an abrupt transition and has a hysteresis (BCEF) while reversing the parameter. Reproduced with permission from Gopalakrishnan and Sujith (2014)	23
2.3	Bifurcation plot for a laminar thermoacoustic system known as Rijke tube showing a sequence of bifurcations for different values of x_f . Reproduced with permission from Kabiraj <i>et al.</i> (2012).	25
2.4	Time series of acoustic pressure (left column) and heat release rate oscillations (right column) acquired at various Reynolds numbers, illustrating the transition to thermoacoustic instability. Reproduced with permission from George <i>et al.</i> (2018b).	26
2.5	Time series of acoustic pressure fluctuations during intermittency acquired from (a) a bluff body stabilised combustor and (b) a swirl stabilised combustor. The zoomed views show epochs of large-amplitude oscillations amidst low-amplitude aperiodic fluctuations. Reproduced with permission from Nair <i>et al.</i> (2014c).	27
2.6	(a) Time series of pressure fluctuations during the transition to thermoacoustic instability in a laminar system where the control parameter K is increased in time. Variation of (b) variance and (c) lag-1 autocorrelation calculated for a moving window of half the size of the time series. A consistent increase or decrease in the value of a measure is expressed as trend. Reproduced with permission from Gopalakrishnan <i>et al.</i> (2016a).	29

2.7	(a) The variation of p_{rms} and the FFT peak during the transition to thermoacoustic instability for a bluff body stabilised combustors as a function of the control parameter Re . The growth of amplitude of oscillations during the transitions is captured by these measures. (b) The corresponding variation of the Hurst exponent (H). H drops to very low values well before the amplitude rises. Redrawn with permission from Nair and Sujith (2014)	32
2.8	Variation of recurrence measures as a function of Re in (a-c) swirl stabilised combustor and (d-f) bluff body combustor. The length of the time series (T) used to estimate the recurrence measures is varied from 0.5 s to 3 s. Reproduced with permission from Nair <i>et al.</i> (2014c).	34
2.9	(a) Variation of rms of pressure and (b-e) complex network measures during the transition to thermoacoustic instability. The network measures, namely, clustering coefficient (C/C_0), characteristic path length (L/L_0), network diameter (D/D_0), and global efficiency (E/E_0) start to vary during the intermittency regime and thereby detect the transition well before P_{rms} . Reproduced with permission from Murugesan and Sujith (2016).	38
2.10	Variations of the average degree of the network as a function of the equivalence ratio for the transition towards lean blowout (decrease in ϕ). The average degree is calculated for horizontal visibility networks constructed using time series of (a) pressure fluctuations and (b) heat release rate fluctuations. The network measure provides early warning for blowout. Reproduced with permission from Gotoda <i>et al.</i> (2017).	39
2.11	The concept of symbolic time series analysis. The time series is partitioned and labelled, and a state probability histogram is then created. Reproduced with permission from Unni <i>et al.</i> (2015).	40
3.1	Schematic of the experimental setups. (a) Turbulent combustor (thermoacoustic system) exhibiting transition to thermoacoustic instability. (b) An aeroacoustic system with two orifices. Vortices are shed when the turbulent flow passes through the orifices. In both of these systems, we measure the acoustic pressure fluctuations inside the duct during the transition to thermoacoustic/aeroacoustic instability. (c) An aeroelastic system where the left end of the beam has a small vertical fin attached to it. When a jet of air passes along the length of the cantilever from left to right, vortices are shed from the fins. We measure the resulting strain on the cantilever close to the fixed end of the beam. In all the cases, Reynolds number (Re) is varied as the control parameter to attain different dynamical states. The dimensions of different experimental setups are not to scale.	58

3.2	Time series of state variables during the transition to oscillatory instability. (a-c) Data representing the acoustic pressure fluctuations acquired from a bluff body stabilized combustor of length 700 mm. The corresponding Re for a, b and c are $(1.9 \pm 0.053) \times 10^4$, $(2.6 \pm 0.069) \times 10^4$ and $(2.8 \pm 0.073) \times 10^4$ respectively. (d-f) Acoustic pressure fluctuations acquired during the transition to aeroacoustic instability ($Re = 5615 \pm 185$, 7283 ± 198 and 9270 ± 212 corresponding to d, e and f). (j-i) The time series of strain experienced by the cantilever in the aeroelastic system the Re is varied (2384 ± 111 , 3972 ± 142 and 4768 ± 159). In all the systems, we observe a transition from low amplitude aperiodic fluctuations (a, d and g) to high amplitude periodic oscillations (c, f and i) via a regime of intermittency (b, e and h) as the control parameter is varied (Re increases from top to bottom). The transition from aperiodicity to periodicity occurs via a regime of intermittency for other configurations of these systems as well.	62
3.3	Amplitude of the dominant mode of oscillations and the Hurst exponent for unsteady pressure signals as a function of Reynolds number (Re). We analyze the data from a laboratory bluff body stabilized combustor of length 700 mm for different Re . The amplitude is obtained from the amplitude spectrum plotted with a resolution of 4 Hz. The amplitude increases steeply near the transition to thermoacoustic instability, whereas the Hurst exponent shows a gradual decrease during the transition and it is approaching zero.	65
3.4	Inverse power law scaling of amplitude with Hurst exponent. Variation of amplitude with Hurst exponent is plotted on a logarithmic scale for the data acquired from different systems. We observe a power law relation with a constant power law exponent around -2.	67
4.1	Schematic of the experimental setups. (a) An optical system for random lasing, wherein we observe a transition towards narrow-band lasing like emission as we increase the excitation pulse energy (EPE) of the laser source. (b) Electronic circuit known as Chua's circuit is used for the experiments. The variable resistor (R) is varied to obtain the transition from a fixed point to limit cycle oscillations. In both the systems, we acquire data for different values of the respective control parameters. For the random laser, the output emission is collected using a fibre optic spectrometer. The voltage (v_1) is measured for the electronic circuit. The dimensions of different experimental setups are not to scale.	73

4.2	<p>Evolution of the spectrum for fluid mechanical, optical and electronic systems. The evolution of power spectrum with variation in the corresponding control parameter is presented on the left side and the normalized spectra for each system is given on the right side of the panel. (a, b) Power spectra obtained using Fast Fourier Transform (FFT) of the acoustic pressure fluctuations for a laboratory-scale bluff body stabilized combustor of length 700 mm. The power spectra exhibit an increasing dominance of a single peak on approaching oscillatory instabilities (for increasing Re) in all the fluid mechanical systems discussed in this paper, and hence this figure is a representative example. (c, d) Emission spectra of the random laser as we progressively increase EPE. The power spectrum is obtained by multiplying the photon count per second for each wavelength with its respective energy. The broad spectrum starts to become a narrow lasing-like peak with increase in EPE. (e, f) Power spectra obtained using FFT of the voltage signal (v_1) measured from Chua's circuit and the corresponding normalized spectra are shown respectively. The peak sharpens during the transition to limit cycle oscillations as the resistance (R) is decreased. The power spectra using FFT are plotted for a resolution of 4 Hz for visualization purpose.</p>	78
4.3	<p>The scaling behaviour of spectral measures with the peak power during spectral condensation in experimental systems and models. Variation of the normalized power (P_0/P_N) corresponding to the dominant mode with the representative spectral measures ($[\mu_2]$, $[\mu_2 \mu_0]$ & $[\mu_4 \mu_4]$) plotted in double logarithmic scale (a-c) for the data acquired from experiments conducted in different systems and (d-f) for the data generated from two models. The extent of spectral condensation and the peak power differs by orders of magnitude across these systems. Hence, we rescale the power corresponding to the dominant peak (P_0) as P_0/P_N to show the lines, $\log(P_0) = k \log([\mu_m^x \mu_n^y]) + C$, in the same plot. The normalization factor, P_N, is the estimated value of peak power for $[\mu_m^x \mu_n^y] = 1$ obtained by extrapolating the line $\log(P_0) = k \log([\mu_m^x \mu_n^y]) + C$ for each system. This choice of P_N forces all lines to have $C = 0$. We observe an inverse power law behaviour for all the spectral measures in the experiments as well as in the models. The uncertainties in the power law exponent are shown for 95% confidence intervals.</p>	81
4.4	<p>Power law exponents obtained from the scaling relation between the spectral measures and the peak power for the higher index spectral measures in different experimental systems and models. Here, the exponential function refers to the functional form of the power spectrum as defined in Eq. 4.1 in the manuscript.</p>	83

5.1	Time series and the corresponding amplitude spectrum of acoustic pressure fluctuations during the transition from CN to TAI. The data obtained for the bluff body stabilized combustor is presented here as a representative case; we observe a similar transition in swirl stabilized combustor as well. (a) The time series representing the state of CN ($Re = (1.9 \pm 0.053) \times 10^4$) consists of low amplitude aperiodic oscillations. (b) The amplitude spectrum shows a broad peak around $f = 250$ Hz. (c) We observe a state of INT at $Re = (2.6 \pm 0.069) \times 10^4$. The time series during INT has bursts of high amplitude periodic oscillations amidst epochs of low amplitude aperiodic oscillations. This reflects as an increase in the amplitude of the peak in the amplitude spectrum (d) . Then, the amplitude of pressure fluctuations increases abruptly during TAI. (e) The time series during TAI (at $Re = (2.8 \pm 0.073) \times 10^4$) comprises high amplitude periodic oscillations and the resultant amplitude spectrum (f) has a sharp peak around $f = 250$ Hz.	89
5.2	The variation of p'_{rms} and the FFT peak during the transition from CN to TAI. The amplitude of dominant mode of oscillations computed from the amplitude spectrum using the Fourier transform is referred to as the FFT peak. Both p'_{rms} and FFT peak are very low during CN. The amplitude of oscillations increases as we approach TAI, which is captured by both p'_{rms} and FFT peak. This figure uses data acquired from a bluff body stabilized turbulent combustor.	90
5.3	Variation of H as a function of Re for the acoustic pressure data from the bluff body stabilized combustor. H approaches a limiting value of zero for LCO, unlike amplitude which is unbounded and can increase to any level depending on the system.	91
5.4	The inverse square law relation between H and FFT peak during the transition to TAI in turbulent systems. We present the scaling for the data acquired from the bluff body stabilized combustor with different lengths and a swirl stabilized combustor. As different configurations of the thermoacoustic system can have different amplitudes of LCO, we normalize the peak amplitude with the amplitude of LCO for that particular case. The normalization is done only for visualization purpose. A dashed red line is drawn to show the inverse power law. .	92
5.5	A representative spectral measure $[\mu_2\mu_0]$ as a function of Re in a semi logarithmic scale. The variation has a fluctuating trend during CN. However, the value of $[\mu_2\mu_0]$ decreases monotonically as we approach TAI.	93

5.6	The inverse power law scaling between FFT peak and $[\mu_2\mu_0]$. The data acquired from the bluff body combustor with different lengths and the swirl combustor obey the power law relation with the same exponent. The FFT peak from the amplitude spectrum is normalized to show all these power laws in the same plot (for the sake of visualization). The normalization factor is the estimated value of FFT peak for $[\mu_2\mu_0] = 1$ obtained by extrapolating power law for each system. The average value of the power law exponent across different systems including thermoacoustic, aeroacoustic and aeroelastic systems is found to be around -0.66 ± 0.1	95
5.7	Estimating the amplitude of limit cycle oscillations using (a) the scaling of FFT peak and H and (b) the scaling of FFT peak and the spectral measure $[\mu_2\mu_0]$. We use a few data points during the state of stable operation (shown as black colour points) and extrapolate the power law behaviour towards TAI, that is towards higher FFT peak. The CN data shown here is obtained from the bluff body stabilized combustor of length 700 mm. The amplitudes in the region between A and B are the estimated amplitude during TAI.	96
5.8	Time series showing aperiodic oscillations during stable operation at $Re = 1.95 \times 10^4$ and the time series with high amplitude limit cycle oscillations during TAI ($Re = 2.78 \times 10^4$). The predicted amplitude (using H), indicated with the red line, reasonably captures the actual limit cycle amplitude. The data presented is for the case of the bluff body stabilized combustor.	98
5.9	(a) low amplitude aperiodic p' during CN and (b) the corresponding amplitude spectrum with two broad peaks around 160 Hz and 500 Hz. (c-d) Both the modes grow as we reach TAI, and the peak at ~ 158 Hz becomes dominant. The predicted amplitudes of these two modes are marked with red circles in the spectrum.	101
6.1	Schematic of the horizontal Rijke tube used for the experiments. It comprises a 1 m long duct, an electrically heated wire mesh and a rectangular chamber called decoupler. The wire mesh is shown separately outside the duct. A piezoelectric transducer is mounted on the duct to acquire the acoustic pressure fluctuations inside the duct.	109
6.2	(a) The variation of rms of the acoustic pressure fluctuations (p'_{rms}) for the quasi-static experiments. p'_{rms} shows an abrupt jump at the heater power ~ 600 W, denoted as μ . (b) A typical variation of voltage (V) at a constant rate of increase ($dV/dt = 60$ mV/s) and the corresponding variation of heater power (P). (c) The pressure signal (p') acquired continuously as the control parameter is varied in time.	110
6.3	Time evolution of p' as a function of time-varying P for three different rates of change of V . The rate of change of rms of fluctuations is also shown in the inset to identify the onset of TAI. Here, the maximum rate of change of p'_{rms} is considered as the onset of oscillations. The delay in the transition, δ , is found to increase with an increase in r . Here, p'_{rms} is calculated for a moving window of 1 s with an overlap of 0.9 s.	111

6.4	Variation of p'_{rms} , lag-1 autocorrelation (AC), variance (VAR), skewness (SKEW), kurtosis (K) and Hurst exponent (H) during the transition to TAI in Rijke tube. Each column corresponds to the results for a particular rate (r) of change of V ((a)-(f): $r = 5\text{mV/s}$, (g)-(l): $r = 30\text{mV/s}$, (m)-(r): $r = 80\text{mV/s}$). The onset of TAI is marked with a red colour dotted line and quasi-static Hopf point μ is marked on the x -axis. p'_{rms} , and VAR starts to increase almost at the onset of TAI, whereas, K and SKEW detect the tipping slightly before p'_{rms} increases. In contrast, AC and H give early warning well-before the transition to TAI for all the cases shown here.	113
6.5	Rate of change of p'_{rms} , lag-1 autocorrelation (AC), and Hurst exponent (H) with P is plotted for different rates of change of V . The maximum rate of change of AC and H occurs much before the maximum growth of p'_{rms} . As the rate of change of input voltage with time (dV/dt) increases (from (a)-(d)), the delay (in terms of P) in growth of amplitude increases.	118
6.6	Variation of p'_{rms} and H evaluated for data acquired at different rates of change of V is plotted as a function of the P (left column - a,c,e,g,i,k) and time (right column - b,d,f,h,j,l). Rate of change of parameter increases from top to bottom. For all these rates, we are able to predict the tipping using H , before p'_{rms} starts to increase. The green dotted line represents to the threshold value of $H = 0.1$. The warning time before the tipping (marked with blue colour) is the difference between the time at which H crosses the threshold and the time at which maximum rate of change of p'_{rms} is observed.	121
6.7	Variation of p'_{rms} and AC is plotted as a function of control parameter, P , (left column - a,c,e,g,i,k) and time, t , (right column - b,d,f,h,j,l) evaluated for data acquired at different rates of change of P . Rate of change of control parameter increases from top to bottom. For all the transitions shown, AC provides an early warning before p'_{rms} starts to rise. The green dotted line represents to the threshold value of AC. The warning time, τ , (marked with blue colour) is the difference between the time at which AC crosses the threshold and the time at which maximum rate of change of p'_{rms} is observed.	122
6.8	The effect of rate of change of control parameter on EWS for critical transitions	123
6.9	Warning time (τ) obtained from (a) AC and (b) H are plotted as a function of r in logarithmic scale. (b) The value of τ decreases with r following an inverse power law relation as $\tau \propto r^n$ with $n = -0.76 \pm 0.10$ and $n = -0.84 \pm 0.08$ for AC and H , respectively. The threshold for obtaining warning is 0.4 for AC and 0.1 for H	124

6.10	The distributions of three different early warning signals (Auto correlation at lag-1 (AC), Hurst exponent (H), and skewness (SKEW)) are shown for the case of the stable system (orange) and the system approaching a critical transition (violet). The corresponding ROC are shown in the bottom row. The dotted diagonal line representing a random classifier such as a coin toss is shown for a comparison. Here, AC and H show better performance than SKEW.	125
6.11	(a) Bifurcation diagram showing the variation of η'_{rms} as a function of linear damping, α . The Hopf point (μ) is at $\alpha = 50$ rad/s, where $\alpha = \beta$. (b) The time series of η obtained by solving Eq. 6.6 for a continuous variation of α is shown along with a zoomed view of the bursts occurring during the fixed point state.	127
6.12	Variation of η'_{rms} , lag-1 autocorrelation (AC), variance (VAR), skewness (SKEW), kurtosis (K) and Hurst exponent (H) with the parameter α during the transition to limit cycle oscillations in the model. Each column corresponds to the results for a particular rate of change of α ((a)-(f): $r = -0.0005$, (g)-(l): $r = -0.05$, (m)-(r): $-r = -5$). The point of the maximum rate of change of η'_{rms} is marked with a red dotted line. For higher values of r , kurtosis and skewness detect the tipping before η'_{rms} and VAR. Here, AC and H consistently give early warning well-before the transition to limit cycle oscillations for all the rates.	129
6.13	Warning time (τ) obtained from (a) AC and (b) H are plotted as a function of r in a double logarithmic plot for both linear (blue colour) and quadratic (green colour) variation of α . We observe a power law relation between τ and AC and τ and H . The threshold chosen for obtaining warning is 0.4 for AC and 0.1 for H	130
6.14	(a-b) Increase in the variance of fluctuations as a function of AC shows a curve increasing faster than exponential (hyperexponential). (c-d) To find the exponent of the hyperexponential function, a linear fit is done on the double logarithmic plot of $\frac{d(A)}{d(AC)}$ vs. VAR.	132
6.15	Autocorrelation as a function of lag for (a) fold bifurcation and (b) Hopf bifurcation. Autocorrelation function is plotted at various parameter values on approaching the bifurcation and are plotted in different colours ranging from blue to orange. As we approach the transition, this autocorrelation function changes as indicated by the arrows. For fold bifurcation, AC increases at all lags. In contrast, the trend of AC depends on the lag for Hopf bifurcation. During the transition, AC increases for lags less than $T/4$ and decreases for lags near $T/2$. Reproduced with permission from Bury <i>et al.</i> (2020).	134

- 6.16 The variation of EWS calculated for pressure fluctuations obtained from a turbulent combustor where the control parameter is varied continuously. Here, the rms and variance increase gradually with increase in the control parameter, whereas AC at lag 1 hardly changes during the transition. However, the Hurst exponent and the variance of AC detects the transition much before p'_{rms} rises. The variance of AC for multiple lags increases and approaches a maximum of 0.5. The autocorrelation is a periodic function of lag for a periodic signal and the variance of AC over two cycles would be 0.5. 135
- 7.1 (A) Schematic of the laboratory-scale turbulent combustor used for this study. A backward-facing step combustor with a combustion chamber having a cross-section of 90 mm × 90 mm and a length of 800 mm is used. The air flow enters through the inlet to the plenum chamber. We vary the Re of the flow continuously. Time series of pressure oscillations acquired for (B) a slow variation ($dRe/dt = 42 s^{-1}$) and (C) a fast variation of Reynolds number ($dRe/dt = 106 s^{-1}$). Initially, we observe a state of low amplitude aperiodic fluctuations for low values of Re in both cases. Then, the system transitions to a state of periodic oscillations with very high amplitude (~ 8000 Pa) for the fast variation of Re . Even though we are varying Re in the same range, we do not observe a high amplitude limit cycle for the slow variation of Re 141
- 7.2 Bifurcation diagram for experiments performed at different dRe/dt . We vary Re in the same range at different rates, thereby having different duration for the experiments. For each experiment, we plot the rms of pressure oscillations as a function of Re . We observe rate-induced tipping to high amplitude limit cycle oscillations for faster variations of the parameter ($dRe/dt > 60.3$). Slower rates of variation below a critical rate do not lead to a jump in p'_{rms} . The inset figure shows the rate of change of p'_{rms} , wherein the maximum increase in amplitude appears as a peak. This helps to define a tipping point when control parameters vary continuously. The advanced onset of thermoacoustic instability with fast rates of change of parameter can be clearly observed here. 145
- 7.3 Variation of wall temperature in time as a function of the control parameter. The dark blue curves, which are increasing up to high temperatures, represent slow rates. In contrast, the faster variations of Re result in comparatively lower values of wall temperature at a given value of Re (dark red). Even though the increase in wall temperature is gradual in time, due to the difference in the duration of the experiments, we obtain significantly different wall temperatures for a given Re for experiments at different dRe/dt . Hence, different paths are obtained in the (Re, T) parameter plane. Note that each curve in the figure corresponds to experiments of different duration. 147

7.4	A representative acoustic pressure signal showing the decay of oscillations when the fuel is cut abruptly. We extract the amplitude envelope of oscillations and fit a line in the semi-log plot to calculate the decay rate.	149
7.5	To explore the dependency of acoustic damping on the wall temperature, we measure the decay rate of the envelope of acoustic pressure oscillations, ζ , as a function of the wall temperature. We conduct a set of experiments wherein the combustion is stopped abruptly by cutting off the fuel supply during the state of periodic oscillations. We fit an exponential function to the envelope of oscillations (Culick and Kuentzmann, 2006; Perry, 1970) to measure the rate of decay of oscillations at different wall temperatures. We observe that the decay rate (a measure of acoustic damping) increases with increasing wall temperature. We fit a straight line to obtain an empirical relation between the decay rate and the wall temperature.	150
7.6	Deterministic bifurcation diagram showing stable and unstable attractors.	152
7.7	Time series of η obtained by solving the model with continuously varying α and β . We vary α at a constant rate and β at different rates: (A) fast ($\dot{\beta} = 1$) and (B) slow ($\dot{\beta} = 0.1$) rates. Here, a constant variation of α corresponds to a linearly increasing damping. Whenever the rate of change of driving is faster than the rate of variation of α , we observe tipping ($\dot{\beta} > \dot{\alpha}$). The high amplitude limit cycle oscillations occur when driving exceeds damping (A). Driving never exceeds damping for $\dot{\beta} < \dot{\alpha}$ (B).	153
7.8	Time series of η and the corresponding variation of α and β are shown for two different rates change of β . In both the cases, $\dot{\beta} > \dot{\alpha}$, i.e., β is faster than α . The onset of tipping is when driving crosses damping. However, as damping varies in time, we need more driving to overcome damping for slow variation of driving.	154
A1	The oscillations in the state z for selected values of ρ of the Lorenz system. The top figure corresponds to the state of periodic oscillations at $\rho = 165$. We observe type I intermittency (middle figure) around $\rho = 166.5$. The fully chaotic state ($\rho = 172$) is shown in the bottom figure.	163
A2	Variation of the amplitude of the dominant mode with Hurst exponent is plotted in a logarithmic scale for the data generated from models showing type I intermittency. (a), (b) correspond the three dimensional Lorenz model and the generalized Lorenz model respectively. There is no particular scaling observed during the transition in both a & b.	164
A3	Time series obtained from a model that shows type II intermittency. The top figure represents periodic oscillations corresponds to $\mu = 1.1$. We observe intermittent transitions to chaos at $\mu = 1.16$ and to a fully chaotic state around $\mu = 1.22$	165

A4	Variation of the amplitude of the dominant mode with Hurst exponent is plotted in a logarithmic scale for the data generated from model showing type II intermittency. There is no particular scaling observed during the transition.	166
A5	Time series obtained from a model of a parametrically excited nonlinear system that shows type III intermittency. The figure represents periodic oscillations (top figure) intermittency (middle figure) and a fully chaotic state (bottom figure). We observe a bifurcation happening from periodic oscillations to chaos through type III intermittency.	167
A6	Variation of the amplitude of the dominant mode with Hurst exponent is plotted in a logarithmic scale for the data generated from models showing type III intermittency. (a) plot of A vs. H for a parametrically excited nonlinear system. (b) plot of A vs. H for generalized Lorenz model with particular values of the parameter. There is no power law scaling observed during the transition in both the cases.	167
B.1	(a) A typical time series representing pressure fluctuations acquired from experiments during TAI and (b) a synthetic sine wave signal. The zoomed view shows the periodic nature of the signal.	168
B.2	(a) Time series showing acoustic pressure signals during the states of stable operation. Three representative signals I, II & III are shown along with the extracted amplitude envelope. (b) Amplitude modulated sinusoidal signals with the envelope of experimental data shown in (a). The time series I - III are acquired during the transition towards TAI; I & II represent CN, and III corresponds to INT. From I - III (b), we observe that the envelope of the signal becomes less noisy. The zoomed plot (c) shows that the signal is sinusoidal with slight amplitude variations. The limit B evaluated for H and $[\mu_2\mu_0]$ for the signals in (b) are shown in (d).	170
C.1	The inverse power law scaling between the warning time and rate of change of parameter is plotted for different values of thresholds for (a) AC and (b) H	171
C.2	Acoustic pressure fluctuations (p') acquired for a constant value of control parameter (voltage = 1.6 V and heater power = 253.7 W), lower than the Hopf point. The time series contains only low amplitude aperiodic fluctuations, and there is no transition to limit cycle oscillations. The rms of pressure fluctuations is plotted along with the signal in the top plot. The corresponding variation of all the EWS is shown as subplots. We calculate the EWS for a moving window of 1 s with an overlap of 0.98 s. p'_{rms} , AC, VAR, SKEW, K and H stay nearly constant for the total duration of the experiment, and we do not observe any significant change in the values of EWS.	172

GLOSSARY

The following are some of the commonly used terms in this thesis:

- Tipping** Sudden change in the state of a system upon gradual variations of parameters
- B-tipping** Critical transitions induced due to bifurcation.
- R-tipping** Critical transitions induced due to fast rates of change of parameter.
- Fractals** Geometric shapes containing detailed structure at different scales and they appear self-similar at various scales. Fractals have non-integer dimension.

ABBREVIATIONS

EWS	Early warning signals
CSD	Critical slowing down
AC	Autocorrelation
VAR	Variance
SKEW	Skewness
FFT peak	Amplitude of dominant mode of oscillations obtained from amplitude spectrum
TAI	Thermoacoustic instability
CN	Combustion noise
LCO	Limit cycle oscillations

NOTATION

English Symbols

H	Hurst exponent
p'	Acoustic pressure fluctuations
Re	Reynolds number
t	Time
V	Volts
I	Current
P	Power
r	Rate of change of parameter
d	Embedding dimension

Greek Symbols

$[\mu_m]^x [\mu_n]^y$	Spectral measures with indices m , n , x , and y
α	Linear damping
β	Linear driving
σ	Standard deviation
Γ	Noise intensity
\mathcal{N}	Gaussian white noise

CHAPTER 1

INTRODUCTION

1.1 CRITICAL TRANSITIONS

Critical transitions are sudden qualitative changes to the state of the system when the system parameters are varied gradually. Certain physical parameter values corresponding to the conditions at which a slight change in the parameters can cause the transition are referred to as critical points. Many natural and human-made systems such as Earth's climate, wildlife population, financial markets, and ecosystems exhibit critical transitions. They often result in dangerous and catastrophic outcomes such as the collapse of ecosystems, epileptic seizures, melting of arctic sea ice, and oscillatory instability in fluid mechanical systems. In contrast, critical transitions are desirable in some instances, such as the onset of coherent lasing in lasers.

External conditions and the system parameters often change gradually with time (Tilman *et al.*, 2001; Scheffer *et al.*, 2001). Some systems may respond in a smooth, continuous way to such changes, while others may not show any change and respond strongly when parameters approach a critical point. The sudden strong response of the system results in a 'catastrophic' transition (Scheffer *et al.*, 2001). Figure 1.1 a and b show examples of non-catastrophic transitions and Fig. 1.1c presents saddle-node or fold bifurcation as an example of catastrophic transition in ecosystems. Such catastrophic switch in the state of the system is common in systems exhibiting multistability (presence of alternate stable attractors). Most importantly, when one monitors the state of the system before the transition, little change in its state may be observed and catastrophic transitions occur typically unannounced. Therefore, obtaining early warning signals are difficult and recovering back to the previous state is hard in cases of multistability. Conditions have to be reversed further back to the forward critical point to recover (Scheffer *et al.*, 2001). Studying catastrophic critical transitions is indeed important as they are prevalent in real-world systems.

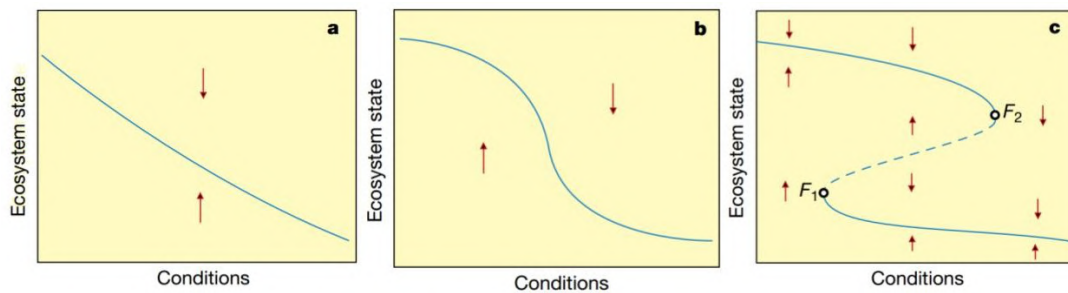


Fig. 1.1: Gradual and abrupt transitions in ecosystems. In (a) and (b), only one possible dynamical state exists for each condition. While the transition in (a) is more gradual, (b) looks like a sigmoid. Whereas, three equilibria exist for a given condition in (c) and the transition between alternative stable states on the upper and lower branches involve sudden jumps. The arrows indicate the direction of change and the dashed line represent unstable attractor (c). Adapted from (Scheffer *et al.*, 2001).

Desertification, shifts between alternate states of lake ecosystems, reef ecosystem, and oceans are some of the concerns in ecology which are generally known as 'regime shifts' in ecology. Critical transitions were studied in physics in the 1960s and were often referred to as phase transitions. Currently, critical transitions in view of climate change are the focus of major research. In climate science, the critical transitions are named 'tipping'. Different regions in the globe are categorized as tipping elements that are considered threatened by critical transitions. This includes the possible melting of Arctic sea ice (Eisenman and Wettlaufer, 2009), the transition from a wet to a dry Indian monsoon system (Zickfeld *et al.*, 2005), etc. We aim to study critical transitions in real-world systems and find commonalities across disparate systems which are related to the underlying bifurcation or the mechanism of transitions. Note that, The critical transition that we are discussing in this thesis are different from the critical phenomena or the concept of self-organized criticality (SOC) introduced by Per Bak and collaborators Bak (2013). We study self-organization to an ordered dynamical state.

1.2 MECHANISMS OF CRITICAL TRANSITIONS

There are several possible methods through which critical transitions can occur. From a mathematical point of view, Ashwin *et al.* (2012) classified critical transitions into three

types based on the mechanism through which tipping occurs.

- (a) Bifurcation induced tipping (B-tipping)
- (b) Noise induced tipping (N-tipping)
- (c) Rate induced tipping (R-tipping)

Here, we briefly explain each of these mechanism of tipping. The bifurcation-induced transition (B-tipping) occurs when a system parameter is varied slowly through the bifurcation point, leading to a transition from one stable state to another. It is commonly known as the slow passage through the bifurcation. A delay in the bifurcation is observed generally when the parameter is swept slowly through the bifurcation point (Baer *et al.*, 1989). When a system approaches and passes through a bifurcation, the stability of the current state of the system changes and the system transitions to a new stable state. A few types of bifurcations which are commonly studied in dynamical systems are saddle-node, transcritical, pitchfork and Hopf bifurcations. During the last decade, bifurcation-induced tipping has been extensively studied, especially in systems with multistability and hysteresis. The two alternative states observed with dominance of different species in the ocean sediment of the North Sea (Van Nes *et al.*, 2007) and loss of the summer sea ice cover in the Arctic (Eisenman and Wettlaufer, 2009) are two examples with alternative stable states in ecology and climate science.

Alternatively, a system can transition to a new stable state due to inherent or extraneous fluctuations, without even undergoing a bifurcation. Noise induced tipping refers to such transitions due to random fluctuations. The state of the system switches to another stable state due to the presence of noise of sufficient amplitude. In other words, noise can drive the system between the coexisting attractors in systems exhibiting multistability. Multistable systems with fractal basins of attraction are very sensitive to noise and prone to N-tipping. In practice, many systems are usually intrinsically or externally forced with perturbations of varying levels. Strong perturbations can cause early transitions well before the deterministic bifurcation, thus early warning indicators may not be reliable or even fail to detect such transitions. Noise-induced tipping

has been observed in laser systems (Huerta-Cuellar *et al.*, 2008), neuron populations (Bressloff, 2010), climate system (Lucarini and Bódai, 2017), etc.

In non-autonomous dynamical systems, rate induced tipping may occur when a rate-sensitive parameter is varied at rates faster than a critical rate. R-tipping is a scenario where the system fails to track the changing quasi-steady state (Ashwin *et al.*, 2012). The rate of variation of parameter plays a more vital role than the actual value of the parameter. Ashwin *et al.* (2012) showed that when a rate-sensitive parameter is varied as a function of time, at a slow rate, the system dynamics follows the quasi-static attractor. For faster rates of change of the parameter, above a critical rate, they observed that the system can be driven outside the basin of attraction of the quasi-static attractor, and can evolve towards a new stable state resulting in R-tipping. On the other hand, by varying the bifurcation parameter in a bistable system, one can achieve preconditioned rate induced tipping, as demonstrated by Tony *et al.* (2017). They reported that the system could be driven towards the basin of attraction of the limit cycle before the actual loss of stability of fixed point, for fast enough rates with a finite amplitude initial perturbation. Here, the tipping depends on the rate of change of control parameter and initial conditions. In these cases, the rate at which the parameter is varied determines the tipping point, not the absolute value of parameter.

R-tipping is especially important for all phenomena where system parameters or environmental (external) parameters change at a different time scale with respect to the internal dynamics of the system (Feudel *et al.*, 2018). However, a tipping in a practical non-autonomous system are usually not due to just one of these mechanisms but often a combination of all the three types of tipping. The interplay between rate of change of parameter and noise in the system can bring high variability in tipping point in practical systems. Therefore, determining the stability margin is difficult for practical systems and efficient early warning signals are necessary for critical transitions in real systems.

1.3 EARLY WARNING SIGNALS FOR CRITICAL TRANSITIONS

Many complex systems experience rapid and often unexpected shifts from one state to another. Changes in temperature and climatic conditions, and financial markets are notorious for catastrophic transitions. However, in most cases it is difficult to get information about values at which system is highly prone to tipping or the critical thresholds. Moreover, these sudden transitions are costly because it is difficult or even impossible to restore to their previous state. Just monitoring the state of the system provides no indication of an impending critical transition. To address these challenges, we need early warning signals that can detect the system's proximity to critical transition. Although predicting such critical transitions is difficult, there is indeed an architecture to such transitions. Dynamics of complex systems close to a critical point have generic properties, even for disparate systems. Many studies have proposed the use of common early warning signals (EWS) that can detect an impending tipping. Such indicators are based on general mathematical properties that are close to the critical transitions across different systems.

Critical transitions to an alternative state are most noticeable when the fluctuations in the system are fairly small. Most of the research on EWS for critical transitions has focused on this scenario, taking advantage of the fundamental property of critical slowing down (CSD) that occur on approaching a bifurcation, when the equilibrium points are about to lose their stability. Far from the transition, any perturbation in the system decays fast, whereas, as the system approaches the critical point, it recovers slowly from the external perturbations. Critical slowing down occurs when the real part of the dominant eigenvalue decreases and finally crosses zero at the bifurcation point. The slowing down starts far from the bifurcation point, and the recovery rate decreases smoothly towards the transition (van Nes and Scheffer, 2007). This slow recovery leads to an increase in the memory of the system.

1.3.1 Conventional EWS based on critical slowing down

The slowness of return to the equilibrium can be identified from the rate of recovery from external perturbations (van Nes and Scheffer, 2007; Veraart *et al.*, 2012) or can be indirectly measured from the small fluctuations in the state of the system caused by the inherent fluctuations in environmental conditions ((Ives, 1995). Information about the type of bifurcation and the distance to the bifurcation point can be obtained by analysing the recovery of the system following a perturbation. However, it is impractical to monitor the recovery rate to the perturbations in real systems, since such an endeavor would require a precisely controlled environment to study the response of the system to perturbations. Also, inherent and extraneous perturbations are always present in most of the systems. However, the decrease in resilience to the perturbations due to critical slowing down leads to an increase in the autocorrelation of fluctuations. Lag-1 autocorrelation is generally used as a measure of the slowness of recovery from natural perturbations. An increased variance of fluctuations can also occur prior to such transitions (Scheffer *et al.*, 2009; Dakos and Bascompte, 2014; Lenton *et al.*, 2012). The increase in lag-1 autocorrelation and variance as we approach a critical transition is mathematically shown by Scheffer *et al.* (2009). The lag-1 autocorrelation and the variance of the fluctuations are two commonly used early warning indicators that work based on critical slowing down. These measures have been proven to predict B-tipping, wherever the tipping is accompanied by a change of stability of the system (Scheffer *et al.*, 2009; Dakos *et al.*, 2008).

Apart from lag-1 autocorrelation and variance, several other early warning signals are commonly used in climate, ecological, financial, and biological systems. These include skewness, kurtosis, low-frequency power spectrum, flickering, spatial variance, spatial correlation and conditional heteroskedasticity (Scheffer *et al.*, 2001; Guttal and Jayaprakash, 2008, 2009; Dakos *et al.*, 2012). These measures are not directly connected to critical slowing down. However, they may show changes upon approaching critical transitions. For instance, skewness and kurtosis are the third and

fourth moments of a distribution, respectively. Skewness is a measure of the symmetry of the data distribution about its mean. In other words, it indicates whether positive fluctuations are statistically more likely than negative fluctuations and vice versa. In contrast, kurtosis provides information about whether the tails of a given distribution contain extreme values and how the tails differ from the tails of a normal distribution (Xie *et al.*, 2019). During a critical transition, these measures show variations if the change in the potential landscape causes a change in the distribution of the values of the state variable (Guttal and Jayaprakash, 2008). Different metrics of CSD with varying sensitivity have been used as EWS in different systems.

1.3.2 Possibilities and limitations of critical slowing down based early warning signals

An important application of CSD-based EWS is that it could be used in real time as a warning of increased risk of imminent transitions. Perhaps the most notable feature of CSD-based indicators is that they are generic for a range of bifurcations such as fold, Hopf and transcritical bifurcations. Unlike any system-specific indicators, the CSD-based indicators described here are related to the fundamental properties of dynamic systems. Therefore, it can be used to obtain warning for different types of bifurcations in many systems with apparently different dynamics. The systems can be as different as the climate system (Dakos *et al.* 2008), a yeast population (Dai *et al.* 2012), a lake (Carpenter *et al.* 2011) or a thermoacoustic system (Gopalakrishnan *et al.*, 2016a). These EWS are universally applicable. Despite these advantages, obviously there are many limitations.

EWS based on critical slowing down has been widely used for early detection of catastrophic regime shifts in complex natural systems. Some of these transitions may be averted if we get a warning well in advance. However, there are several difficulties in the detectability of EWS for practical systems. Critical slowing down based methods assume that the system is brought closer to the bifurcation by the variation

of parameters. This assumption does not hold for other alternative mechanisms of transition, such as noise-induced and rate-induced transitions. A large perturbation of the state of the system can trigger switching to an alternative basin of attraction, which we cannot expect to forecast (Boettiger and Hastings, 2012a). Since there are no changes in the underlying potential, CSD based EWS cannot be used to predict noise-induced abrupt transitions (Livina *et al.*, 2012). In another scenario where the control parameter changes very fast or highly nonlinearly, causing rate-induced transition, critical slowing down is not observed (Ritchie and Sieber, 2016).

Apart from these difficulties in application, we need to characterise the expected error rates, false positives, and other uncertainties involved in forecasts. Boettiger and Hastings (2012b) discussed the importance of quantifying the reliability of EWS in avoiding false alarms and their sensitivity to missing subtle warning signs. The trade-off between sensitivity and reliability of EWS needs to be quantified in order to compare the performance of different EWS for different systems. In some cases, we would rather not predict a transition than making a false alarm, and the opposite is preferred for some other systems. To avoid such confusion, they proposed using a receiver-operating characteristics (ROC) curve representing the rate of false alarms corresponding to any sensitivity. By estimating both the risk of failed detection and false alarms, the ROC curve helps us compare the performance of the different EWS with different levels of sensitivity. This curve can be used to decide which indicator to use for a particular data or system.

The performance of EWS depends on the characteristics of the data as well. Certain EWS requires the data to be evenly sampled. Interpolating the data to obtain uniformly distributed points may introduce artificially high autocorrelation. Another difficulty encountered in the application of EWS is the choice of the window size and the overlap of consecutive windows. Lenton *et al.* (2012) showed that the choice of window size could influence the results. While a shorter sliding window provides a fluctuating and less reliable indicator, large sliding windows provide smoother values (Dutta *et al.*,

2018). A large window does not help capture time varying dynamics, and a relatively smaller windows should be used. For different EWS, the optimum window size needed to have convergence in the estimates is different.

In addition to these challenges, when typical patterns in statistical measures are used as warning signals such as variance, autocorrelation, and skewness, a quantitative definition of a statistically significant detection is crucial. For EWS derived from statistical characteristics of time series, the quality of the data available is critical to the usefulness of these indicators. In some cases, detecting EWS may require high-resolution, high-quality data (Carpenter *et al.*, 2011; Dakos *et al.*, 2008; Clements *et al.*, 2015).

1.4 SCALING DURING CRITICAL TRANSITIONS

Critical transitions are often accompanied by power laws in the system properties with a singularity at the critical point. From 1960s, there have been considerable research in the field of critical phenomena, both theoretically and experimentally. One of the major aims was to determine the form of the singularities that appears in equilibrium properties at the critical point. Magnetization or susceptibility for a magnetic system and the density and compressibility for a gas-liquid transition were the commonly studied equilibrium properties. Although studying this problem theoretically was difficult for practical systems, the 2D Ising model solution paved the way for many numerical and phenomenological studies. Kadanoff [Kadanoff Physics 2, 1966] attempted to provide a generic description of Ising model, which can be applied to various systems. He proposed scaling theory with various critical exponents which are assumed to characterize the complete nature of the singularities. This was similar to the scaling relations derived by Widom [B. Widom 1965] for critical point anomalies in experiments. Several others have proposed similar relations and critical exponents for various systems, from empirical observations or heuristic arguments [JW Essam 1963, ME Fisher 1967, C. Domb 1965].

1.4.1 Universality and data collapse

The concept of universality has become one of the pillars of statistical physics. The emergence of universality and data collapse is widespread and it appears in various forms. To give an introduction to universality accompanied by data collapse, let us see the example of critical phenomenon of liquid-gas transition in fluids [Hohenberg, P. C, 1977, Stanley, H. E, 1999, Lübeck 2004]. When a gas is isothermally compressed, at a certain pressure it changes to liquid state without any change in pressure. If the process is repeated at a higher temperature, the same phenomenon occurs, but at a different value of pressure. After a particular temperature, $T = T_c$, liquefaction of the gas is not possible by increasing the pressure. At this critical point liquid-vapour boundary vanishes. In the close vicinity of T_c , the fluid shows large fluctuations, since it is between a relatively ordered liquid state and a disordered gaseous state. Density fluctuations very close to the critical point are related to short-lived liquid state bubbles in the gas. When the critical point is approached, these fluctuations become long lived and infinitely long ranged, and liquid and vapor state coexist. Such behaviour of infinite lifetime of fluctuations and the infinite range of correlation close to the critical point, is not sensitive to the type of gas considered.

All the gases behave the same way near the critical point and this referred as universality. Although the critical point (temperature, volumes and pressure) is different for each of the gases, the equation of state near the critical point with variables scaled with the critical point (P/P_c , T/T_c & V/V_c) will be just one curve. Therefore, the equation of state collapses into a single equation, regardless of the nature of the fluid. Universality and data collapse are observed everywhere in various forms in network dynamics [Barzel, B, 2013], financial markets [Denys, M., 2016], Bose–Einstein condensate [Klinder, J., 2015], supercritical fluids [Ha, M. Y., 2020], neuronal network [Friedman, N, 2012], brain [Bhattacharya, J. ,2001, Serafino, M. et al 2021], etc. A fundamental and deeper understanding of universality and scaling is provided by Wilson’s renormalisation group theory (Wilson, 1971*a,b*), which is a topic in itself.

Scaling laws have received a lot of attention in equilibrium thermodynamics for critical transitions. Kadanoff proposed scaling relations near critical points in both theory and experiments. The basic theoretical concepts are brought via the molecular field theory approach, that uses the concept of an order parameter and indicates the close relations among different phase transition problems (Kadanoff, 1966; Kadanoff *et al.*, 1967). Halperin and Hohenberg (1967, 1969) generalized Kadanoff's scaling laws to dynamic critical phenomena. Further, the renormalization group is used to explain Kadanoff's scaling theory (Wilson, 1971*a*). The concept of scaling, universality, and renormalization became popular and are considered as the three pillars of the modern theory of critical phenomena (Stanley, 1999).

1.4.2 Equilibrium phase transitions

A unified theoretical framework has been established for the case of equilibrium phase transitions. Perhaps the best-known classic example of the equilibrium phase transition is the Ising model, which can describe the liquid-vapor phase transition and the transition from order to disorder in magnetic materials. The phase transition of an equilibrium system is characterized by the singularity of the free energy and its derivatives. A discontinuity in physical quantities on approaching the critical point are observed due to this singularity. An order parameter is defined to describe the phase transition, which have non-zero value in the ordered phase and goes to zero for the disordered phase.

The paradigmatic example of equilibrium phase transitions, the Ising model, is a simplified model for paramagnetic to ferromagnetic transitions in magnetic systems. This model is defined on a d -dimensional lattice with N sites and each site, i , can take spin $S_i = \pm 1$. Magnetization, $M = (1/N) \sum_i S_i$ can be considered as the order parameter. At a critical temperature, the Ising model exhibits a phase transition from a state of non-zero magnetization to zero magnetization similar to ferromagnetic to paramagnetic phase. Although magnetization varies continuously at $T = T_c$, its

derivatives or change in the magnetization at T_c is singular and is described by a continuous second order phase transition [Henkel et al. 2008 (book)]. If the system undergoes phase transition for $T < T_c$ by varying an external magnetic field, the magnetization changes discontinuously which can be referred to as first order phase transitions. Such sudden changes in system properties with a slight change in the parameter, or first-order phase transitions, are often known as catastrophes (Thom 1972; Zeeman 1977; Gilmour 1981; Arnold 1984; Poston and Stewart 1978; Deakin 1980; Jackson 1991).

1.4.3 Non-equilibrium phase transitions

The models for equilibrium systems such as Ising model are elegant examples of how complex dynamics emerges from local interactions. The idealized and simplified concept of equilibrium systems could illustrate phase transitions, universality in the dynamics close to critical point, etc., and had a great impact in setting up the framework for studying critical phenomena in practical systems. In fact, almost all systems in nature are out-of-equilibrium. Most of them are open systems where they are connected to external reservoirs and the exchange of energy, particles, or other conserved quantities with reservoirs results in nonvanishing energy, mass, or current flow. Besides, real systems may experience strong time-dependent external perturbations. While theoretical description of equilibrium systems has been understood for more than a century, a fundamental conceptual framework for nonequilibrium systems does not yet exist in spite of considerable efforts. A complete classification of all possible universality classes in non-equilibrium systems remains difficult to this day, due to the increasing complexity.

Nevertheless, in the past decades, there were some advances in the investigation of nonequilibrium phase transitions in stochastic dynamical systems using numerical and theoretical methods. Critical transitions in non-equilibrium systems have garnered much research interest in the last few decades. As with equilibrium critical phenomena,

the concept of universality and scaling are the most important tool for characterizing the wide variety of non-equilibrium phase transitions. All systems within a particular universal class follow certain scaling functions which are identical near the critical point and they possess the same set of critical exponents. As the concept of universality is well studied and established for equilibrium phase transitions, the central concept of universality, which proved to be so useful, can be extended to the non-equilibrium case as well.

For various kinds of transitions such as the transition to turbulence, critical transitions and order emerging from chaos, there exist some universal scaling laws. Let us see the case of transition to turbulence or the onset of chaos. The studies done by Huberman and Rudnick (1980) identified a scaling behavior of chaotic flows. Near the critical point for the onset of chaos, the envelope of Lyapunov exponent seems to approach zero with a power-law behavior in systems exhibiting period doubling bifurcation. There are many well-understood transitions to chaotic solutions. The three popular routes to turbulence in dissipative systems Eckmann (1981), corresponding to universality classes, are namely period doubling route, intermittency route and quasi-periodicity route.

Feigenbaum discovered universal constants that determine the transition to turbulent behavior for a large class of nonlinear systems undergoing period doubling route to chaos (Feigenbaum, 1978, 1979, 1983; Bountis, 1981). The second route to chaos observed is via intermittency wherein intermittent transition to turbulence happens in dissipative systems (Pomeau and Manneville, 1980). Intermittency refers to a state in which laminar flow is interrupted by turbulent bursts at apparently random intervals. During the bursts, the trajectory goes to a larger chaotic attractor with the old attractor as a subset of the larger one. Three types of bifurcations show these characteristics, namely, cyclic fold, subcritical Hopf, and subcritical period doubling bifurcations (Nayfeh and Balachandran, 2008a) and the intermittencies corresponding to these bifurcations are labeled as type I, type II and type III, respectively (Pomeau

and Manneville, 1980). Different types of intermittency follow characteristic scaling laws (Schuster and Just, 2006). The scaling suggests that the duration of the laminar region is $O(\epsilon^{-1/2})$ for type I intermittency, $O(\epsilon^{-1})$ for type II and type III intermittency, ϵ being a control parameter. Apart from these three standard types, there are other kinds of intermittencies such as on-off intermittency with a power law exponent of $-3/2$ (Heagy *et al.*, 1994) and spatio-temporal intermittency for which critical exponents are still not settled. Intermittency is observed both in experiments involving turbulent flows and in models based on nonlinear system of equations such as Lorenz equations employed by Pomeau and Manneville (1980). Another established route to chaos is the quasi-periodic route, wherein a finite number of Hopf bifurcations lead to chaos (Ruelle and Takens, 1971).

Similar to the universalities observed in equilibrium critical transitions, there are scaling behavior identified for self-organization in turbulence. There are studies on the emergence of order in plasma and fluids as self-organization in turbulence (Shats *et al.*, 2006). The plasma self-organizes from plasma turbulence to a quasi-coherent state. For this transition, Tham and Sen (1994) experimentally obtained simple scaling relationships between the electrostatic fluctuation levels and the linear growth rate. Universality and scaling behavior have been investigated and well-understood for equilibrium critical transitions and the transition to turbulence. However, universal scaling behavior for order emerging from turbulent flows as self-organization is not thoroughly established. Furthermore, although emergence of order and pattern formation are widely observed in natural and engineering systems, universal characteristics of self-organization to ordered dynamics in disparate physical systems are unexplored.

1.5 THE CURRENT SCENARIO AND MOTIVATION

Critical transitions in real-world complex systems are not well understood and are challenging, while they are extensively studied in simple isolated systems (Scheffer

et al., 2012). Thus, investigating critical transitions in practical systems has great relevance. We aim to explore the dynamics during critical transitions in various systems such as fluid mechanical, optical and electronic systems. Also, studying critical transitions in fluid mechanical systems has immediate applications in solving industrial problems such as forewarning and mitigation of catastrophic transitions in power producing gas turbines, rockets, etc.

Systems with an underlying turbulent flow can often exhibit transitions to oscillatory instabilities as a result of interactions among the subsystems. The emergence of such oscillatory instability in practical systems such as thermoacoustic, aeroacoustic and aeroelastic systems can lead to catastrophic outcomes (Lieuwen and Yang, 2005; Flandro and Majdalani, 2003; Larsen and Walther, 1997). For example, oscillatory instabilities result in losses worth billions of dollars for the gas turbine industry (Fleming, Feb 13, 1998). Extensive research has been carried out to understand the dynamics of each of these systems independently. So far, the emergence of such oscillatory instabilities in different systems such as thermoacoustic, aeroacoustic and aeroelastic systems has been studied using different approaches. The various frameworks used to study oscillatory instabilities are very system-specific. Also, the attempts to find common elements across these systems are rare. We aim to analyse critical transitions in diverse physical systems to explore universal dynamical behavior close to critical transitions.

Apart from the transition to oscillatory instabilities in fluid mechanical systems, we extend our investigation of generic features during critical transitions to emergence of order from disorder to more diverse systems such as optical and electronic systems. While critical transitions in these systems have been studied, ‘universal characteristics’ of the transition to ordered dynamics garnered less attention. Finding an element of commonality during such critical transitions means that the solution to a given problem is independent of the details of the problem set-up, and entirely different physical systems can be described in the same way (Kadanoff, 1990).

Understanding the universal features during critical transitions in real-world systems will help in devising predictive schemes for undesirable critical transitions. In the case of transition to oscillatory instabilities, knowing beforehand the amplitudes of oscillations that are expected after transition helps devise strategies to mitigate the effects. The universal features close to the transition or scaling relations can be used to predict the onset and the amplitude of oscillatory instability.

Furthermore, much of the literature on critical transitions and their early warning signals (EWS) focuses on quasi-steady variation of control parameters to determine the stability of the system. Most critical transitions occurring in nature involve system parameters changing continuously (Tsotsis *et al.*, 1988; Kapila, 1981) along with a considerable intensity of noise in the system. The existing studies focused on the continuous variation of parameters employ numerical analysis of standard bifurcation models (Bilinsky and Baer, 2018; Ashwin *et al.*, 2017) and limited experimental studies are available (Bonciolini *et al.*, 2018; Scharpf *et al.*, 1987; Tony *et al.*, 2017; Pisarchik *et al.*, 2014). We aim to study the effects of rate of change of control parameter on the performance of various EWS by investigating the variation of warning time provided by EWS with the rate of change of parameter. When the system parameters vary continuously, the effect of rate of change of parameter on warning time has never been explored before. Apart from the effects of the rate of change of parameters on bifurcation, there are scenarios where the rate can induce sudden transitions without having an underlying bifurcation. Ashwin *et al.* (2012) classified this as rate induced transition (R-tipping). While the quasi-steady variation of parameter exhibits no bifurcation, a continuous variation at a rate faster than the critical rate can cause transitions. Tony *et al.* (2017) achieved preconditioned R-tipping in an experimental system with subcritical Hopf bifurcation. We investigate and demonstrate the mechanism of R-tipping in a real-world system.

1.6 OBJECTIVES OF THE CURRENT THESIS

The primary objective of the thesis is to identify universal features of critical transitions in diverse physical systems and develop predictive schemes for impending critical transitions. Another objective is to study the effect of the rate of change of parameters on critical transitions and their early detection. The specific objectives are:

- (a) Analysis of critical transitions in diverse physical systems to explore universal dynamical behavior close to critical transitions.
- (b) Characterize the dynamics during the emergence of order from disorder in fluid mechanical, optical, and electronic systems by analysing time series data of the system variables acquired experimentally and their power spectra.
- (c) Develop early warning and predictive schemes for undesirable critical transitions from the inferences obtained by studying the generic properties of critical transitions. Forewarn the onset of oscillatory instabilities and predict their amplitude at the onset, well before the transition.
- (d) Investigate critical transitions in non-autonomous systems to identify the effect of the rate of change of parameters on critical transitions and their early warning signals.
- (e) Demonstrate rate-induced transition in experiments and identify the mechanism of rate induced critical transitions for fast variation of parameters.

1.7 OVERVIEW AND SCOPE OF THE THESIS

We study critical transitions in diverse physical systems. Universal characteristics of critical transitions are explored in fluid mechanical, optical and electronic systems. A significant part of this work is done by analyzing the critical transitions to oscillatory instabilities in thermoacoustic systems and then by performing similar experiments in other systems. Therefore, we carry out a detailed literature survey on critical transitions in thermoacoustic systems, which is summarized in Chapter 2. Moreover, the results of our work find immediate applications in real-world thermoacoustic systems such as gas turbine and liquid rocket engine combustors.

The transition to oscillatory instabilities in turbulent fluid mechanical systems has been studied extensively in the past in different system-specific methods. A universal route through which oscillatory instabilities emerge in turbulent flows is presented in Chapter

3. Then, we consider a wider variety of systems showing the emergence of order from disorder and investigate the evolution of power spectrum during such transitions and arrive at scaling laws in Chapter 4. Chapters 3 & 4 are focused on arriving at scaling laws. Subsequently, the estimation of amplitude of oscillatory instabilities using the results from Chapters 3 & 4 is illustrated in Chapter 5.

The chapters 6 & 7 focus on critical transitions in non-autonomous systems, where the control parameter is varied at different rates to study the effect of rate of change of parameter on the onset of critical transition and their EWS. Underlying mechanisms of R-tipping are unexplored in real complex systems. Chapter 7 demonstrates a mechanism of R-tipping in a turbulent thermoacoustic system. Finally, in Chapter 8, we summarize our findings and their implications, and discuss some directions for future research.

CHAPTER 2

Critical transitions to oscillatory instability and their early warning signals in thermoacoustic systems

¹Oscillatory instabilities in fluid mechanical systems are prevalent across natural and engineering systems. They manifest as high amplitude periodic oscillations in the system variables. The phenomenon of oscillatory instability with large amplitude self-sustained oscillations can cause catastrophic damages in many engineering systems. For instance, thermoacoustic instability encountered in practical combustion devices such as gas turbine engines and rocket motors is a significant challenge faced by the propulsion and power industry (Juniper and Sujith, 2018; Lieuwen and Yang, 2005). The spontaneous emergence of high amplitude oscillations results in severe vibrations, fatigue, wear and tear, structural failure, failure of navigation and control systems, and reduced life span of the combustor. Further, the consequences of thermoacoustic instability include enhanced heat transfer leading to increased thermal and mechanical loading to the combustor and eventual failure of the thermal protection system. In extreme cases, thermoacoustic instability has resulted in forced shutdowns of power-producing gas turbines (Lieuwen and Yang, 2005) and mission failures in the case of rockets (Fisher and Rahman, 2009).

Note that the oscillatory instabilities that we are discussing in this thesis are stable limit cycle oscillations according to the definition of dynamical systems theory. However, these dynamically stable limit cycle oscillations appear as violent, dangerous oscillations in fluid mechanical systems. The state of oscillatory instability is not a stable configuration, considering the health of the system. Thus, the term oscillatory ‘instability’ has been used to describe high amplitude limit cycle oscillations in thermoacoustic, aeroacoustic and aeroelastic systems.

¹Contents of this chapter are published as a review paper (Pavithran *et al.*, 2021*b*).

The transition to oscillatory instability often occurs when a system parameter is varied. Under certain operating conditions, the interaction among the subsystems of the fluid mechanical system results in the establishment of a positive feedback mechanism (Rayleigh, 1878). Thermoacoustic instability arises due to this positive feedback between the unsteady heat release rate fluctuations and the acoustic field in a confinement (Fig. 2.1) (Poinsot *et al.*, 1987; Güthe and Schuermans, 2007; Pawar *et al.*, 2017; McManus *et al.*, 1993; Mondal *et al.*, 2017). During the transition from a stable operating state to an oscillatory state, the dynamics of the system undergoes a sudden qualitative change.

A turbulent thermoacoustic system is a complex system wherein the nonlinear interactions between the turbulent flow and the other subsystems lead to the emergence of self-organised and ordered dynamical states (Sujith and Unni, 2020). During the occurrence of thermoacoustic instability, spatially ordered patterns such as large coherent structures are formed (George *et al.*, 2018*b*), while we observe periodic oscillations in the temporal evolution of the system variables. The emergence of coherent dynamics in the flow, in turn, affects the coupling between the subsystems. During this state of thermoacoustic instability, the interaction among the subsystems is very strong and accompanied by ruinously large amplitude self-sustained pressure oscillations.

The transition to thermoacoustic instability is a critical transition. When the control parameter is changed gradually, a minor change can trigger a transition to a contrasting state. The value of the parameter at which the state of the system shifts abruptly to another state in response to a slight change in the parameter is known as 'critical point'. This sudden shift in the state of a system when parameters are changed past a critical point is commonly referred to as critical transition or tipping (Scheffer *et al.*, 2009, 2012). What causes some systems to have such critical transitions? The basic factor causing critical transitions is a positive feedback mechanism (Scheffer *et al.*, 2012; Angeli *et al.*, 2004). According to Scheffer *et al.* (2012), while these concepts are

well studied in simple isolated systems, critical transitions in real complex systems are challenging. Thus, studying critical transitions in thermoacoustic systems has great relevance as it is a practical complex system that can be used as a test bed for tools from complex systems theory.

Until recently, thermoacoustic transitions have not been studied from the point of view of critical transitions. Critical transitions in a practical thermoacoustic system are undesirable. Therefore, there is an increasing demand in developing early warning signals (EWS) to detect the proximity of the system to a critical transition (Gopalakrishnan *et al.*, 2016a). Early detection of thermoacoustic transitions is of utmost importance as it enables us to initiate appropriate control strategies to prevent or mitigate the consequences of the impending catastrophe.

Flame blowout is another undesirable dynamics of a combustion system that leads to unscheduled shutdown of engines. Combustors operating in lean fuel conditions may experience flame blowout (Shanbhogue *et al.*, 2009). Flame blowout can be described as a transition from a reacting state to a non-reacting state in combustion systems. Blowout can lead to flame extinction, which is highly detrimental in gas turbine and aircraft engines. Therefore, early detection of blowout and the development of strategies to mitigate it are crucial from a practical viewpoint (Sujith and Unni, 2021).

Here, we discuss the early warning signals used for critical transitions in both laminar and turbulent thermoacoustic systems. A thermoacoustic system can either be in laminar or turbulent regime, each exhibiting significantly different dynamics. In laminar systems, the transition to thermoacoustic instability is equivalent to the transition from a fixed point to limit cycle oscillations. In contrast, the transition in turbulent thermoacoustic systems has been shown to be a transition from chaos to order (Nair *et al.*, 2013; Tony *et al.*, 2015). The transitions in both laminar and turbulent systems are detailed in the forthcoming sections. Different types of EWS are used to detect the transitions for these systems. This review focuses primarily on highlighting how the presence of inherent fluctuations in the system during the stable operation provides

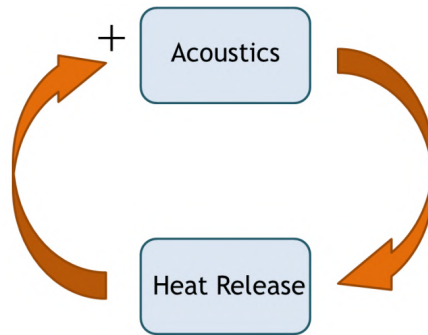


Fig. 2.1: A schematic representation of the feedback mechanism between the subsystems during thermoacoustic instability. The coupling between the acoustic field in the combustor and the unsteady heat release rate fluctuations drives self-sustained oscillations.

EWS.

2.1 TRANSITIONS IN LAMINAR SYSTEMS

Traditionally, transition to thermoacoustic instability was viewed as a transition from a fixed point to limit cycle oscillations (Lieuwen, 2002; Ananthkrishnan *et al.*, 2005). Ideally, this paradigm is appropriate only for the case of laminar thermoacoustic systems. The stable operation prior to the onset of thermoacoustic instability has a quiescent dynamical state with very low amplitude pressure fluctuations. These negligibly low amplitude pressure fluctuations are comparable to the inherent noise in the system or may even correspond to the measurement noise. This state of the system can be considered as a stable fixed point in terms of dynamical systems theory. Any small perturbations in the system decay during this stable operating state. On the other hand, during thermoacoustic instability, we have a state of stable limit cycle oscillations. We observe a Hopf bifurcation from a fixed point to limit cycle oscillations in laminar thermoacoustic systems. The bifurcation can be either subcritical or supercritical Hopf bifurcation depending on the operational conditions and the control parameter (Etikyala and Sujith, 2017). The transition occurs gradually for supercritical bifurcation; while reversing the parameter, limit cycle oscillations disappear at the Hopf point (Fig. 2.2a). In contrast, there is a jump in the amplitude for subcritical Hopf bifurcation as we cross

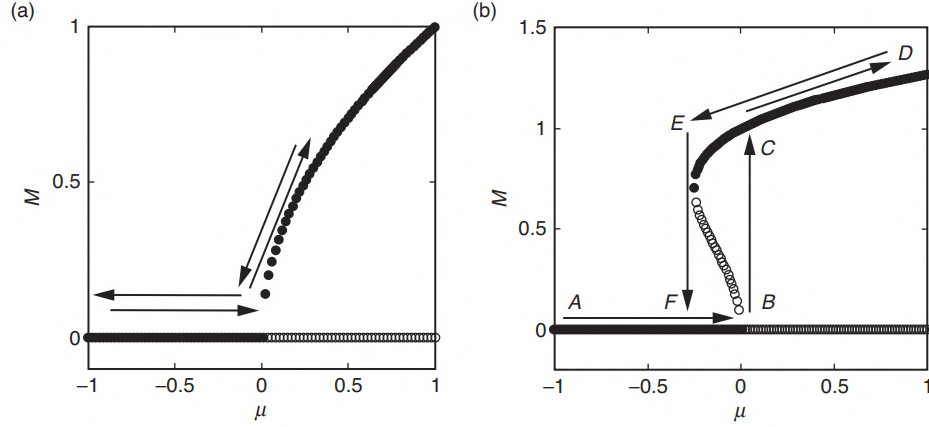


Fig. 2.2: (a) Supercritical bifurcation and (b) Subcritical bifurcation plots representing transitions in laminar systems. The filled and the empty circles denote the stable and unstable solutions of the the normal form equations of Hopf bifurcation, respectively. Supercritical bifurcation has a continuous transition, whereas subcritical bifurcation has an abrupt transition and has a hysteresis (BCEF) while reversing the parameter. Reproduced with permission from Gopalakrishnan and Sujith (2014)

the bifurcation point (Hopf point). Further, a subcritical bifurcation exhibits hysteresis, where a simple reversal of the parameter to the Hopf point is not sufficient to revert back to the fixed point state of the system (Fig. 2.2b). The parameter needs to be reversed until the fold point to go back to the fixed point. In this case, the system is bistable in the hysteresis region, as it has both stable fixed point and limit cycle solutions. Based on the initial condition or the level of perturbations, the dynamics can be attracted either to the fixed point or to the limit cycle (Etikyala and Sujith, 2017; Subramanian *et al.*, 2010; Gopalakrishnan *et al.*, 2016b).

Bifurcations other than Hopf bifurcations also occur in thermoacoustic systems (Jahnke and Culick, 1994; Lei and Turan, 2009; Sterling, 1993). Jahnke and Culick (1994) showed a pitchfork bifurcation and a torus bifurcation leading to quasiperiodic oscillations. Lei and Turan (2009) have reported chaotic oscillations using a mathematical model for a thermoacoustic system, and Sterling (1993) has observed a period doubling transition in a simple nonlinear model of a thermoacoustic system. In an experimental study in a ducted laminar premixed combustor, Kabiraj *et al.* (2012) observed a series of bifurcations. They observed periodic, quasiperiodic, aperiodic or

chaotic oscillations. As they changed the location of the flame inside the duct, there was a qualitative change in the dynamics. First, the steady-state characteristics in the laminar premixed combustor changed to periodic oscillations via subcritical Hopf bifurcation. In the subsequent bifurcations, the dynamics of the combustor transitioned to oscillations having more than one dominant frequency. The periodic signal changed to quasiperiodicity through a Neimark-Sacker bifurcation, and then to chaos through the Ruelle-Takens route (Nayfeh and Balachandran, 2008a). Figure 2.3 shows this bifurcation diagram. Recently, the presence of strange non-chaotic oscillations was reported in the same system (Premraj *et al.*, 2020).

Apart from these types of dynamics, Kabiraj and Sujith (2012) observed a state of intermittency during the transition to flame blowout. The intermittency route to chaos in a laminar thermoacoustic system was recently demonstrated by Guan *et al.* (2020). Here, intermittency is characterised by alternating epochs between high-amplitude irregular or chaotic dynamics and low amplitude periodic dynamics. Ananthkrishnan *et al.* (1998) has explained another route to large amplitude oscillations as a primary Hopf bifurcation followed by a secondary fold bifurcation. Such a secondary bifurcation has been observed experimentally in a laminar system by Mukherjee *et al.* (2015) and in a turbulent system by Singh *et al.* (2020).

There have been several studies on developing models to explain these bifurcations and the nonlinear dynamical behaviours observed in thermoacoustic systems. Lei and Turan (2009) modelled the dynamics by considering a simple non-autonomous system. Subramanian *et al.* (2013) described the bifurcations in a laminar thermoacoustic system known as Rijke tube, using Stuart-Landau equations. Further, they analytically derived the relation between the nonlinearity in the model and the criticality of the bifurcation. Kashinath *et al.* (2014) used multi-mode simulations to show the significant contributions of the higher harmonics to the nonlinear dynamics and were able to replicate similar results as observed in experiments conducted by Kabiraj and Sujith (2012). Later, models based on synchronisation of oscillators have been developed to

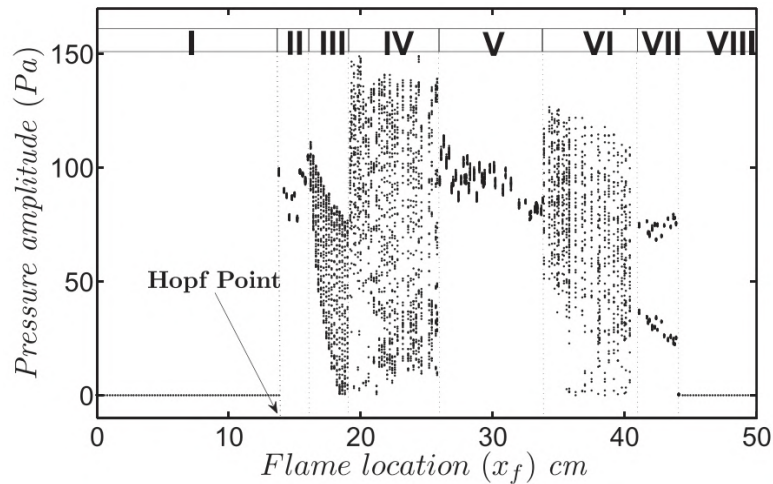


Fig. 2.3: Bifurcation plot for a laminar thermoacoustic system known as Rijke tube showing a sequence of bifurcations for different values of x_f . Reproduced with permission from Kabiraj *et al.* (2012).

explain the transition to chaos in laminar thermoacoustic systems (Weng *et al.*, 2020).

2.2 TRANSITIONS IN TURBULENT SYSTEMS

Most practical thermoacoustic systems are turbulent in nature. As mentioned earlier, the transition from fixed point to limit cycle oscillations is an apt description for laminar systems, but inadequate to describe the transition occurring in turbulent combustors. Fundamentally, the characteristics of transitions observed in turbulent systems are significantly different from those of laminar systems.

The dynamics during the stable operating state of a turbulent combustor cannot be approximated as a fixed point; rather, the turbulent background flow brings inherent fluctuations in the system variables such as acoustic pressure, heat release rate, and velocity. For turbulent fluid mechanical systems, the stable operating state with low amplitude aperiodic fluctuations was identified as high dimensional deterministic chaos contaminated with measurement and dynamic noises (Nair *et al.*, 2013; Tony *et al.*, 2015). In addition, this state is observed to have multifractal characteristics arising from the underlying turbulent fluctuations (Nair and Sujith, 2014). As we approach the onset of thermoacoustic instability, we observe bursts of periodic oscillations amidst low amplitude chaotic oscillations (Fig. 2.4). In general, a state of intermittency presages the

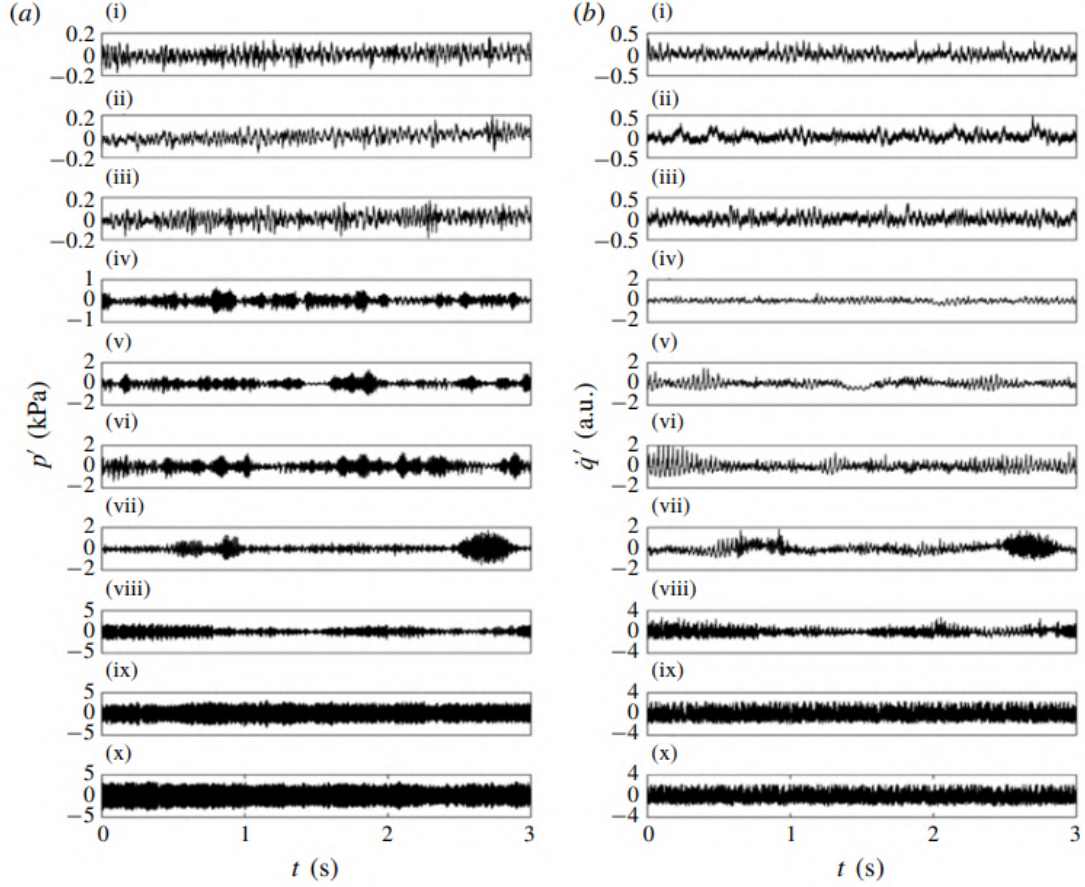


Fig. 2.4: Time series of acoustic pressure (left column) and heat release rate oscillations (right column) acquired at various Reynolds numbers, illustrating the transition to thermoacoustic instability. Reproduced with permission from George *et al.* (2018b).

transition to self-sustained periodic oscillations in turbulent fluid mechanical systems such as thermoacoustic, aeroacoustic, and aeroelastic systems (Nair *et al.*, 2014c; Nair and Sujith, 2016; Venkatramani *et al.*, 2016). A turbulent system exhibits rich dynamical behaviour during the transition to oscillatory instability. Statistical measures such as rms and variance of pressure fluctuations vary more gradually during the transition from chaos to limit cycle oscillations via intermittency as compared to a classical subcritical Hopf bifurcation.

While studying this transition, the effects of turbulence are often neglected as background noise in the traditional approach, where we separate the measured variables into signal and noise. However, treating these fluctuations with their inherent

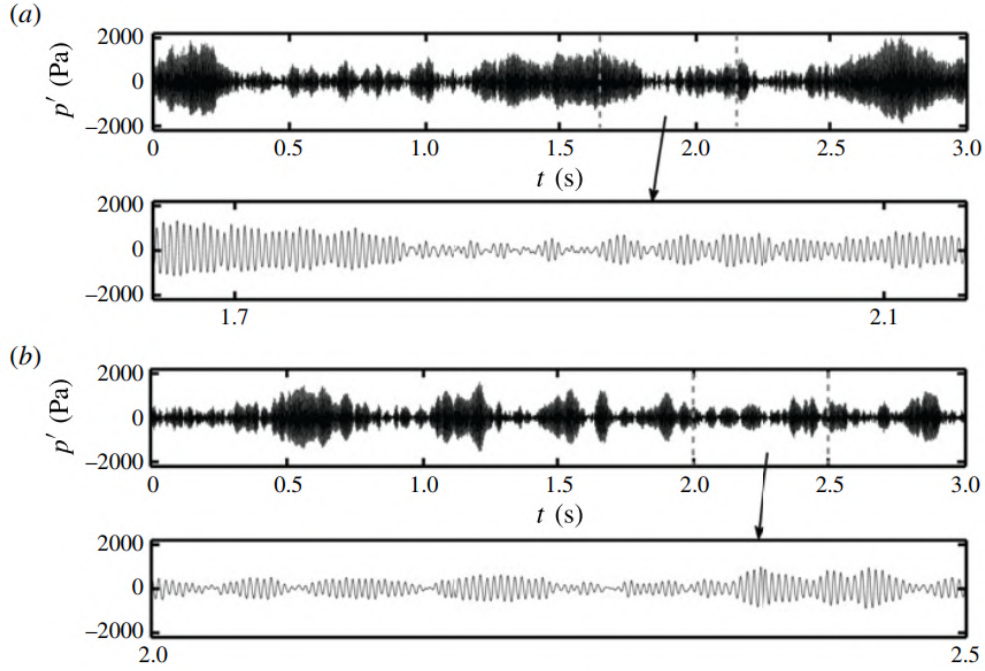


Fig. 2.5: Time series of acoustic pressure fluctuations during intermittency acquired from (a) a bluff body stabilised combustor and (b) a swirl stabilised combustor. The zoomed views show epochs of large-amplitude oscillations amidst low-amplitude aperiodic fluctuations. Reproduced with permission from Nair *et al.* (2014c).

complexities, as opposed to the ‘signal plus noise’ approach, enables us to obtain precursors to the impending transitions in practical systems. Moreover, quantifying the complexity using tools from nonlinear dynamics enables the prediction of these transitions well before the growth of amplitude of pressure oscillations. In this context, characterising the intermittency statistics also helps in forewarning the transitions (Nair *et al.*, 2014c). Further, the intermittency observed during the transition to oscillatory instabilities (Fig. 2.5), has large amplitude periodic oscillations and low amplitude aperiodic fluctuations as opposed to the intermittency types (I, II and III) described by Pomeau and Manneville (1980). Hence, we have a different type of intermittency compared to classical intermittencies. The presence of a particular type of intermittency indicates that the transition to oscillatory instability in turbulent fluid mechanical systems occurs via a unique route. Such transitions have not been explored from the perspective of critical transitions.

2.3 EWS FOR CRITICAL TRANSITIONS

2.3.1 Critical slowing down based EWS

Critical slowing down occurs for a range of bifurcations such as fold, Hopf and transcritical bifurcations. It is a phenomenon associated with the loss of stability as the control parameter approaches a bifurcation point. The phenomenon of slowing down of the dynamics on approaching a transition is known as critical slowing down (CSD) and a detailed explanation is presented in Sec. 1.3.1. The slowing down starts far from the bifurcation point, and the recovery rate decreases smoothly towards the transition (van Nes and Scheffer, 2007).

The perturbations can be anything such as stochastic contents in the system or extraneous noise. In most cases, when approaching a catastrophic bifurcation where the current state loses stability, the potential landscape changes. Therefore, far from the transition, if such a system is stochastically forced, the time evolution of the system is characterised by low values of correlations in the time series. When the system is close to the transition, the basin of attraction may shrink, and recovery from perturbations is slow. Consequently, there is a longer memory for perturbations. A stronger correlation between states at subsequent time intervals and the dynamics in the presence of noise are characterised by a larger standard deviation. Lag-1 autocorrelation is generally used as a measure of the slowness of recovery from natural perturbations. An increased variance of fluctuations can also occur prior to such transitions (Scheffer *et al.*, 2009; Dakos and Bascompte, 2014; Lenton *et al.*, 2012).

Several other early warning signals such as skewness, kurtosis, low-frequency power spectrum, flickering, spatial variance, spatial correlation and conditional heteroskedasticity are commonly used in climate, ecological, financial, and biological systems (Scheffer *et al.*, 2001; Guttal and Jayaprakash, 2008, 2009; Dakos *et al.*, 2012). Skewness is a measure of the symmetry of the data distribution about its mean. In contrast, kurtosis provides information about whether the tails of a given distribution contain extreme values and how the tails differ from the tails of a normal distribution.

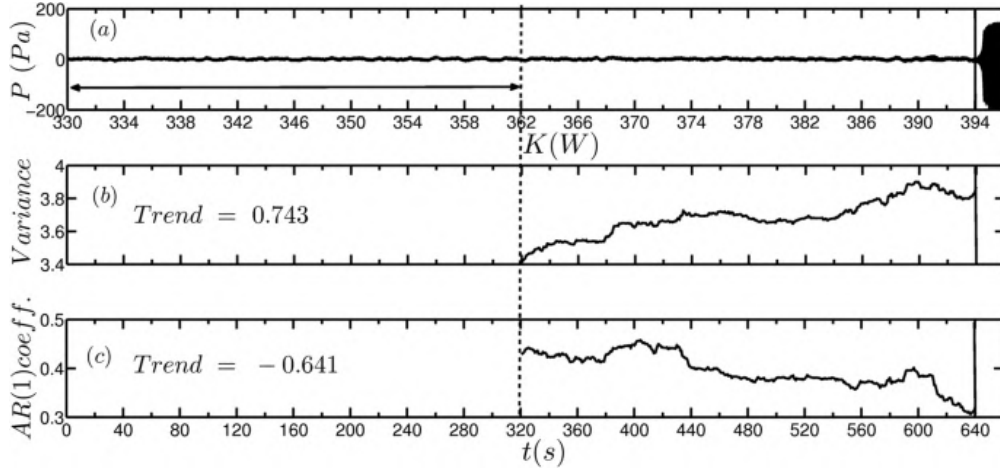


Fig. 2.6: (a) Time series of pressure fluctuations during the transition to thermoacoustic instability in a laminar system where the control parameter K is increased in time. Variation of (b) variance and (c) lag-1 autocorrelation calculated for a moving window of half the size of the time series. A consistent increase or decrease in the value of a measure is expressed as trend. Reproduced with permission from Gopalakrishnan *et al.* (2016a).

These measures detect the change in distribution of the data during critical transition and are discussed in Sec. 1.3.1.

In a laminar thermoacoustic system, Gopalakrishnan *et al.* (2016a) demonstrated the working of CSD based early warning signals for a subcritical Hopf bifurcation. They performed experiments in a laminar thermoacoustic system by varying the control parameter every 20 s. They calculated CSD based EWS such as the lag-1 autocorrelation, variance, and conditional heteroskedasticity (Seekell *et al.*, 2011). They found that the variance provides the most robust early warning sign of impending thermoacoustic transitions (Fig. 2.6). Conditional heteroskedasticity was estimated by considering the time series as an autoregressive process, and it captured the transition in all the cases they analysed. The lag-1 autocorrelation showed an unexpected decreasing trend on approaching the critical point for experimental data. They attributed the lack of robustness of autocorrelation (AC) to the use of only a single realisation of the data. Recently, An *et al.* (2019) used these critical slowing metrics for the data acquired in a combustor during testing of a gas turbine engine to develop early warning signals for imminent thermoacoustic instability.

Other traditional measures such as root mean square of oscillations (rms), and the amplitude of the dominant mode of oscillations from the amplitude spectrum are generally used (Lee and Santavicca, 2003; Richards *et al.*, 2003). Lieuwen (2005) used the envelope of AC as a function of lags to calculate the damping coefficient at each operating condition. The envelope of the oscillatory AC is calculated using the Hilbert transform, and the damping coefficient is estimated by fitting an exponential decay function to this envelope of autocorrelation. They used this methodology to determine the dynamic stability margin, as the damping coefficient decreases during the transition.

2.3.2 Fractal and multifractal measures

Fractal patterns are everywhere in nature, including trees, rivers, mountains, clouds, seashells, coastlines, etc. Geometrically, fractals have non-integer dimensions. Fractals exhibit self-similar patterns across different scales, and statistical measures of a fractal such as length, surface area and volume depend on the scale of measurement. A double logarithmic plot of these measures as a function of the scale of measurement would show a straight line, and the negative of the slope of this line is referred to as the ‘fractal dimension’ of the fractal object.

A fractal time series displays properties dependent on the time scales of observation and has a dimension between one and two (Mandelbrot, 1983). A mathematical fractal time series $x(t)$ at some scaling c is written as $x(ct) = x(t)/c^H$, where H is a constant (West *et al.*, 2003). The scaling exponent H refers to the Hurst exponent of the time series and $H = 2 - D$, where D is the fractal dimension. There are several algorithms for calculating the Hurst exponent, such as multifractal detrended fluctuation analysis (MFDFA) (Kantelhardt *et al.*, 2002; Ihlen, 2012; Mandelbrot and Wallis, 1969), rescaled range analysis (R/S) (Mandelbrot and Wallis, 1969), wavelet approach (Kantelhardt *et al.*, 2002), and multifractal detrended moving average (MFDMA) (Carbone *et al.*, 2004).

The Hurst exponent provides information on the persistence or correlation of the time

series. $H > 0.5$ indicates that the time series is persistent, wherein an increase in value is mostly followed by another increase or vice versa. $H < 0.5$ represents an antipersistent time series (an increase/decrease in value is mostly followed by a decrease/increase), and $H = 0.5$ characterises an uncorrelated signal (Kantelhardt *et al.*, 2002; Ihlen, 2012). For a sinusoidal signal, we obtain $H = 0$, as the measures do not depend on the scale of measurement (for scales greater than one cycle). Note that, this sinusoidal signal may appear as a persistent one if we were to consider scales smaller than one cycle. Hence, it is important to choose the appropriate range of scales to calculate H .

Real-world fractal time series are self-similar only over a finite range of scales, unlike mathematical fractals, which can be self-similar across a wide range of scales. Further, H approaching a value of zero can be regarded as an indication of the emergence of periodicity during the transition. H is a good EWS for detecting transitions with changing fractal characteristics. In practical systems, a single fractal dimension cannot completely represent certain complex topologies; rather, these objects can be described with a range of fractal dimensions. Also, fluctuations with different amplitudes in the signal follow different scaling behaviour. Fractal characteristics of such a signal can be quantified using a multifractal spectrum.

In thermoacoustics, multifractal characteristics of aperiodic pressure fluctuations were first identified by Gotoda *et al.* (2012). The dynamics close to lean blowout exhibits self-affine structures dominated by stochastic fluctuations. As the control parameter changes, the behaviour significantly changes to chaotic oscillations. They used the box-counting method to estimate the multifractal spectrum from the phase space reconstructed using pressure fluctuations. Then, Nair and Sujith (2014) used MFDFA to quantify the fractal signatures of the pressure time series; they estimated H from the second-order structure-function for a range of scales from 2 to 4 acoustic cycles. The variation of H is used as a precursor for the onset of thermoacoustic instability (Nair *et al.*, 2017). They discovered that the stable operating state with low amplitude

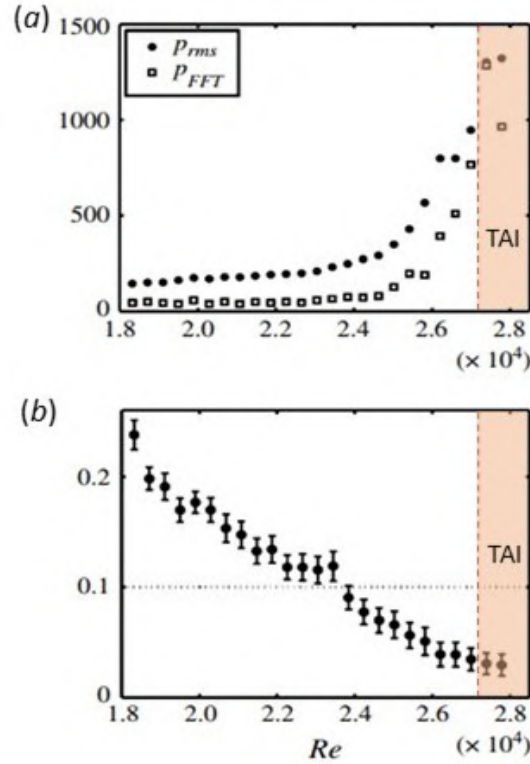


Fig. 2.7: (a) The variation of p_{rms} and the FFT peak during the transition to thermoacoustic instability for a bluff body stabilised combustors as a function of the control parameter Re . The growth of amplitude of oscillations during the transitions is captured by these measures. (b) The corresponding variation of the Hurst exponent (H). H drops to very low values well before the amplitude rises. Redrawn with permission from Nair and Sujith (2014)

chaotic oscillations exhibits multifractal characteristics. This multifractality is lost during the transition to periodic oscillations. The broad multifractal spectrum observed during stable operation collapses to a small spectrum during the state of limit cycle oscillations. The value of H decreases on approaching the transition as shown in Fig. 2.7b (for a bluff-body combustor). Initially, H has high values (≤ 0.5) representing the antipersistent nature of acoustic fluctuations and then decreases towards zero for periodic oscillations. The drop in H happens gradually, well before rms of pressure increases (shown in Fig. 2.7a) and H works as a good EWS for the onset of oscillatory instability in turbulent systems (Nair and Sujith, 2014; Venkatramani *et al.*, 2016; Nair and Sujith, 2016; Kerres *et al.*, 2016). Unni and Sujith (2015) studied the multifractal characteristics of combustor dynamics close to the flame blowout and suggested that

the H could forewarn an impending blowout (Unni *et al.*, 2019b).

2.3.3 Recurrence quantification analysis

Recurrence of phase space trajectories is a fundamental property of a deterministic dynamical system. A recurrence plot is a 2D representation of the time instants at which the trajectory revisits roughly the same region in the phase space (Eckmann *et al.*, 1995). Recurrences in the phase space can be written as a matrix, $R_{i,j} = \Theta(\epsilon - \|\vec{X}_i - \vec{X}_j\|)$ where, $i, j = 1, 2, \dots, n$ and \vec{X}_i, \vec{X}_j represent the state vectors of the system at time t_i & t_j , respectively. Θ is the Heaviside step function, and ϵ is the size of the small neighbourhood area considered around each point in the phase space. Whenever the trajectory revisits the area within the ϵ threshold, $R_{i,j}$ is marked as 1 in the recurrence matrix and can be indicated by a black point in the recurrence plot. We can use the patterns in recurrence plots to study the topology of the phase space attractor, identify the type of intermittency, etc. More details of the construction of recurrence plots and the selection of threshold can be found in Webber Jr and Marwan (2015).

In practical systems where there is no access to all the independent system variables, we perform recurrence analysis on the reconstructed phase space using the time series of a single variable (Takens, 1981). Further, recurrence quantification analysis characterises the organisation of black and white points in the recurrence plot, and several statistical measures can be derived (Webber Jr and Marwan, 2015). These measures can be used to quantify the transition to thermoacoustic instability. As the dynamics change from low amplitude chaotic oscillations to high amplitude periodic oscillations, the topology of the phase space attractor changes, and is reflected as a change in patterns in the recurrence plots. The recurrence plot corresponding to limit cycle oscillations consists of equally spaced diagonal lines indicative of the periodic dynamics. The recurrence plot of a chaotic system has complex patterns with broken lines (Marwan *et al.*, 2007). In thermoacoustics, Kabiraj and Sujith (2012) used recurrence plots to characterise the dynamics during the state of intermittency in a laminar system. In a turbulent system,

Nair *et al.* (2014c) showed recurrence plots during the stable operation, intermittency, and thermoacoustic instability. The recurrence plot corresponding to the chaotic oscillations during the stable operation has black points and small rectangular black patches. During intermittency, short diagonal line segments start to appear in the recurrence plot, representing the periodic bursts. Limit cycle oscillations during the state of thermoacoustic instability result in a parallel diagonal line structure in the recurrence plot.

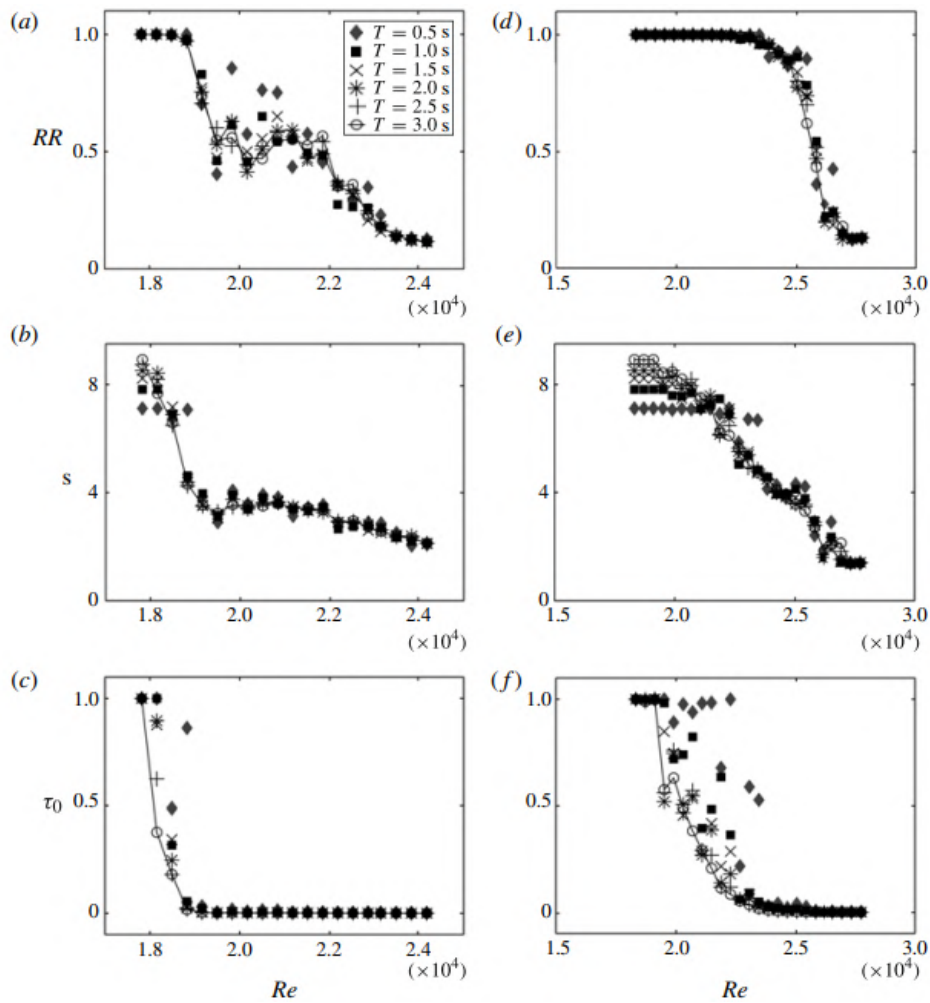


Fig. 2.8: Variation of recurrence measures as a function of Re in (a-c) swirl stabilised combustor and (d-f) bluff body combustor. The length of the time series (T) used to estimate the recurrence measures is varied from 0.5 s to 3 s. Reproduced with permission from Nair *et al.* (2014c).

In later studies by Nair *et al.* (2014b) and Gotoda *et al.* (2014), the patterns in the recurrence plot were quantified to obtain early warning signals for an impending

thermoacoustic instability, using measures such as recurrence rate (RR), Shannon entropy (s) and trapping time (τ). Figure 2.8 shows the variation of these measures during the transition for a swirl stabilised and a bluff body stabilised combustors. Most of them detect the transition in advance, compared to the steep rise in acoustic pressure amplitude. The physical interpretation of decreasing values of these measures depends on how the recurrences in the phase space within an ϵ -neighbourhood is defined. The results shown in Fig. 2.8 are obtained by keeping the values of ϵ constant during the dynamical transition. RR is the percentage of black points in the recurrence plot, s is the Shannon entropy of the probability distribution of the diagonal line lengths and τ is the average length of vertical lines, which is a measure of the duration for which the trajectory is trapped in the same region. Here, decrease in these measures forewarns the emergence of an ordered periodic motion. The recurrence measures provide precursors for lean blowout as well (Unni and Sujith, 2016).

Godavarthi *et al.* (2017) constructed recurrence networks based on recurrences in the phase space reconstructed from the time series of pressure fluctuations acquired from a turbulent combustor. They selected the recurrence threshold following the approach proposed by Jacob *et al.* (2016). The network measures derived from the topology of the network, such as characteristic path length and average betweenness centrality, were used as indicators of transitions in the thermoacoustic system. In a subsequent work (Godavarthi *et al.*, 2018), they applied the framework of synchronisation along with the recurrence analysis to study the coupled behaviour of acoustic pressure and heat release rate oscillations. They selected the recurrence threshold in such a way that the recurrence rate is fixed for all the states throughout the transition (Zbilut *et al.*, 2002; Kraemer *et al.*, 2018). They characterised the transition using cross recurrences and joint recurrences of the two system variables. They presented this transition as a transition from desynchronisation to intermittent synchronisation, then to phase synchronisation, and finally to generalised synchronisation. The measures derived from the joint and cross recurrence networks vary gradually during this

transition and can be used as early warning signals. Likewise, Chiocchini *et al.* (2018) applied synchronisation theory for thermoacoustic instability detection using an interdependence index related to the coupling between the variables.

Kasthuri *et al.* (2019) showed several measures based on multifractal theory and recurrence quantification analysis. They find that these are robust measures in distinguishing dynamical states occurring in a model rocket engine combustor. Braun *et al.* (2021) proposed lacunarity as a novel recurrence quantification measure and demonstrated its efficacy in detecting transitions in thermoacoustic systems. Lacunarity is a measure of heterogeneity in the temporal recurrence patterns in recurrence plots. It is a broadly applicable measure as it works in the presence of noise and non-stationarity, even for short time series. Apart from detecting transitions, lacunarity can also distinguish between stable operation and near blowout states of thermoacoustic systems. Dynamics prior to blowout exhibit dragon-king extreme events (Premraj *et al.*, 2021), which can serve as an early warning signal for blowout in combustors.

2.3.4 Complex networks

The high dimensionality and nonlinear properties of complex fluid mechanical systems impose substantial methodological challenges to analyse and interpret the dynamics from the data, especially in turbulent systems. Several methods based on statistics, analytical formulation, and dynamical systems theory have been employed to study the dynamics of complex systems in the past. Complex network theory has been largely adopted in several areas such as climate systems, social networks, and biology (Costa *et al.*, 2011). Complex systems have interacting subsystems, and they often exhibit the emergence of collective dynamics due to these interactions. Complex networks can be constructed considering these subsystems as nodes and the interactions as links. The evolution of network topology in complex systems can exhibit emergent dynamics.

Mathematically, complex networks are represented in terms of their adjacency matrix A , where $A_{ij} = 1$ if the nodes i and j are connected, otherwise $A_{ij} = 0$, and $A_{ii} = 0$ to

avoid self connections. Complex networks can be constructed from temporal or spatial data. Methodologies developed to map the time series to a network include proximity networks, visibility networks, cycle networks, and transition networks (Zou *et al.*, 2019). Different network properties can be applied to quantify the varying network topology during critical transitions.

Murugesan and Sujith (2015) introduced complex networks derived from acoustic pressure data to study the transitions in a thermoacoustic system. They constructed visibility graphs for the time series data at different operating conditions during the transition to thermoacoustic instability. The peaks in the time series are considered as nodes, and a link is activated between them based on the visibility criterion. We connect the nodes if we can draw a straight line between them without intersecting the part of the time series in between the two peaks. The network has different topologies for the state of stable operation, intermittency, and thermoacoustic instability. The degree (k) of a node is defined as the number of connections of that node. The distribution of the percentage of nodes having degree k (degree distribution) during the stable operation and intermittency follows a power law behaviour indicating the scale free nature of the network. The network changes to a regular network as the system transitions to thermoacoustic instability.

Such topological changes of the complex networks are quantified using various network properties to provide early warning signals to detect the onset of impending thermoacoustic instability (Murugesan *et al.*, 2019). The variation of the clustering coefficient, the characteristic path length, the network diameter, and the global efficiency are found to capture the change in system dynamics well before the increase in the amplitude of oscillations (Fig. 2.9). The clustering coefficient (C) of a node is the ratio of the number of connections in the neighbourhood of a node to the maximum possible connections in the neighbourhood. The average C reduces during the transition (Fig. 2.9b). The characteristic path length is a measure of the shortest path length in a network and it is related to the efficiency of information transport in a network.

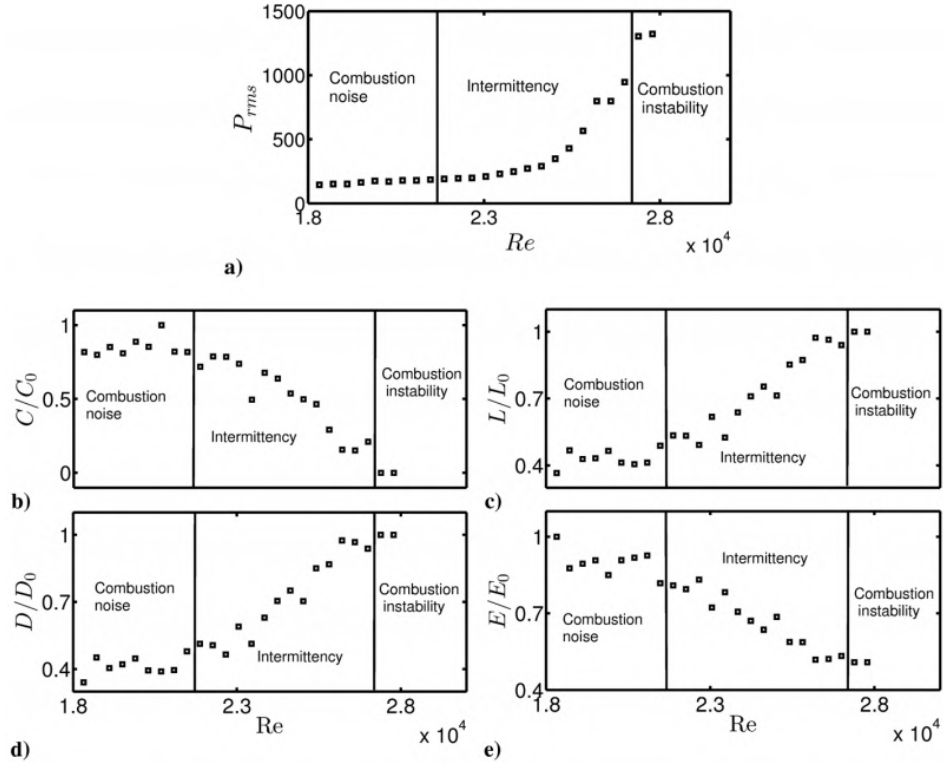


Fig. 2.9: (a) Variation of rms of pressure and (b-e) complex network measures during the transition to thermoacoustic instability. The network measures, namely, clustering coefficient (C/C_0), characteristic path length (L/L_0), network diameter (D/D_0), and global efficiency (E/E_0) start to vary during the intermittency regime and thereby detect the transition well before P_{rms} . Reproduced with permission from Murugesan and Sujith (2016).

The reader may refer to Murugesan and Sujith (2016) for more details and physical interpretations of all the measures during the thermoacoustic transition.

Gotoda *et al.* (2017) used a modified version of the visibility graph to forewarn blowout, and the average degree is found to detect the onset of blowout (Fig. 2.10). Further, using recurrence networks, they detected the presence of a small-world nature in networks constructed from the dynamical state close to blowout. Later, using recurrence network, Godavarthi *et al.* (2017) reported the scale-free nature of the network in a stable thermoacoustic system. Further, they used characteristic path length and betweenness centrality measures to detect the transition to thermoacoustic instability and lean blowout. Recently, Tandon and Sujith (2021) used cycle networks to characterise the topological transformations in the phase space, thereby providing

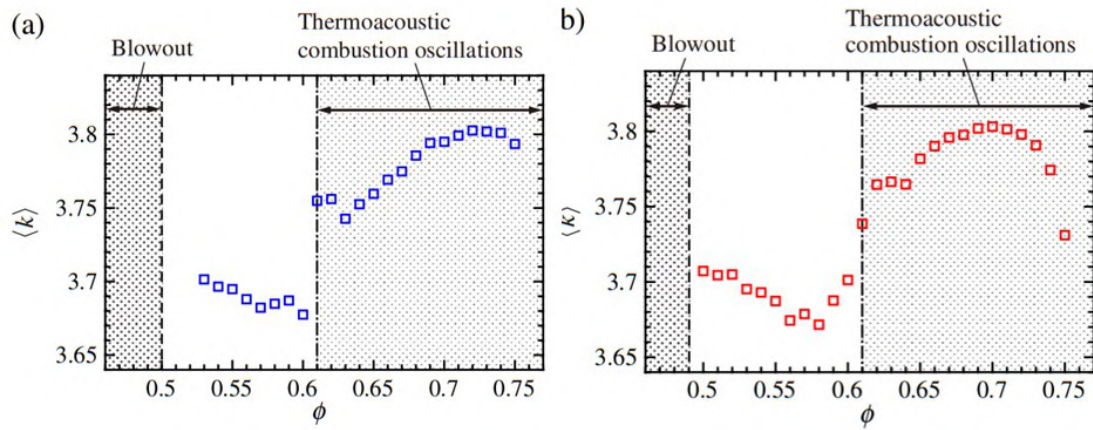


Fig. 2.10: Variations of the average degree of the network as a function of the equivalence ratio for the transition towards lean blowout (decrease in ϕ). The average degree is calculated for horizontal visibility networks constructed using time series of (a) pressure fluctuations and (b) heat release rate fluctuations. The network measure provides early warning for blowout. Reproduced with permission from Gotoda *et al.* (2017).

precursors for thermoacoustic instability.

2.3.5 Symbolic time series analysis

Symbolic dynamic approach for pattern recognition has been developed for anomaly detection in complex systems. Anomaly is the deviation of a system from its nominal behaviour, which is often associated with changes in system parameters. Early detection of anomalies in complex systems can be done using the concepts of symbolic dynamics (Ray, 2004; Daw *et al.*, 2003). A symbolic time series is created by first partitioning the phase space of a dynamical system into a finite number of cells. Then, each of these compact regions is labelled with a symbol. By following the trajectory, we find the symbols corresponding to the boxes which the trajectory passes through or touches. Thereby, the evolution of the trajectory can be mapped into a sequence of symbols. Even though there is a possible loss of information due to the discretisation of the phase space, the important features of the dynamics are mostly preserved in the symbolic time series.

A state vector is constructed corresponding to the symbolic time series, representing the

dynamics of the particular state. From the symbolic time series, probabilistic finite state automata (PFSA) is constructed assuming that the PFSA is a Markov chain of order D . A reference state is identified and partitioned such that the PFSA constructed will have a uniform probability for all symbols. Then, an anomaly measure can be defined, which will capture the deviation of a state from the reference state. The method of anomaly detection has been used as an early warning for thermoacoustic instability.

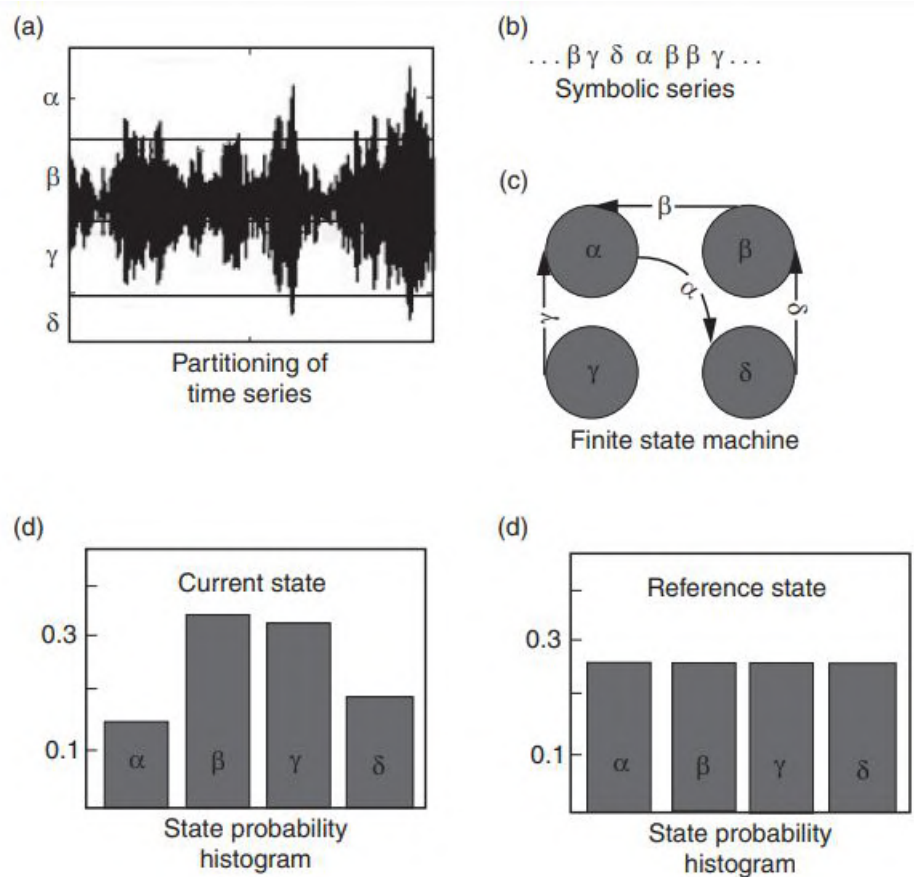


Fig. 2.11: The concept of symbolic time series analysis. The time series is partitioned and labelled, and a state probability histogram is then created. Reproduced with permission from Unni *et al.* (2015).

In a mathematical model for a thermoacoustic system, anomaly detection using symbolic dynamics was shown to identify flame blowout (Gupta *et al.*, 2006; Chakraborty *et al.*, 2008; Datta *et al.*, 2006). In a later study, Mukhopadhyay *et al.* (2013) used symbolic time series analysis to obtain precursors for lean blowout in a laboratory-scale gas turbine combustor. Unni *et al.* (2015) illustrated the application

of symbolic time series analysis for the online detection of impending thermoacoustic instability (Unni *et al.*, 2018b). They constructed symbolic time series from the time series of acoustic pressure, and the onset of thermoacoustic instability is considered as the reference state. The anomaly measure detects the deviation from the reference state and decreases as the system approaches the onset of thermoacoustic instability.

There have been studies on the combined application of symbolic time series analysis and machine learning techniques such as deep convolutional neural networks (Sarkar *et al.*, 2015b,a), for early detection of combustion instability. Sarkar *et al.* (2015b) used symbolic time series analysis as a data-driven method to predict thermoacoustic instability in a swirl stabilised combustor. Recently, Ghalyan *et al.* (2019) tested the decision making ability of symbolic time series analysis utilising a novel hidden Markov model-based partitioning method. They could capture the dynamics using short length time series data from laboratory-scale thermoacoustic experiments. Real-time decision-making and active monitoring of dynamical systems often require algorithms that work with short-length time series of sensor data.

2.3.6 Machine learning-based precursors

Critical transitions in thermoacoustic systems exhibit the emergence of periodic patterns in the dynamics. Machine learning methods provide powerful tools for detecting patterns in data. Data generated from a number of experiments under different operating conditions can be used to learn the dynamics of the system. Recently, there has been much interest in the early detection of thermoacoustic instability using data-driven methods.

Kobayashi *et al.* (2019) developed a new method for early detection of thermoacoustic instability by combining complex networks and machine learning techniques. To detect a precursor to thermoacoustic instability, they used the standard support vector machine (SVM) (Vapnik, 1999), which is a binary classifier recognising patterns. They constructed transition networks with order patterns (permutation patterns). The order

patterns are the nodes of the network, and the transition sequence of order patterns determines the weight of an edge. The SVM helps in the classification of the dynamics into three regimes on the feature space.

In another study by the same group (Hachijo *et al.*, 2019), early detection of thermoacoustic instability is realised by a combined method of permutation entropy and machine learning. Permutation entropy is a measure of complexity of the dynamics in the phase space. By reconstructing the phase space from the time series of pressure fluctuations, they estimated the number of realisations of all possible permutations of these phase space vectors. Entropy of permutation for all the vectors is known as permutation entropy. The variation of permutation entropy can be used to detect the transitions in thermoacoustic systems (Domen *et al.*, 2015). Hachijo *et al.* (2019) applied a support vector machine along with the measure of statistical complexity for early detection of thermoacoustic instability.

In a prior work, Chattopadhyay *et al.* (2017) systematically quantified the map of stability regions. Using the limited experimental data at certain conditions, they used a Bayesian non-parametric method to predict the stability of the combustor system at operating conditions at which experimental data are unavailable. The combustor operators can use this stability map for predicting the system response by statistically quantifying the uncertainties at operating conditions for which experimental data may not be available. This information helps in the identification of the combustion system parameters. More details on feature extraction and training the algorithm can be found in the Chattopadhyay *et al.* (2017).

In a study by Sarkar *et al.* (2015a), early detection of thermoacoustic instability was achieved by using a combination of deep convolutional neural networks (CNN) and symbolic time series analysis (STSA). They used CNN as a feature extractor from spatial data and learned meaningful patterns from unstable states, such as coherent structures in the flow field. An STSA then captures the temporal dynamics of such patterns as the system transitions to an unstable state, leading to early detection of

thermoacoustic instability. An unsupervised pre-training approach with deep-belief networks (DBN) is used to automatically extract the coherent structures in a very similar study by Sarkar *et al.* (2015b). Ruiz *et al.* (2021) demonstrated the detection of the extent of periodicity from recurrence plots during intermittency using a CNN, enabling the prediction of proximity to the onset of thermoacoustic instability.

Very recently, a paper by Mondal *et al.* (2021) provides a proof-of-concept demonstration of transfer learning, in which a deep neural network is trained on relatively less expensive experiments in an electrically heated Rijke tube. Then, this trained algorithm is used to predict thermoacoustic instability in a more practical system such as a swirl-stabilised laboratory-scale combustion system. Dhadphale *et al.* (2022) introduced a neural ordinary differential equation (neural ODE) framework to model the coupled interactions of the subsystems of a thermoacoustic system. They used simultaneously measured the pressure fluctuations and the heat release rate as input for the neural ODE. Then, they defined an anomaly measure representing the system's proximity to periodic oscillations to provide early warning for the onset of thermoacoustic instability. Waxenegger-Wilfing *et al.* (2021) applied a machine learning approach to detect thermoacoustic instabilities in a cryogenic rocket thrust chamber. Further, studies by Xiong *et al.* (2018), Bhattacharya *et al.* (2020); Bhattacharya and Ray (2020), Mondal *et al.* (2018) and Sengupta *et al.* (2020) are some recent works based on machine learning methods for early detection in thermoacoustic instability. To detect the type of bifurcation, Bury *et al.* (2021) combined two network architectures (convolutional neural networks (CNN) and long short-term memory (LSTM) networks) and trained on simulated data from four types of bifurcation models: fold, Hopf, and transcritical and neutral processes. This network detects each of these four types in both empirical and model data, and has been tested to identify the transition to thermoacoustic instability. A summary of the review on EWS is presented as a table (Table. 2.1).

Table 2.1: Early warning signals for critical transitions in thermoacoustic systems

Phenomenon/ indicator	Data source	Laminar/ Turbulent	References
Critical slowing down	Experiment & model Experiment	Laminar Turbulent	Gopalakrishnan <i>et al.</i> (2016a) An <i>et al.</i> (2019)
Multifractality	Experiment	Turbulent	Nair and Sujith (2014)
Recurrence analysis	Experiment Experiment Experiment Experiment Experiment Experiment & model	Laminar Turbulent Turbulent Turbulent Turbulent Turbulent	Kabiraj and Sujith (2012) Nair <i>et al.</i> (2014c) Gotoda <i>et al.</i> (2014) Godavarthi <i>et al.</i> (2017) Chiocchini <i>et al.</i> (2018) Braun <i>et al.</i> (2021)
Complex networks	Experiment Experiment Experiment Model Experiment	Turbulent Turbulent Turbulent – Turbulent	Murugesan and Sujith (2015, 2016) Godavarthi <i>et al.</i> (2018) Gotoda <i>et al.</i> (2017) Hashimoto <i>et al.</i> (2019) Tandon and Sujith (2021)
Symbolic time series	Model Model Model Experiment Experiment Experiment Experiment	– – – Turbulent Turbulent Laminar Laminar	Gupta <i>et al.</i> (2006) Chakraborty <i>et al.</i> (2008) Datta <i>et al.</i> (2006) Unni <i>et al.</i> (2015) Sarkar <i>et al.</i> (2015b,a) Ghalyan <i>et al.</i> (2019) Mondal <i>et al.</i> (2020)
Machine learning	Experiment Experiment Experiment Experiment Experiment Experiment & Model Experiment & Model Experiment Experiment Experiment Experiment Experiment Experiment Experiment Experiment	Turbulent Turbulent Turbulent Turbulent Turbulent Laminar Laminar Laminar Turbulent Turbulent Turbulent Turbulent Turbulent Turbulent Turbulent	Sarkar <i>et al.</i> (2015b,a) Kobayashi <i>et al.</i> (2019) Hachijo <i>et al.</i> (2019) Chattopadhyay <i>et al.</i> (2017) Xiong <i>et al.</i> (2018) Bhattacharya and Ray (2020) Bhattacharya <i>et al.</i> (2020) Mondal <i>et al.</i> (2018) Sengupta <i>et al.</i> (2020) Ruiz <i>et al.</i> (2021) Sengupta <i>et al.</i> (2021) Dhadphale <i>et al.</i> (2022) Waxenegger-Wilfing <i>et al.</i> (2021) Bury <i>et al.</i> (2021)
Damping coefficient	Experiment	Turbulent	Lieuwen (2005)
System identification	Experiment & Model Model	Turbulent –	Lee <i>et al.</i> (2020) Rouwenhorst <i>et al.</i> (2017)

2.4 MODELS TO STUDY CRITICAL TRANSITIONS IN THERMOACOUSTIC SYSTEMS

2.4.1 Forced acoustic oscillator type models

Mathematical models have been developed to represent the dynamics of thermoacoustic systems qualitatively. Many such models successfully capture the dynamics during the transition to thermoacoustic instability. Noiray and Schuermans (2013) introduced a model of a noise driven Van der Pol oscillator for transitions in a turbulent combustor. They demonstrated a methodology to estimate the linear growth rates of the system from the pressure signals recorded during thermoacoustic instability. A strong stochastic forcing due to the turbulent reactive flow drives the limit cycle oscillations in their model. Then, they extracted the linear growth rate from the stochastically forced limit cycle oscillations using stochastic differential equations. This model could replicate intermittency-like behaviour, although this work did not focus on the intermittency route to thermoacoustic instability.

Matveev (2003) described thermoacoustic instability in a bluff-body stabilised combustor using a kicked oscillator model. This model describes the coupling between vortex shedding, heat release rate, and the acoustic field in the thermoacoustic system. The acoustic field is considered as a kicked oscillator. The increased heat release during impingement of a vortex with the wall or the flame holder adds energy to the acoustic field, and such events are considered as 'kicks' to the acoustic oscillator. When a vortex carrying well-mixed reactant mixture impinges on the combustor walls or on the flame holder, there is a sudden increase in the reaction and consequently a spike in the heat release. In this model, they assume that the periodic vortex shedding results in a periodic oscillation of heat release rate during thermoacoustic instability. Consequently, the acoustic field is driven by these periodic kicks of intense heat release. However, the model does not capture the intermittent behaviour observed in turbulent thermoacoustic systems. Then, Nair and Sujith (2015) proposed a modified kicked oscillator model considering the turbulence and its interaction with other subsystems.

To account for the effects of turbulence, Nair and Sujith (2015) used stochastic terms to model the variations in the size and the velocities of the vortices in the turbulent flow. As a result, they could capture the dynamics during the state of intermittency. This model qualitatively captured the dynamics during the transition via intermittency. However, the aperiodic fluctuations during the stable operation have been reported to be deterministic chaos (Tony *et al.*, 2015). Therefore, Seshadri *et al.* (2016) developed a deterministic model that captures the dynamical transition via intermittency. Furthermore, they have incorporated the feedback from acoustics to hydrodynamics to adjust the kicking times without using stochasticity. Using such a model and by deriving an amplitude equation based on the intermittency statistics, Seshadri *et al.* (2018a) developed a novel methodology to predict the amplitude of limit cycle oscillations (Sujith *et al.*, 2021). Recently, the model of stochastically forced coupled oscillators proposed by Bonciolini *et al.* (2021) also could qualitatively reproduce the experimentally observed dynamics. Another approach of modelling was fractional calculus, assuming an underlying fractional dynamics for the thermoacoustic system. Varghese *et al.* (2021) obtained a fractional-order model for pressure fluctuations which captures the multifractality in the pressure fluctuations during the stable operation.

2.4.2 Synchronisation based models

The synchronisation framework has been used to study the onset of oscillatory instabilities in fluid mechanical systems. The transition from chaos to limit cycle oscillations during thermoacoustic instability is identified as synchronisation between the unsteady heat release rate and the acoustic field in a turbulent thermoacoustic system. Pawar *et al.* (2017) investigated the synchronisation between these subsystems in a turbulent combustor, both experimentally and also using a model. In the framework of synchronisation, the transition to thermoacoustic instability is described as a transition from a desynchronised state (stable operation) to a generalised synchronised

state (strong thermoacoustic instability) via an intermittent phase synchronised state (intermittency) and a phase synchronised state (weak thermoacoustic instability).

To model the mutual interactions between the subsystems such as combustion, hydrodynamics, and acoustic field, synchronisation between coupled oscillators could be an appropriate approach. Using synchronisation properties, Dutta *et al.* (2019) modelled the dynamics in a swirl stabilised combustor using Kuramoto oscillators arranged circumferentially around the swirler. They obtained similar dynamics as observed in the experiments by increasing the coupling strength between the oscillators. However, a turbulent thermoacoustic system is a spatially extended system exhibiting spatiotemporal self-organisation, forming large coherent structures as a spatially ordered pattern.

Mondal *et al.* (2017) studied the spatiotemporal dynamics during the transition to thermoacoustic instability. They analysed the spatial data representing instantaneous heat release rate (\dot{q}') acquired simultaneously with the acoustic pressure (p'). The phase difference between p' and \dot{q}' at each location is represented as a phasor and embedded over the spatial domain for each time instant. They observed a desynchronised arrangement of phasors during the stable operation, whereas all the phasors are synchronised during the occurrence of thermoacoustic instability. Interestingly, during intermittency, there are regions of synchronised phasors and desynchronised phasors coexisting, and these regions of synchrony and asynchrony change in time.

To model the dynamics of such a complex system, it is important to consider the temporal and spatiotemporal synchronisation route to thermoacoustic instability. Here, the mutual synchronisation among the oscillators of the turbulent reactive flow and acoustic field results in the onset of thermoacoustic instability. Godavarthi *et al.* (2020) developed a model using a network of locally coupled chaotic oscillators, which is globally coupled to another chaotic oscillator. They considered a chaotic Van der Pol oscillator to be analogous to the global acoustic field and the grid of Rössler oscillators to be analogous to the heat release rate field. Rössler oscillators are mutually coupled

to the neighbours in the grid and to the Van der Pol oscillator. As the coupling from Van der Pol to Rössler oscillators increases (all the other coupling terms are set to change proportionally), the dynamics change from a desynchronised state to the generalised synchronised state through an intermittent phase synchronisation and phase synchronisation. The model successfully captured the dynamics observed in experiments in a turbulent combustor.

More recently, Weng *et al.* (2020) developed a synchronisation based model which captures the multiple bifurcations in a thermoacoustic system. They considered the acoustic field and heat release rate as nonlinearly coupled damped simple harmonic oscillators. They reported a transition from limit cycle oscillations to chaos via quasiperiodic route upon varying the coupling strength. During the transition, the coupled oscillators undergo synchronisation, capturing the nonlinear dynamical behaviour of a laminar thermoacoustic system.

2.5 CONTINUOUS VARIATION OF CONTROL PARAMETERS

Most studies investigating dynamical transitions vary the system parameters in a quasi-steady manner. However, in many real systems, the system parameter is often changed continuously. In such cases, the rate of variation of the parameter has a vital role in determining the tipping point. Continuous variation of the parameter can delay the transition from the point predicted by quasi-steady bifurcation analysis due to memory effects (Baer *et al.*, 1989). In some cases, it can advance the transition if the variation of a rate-sensitive parameter is faster than a critical rate, as explained by Ashwin *et al.* (2012). They observed rate-induced tipping (R-tipping), where the system can be driven towards another stable state outside the basin of attraction of the quasi-static attractor. In a laminar thermoacoustic system, Tony *et al.* (2017) discovered preconditioned rate-induced tipping. With a fast enough variation of parameter and a finite amplitude initial perturbation, they could attain tipping to limit cycle state before the actual Hopf bifurcation. Bonciolini *et al.* (2018) investigated the rate-dependent transition

delay along with the effect of noise in a laboratory-scale combustor system. In a subsequent study, Bonciolini and Noiray (2019) presented a method of bifurcation dodging to avoid thermoacoustic instability by varying the parameter at fast rates. In a recent experimental study, Manikandan and Sujith (2020) reported R-tipping to thermoacoustic instability via intermittency in a turbulent afterburner. Further, Zhang *et al.* (2020, 2021) studied rate-dependent transitions in a mathematical model for thermoacoustic systems. Unni *et al.* (2019a) investigated the interplay between the noise in the system and the rate of change of the parameter in determining the tipping point. The combined effects of rate and inherent noise in the system bring high variability to the tipping point. Therefore, devising early warning signals for practical systems where parameters change continuously is very important.

2.6 SPATIOTEMPORAL DYNAMICS OF THERMOACOUSTIC SYSTEMS

Many dynamical systems that exhibit critical transitions are spatially extended systems. Hence, identifying tipping behaviour of such systems requires analysis of the spatiotemporal dynamics as we approach the transition. Spatial heterogeneities can cause variability in local temporal dynamics and hence introduce spatial inhomogeneity in precursory events associated with the transition. Hence, it is essential to explore the spatiotemporal dynamics during the transition to thermoacoustic instability. During self-organisation leading to oscillatory instabilities, turbulent spatiotemporal systems exhibit other behaviours such as the emergence of critical regions. As we approach thermoacoustic instability, the interactions between the small scale vortices in the reactive flow field, the acoustic field, and the flame lead to the formation of patterns with large scale coherent structures in spatially extended systems (George *et al.*, 2018b). The periodic emergence of such coherent structures in the flow field alters the acoustic field, and that in turn affects the pattern of vortex shedding. Such strong feedback between the subsystems leads to self-organisation towards a stable spatiotemporal pattern during thermoacoustic instability.

Synchronisation analysis of spatial data representing instantaneous heat release rate with the acoustic pressure enabled the discovery of chimera like patterns during intermittency in a turbulent combustor (Mondal *et al.*, 2017). Chimera state has coexisting regions of spatial synchrony and desynchrony, and these regions change in time. Later, Hashimoto *et al.* (2019) performed spatiotemporal analysis on a model rocket combustor using the theories of complex networks and synchronisation and identified such chimera like states. Based on synchronisation analysis, they proposed a 'phase parameter' for early detection of thermoacoustic instability.

In thermoacoustics, complex networks constructed from spatial data can aid the understanding of the self-organisation of turbulent flow field leading to ordered patterns. Unni *et al.* (2018a) and Krishnan *et al.* (2019, 2021) identified critical regions in the flow field using correlation networks based on the velocity field. The detection of critical regions in the system promoted the implementation of effective control strategies to mitigate thermoacoustic instability (Krishnan *et al.*, 2019, 2021). Recently, Roy *et al.* (2021) demonstrated a passive control strategy for suppressing thermoacoustic instability in a laboratory scale combustor by targeting critical regions with a steady injection of micro-jet of air. The critical region to optimise the injection is determined from the spatial distribution of the Hurst exponent measured from the turbulent velocity field.

Further, Unni and Sujith (2017) compared the spatiotemporal characteristics of the intermittency prior to and post thermoacoustic instability. They observed that the flame switches between two types of dynamics. The flame oscillating in an aperiodic manner switches to periodic roll-up due to periodic vortex shedding. They also identified different flame dynamics during intermittency before and after thermoacoustic instability. More recently, Raghunathan *et al.* (2020) explored the multifractal characteristics of spatiotemporal dynamics from the spatial wrinkles on the flame surface and found that there is a periodic oscillation of multifractal spectrum obtained from the flame topology, corresponding to the periodic emergence of coherent

structures in the flow field.

Further, the use of spatial data may help to study the origin of critical transitions, as the tipping involves spatial reorganisation and pattern formation. We have to look at spatiotemporal data for systems that embody spatiotemporal dynamics to explore the spatial aspects of EWS. For instance, Stolbova *et al.* (2016) presented a method for prediction of the onset and withdrawal of Indian monsoon using the relative variance of fluctuations at different locations. For such a spatially extended complex system, they identified particular geographic regions as tipping elements and used them as observation locations for predicting monsoon timings. These locations were treated as coupled reference points for the prediction. The prediction was made based on the prebifurcation growth of fluctuations, a critical transition precursor, at the selected geometric regions. A similar method is applied to a turbulent thermoacoustic systems to identify tipping elements as early manifestation of the onset of thermoacoustic instability (Raghunathan *et al.*, 2022).

In another study, Stolbova *et al.* (2014) applied a complex network approach to study the evolution of the network of extreme precipitation and thereby identified the origins of dynamics in the organisation of extreme rainfall before, during, and after the Indian summer monsoon. Such a spatiotemporal analysis translates into various of ways to reveal additional information about the dynamics, including the origin of critical transitions such as tipping elements and critical regions. Also, in a spatially extended system, spatial interactions should be considered while studying the dynamics. For instance, spatial mean, variance and skewness are found to be leading indicators for regime shifts in ecological systems (Guttal and Jayaprakash, 2009). In summary, quantifying the spatiotemporal evolution of the interaction among the subsystems is essential for a deeper understanding of critical transitions in thermoacoustic systems.

2.7 SUMMARY

A thermoacoustic system is a complex system that exhibits a critical transition to a state of oscillatory instability known as thermoacoustic instability. We discussed the dynamics during the transition to thermoacoustic instability in laminar and turbulent systems. In real-world systems, inherent fluctuations are always present in the system variables, especially in turbulent systems. The presence of such inherent fluctuations in the system can cause new dynamical states such as intermittency during the critical transition. Several early warning signals to detect the transition from stable operation to thermoacoustic instability have been developed by characterising such states presaging a critical transition. A brief review of early warning signals for oscillatory instabilities in thermoacoustic systems is presented in this chapter.

In contrast with the transition from a fixed point to limit cycle oscillations in laminar systems, turbulent systems exhibit a transition from a chaotic state to a limit cycle via a state of intermittency. Due to the presence of such intermediate states, tipping in the presence of inherent fluctuations or noise may not look like a clean critical transition. However, it has several characteristics of critical transitions. We highlight the importance of the inherent fluctuations in the system in providing early warning signals for critical transitions. Currently, there are early warning signals developed using a combination of physics and artificial intelligence-based methods. The scope for such data-driven methods is increasing day by day, as these are more suitable for the online detection of critical transitions. Further, we discussed the importance of characterising spatiotemporal dynamics in spatially extended systems to understand critical transitions better. Studies on spatiotemporal dynamics are necessary to identify regions where the early manifestation of critical transitions occur, and such studies will help the investigations on the origin of critical transitions.

Finally, to summarise, transitions to oscillatory instabilities is a significant class of problems for investigating EWS in the context of critical transitions or tipping. The dynamical transition in turbulent fluid mechanical systems is a challenging platform

to apply tools from nonlinear dynamics, where many aspects are yet to be explored. Further, we can extend the understanding and the measures developed for fluid mechanical systems to study tipping in other spatiotemporal systems as well. Studying critical transitions in real-world systems is relevant for both the engineering and the science community and has practical applications.

CHAPTER 3

Universality during critical transitions to oscillatory instabilities in turbulent flows

¹ Fractal characteristics of the time series undergo changes during a system variable during critical transition to oscillatory instabilities. First, we discuss the transition to oscillatory instabilities and the dynamics observed during transition by analysing a fluctuating system variable. Finally, a scaling relation between the amplitude of dominant mode of oscillations and Hurst exponent (a measure related to the fractal dimension of the time series) is presented.

3.1 SELF-ORGANIZATION LEADING TO OSCILLATORY INSTABILITIES

A large number of physical systems involve turbulent flows that have chaotic variations in properties such as pressure and velocity. Turbulent flows are characterized by eddies of different length and time scales that interact nonlinearly. The transfer of energy across eddies of different length scales takes place through various cascade processes (Richardson, 1926; Kraichnan, 1967). A unique collective behaviour can often arise from the interaction of multiple subsystems resulting in various phenomena at many different scales. Turbulent flow systems can therefore be regarded as a complex system. Although turbulent flows are chaotic, self-organization due to feedback in such a complex system can cause the emergence of order from chaos.

Self-organization is a fundamental property of a complex system, where some form of macroscopic order emerges from interactions between subsystems of an initially disordered system. In turbulent flows, spatially extended patterns such as large coherent structures are formed due to self-organization, for example, devastating cyclones in atmospheric flows. Self-organization driven by feedback between subsystems in turbulent systems can lead to oscillatory instabilities as observed in thermoacoustic

¹The results presented in this chapter are published in (Pavithran *et al.*, 2020b).

(Juniper and Sujith, 2018), aeroacoustic (Flandro and Majdalani, 2003), and aeroelastic systems (Hansen, 2007). These oscillatory instabilities cause high amplitude vibrations which are undesirable in engineering systems. In the present work, we study the emergence of such oscillatory instabilities in three different fluid mechanical systems, namely thermoacoustic, aeroacoustic, and aeroelastic systems.

Feedback between turbulent flow and other subsystems is often the cause for oscillatory instabilities. Thermoacoustic instability arises due to the nonlinear coupling between the reactive flow field and the acoustic field in a confinement (Lieuwen and Yang, 2005). Similarly, aeroacoustic instability is caused by the interaction between the acoustic field in a confinement and vortex shedding in turbulent flows (Flandro and Majdalani, 2003). Examples include the pleasant sounds generated in a flute or the destructive large amplitude oscillations established in gas-transport pipelines (Kriesels *et al.*, 1995). Aeroelastic instability occurs as a consequence of the interaction of the flow with the structural elements of the system (Hansen, 2007), *e.g.*, the catastrophic collapse of the Tacoma Bridge (Larsen and Walther, 1997). The transition to such oscillatory instabilities from a state of chaotic oscillations in turbulent systems occurs via intermittency (Nair *et al.*, 2014c; Nair and Sujith, 2016; Venkatramani *et al.*, 2016). We attribute the emergence of ordered periodic oscillations from high dimensional chaos to self-organization due to feedback between subsystems.

Conventionally, oscillatory instabilities in fluid mechanical systems are modeled as a transition from a stable fixed point to periodic oscillations (*i.e.*, Hopf bifurcation) as the control parameter is varied. According to linear theory, the amplitude grows exponentially during this transition, but then nonlinearities kick in and the amplitude saturates. In the study of such oscillatory instabilities, the effects of turbulence are often considered as background noise and are neglected in the traditional ‘signal plus noise’ approach.

For turbulent flows, the stable operating point is never quiet, but is instead characterized by low amplitude fluctuations arising due to the presence of turbulence. Recently, for

turbulent fluid mechanical systems, the stable operating state with aperiodic fluctuations was identified as high dimensional deterministic chaos (Tony *et al.*, 2015). This state with underlying turbulent fluctuations possesses inherent complexity and multifractal characteristics (Nair and Sujith, 2014; Venkatramani *et al.*, 2017). Recent studies have shown that treating these fluctuations with their inherent complexities (as opposed to considering them as noise) is very rewarding in terms of obtaining precursors to such instabilities in practical application (Nair *et al.*, 2014c; Nair and Sujith, 2016; Venkatramani *et al.*, 2016).

Further, a state of intermittency presages the transition to the self-sustained periodic oscillations in turbulent fluid mechanical systems (Nair *et al.*, 2014c; Nair and Sujith, 2016; Venkatramani *et al.*, 2016). The emergence of oscillatory instabilities in fluid mechanical systems may then be regarded as the loss of complexity in the dynamics (Nair and Sujith, 2014; Venkatramani *et al.*, 2017). Thus, considering the emergence of oscillatory instabilities from turbulence as a linear stability problem may not be the most appropriate and useful way. A more comprehensive way is to view the onset of oscillatory instabilities in a turbulent fluid mechanical system as order emerging from chaos using the framework of self-organization due to feedback between subsystems.

We explore the scaling behaviour of such self-organization leading to oscillatory instabilities in turbulent fluid mechanical systems. The proximity to the onset of oscillatory instability in each system is quantified using the Hurst exponent (H) which also serves as a system independent parameter to study the scaling behaviour of self-organization. An unsteady variable of each of the three systems is measured as we vary an appropriate system-specific control parameter to approach oscillatory instability. We estimate H , which is related to the fractal dimension (D) as $H = 2 - D$, for the time series corresponding to each state (Mandelbrot, 1982).

3.2 DETAILS OF THE EXPERIMENTS AND DATA USED

We analyze data from thermoacoustic, aeroacoustic and aeroelastic systems to study the transition from stable operation to oscillatory instabilities by changing the respective control parameters. Here, we will briefly discuss the experiments and the range of variation of control parameters. For all the three systems, the Reynolds number (Re) is considered as the control parameter and Re increases as we increase the mass flow rate of air. The system variables used for the analysis are acoustic pressure fluctuations for thermoacoustic, and aeroacoustic systems, whereas in the case of aeroelastic system, the strain experienced by the structure is used for as the system variable.

3.2.1 Experiments on Thermoacoustic system

The schematic of the experimental setup is shown in Fig. 3.1a. The setup consists of a settling chamber, a burner, a flame holding device and a combustion chamber with variable duct length. The length of the combustion chamber is varied to achieve different acoustic length scales and timescales. Also, the combustor can be equipped with different flame stabilization mechanisms. The flame holding device (a bluff body or a swirl) is attached to the burner by a central shaft. Then, there is a sudden expansion from the circular burner to a square chamber. In this present work, data is presented for a bluff-body stabilized combustor for two lengths: 700 mm and 1400 mm. As opposed to this configuration, we also present data for a swirl stabilized combustor of length 700 mm. The two flame stabilizing mechanisms render completely different flow physics in the combustor leading to different mechanisms causing thermoacoustic instability (Ghoniem *et al.*, 2005; Steinberg *et al.*, 2010). Liquefied petroleum gas (LPG: butane 60% and propane 40% composition by mass) is used as the fuel. Air is partially premixed with LPG before the reactant mixture enters the combustion chamber. We ignite this fuel-air mixture using a spark plug. The equivalence ratio is decreased in order to attain different dynamical states in the system. The equivalence ratio is defined as $\phi = \frac{(\dot{m}_f/\dot{m}_a)_{actual}}{(\dot{m}_f/\dot{m}_a)_{stoichiometry}}$, where \dot{m}_f and \dot{m}_a are the mass flow rates of fuel and air,

respectively. The mass flow rate of air is increased by keeping the mass flow rate of fuel constant to decrease ϕ . The mass flows rates of air and fuel are controlled using mass flow controllers (Alicat MCR series) with an uncertainty of $\pm (0.8\% \text{ of reading} + 0.2\% \text{ of full scale})$.

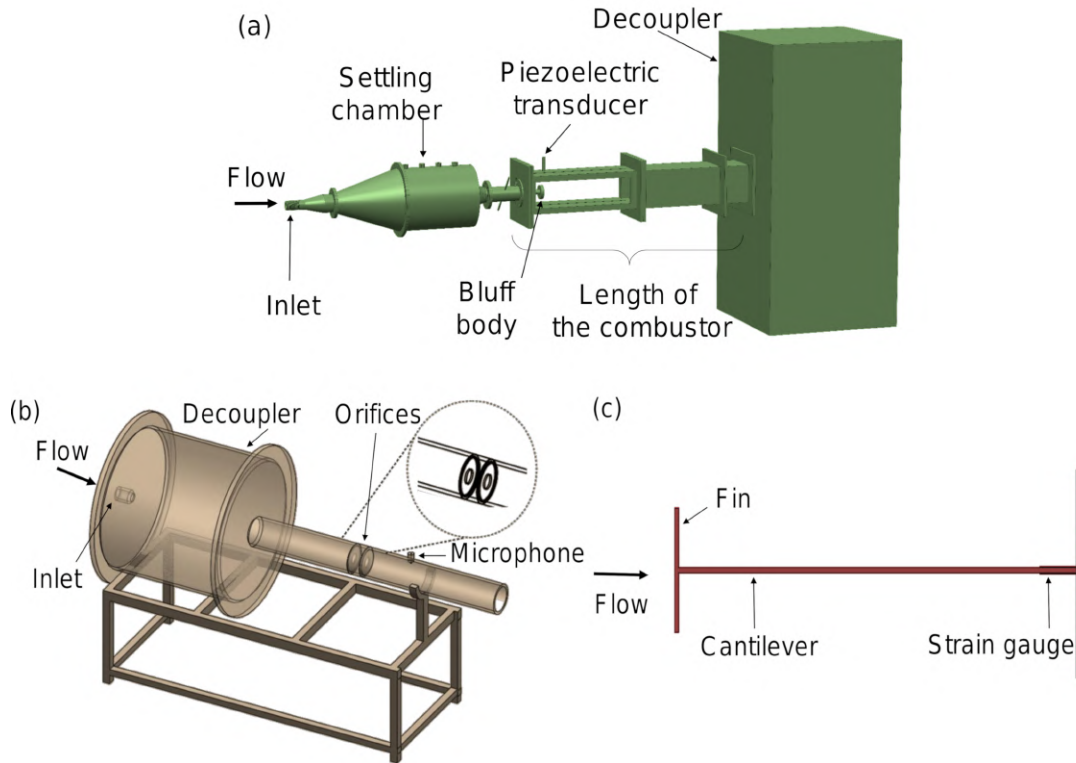


Fig. 3.1: Schematic of the experimental setups. (a) Turbulent combustor (thermoacoustic system) exhibiting transition to thermoacoustic instability. (b) An aeroacoustic system with two orifices. Vortices are shed when the turbulent flow passes through the orifices. In both of these systems, we measure the acoustic pressure fluctuations inside the duct during the transition to thermoacoustic/aeroacoustic instability. (c) An aeroelastic system where the left end of the beam has a small vertical fin attached to it. When a jet of air passes along the length of the cantilever from left to right, vortices are shed from the fins. We measure the resulting strain on the cantilever close to the fixed end of the beam. In all the cases, Reynolds number (Re) is varied as the control parameter to attain different dynamical states. The dimensions of different experimental setups are not to scale.

As we approach thermoacoustic instability, the small vortices in turbulent reactive flows interact with each other, with the flame and with the acoustic field creating larger coherent structures. This emergent coherent dynamics in the flow field leads to the establishment of a coherent acoustic field which, in turn, affects the pattern of vortex

shedding. Such alteration in the flow also changes the coupling between the subsystems. During thermoacoustic instability, the inter-subsystem interaction is very strong and a stable spatio-temporal pattern is formed due to self-organization, accompanied by large amplitude pressure oscillations (George *et al.*, 2018b).

The Reynolds number (Re) is considered as the control parameter and Re increases as we increase the the mass flow rate of air. The Reynolds number is calculated as $Re = 4\dot{m}D_1/\pi\mu D_0^2$ where \dot{m} is the mass flow rate of air-fuel mixture, D_0 is the diameter of the burner and μ is the dynamic viscosity of the mixture. For bluff body stabilized case, D_1 is the diameter of the bluff body and for swirl stabilized case, $D_1 = D_0$. We choose a range of Re values for different configurations so as to achieve the transition from the low amplitude aperiodic fluctuations to the high amplitude limit cycle oscillations. For thermoacoustic systems, the range of Re values are appropriately chosen for different configurations so as to achieve the transition from the low amplitude aperiodic fluctuations to the high amplitude limit cycle oscillations. For the bluff body stabilized combustor of length 700 mm (frequency of oscillations, $f \sim 250$ Hz), Re is varied from $(1.81 \pm 0.052) \times 10^4$ to $(2.8 \pm 0.073) \times 10^4$. For bluff body stabilized combustor of length 1400 mm ($f \sim 120$ Hz), Re varies from $(1.96 \pm 0.006) \times 10^4$ to $(3.53 \pm 0.099) \times 10^4$. Re variation for swirl stabilized combustor (length = 700 mm and $f \sim 250$ Hz) is from $(1.61 \pm 0.041) \times 10^4$ to $(1.96 \pm 0.060) \times 10^4$. The unsteady pressure fluctuations inside the combustion chamber are measured using piezoelectric transducers at different values of Re in the above mentioned ranges. PCB106B50 transducer (sensitivity 72.5 mV/kPa and resolution 0.48 Pa) is used for the combustor with 700 mm length and PCB103B02 (sensitivity 217.5 mV/kPa and resolution 0.15 Pa) transducer is used for the combustor with length 1400 mm. The transducer is located at the antinode of pressure oscillations which is near the backward facing step. This location helps us to record the maximum amplitude of the standing wave. The pressure data is sampled at a rate of 10 kHz. The thermoacoustic data analyzed in this study are reported in Nair and Sujith (2014), Nair *et al.* (2014c) and Unni and Sujith (2015), and

we use the same data. More detailed descriptions of the experiments can be found in these references.

3.2.2 Experiments on Aeroacoustic system

An aeroacoustic system consists of orifices located inside a duct. Vortices are shed when the turbulent flow passes through the orifices. The interaction between the vortex shedding and the acoustics inside the duct determines the dynamics of the aeroacoustic system. The schematic of the aeroacoustic experimental setup is shown in Fig. 3.1b. The current experimental setup consists of a cylindrical chamber, two pipes (lengths: 300 mm and 225 mm respectively), and two circular orifices of diameter 20 mm each, thickness 2.5 mm and separated by a distance of 18 mm (a zoomed view is shown in the circle). The turbulent flow enters the pipe through the large cylindrical chamber, referred to as the decoupler, which isolates the duct from the upstream pressure fluctuations. Thus, the pressure at both ends of the duct are maintained at the ambient pressure. The mass flow rate of air is controlled using a mass flow controller (Alicat MCR series) with an uncertainty of $\pm(0.8\%$ of reading + 0.2% of full scale). The experiments are conducted by increasing the mass flow rate of the air in the duct from 1.633 ± 0.054 g/s to 2.695 ± 0.062 g/s in steps of 0.041 g/s. The Reynolds number is calculated as $Re = \rho u d / \mu$ where ρ is the density of air, u is the velocity of inlet flow, d is the diameter of the orifice and μ is the dynamic viscosity of air. Re is varied from 5615 ± 185 to 9270 ± 212 . Here, f varies from 484 Hz to 540 Hz as we increase the velocity of the inlet flow. We measure the pressure fluctuations inside the duct using a pressure field pre-polarized microphone and a preamplifier system (PCB make, model number 378C10, 1 mV/Pa sensitivity and 28.3 Pa resolution) fixed at a distance of 100 mm from the second orifice. The data is sampled at a rate of 10 kHz. I designed and performed the experiments in aeroacoustic system at IIT Madras.

3.2.3 Experiments on Aeroelastic system

In a similar manner, we study the transition to aeroelastic instability in a laboratory scale aeroelastic system (Fig. 3.1c). The experimental setup consists of a cantilever beam having 45 mm length, 25 mm width and 0.5 mm thickness. The right side of the beam is fixed, and the left side of the beam is free. Note that the left end of the beam has a small vertical fin (12 mm length) attached to it, akin to a winglet of an aircraft wing. When a jet of air passes along the length of the cantilever from left to right, vortices are shed from the fins. These vortices impart unsteady aerodynamic load to the cantilever. We measure the resulting strain on the cantilever close to the fixed end of the beam (5 mm from the fixed end), using a strain gauge (Micro measurements make, pattern: 125LW, 3% strain range). For particular flow rates, the oscillations in the cantilever beam becomes periodic and self-sustained, resulting in aeroelastic instability. The Reynolds number is calculated as $Re = \rho u d / \mu$ where ρ is the density of air, u is the velocity of the inlet flow, d is the size of the fin at the left end of the cantilever and μ is the dynamic viscosity of air. Here, we increase Re from 2384 ± 159 to 4768 ± 111 to capture the transition to aeroelastic instability ($f \sim 60$ Hz). We record the strain data corresponding to the structural vibrations in the system for different values of the control parameter. Aeroelastic experiments were designed and performed by Dr. Vishnu R. Unni and Prof. Abhishek Saha at University of California San Diego.

3.3 TRANSITION FROM CHAOS TO LIMIT CYCLE OSCILLATIONS VIA INTERMITTENCY

In Fig. 3.2, we show representative datasets from all the three systems.

I) Figure 3.2a-c shows the acoustic pressure fluctuations in a thermoacoustic system (case (i)) during the transition to thermoacoustic instability. Figure 3.2a corresponds to a chaotic state far from the oscillatory instability. The time series consists of low amplitude aperiodic fluctuations. Recently, Tony *et al.* (2015) showed that these aperiodic fluctuations have features of high-dimensional chaos contaminated

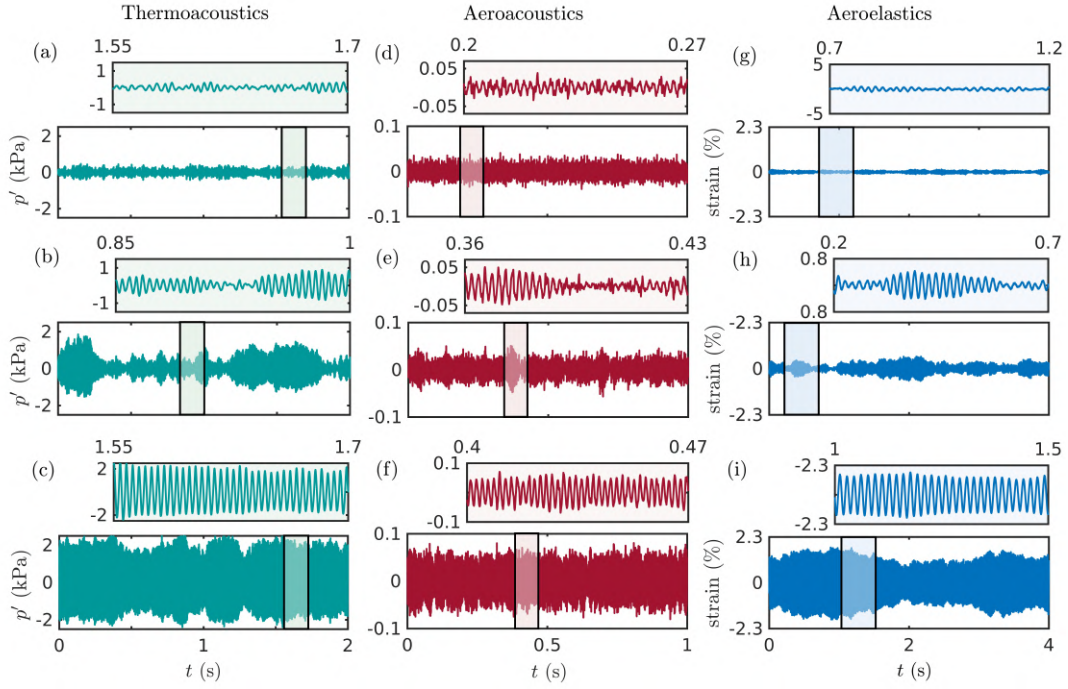


Fig. 3.2: Time series of state variables during the transition to oscillatory instability. (a-c) Data representing the acoustic pressure fluctuations acquired from a bluff body stabilized combustor of length 700 mm. The corresponding Re for a, b and c are $(1.9 \pm 0.053) \times 10^4$, $(2.6 \pm 0.069) \times 10^4$ and $(2.8 \pm 0.073) \times 10^4$ respectively. (d-f) Acoustic pressure fluctuations acquired during the transition to aeroacoustic instability ($Re = 5615 \pm 185$, 7283 ± 198 and 9270 ± 212 corresponding to d, e and f). (g-i) The time series of strain experienced by the cantilever in the aeroelastic system the Re is varied (2384 ± 111 , 3972 ± 142 and 4768 ± 159). In all the systems, we observe a transition from low amplitude aperiodic fluctuations (a, d and g) to high amplitude periodic oscillations (c, f and i) via a regime of intermittency (b, e and h) as the control parameter is varied (Re increases from top to bottom). The transition from aperiodicity to periodicity occurs via a regime of intermittency for other configurations of these systems as well.

with white and coloured noise. Nair *et al.* (2014c) discovered that the transition to thermoacoustic instability occurs through a state of intermittency, which contains epochs of high amplitude periodic oscillations amidst low amplitude aperiodic oscillations (Fig. 3.2b). Thermoacoustic instability (Fig. 3.2c) corresponds to a state of high amplitude periodic oscillations. We observe a similar behaviour for all the above mentioned combustor configurations during the transition to thermoacoustic instability.

II) Figure 3.2d-f shows the time series of pressure fluctuations corresponding to the

transition to aeroacoustic instability. The temporal behaviour of acoustic pressure during this transition is similar to that in the thermoacoustic system, despite the fact that the amplitude levels in both systems differ by orders of magnitude.

III) Figure 3.2g-i represents the time series of strain experienced by the structure during the transition to aeroelastic instability. The observed oscillations are similar to those of the thermoacoustic and aeroacoustic systems, even though we are measuring a completely different unsteady variable.

From Fig. 3.2, we clearly see that these turbulent systems considered here follow an intermittency route to oscillatory instability. We observe a similar transition in all the three classes of systems even though the interacting subsystems and the physical mechanisms involved are different.

3.4 FRACTAL CHARACTERISTICS AND HURST EXPONENT

Next, we quantify the proximity to the onset of oscillatory instability in the discussed systems using the Hurst exponent (H). As mentioned earlier, the periodic content in time series of the unsteady variable increases as we approach an oscillatory instability. The state of low amplitude aperiodic oscillations has a fractal nature which is born out of the inherent fractal nature of turbulence. As the system self-organizes into oscillatory instability, the fractal time series transitions to a more regular periodic signal (Nair and Sujith, 2014). We capture the variation of fractal characteristics of the time series by calculating H .

Fractal objects exhibit self-similar features at various scales of magnification; therefore, measures such as length, area, and volume are dependent on the scale of measurement. For a fractal time series, the scaling of the rms of the standard deviation of fluctuations with the length of the data segment gives H . For non-fractal objects such as sinusoidal signals, $H \approx 0$ as there is no scaling with the data length or the scale of the measurement. We briefly describe the procedure of estimation of Hurst exponent in Sec. 3.4.1.

3.4.1 Estimation of Hurst exponent

There are several algorithms for calculating the Hurst exponent (H). They include multifractal detrended fluctuation analysis (MFDFA) (Kantelhardt *et al.*, 2002), rescaled range analysis (R/S) (Mandelbrot and Wallis, 1969), wavelet approach (Kantelhardt *et al.*, 2002), and multifractal detrended moving average (MFDMA) (Carbone *et al.*, 2004). Among these techniques, we use MFDFA (Kantelhardt *et al.*, 2002; Ihlen, 2012).

For a given time series $x(t)$ of length N , the mean subtracted cumulative deviate series $Y(k)$ is defined as,

$$Y(k) = \sum_{t=1}^k [x_t - \langle x \rangle], \quad k = 1, 2, \dots, N, \quad (3.1)$$

where $\langle x \rangle$ is the mean of the time series. We first divide the deviate series $Y(k)$ into $N_w = [N/w]$ non-overlapping segments of equal length w , where $[N/w]$ represents the greatest integer function. Then, we calculate the local trend for each of these segments i by a polynomial fit of the series and obtain the fluctuations by subtracting the polynomial fit (\bar{Y}_i) from the deviate series (Y_i). The polynomial fit we use in the current study is of order 1. The variance of fluctuations is determined as,

$$F^2(w, i) = \frac{1}{w} \left[\sum_{t=1}^w (Y_i(t) - \bar{Y}_i)^2 \right], \quad (3.2)$$

for each segment $i = 1, 2, \dots, N_w$.

The structure function of order 2 and span w , F_w^2 can be obtained as follows:

$$F_w^2 = \left[\frac{1}{N_w} \sum_{i=1}^{N_w} F^2(w, i) \right]^{1/2}. \quad (3.3)$$

We repeat the above steps for different time scales or span w . The slope of the linear regime in a log-log plot of F_w^2 , for a range of span sizes w gives the Hurst exponent (H). The Hurst exponent represents the scaling of the *rms* of the standard deviation of

fluctuations with the scale size or the time interval considered for obtaining the fluctuations. Generally, H has values between 0 and 1 for time series (*i.e.*, fractal dimension between 1 and 2). It provides a measure of persistence in a time series. For a persistent time series wherein subsequent values are highly correlated, $H > 0.5$. An antipersistent signal has $H < 0.5$, in which a high value of the signal is most likely followed by a low value. $H = 0.5$ corresponds to an uncorrelated random process.

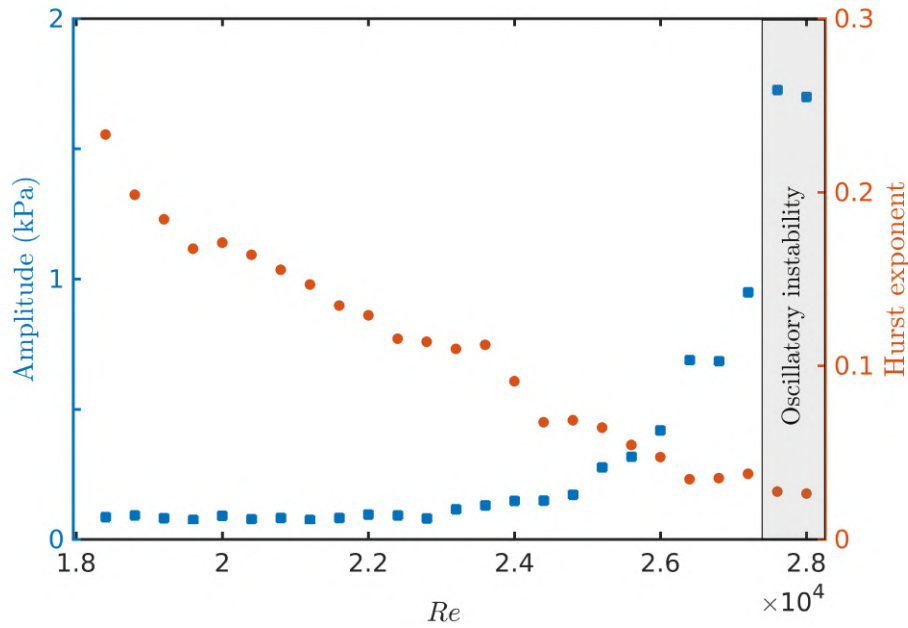


Fig. 3.3: Amplitude of the dominant mode of oscillations and the Hurst exponent for unsteady pressure signals as a function of Reynolds number (Re). We analyze the data from a laboratory bluff body stabilized combustor of length 700 mm for different Re . The amplitude is obtained from the amplitude spectrum plotted with a resolution of 4 Hz. The amplitude increases steeply near the transition to thermoacoustic instability, whereas the Hurst exponent shows a gradual decrease during the transition and it is approaching zero.

In our analysis, we compute H for the time series corresponding to the unsteady variable obtained at each state during the transition to oscillatory instability in thermoacoustic, aeroacoustic and aeroelastic systems. H for each state is calculated from the time series segments of selected duration. Unlike mathematical fractal objects which possess self-similarity across a wide range of scales extending up to infinity, real fractal objects appear to be self-similar only over a limited range of scales; one cannot keep on zooming in indefinitely to see the same structure. Thus, the time scales for calculation

of H need to be selected carefully. The choice of the range of scale (or segment length) should be optimal to capture the transition from an aperiodic to a periodic state (Kerres *et al.*, 2016). The periodicity at the onset of oscillatory instability will not be captured if we select segments of the length corresponding to less than one cycle of oscillation. Further, the fluctuations will be averaged out if we choose segments with a large number of cycles. Therefore, we choose two to four cycles of oscillations during the periodic regime as the optimum scale.

In Fig. 3.3, we plot the amplitude of the dominant mode of oscillations (A) and the Hurst exponent (H) for the time series of pressure oscillations as a function of Reynolds number (Re) for the thermoacoustic system (described earlier as case (i)). Note that, A is the amplitude of the dominant peak from the amplitude spectrum of the fluctuating state variable obtained using fast Fourier transform. The signal corresponding to thermoacoustic instability has H very close to 0, as the signal is perfectly periodic. We observe that during the transition, A increases steeply near the onset of thermoacoustic instability as we vary the control parameter. In contrast, H gradually decreases towards zero during the transition. The amplitude of oscillations or the value of A at the onset of oscillatory instability depends on the specific system under consideration. On the other hand, the variation of H describes the self-organization in turbulent flows into oscillatory instabilities, independent of the system features.

3.5 SCALING OF HURST EXPONENT WITH THE AMPLITUDE OF OSCILLATIONS

We plot the variation of A/A_I with H in log-log scale (Fig. 3.4) for the five different cases mentioned earlier. Here, we normalize A of each system with the amplitude of oscillations at the onset of instability (A_I) for the given system. We observe that all the data points collapse to a single straight line and this reveals an inverse power law relation between A and H during the intermittency regime. For all the data irrespective of the frequency of oscillations or the physics of the system, the experimentally

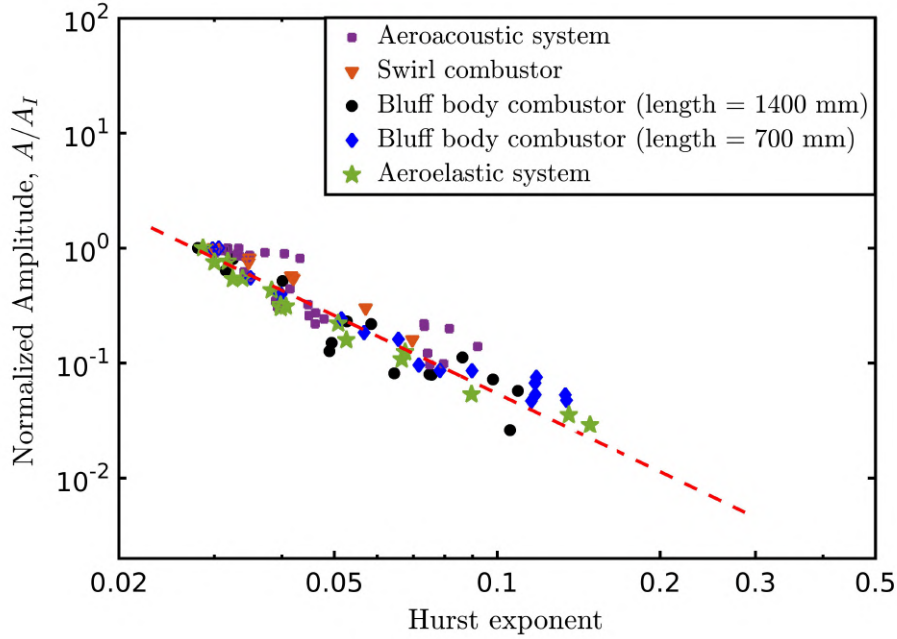


Fig. 3.4: Inverse power law scaling of amplitude with Hurst exponent. Variation of amplitude with Hurst exponent is plotted on a logarithmic scale for the data acquired from different systems. We observe a power law relation with a constant power law exponent around -2.

observed value for the power law exponent is found to remain constant around -2 (-1.83 ± 0.17 for the bluff body combustor with length 700 mm, -2.22 ± 0.58 for the bluff body combustor with length 1400 mm, -2.06 ± 0.24 for the swirl combustor, -2.02 ± 0.32 for the aeroacoustic system and -2.21 ± 0.19 for the aeroelastic system). The uncertainties are estimated for 90% confidence intervals. The points with $H > 0.1$ are ignored while finding the power law exponent as they represent the low amplitude aperiodic oscillations far away from the self-organized state.

Scaling laws and universality are important concepts in statistical physics. They describe the striking similarity in the behaviour during critical transitions among systems that are otherwise different. Scaling in non-equilibrium phase transitions is a topic of interest in recent years (Täuber, 2017). For example, Tham and Sen (1994) experimentally obtained a similar power law scaling relationship between the electrostatic fluctuation levels and the linear growth rate for self-organization in turbulent plasma leading to a quasi-coherent state.

Transition to oscillatory instability in the class of turbulent fluid mechanical systems discussed here occurs via the state of intermittency and we observe a universal scaling law during the transition. In fluid dynamics literature, intermittency refers to a state in which a laminar flow is interrupted by high amplitude turbulent bursts at apparently random intervals (Nayfeh and Balachandran, 2008*b*). During the bursts, the phase space trajectory goes to a larger chaotic attractor with the original periodic attractor as its subset. Three types of bifurcations are associated with such intermittencies, namely, cyclic fold, subcritical Hopf, and subcritical period-doubling bifurcations. Intermittencies corresponding to these bifurcations are labelled as type I, II and III, respectively (Manneville and Pomeau, 1979; Pomeau and Manneville, 1980)².

In our case, to begin with, the system is chaotic and is Lyapunov stable. However, during intermittency, this stability is lost and the system intermittently approaches limit cycle oscillations. In contrast to the known types of intermittencies discussed above, here, the intermittency comprises of high amplitude periodic oscillations amidst epochs of low amplitude aperiodic oscillations (Pawar and Sujith, 2018). The trajectory in the phase space goes to a larger periodic attractor from a smaller chaotic attractor during the intermittent bursts (Fig. 3.2 b, e and h). Thus, there is an inherent difference in the type of intermittency observed during the emergence of oscillatory instabilities in turbulent flows, as observed for example in thermoacoustic, aeroacoustic and aeroelastic systems compared to the classical ones.

In the present study, we observe the scaling behaviour in all the systems we have examined, where oscillatory instabilities emerge in turbulent flows. We do not observe this inverse power law relation in models such as kicked oscillator (Seshadri *et al.*, 2016) or noisy Hopf bifurcations (Noiray, 2017), even though they capture the transition from chaos to limit cycle via intermittency. Further, this scaling is not exhibited by models which capture the transition from chaos to periodic oscillations through type I, II and III intermittencies (shown in the Supplementary material). This experimentally observed

²Several other types of intermittencies have been reported and discussed (Schuster and Just, 2006).

scaling appears to be a universal property for a class of systems in which order emerges from chaos, as a result of self-organization in turbulence following an intermittency route.

Fully developed, isotropic turbulence has a well-known power-law scaling for its energy spectrum (Richardson, 1926; Kraichnan, 1967), which shows the distribution of energy across different wave numbers. The instances of self-organization in turbulence leading to oscillatory instability discussed in this paper are associated with the emergence of periodically shed, large coherent structures in the flow. This emergence of oscillatory instability is accompanied by the redistribution of energy across different length scales and thus deviation from the scaling observed in fully developed turbulent flows. In the various systems which we examine, as we approach oscillatory instabilities by changing some control parameter of each system, the redistribution of energy into the most dominant scale (*i.e.*, scale of coherent structure) in each system is captured by studying the amplitude spectra of an appropriate state variable of the system. In our study, we used unsteady pressure measurements for thermoacoustic and aeroacoustic systems and strain rate for the aeroelastic system.

Oscillatory instabilities in engineering systems such as rocket engines, power-producing gas turbine engines, gas transport pipelines and swaying skyscrapers are undesirable and can produce ruinously high-amplitude vibrations with catastrophic consequences. Using this scaling between H and A , we predict the amplitude of oscillations well before the onset of oscillatory instability using the data points obtained during the stable operation (Pavithran *et al.*, 2018a). This a priori estimation of amplitude helps in devising strategies to mitigate such oscillatory instabilities and also helps save a lot of money involved in testing the hardware.

3.6 SUMMARY

In the present study, using three different systems, we describe a universal route through which oscillatory instabilities emerge in turbulent flow. The amplitude of the dominant

mode of oscillations increases following an inverse power law scaling with the Hurst exponent of the time series of the appropriate state variable, and the scaling exponent is invariant across the three systems considered. The proximity to the onset of oscillatory instabilities is quantified by the Hurst exponent, which serves as a system independent measure of self-organization. Here, the spectral amplitude of the dominant mode of oscillations serves as the order parameter of the system.

Power law scaling have been discovered for various critical transitions. Here, we report the experimental observation of a scaling behaviour ($A \propto H^{-2}$) for a class of non-equilibrium systems. The discovery of this unique scaling enables a priori estimation of the amplitude of oscillations at the onset of oscillatory instability. This information of the amplitude can be critical in devising the counter measures needed to limit the possible damages from such oscillatory instabilities.

CHAPTER 4

Universality in spectral condensation

¹We extend our work on the universal behaviour of transitions to oscillatory instabilities to more diverse phenomena such as the onset of lasing in a random laser and Hopf bifurcation in Chua's circuit. Here, we try to bring different systems exhibiting the emergence of ordered dynamics due to self-organization under the same umbrella, since 'universal characteristics' of the transition to ordered dynamics in these systems garnered less attention.

4.1 TRANSITIONS TO AN ORDERED STATE (PATTERN FORMATION) IN FLUID MECHANICAL, OPTICAL, AND ELECTRONIC SYSTEMS

Self-organization is the spontaneous formation of spatial, temporal, or spatiotemporal patterns in complex systems far from equilibrium. In other words, an ordered pattern emerges from an initially disordered state. In dynamical systems, a pattern can be any regularly repeating arrangements in space, time or both (Cross and Hohenberg, 1993). For example, a laser emits random wave tracks like a lamp until the critical pump power, above which the laser emits light as a single coherent wave track with high-intensity (Haken, 1984). A macroscopic change is observed in the laser system as a long-range pattern emerges in time. Another example is the Rayleigh-Bénard system. For lower temperature gradients, the fluid parcels move randomly. As the temperature gradient is increased, a rolling motion sets in and the fluid parcels behave coherently to form spatially extended patterns. The initial random pattern can be regarded as a superposition of a variety of oscillatory modes and eventually some oscillatory modes dominate, resulting in the emergence of a spatio-temporal pattern (Croquette, 1989; Kelso, 1995).

¹The results presented in this chapter are published in (Pavithran *et al.*, 2020a).

Self-organization often results in the redistribution of energy from a wide range of frequencies to a few dominant modes to form periodic patterns. Such a condensation in the spectrum is analogous to the condensation phenomenon observed in classical and quantum systems and we call this phenomenon spectral condensation. Bose-Einstein condensation (BEC) occurring in quantum systems is characterized by occupation of the same energy level by a large fraction of the particles as temperature approaches absolute zero (Davis *et al.*, 1995; Ketterle, 1999). The transition to the condensate state, where the particles act collectively as a wave, can be viewed as the emergence of an ordered pattern from a disordered state of particles having different energy. Researchers have reported the observation of light condensation with the emission spectrum collapsing to the frequency of the lowest-loss mode (Fischer and Weill, 2012; Klaers *et al.*, 2010; Conti *et al.*, 2008; Fischer and Bekker, 2013). Similarly, by drawing parallels to BEC, condensation phenomenon has been used to explain several dynamical transitions where an ordered final state is achieved from an initially disordered state even in classical systems (Sun *et al.*, 2012). For instance, a population of coupled oscillators forms a dynamical condensate where the condensation phenomenon leads to global synchronization among the group of oscillators (Zanette and Mikhailov, 1998). Likewise, the framework of BEC has been utilized in predicting the competitive dynamics in the evolution of complex networks (Bianconi and Barabási, 2001).

During self-organization, energy distributed in a broadband of frequencies gets condensed into a dominant mode, analogous to a condensation phenomena. We call this phenomenon spectral condensation and study its occurrence in fluid mechanical, optical and electronic systems using the power spectrum of the appropriate system variables (in the emission spectrum for the optical system). In conditions where the system is influenced by external noise or inherent fluctuations, the emergence of such a periodic pattern can be gradual as the parameter is varied. In this study, we quantify spectral condensation across various systems by defining a set of spectral measures based on the power spectrum. The power of the dominant mode is found to scale with these spectral

measures following an inverse power law. From experimental observations, we find that systems exhibiting self-organization driven by positive feedback follow unique way of spectral condensation in spite of different underlying physical mechanisms. Note that the self-organization that we are discussing in this paper is different (Watkins *et al.*, 2016) from the concept of self-organized criticality (SOC) introduced by Per Bak and collaborators (Bak *et al.*, 1987; Bak, 1996).

4.2 EXPERIMENTS

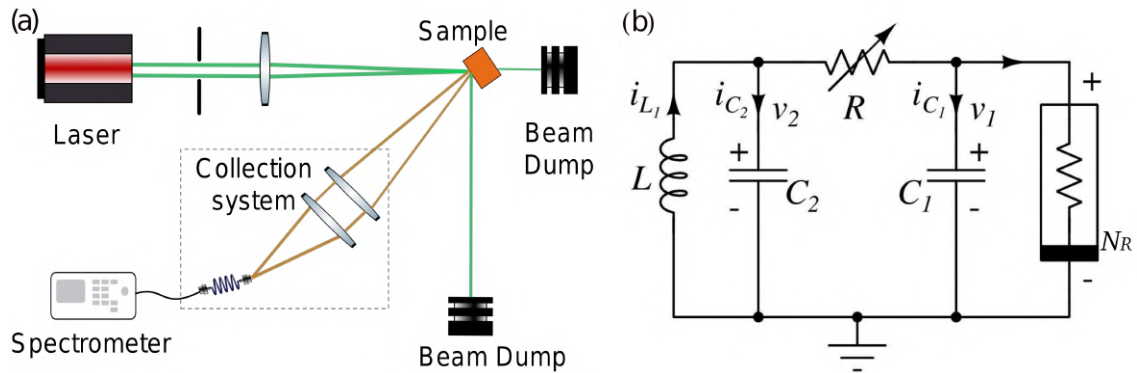


Fig. 4.1: Schematic of the experimental setups. (a) An optical system for random lasing, wherein we observe a transition towards narrow-band lasing like emission as we increase the excitation pulse energy (EPE) of the laser source. (b) Electronic circuit known as Chua's circuit is used for the experiments. The variable resistor (R) is varied to obtain the transition from a fixed point to limit cycle oscillations. In both the systems, we acquire data for different values of the respective control parameters. For the random laser, the output emission is collected using a fibre optic spectrometer. The voltage (v_1) is measured for the electronic circuit. The dimensions of different experimental setups are not to scale.

Fluid mechanical systems examined in this study include thermoacoustic, aeroacoustic and aeroelastic systems which exhibit transition to oscillatory instabilities upon varying a control parameter. Details about the experiments are discussed in Chapter 3. We analyze the power spectrum of a fluctuating system variable in the following cases: a thermoacoustic system with different flame holding mechanisms and different combustor lengths (Fig. 3.1a), an aeroacoustic system (Fig. 3.1b) and an aeroelastic system (Fig. 3.1c). Thermoacoustic system with different combustor lengths helps to

achieve different characteristic time scales. Further, the two flame holding mechanisms in the combustor causes different mechanisms of thermoacoustic instability.

4.2.1 Optical system

A random lasing system consists of an optical gain medium with a large number of scatterers dispersed in a random arrangement (Cao, 2003). The gain medium emits light upon excitation by a suitable wavelength. Analogous to the standard cavity mirrors, the feedback obtained through appropriate multiple scattering scenarios accounts for the amplification. We perform random lasing experiments with zinc oxide particles (ZnO) as scatterers and Rhodamine 6G dye as the gain medium. 50 mg of ZnO powder and 1 mg of Rhodamine 6G dye are dissolved in 3 ml of ethylene glycol to make a colloid and is filled in a quartz cuvette for the experiment. Figure 1d represents the experimental setup for the random lasing. We excite the sample with the second harmonic of an Nd:YAG laser source ($\lambda = 532$ nm) with a repetition rate of 10 Hz and a pulse duration of 120 ps. The sample is positioned at an acute angle ($50^\circ \pm 0.5^\circ$) to the incident beam and the emission is captured by the collection lenses from the side. This arrangement helps to avoid the reflected rays of the excitation source from the cuvette. We increase EPE to achieve lasing. The output emission is collected by the tip of the fiber optic cable. The emission spectrum is obtained using Research India RIS-T1708 spectrometer. I have conducted the experiment at IIT Madras.

4.2.2 Electronic circuit

Chua's circuit is used to study spectral condensation during the transition from a fixed point to a limit cycle (Fig 1e shows the schematic of the circuit). It is a third-order, autonomous electronic circuit having a linear resistor, two linear capacitors, a linear inductor and one nonlinear element, known as Chua's diode (Kennedy, 1992; Lakshmanan and Murali, 1996). Chua's diode has a nonlinear (piecewise-linear) $v - i$ characteristics (Lakshmanan and Rajaseekar, 2012). More details and diagram can be found in Kennedy (1992). The circuit parameters are chosen to be $C_1 = 10$ nF,

$C_2 = 100 \text{ nF}$ and $L = 18 \text{ mH}$. By reducing the variable resistor, R from 2000 Ω towards 0 Ω , Chua's circuit exhibits a sequence of bifurcations. Here, we vary the control parameter R to observe a transition from a fixed point to limit cycle oscillations. The voltage (v_1) is acquired using a 16 bit A/D card (NI6343) at a sampling rate of 200 kHz. I along with a co-author performed the experiments in aeroacoustic system at IIT Madras.

4.3 MATHEMATICAL MODELS

4.3.1 Kicked oscillator model describing the thermoacoustic system

We use a kicked oscillator model to study the scaling observed during the transition to limit cycle oscillations. Fluid mechanical systems that involve vortex shedding can be modelled as kicked oscillators (Seshadri *et al.*, 2016). In the model, the kicks are random when we are far from the self-organized state and become periodic as we approach the onset of oscillatory instability. In lasers, we observe a similar behaviour. The individual electrons emit light wave-tracks randomly, and those running in the axial direction are reflected multiple times between the mirrors and stay longer in the medium, while all other tracks leave it. At a threshold excitation power, suddenly all of them start to emit light in phase, and light intensity increases drastically (Haken, 1984). All the emitted light are in phase forming a giant wave track leading to a typical synergetic phenomenon.

The kicked oscillator model captures the state of aperiodic oscillations, intermittency and limit cycle oscillations as observed in practical systems mentioned earlier. Seshadri *et al.* (2016) used a Galerkin expansion to express the acoustic variables in terms of the natural modes of the duct. They obtained a kicked oscillator equation for the acoustics modes as follows:

$$\ddot{\eta}_n + \xi_n \dot{\eta}_n + \omega_n^2 \eta_n = B_n \sum_j \delta(t - t_j) \quad (3)$$

Here B_n is the kicking strength, t_j s known as the kicking times are the time instants of each kick. The kicking time instants t_j s are defined as follows:

$$t_j = t_{j-1} + (1 - C(p_a))T_a + C(p_a)\sigma T_a |\mathcal{N}(0, 1)| \quad (4)$$

Here T_a is the dominant time period, $\mathcal{N}(0, 1)$ is the Gaussian white noise and σ is the strength of the noise. C is a biased coin toss where 1 occurs with probability p_a and 0 with a probability $1 - p_a$ and p_a is called the aperiodic probability. p_a is an estimate of the aperiodic content in the time series. Here, we can think of the aperiodic probability as a parameter (like the Reynolds number) that we are varying to achieve the different dynamical states of the system. From equation (3) and (4) we can observe that for $p_a = 0$, the kicks are periodic and hence the dynamics correspond to a state of limit cycle oscillations. Whereas $p_a = 1$, the kicks occur at random time instants and hence this corresponds to a state of aperiodic oscillations.

Following Seshadri *et al.* (2016), the kicking strength B is kept constant as 100 for this study and the noise strength σ is selected as 5 and 1 for the aperiodic case and limit cycle respectively. We vary the aperiodic probability from 1 to 0 (corresponding to aperiodic fluctuations to limit cycle) in steps of 0.001 to obtain time series corresponding to each aperiodic probability. Now for each of these time series, the Fourier transform was evaluated and the spectral measures are computed. Now the variation of spectral measures and the power corresponding to the dominant mode of oscillations are plotted (Fig. 3d-f). We can see that this model captures the inverse power law relationship that was observed in the experimental data.

4.3.2 Noisy Hopf bifurcation model

We examine another model of a nonlinear oscillator in the presence of noise which exhibits subcritical and supercritical Hopf bifurcation.

$$\ddot{\eta} + \alpha\dot{\eta} + \omega^2\eta = \dot{\eta}(\beta + K\eta^2 - \gamma\eta^4) + \xi \quad (5)$$

Here, α and β are linear damping and driving respectively. Following Noiray (2017), we use additive white noise ξ of intensity Γ and having an autocorrelation $\langle \xi \xi_\tau \rangle = \Gamma \delta(\tau)$. The values of the parameters ω , β , γ , K and Γ are kept constant ($\omega = 2\pi \times 120$ rad/s, $\beta = 50$ rad/s, $\gamma = 0.7$, $K = 9$, $\Gamma = 10^5$). The linear damping (α) is varied from 95 rad/s to 56 rad/s to capture the transition from an aperiodic state to a high amplitude limit cycle oscillation. The corresponding time series of η for each value of α is obtained and the spectral measures are evaluated from the power spectra of the time series of η . As observed for the experiments, the spectral measures follow inverse powerlaw scaling with peak power for noisy Hopf bifurcation as well, where periodicity arises out of a noisy environment.

4.4 SPECTRAL CONDENSATION: SHARPENING OF THE POWER SPECTRUM DURING PATTERN FORMATION

We analyze the sharpening of the dominant peak in the power spectrum of a fluctuating system variable during the emergence of order. All the three fluid mechanical systems exhibit a transition to oscillatory instability as we increase the Reynolds number (Re) as shown in Fig. 3.2. Here, we present the evolution of the power spectrum only for a representative set of data (Fig. 4.2a), although all aforementioned cases of the fluid mechanical systems have been analyzed. The power spectrum has a broad peak for low values of Re . We observe the transition of power spectra from a broad peak to a sharp one as we approach the onset of the oscillatory instability. Each spectrum is normalized with its maximum amplitude to emphasize the narrowing of the peak (Fig. 4.2b).

The optical system chosen for this study is a random lasing system (Fig. 4.1d). Unlike conventional lasers, the lasing action in random lasers is achieved by strong multiple scattering in the optical gain medium. The large number of scatterers which are dispersed in the gain medium causes the light rays to scatter multiple times before they exit the gain medium (Cao, 2003; Gummaluri *et al.*, 2018). The emission spectrum of a random laser, upon excitation by a pulse of suitable wavelength, is acquired using a fibre

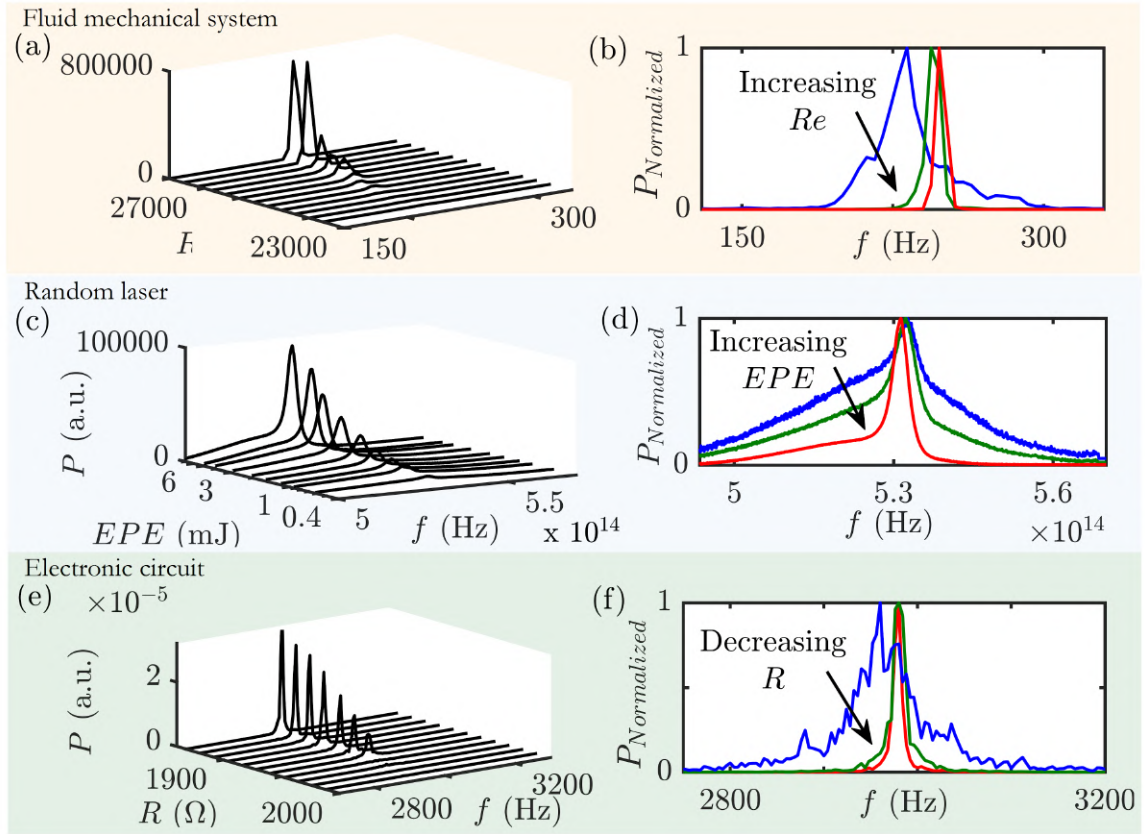


Fig. 4.2: Evolution of the spectrum for fluid mechanical, optical and electronic systems. The evolution of power spectrum with variation in the corresponding control parameter is presented on the left side and the normalized spectra for each system is given on the right side of the panel. **(a, b)** Power spectra obtained using Fast Fourier Transform (FFT) of the acoustic pressure fluctuations for a laboratory-scale bluff body stabilized combustor of length 700 mm. The power spectra exhibit an increasing dominance of a single peak on approaching oscillatory instabilities (for increasing Re) in all the fluid mechanical systems discussed in this paper, and hence this figure is a representative example. **(c, d)** Emission spectra of the random laser as we progressively increase EPE. The power spectrum is obtained by multiplying the photon count per second for each wavelength with its respective energy. The broad spectrum starts to become a narrow lasing-like peak with increase in EPE. **(e, f)** Power spectra obtained using FFT of the voltage signal (v_1) measured from Chua's circuit and the corresponding normalized spectra are shown respectively. The peak sharpens during the transition to limit cycle oscillations as the resistance (R) is decreased. The power spectra using FFT are plotted for a resolution of 4 Hz for visualization purpose.

optic spectrometer. There is an appreciable narrowing in the emission profile (Fig. 4.2c) with the increment in excitation pulse energy (EPE), as is evident in Fig. 4.2d where

each spectrum is normalized with its maximum power.

To study spectral condensation in electronic systems, we select Chua's circuit (Fig. 4.1e) which has become a paradigm for chaos (Chua *et al.*, 1987; Lakshmanan and Murali, 1996). It consists of two capacitors, an inductor, a resistor and one nonlinear element known as Chua's diode. The system exhibits period-doubling bifurcation from a fixed point to chaos with change in the resistance, R . Here, we focus on the transition from a fixed point to a period-1 limit cycle. In experiments, external noise or inherent fluctuations including thermal fluctuations of the electronic devices, their inaccuracies and electromagnetic interference will make the fixed point noisy (Prebianca *et al.*, 2018). Thus, for the conditions for which a fixed point is expected, we observe low amplitude noisy oscillations with a broad peak in the power spectrum centered around the natural frequency. During this transition to limit cycle (noisy Hopf bifurcation), we find a narrowing of the power spectrum (Fig. 4.2e, f) akin to that observed in fluid mechanical and optical systems.

4.4.1 Spectral measures

Next, we quantify the sharpening of the power spectrum during spectral condensation by defining 'spectral measures'. The general expression for the spectral measure is:

$$[\mu_m^x \mu_n^y] = \left[\int_{-\delta F}^{+\delta F} \frac{P(F)}{P_0} \left| \frac{F}{f_0} \right|^m dF \right]^x \times \left[\int_{-\delta F}^{+\delta F} \frac{P(F)}{P_0} \left| \frac{F}{f_0} \right|^n dF \right]^y. \quad (1)$$

Here, μ_m is the m^{th} moment of the power spectrum. $P(F)$ represents the power corresponding to the modified frequency $F = f - f_0$, where f is a variable indicating the frequency of oscillations, f_0 is the frequency corresponding to the dominant peak in the power spectrum, and $P_0 = P(f_0)$. The indices m , n , x & y of the spectral measure are chosen to be positive integers. As our interest is to study the condensation towards a single peak, we compute the spectral measures $[\mu_m^x \mu_n^y]$ only in the neighbourhood of width δF centered at f_0 . We set δF to $f_0/5$, based on our analysis of a collection

of data with vastly different values of f_0 . Also, the amplitude of the peak reduces significantly within this range. Variations in the choice of δF can be tried out, based on the appearance of the spectrum, such that it covers the spread of the peak during condensation. The spectral measures, $[\mu_m^x \mu_n^y]$ can be considered as the products of moments of the power spectrum raised to integer powers. According to the definition of the spectral measures, $[\mu_m^x \mu_n^y]$ decreases as the peak gets sharper. In this study, we present the analysis of three representative spectral measures, $[\mu_2]$, $[\mu_2 \mu_0]$ & $[\mu_4 \mu_4]$. Note that $[\mu_2]$ is the second moment of the power spectrum in the δF neighbourhood of f_0 , whereas, $[\mu_2 \mu_0]$ & $[\mu_4 \mu_4]$ are the products of higher moments of the distribution. Higher moments give more weightage to the tail ends of the spectrum and thus its variation indicates how the broad tails diminish.

4.5 INVERSE POWER-LAW SCALING OF SPECTRAL MEASURES WITH THE PEAK POWER

We uncover an inverse power law relation between the spectral measures and the power corresponding to the dominant peak (Fig. 4.3a-c) during spectral condensation. All the data sets for the fluid mechanical, the optical and the electronic systems collapse to an inverse power law scaling in spite of the different physics involved in the process of condensation. We also present the analysis of data obtained from two models: kicked oscillator model (Seshadri *et al.*, 2016) and noisy Hopf bifurcation model (Noiray, 2017) discussed in Sec. 4.3. Both the models exhibit a transition from low amplitude aperiodic oscillations to a high amplitude limit cycle, thereby a condensation behaviour is observed in the power spectrum. We detect a similar scaling relation between $[\mu_m^x \mu_n^y]$ and P_0/P_N (Fig. 4.3d-f) as observed in experiments. This inverse power law behaviour appears to be a universal characteristic of spectral condensation and the experimentally observed value for the power law exponent (k) corresponding to the spectral measures $[\mu_2]$, $[\mu_2 \mu_0]$ & $[\mu_4 \mu_4]$ are around -1.12 ± 0.13 , -0.7 ± 0.08 and -0.50 ± 0.06 respectively (averaged across systems). The exponent (k) is found to reduce for the

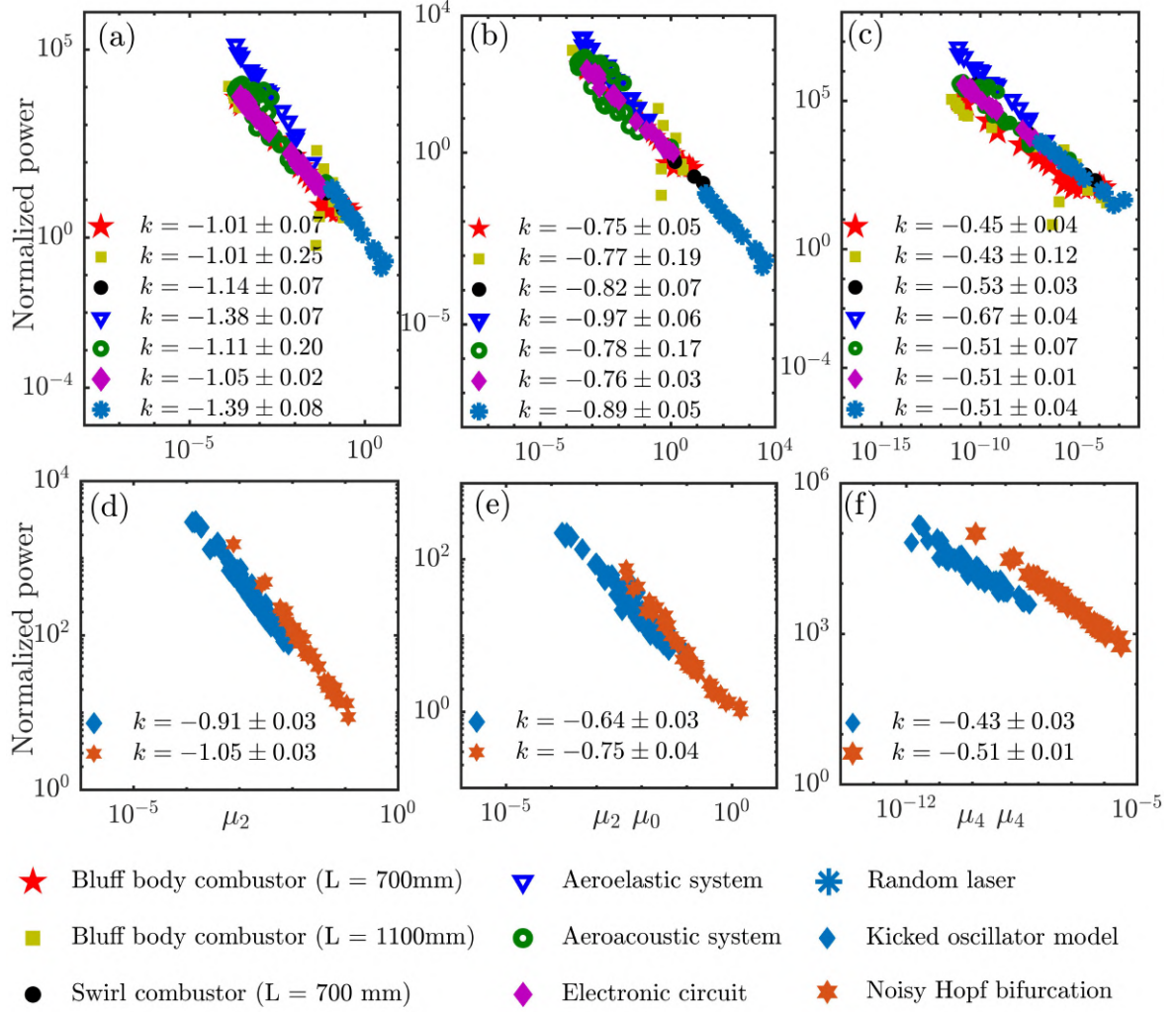


Fig. 4.3: The scaling behaviour of spectral measures with the peak power during spectral condensation in experimental systems and models. Variation of the normalized power (P_0/P_N) corresponding to the dominant mode with the representative spectral measures ($[\mu_2]$, $[\mu_2 \mu_0]$ & $[\mu_4 \mu_4]$) plotted in double logarithmic scale (a-c) for the data acquired from experiments conducted in different systems and (d-f) for the data generated from two models. The extent of spectral condensation and the peak power differs by orders of magnitude across these systems. Hence, we rescale the power corresponding to the dominant peak (P_0) as P_0/P_N to show the lines, $\log(P_0) = k \log([\mu_m^x \mu_n^y]) + C$, in the same plot. The normalization factor, P_N , is the estimated value of peak power for $[\mu_m^x \mu_n^y] = 1$ obtained by extrapolating the line $\log(P_0) = k \log([\mu_m^x \mu_n^y]) + C$ for each system. This choice of P_N forces all lines to have $C = 0$. We observe an inverse power law behaviour for all the spectral measures in the experiments as well as in the models. The uncertainties in the power law exponent are shown for 95% confidence intervals.

higher indices of the measure and k for higher moments have much narrower dispersion across different systems (Sec. 4.5.2). It may be noted that we do not ignore any points as power law tails and do not introduce any cutoffs in the power law scaling.

4.5.1 Functional form for the power spectrum

The existence of multiple invariant exponents motivates us to think about the existence of a universal form for the power spectrum in the neighbourhood of f_0 . The power law relations indicate that given a distribution of power over a range of frequencies, the spectral measures at all levels of spectral condensation is already determined by the inverse power law relations. Further, the power spectrum decays away from f_0 and this decay is steeper for a sharp peak with higher amplitude. Thus, we consider a functional form for the power spectrum which is a function of F and has P_0 and f_0 as two parameters, and is as follows:

$$P(F) = P_0 e^{\left[-(P_0)^\alpha \left(\frac{F}{f_0} \right)^\beta \right]}, \quad (2)$$

where all the symbols retain their definitions. Here, both α and β have to be strictly positive. By comparing with the experimentally obtained values of power law exponents (k) for a set of spectral measures (for combinations of m , n , x & y), we estimate the optimal values of the parameters α and β iteratively as $\alpha = 0.125 \pm 0.017$ and $\beta = 0.317 \pm 0.024$ respectively.

4.5.2 Power law exponents for a set of spectral measures

The set of spectral measures show an inverse power law relation with the power corresponding to the dominant mode during spectral condensation. The power law exponents decrease for the higher indices of the measure. The power law exponents calculated for different indices up to $m = 4$ and $n = 4$ are summarized in Fig. 4.4. We have compared the exponents for different experimental systems and models. In Fig. 4, bluff body combustor A and B represent bluff body combustor with length 700 mm and

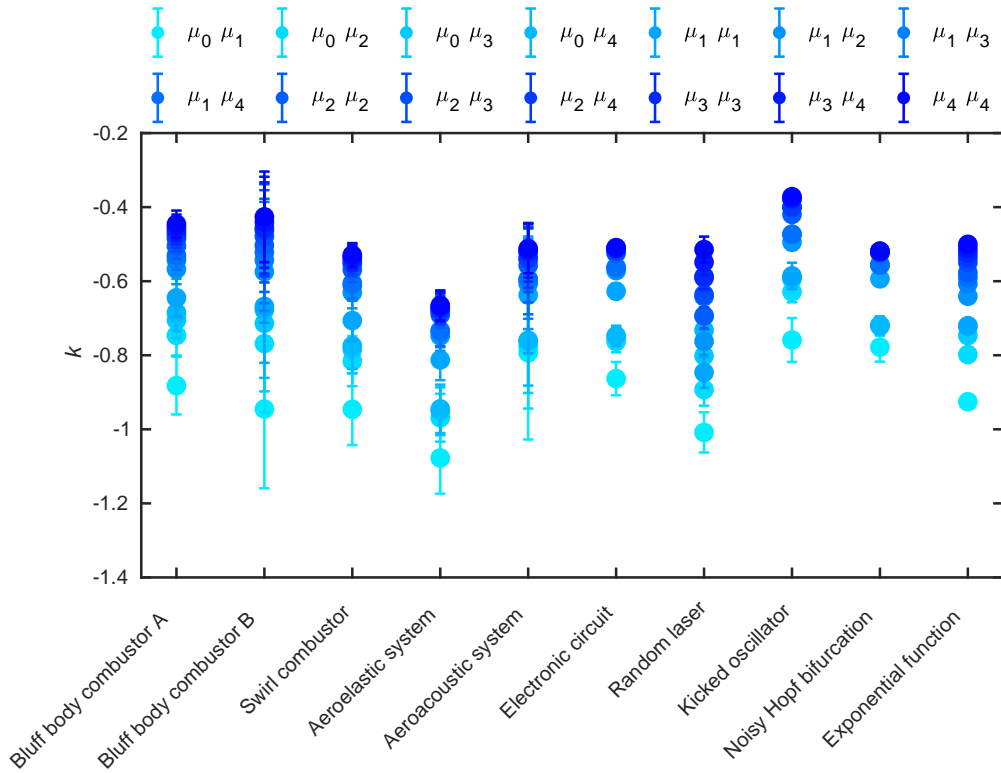


Fig. 4.4: Power law exponents obtained from the scaling relation between the spectral measures and the peak power for the higher index spectral measures in different experimental systems and models. Here, the exponential function refers to the functional form of the power spectrum as defined in Eq. 4.1 in the manuscript.

1100 mm respectively.

4.6 SUMMARY

During the transition to an ordered dynamics, there is a condensation of spectral power to a dominant mode of oscillations, we call this as spectral condensation. We define spectral measures to compare and quantify spectral condensation in different systems and we uncover a universal route through which spectral condensation occurs in fluid mechanical, optical and electronic systems. The dominant peak in the power spectrum sharpens with an increase in peak power following inverse power law relations with the spectral measures. Interestingly, the scaling exponents are found to be within a small range across all the systems studied. In addition, we note that the area under the curve in

the power spectrum is not constant during the process of spectral condensation. It is not merely a redistribution of energy in the power spectrum; there is amplification due to transfer of energy across subsystems through the positive feedback mechanism. Thus, the total power associated with the system variable is not conserved during spectral condensation.

From a practical viewpoint, these spectral measures can be used as a system independent method to quantify dynamical transitions in systems where an emergent periodic behaviour is observed. During spectral condensation in fluid mechanical systems, the condensation of power to a dominant mode causes high amplitude periodic oscillations which can have catastrophic effects on the system. In such cases estimating the peak power during oscillatory instability will help to design control strategies to mitigate oscillatory instabilities (Pavithran *et al.*, 2020*b*). In future studies, it will be interesting to study this scaling behaviour for biological systems.

CHAPTER 5

Predicting the amplitude of oscillatory instabilities using the scaling

¹Oscillatory instability, especially thermoacoustic instability (TAI) is a severe problem faced by the propulsion and power industry (Juniper and Sujith, 2018). Practical combustion applications such as gas turbine engines and rocket motors often encounter thermoacoustic instability. Thus, there has been an increasing demand for methodologies to mitigate TAI. One solution to mitigate TAI involves implementing control strategies to suppress these oscillations. In general, passive control strategies are preferred. The control mechanisms generally involve modifications of the combustor geometry, fuel injector geometry or microjet injection (Schadow and Gutmark, 1992). These strategies are implemented based on ad hoc modifications, investing a lot of money and time.

Alternately, there has been work on development of precursors to predict the proximity to TAI, methods to estimate the amplitude of TAI using the data acquired during stable operation, and implementing control strategies to suppress these oscillations. It would be desirable to perform the detection and control before the system reaches TAI rather than looking at the amplitude or root mean square (rms) of the fluctuations. There have been successful attempts to predict the onset of TAI. The stability margin was determined using several methods such as autocorrelation of the acquired pressure signal (Lieuwen, 2005), exhaust flow and fuel injection rate modulation (Johnson *et al.*, 2000), etc. Recently, researchers have developed techniques to determine stability boundaries based on only acoustic pressure measurements. There are several methods to obtain early warning signals based on multifractality (Nair and Sujith, 2014), recurrence quantification (Nair *et al.*, 2014b; Gotoda *et al.*, 2014), complex networks (Godavarthi *et al.*, 2018; Murugesan and Sujith, 2016), synchronization index, modified permutation

¹The results presented in this chapter are published in (Pavithran *et al.*, 2021a).

entropy (Gotoda *et al.*, 2012), and a combination of artificial intelligence with physics-based precursors (Kobayashi *et al.*, 2019; Hachijo *et al.*, 2019; Bhattacharya *et al.*, 2020). A detailed description of early warning signals for thermoacoustic instability can be found in Chapter 2.

Being able to determine the amplitude during TAI helps to design appropriate control strategies. If the estimated amplitude is low enough that the combustor can handle it, then the combustor can be operated safely during TAI as well. However, if the amplitude is deemed dangerous for the combustor, either we can evade TAI or appropriate countermeasures such as increasing the flame length by using alternate fuel paths can be made. Several studies have been conducted in the past to estimate the amplitude of limit cycle oscillations (LCO) during thermoacoustic instability. Traditionally, the amplitude is estimated utilizing flame describing functions (FDF) (Ćosić *et al.*, 2013; Stow and Dowling, 2004). FDF characterizes the linear or nonlinear response of flame to external perturbations of different amplitudes and frequencies. For better predictions, Krediet *et al.* (2010) considered acoustic boundary losses along with the FDF, and the accuracy of the predictions could depend upon both the FDF and the acoustic losses (Krediet *et al.*, 2010).

Even though predicting the amplitude using FDF has been reported to be successful in many cases, forcing the system at high amplitudes to obtain FDF is costly and difficult for industrial engines. It is hard to design actuators to produce high amplitude oscillations, and exciting such high amplitudes in high pressure gas turbine combustors is not advisable. Recently, Seshadri *et al.* (2018b) proposed a methodology for predicting the amplitude based on intermittency statistics where TAI is associated with vortex shedding. They considered the acoustic field as a kicked oscillator and the impingement of a vortex carrying unburned reactant mixture results in a burst of heat release which, in turn, adds energy to the acoustic field. Then, an equation is derived for the slow-varying amplitude of oscillations from the reduced-order model for a combustion system with vortex shedding. They were able to predict the amplitude

of LCO successfully for bluff body and swirl stabilized combustors.

While studying the transition to TAI, the effects of turbulence are often considered as background noise and are neglected in the traditional approach. We treat these fluctuations with their inherent complexities as opposed to considering them as noise and quantify the fractal characteristics of the acoustic pressure fluctuations using a measure known as Hurst exponent (H). H describes how the rms of the standard deviation of fluctuations scales with the time over which it is calculated. While the amplitude of pressure fluctuations increases steeply near the onset of the TAI, H decreases smoothly and relatively much earlier than the rise in amplitude. The amplitude of the dominant mode of oscillations follows an inverse square law scaling with the Hurst exponent (Chapter 3). In the current study, we use this concept to predict the amplitude of the LCO during TAI. Irrespective of the frequency of oscillations or the underlying physics of the problem, the data acquired from various configurations of thermoacoustic, aeroacoustic and aeroelastic systems obey this inverse square law. Hence, we estimate the amplitude of LCO by extrapolating the universal power law relation towards TAI (i.e., H tending to zero).

We also present a methodology to estimate the amplitudes of different modes of oscillations separately using ‘spectral measures’ which quantify the sharpening of peaks in the power spectrum. The spectral measures are calculated as the product of different moments of the normalized power spectrum raised to integer powers, and they follow inverse power law relations with the corresponding peak power (Chapter 4). Once we have the time series of acoustic pressure oscillations during the stable operation, we can generate the power spectrum and identify all the possible modes that are expected to grow. The scaling relation enables us to predict the amplitude during TAI, given the value of spectral measures and the amplitude at the safe operating condition. The objective of this study is to present the application of the patent-pending methodologies (Pavithran *et al.*, 2018*a,b*) for predicting the amplitude of TAI.

In the rest of this chapter, we discuss the results which include characterizing the

transition to TAI using the two methods and the interpretation of the inverse power laws. Then, we detail the procedure of estimation of amplitude and illustrate its efficacy using some examples. Details of experiments are provided in Chapter 3. Experiments were performed with both bluff-body stabilized combustor and a swirl stabilized combustor with different lengths of 700 mm, 1100 mm and 1400 mm. We focus on the transition from the state of combustion noise (CN) to TAI following an intermittency (INT) route in turbulent thermoacoustic systems. The Reynolds number (Re) is considered as the control parameter to study this transition. We use the same data reported in Nair and Sujith (2014), Unni and Sujith (2015) and Nair *et al.* (2014a), and discussed in Ch. 3.

5.1 TRANSITION TO THERMOACOUSTIC INSTABILITY: HURST EXPONENT AND SPECTRAL MEASURES

The time series of acoustic pressure fluctuations acquired at different values of Re during the transition are analyzed. Figure 5.1 shows three such time series and the corresponding amplitude spectra for the states of CN, INT and TAI. The time series during CN comprises low amplitude aperiodic oscillations which are multifractal (Nair and Sujith, 2014). As we approach TAI, we start to observe bursts of periodic oscillations in the data. A state of intermittency which consists of epochs of high amplitude periodic oscillations amidst low amplitude chaotic oscillations is present during the transition to TAI. The periodic content increases and becomes self-sustained limit cycle oscillations (LCO) during the state of full-blown instability (discussed in Chapter 3). Along with this, the dominant peak in the amplitude spectrum changes from a broad peak to a sharp one (as discussed in Chapter 4).

Figure 5.2 shows the variation of p'_{rms} and the amplitude of dominant mode (FFT peak) as a function of Re . For relatively lower Re , both p'_{rms} and FFT peak are very low due to the presence of low amplitude aperiodic fluctuations during CN. We note that p'_{rms} is slightly greater than the FFT peak during CN, as the time series is aperiodic to a great extent and the energy is distributed over a wide range of frequencies. The FFT

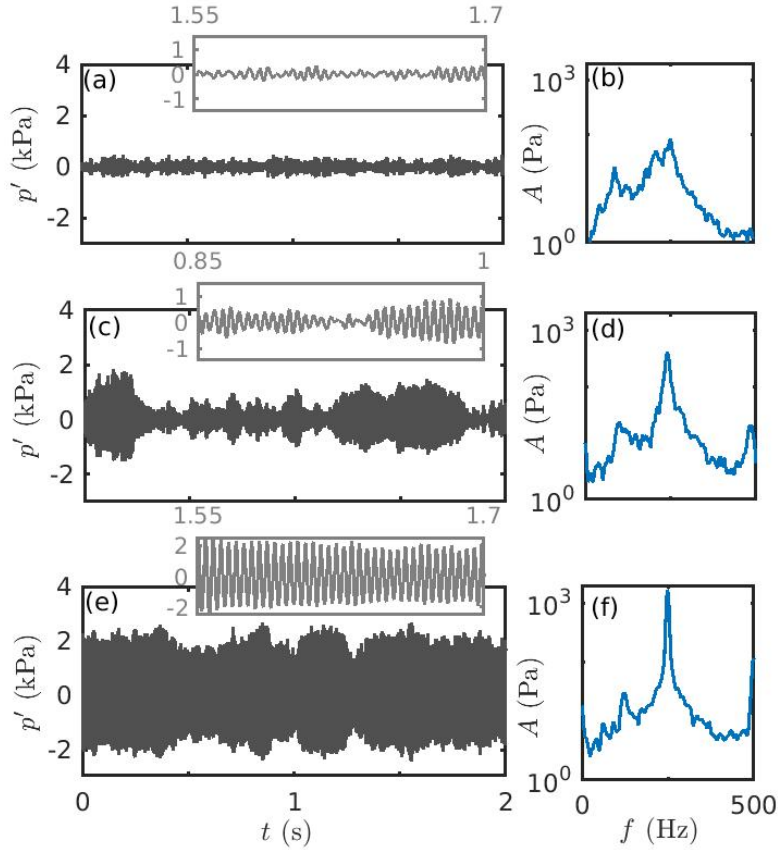


Fig. 5.1: Time series and the corresponding amplitude spectrum of acoustic pressure fluctuations during the transition from CN to TAI. The data obtained for the bluff body stabilized combustor is presented here as a representative case; we observe a similar transition in swirl stabilized combustor as well. **(a)** The time series representing the state of CN ($Re = (1.9 \pm 0.053) \times 10^4$) consists of low amplitude aperiodic oscillations. **(b)** The amplitude spectrum shows a broad peak around $f = 250$ Hz. **(c)** We observe a state of INT at $Re = (2.6 \pm 0.069) \times 10^4$. The time series during INT has bursts of high amplitude periodic oscillations amidst epochs of low amplitude aperiodic oscillations. This reflects as an increase in the amplitude of the peak in the amplitude spectrum **(d)**. Then, the amplitude of pressure fluctuations increases abruptly during TAI. **(e)** The time series during TAI (at $Re = (2.8 \pm 0.073) \times 10^4$) comprises high amplitude periodic oscillations and the resultant amplitude spectrum **(f)** has a sharp peak around $f = 250$ Hz.

peak accounts for only the amplitude of the dominant mode. Hence, during TAI, we observe that the FFT peak becomes higher than p'_{rms} by a factor of $\sqrt{2}$ as expected for a sinusoidal signal because all the energy is being transferred to a single frequency. Also, the oscillations grow to a very high amplitude during TAI. We use Hann windowing while performing fast Fourier transform (FFT). The method of windowing helps to get

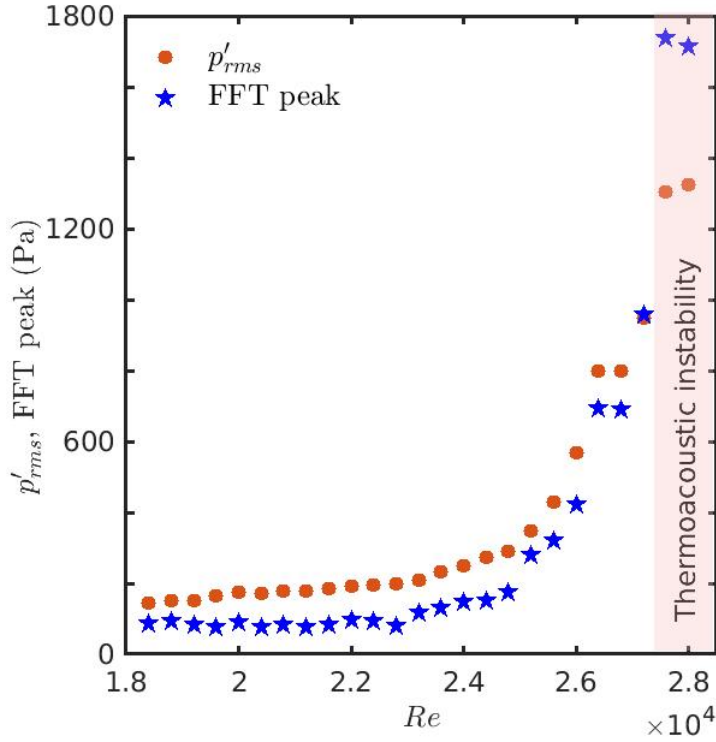


Fig. 5.2: The variation of p'_{rms} and the FFT peak during the transition from CN to TAI. The amplitude of dominant mode of oscillations computed from the amplitude spectrum using the Fourier transform is referred to as the FFT peak. Both p'_{rms} and FFT peak are very low during CN. The amplitude of oscillations increases as we approach TAI, which is captured by both p'_{rms} and FFT peak. This figure uses data acquired from a bluff body stabilized turbulent combustor.

a consistent estimation of the peak amplitude. We can minimize issues of spectral leakage by applying windowing. In this case, we use a Hann window for 0.25 s long data segments, thereby fixing a resolution of 4 Hz for the FFT. We find the FFT peak as the average of peak amplitudes of these 0.25 s windows for the full 3 s data.

5.2 FRACTAL CHARACTERISTICS AND UNIVERSAL SCALING

To quantify the fractal characteristics of acoustic pressure fluctuations during the transition to TAI, we use the Hurst exponent (H). For a time series, H is related to the fractal dimension (D) as $H = 2 - D$. We calculate H following the procedure of Multifractal Detrended Fluctuation Analysis (MF DFA) (Ihlen, 2012). In MF DFA, we first subtract the mean (\bar{x}) from the time series of length N , and calculate the cumulative

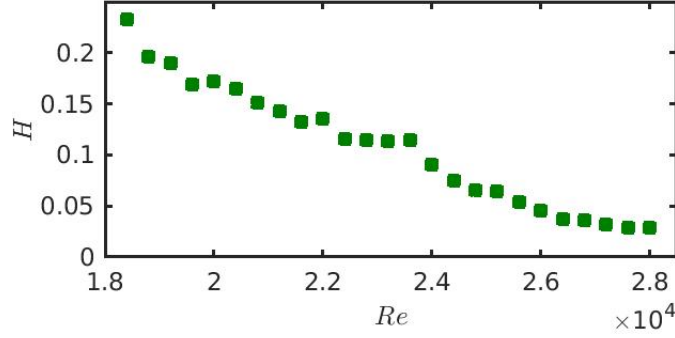


Fig. 5.3: Variation of H as a function of Re for the acoustic pressure data from the bluff body stabilized combustor. H approaches a limiting value of zero for LCO, unlike amplitude which is unbounded and can increase to any level depending on the system.

deviate series $Y(k)$ as, $Y(k) = \sum_{t=1}^k [x_t - \bar{x}]$, where $k = 1, 2, \dots, N$. Then, the deviate series $Y(k)$ is divided into non-overlapping segments of size w , and the number of such segments, N_w is the greatest integer of N/w . To obtain the fluctuations, we subtract the polynomial fit from the deviate series (Y_i) for each segment i . The structure function of order 2 is defined as follows:

$$F_2(w) = \left[\frac{1}{N_w} \sum_{i=1}^{N_w} \left[\frac{1}{w} \sum_{t=1}^w (Y_i(t) - \bar{Y}_i)^2 \right] \right]^{1/2}. \quad (5.1)$$

We calculate the structure function for different time scales w . The slope of the linear regime of the plot of variation of F_2 with the span w in a double logarithmic scale is known as the Hurst exponent (H).

H takes values between 0 and 1 for time series, corresponding to fractal dimension between 1 and 2. $H > 0.5$ indicates that the time series is a persistent one, *i.e.*, an increase (decrease) in the value of time series is likely to be followed by an increase (decrease) in its value. In contrast, an antipersistent signal would have $H < 0.5$, which is characterized by a decrease (increase) in the value is most likely to be followed by an increase (decrease) in its value and vice versa. An uncorrelated random process has $H = 0.5$. Unlike mathematical fractal objects, real fractal time series (experimental data) possess fractal nature only for a certain range of time scales. Hence, we need to

select a range of scales that is optimal to capture the fractal characteristics during the transition. Here, we choose two to four acoustic cycles of oscillations of the natural frequency of the system (Nair and Sujith, 2014; Kerres *et al.*, 2016). If we select scales with a length corresponding to less than one cycle of oscillation, then the periodicity in the data may not be captured. Also, the fluctuations are averaged out for long segments with a large number of cycles.

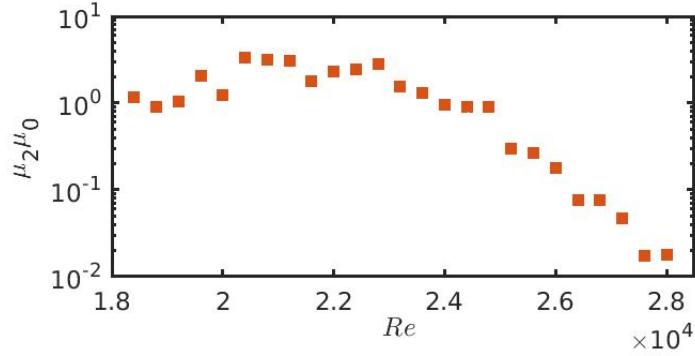


Fig. 5.4: The inverse square law relation between H and FFT peak during the transition to TAI in turbulent systems. We present the scaling for the data acquired from the bluff body stabilized combustor with different lengths and a swirl stabilized combustor. As different configurations of the thermoacoustic system can have different amplitudes of LCO, we normalize the peak amplitude with the amplitude of LCO for that particular case. The normalization is done only for visualization purpose. A dashed red line is drawn to show the inverse power law.

The aperiodic fluctuations observed during the state of CN has $H > 0.2$ (Fig. 5.3). As the periodic content in the signal increases during the transition, the fractal nature is lost. H captures this changing fractal characteristics, exhibiting a monotonic decrease in value tending towards zero. Moreover, the value of H is bounded. H decreases smoothly during the transition, while the FFT peak increases steeply near the onset of the TAI. The amplitude of the dominant mode of oscillations scales with the Hurst exponent following an inverse power law, $A_0 \propto H^{-2.0 \pm 0.2}$ (Fig. 5.4). We observe this scaling relation during the emergence of oscillatory instabilities from turbulence, in different configurations of thermoacoustic systems, aeroacoustic and aeroelastic systems (Chapter 3). The average power law exponent is -2 ± 0.2 across these systems.

We disregard the states with $H > 0.15$ as the tail of the power law; we observe the scaling approximately from $H < 0.15$. The tail of the power law consists of the states which are far from TAI.

5.3 SPECTRAL MEASURES TO ESTIMATE THE AMPLITUDE OF INDIVIDUAL MODES OF OSCILLATIONS

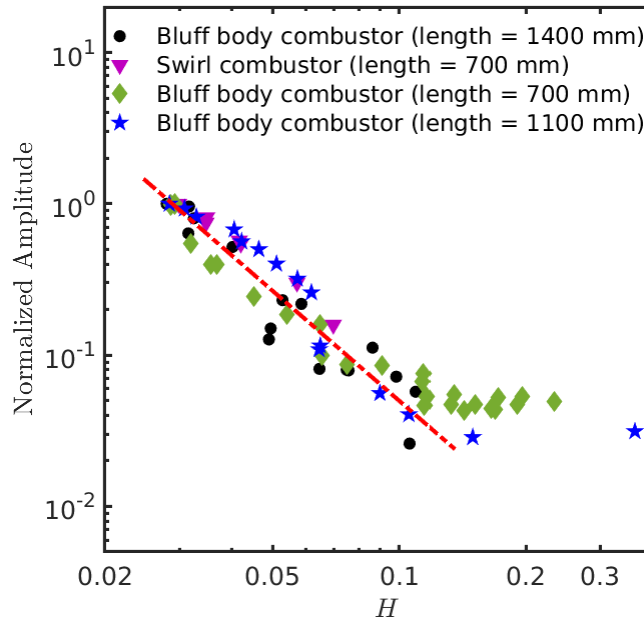


Fig. 5.5: A representative spectral measure $[\mu_2\mu_0]$ as a function of Re in a semi logarithmic scale. The variation has a fluctuating trend during CN. However, the value of $[\mu_2\mu_0]$ decreases monotonically as we approach TAI.

The emergence of self-sustained periodic oscillations from an initially disordered state in various systems is accompanied by the phenomenon of spectral condensation, which is the narrowing of the peak in the amplitude spectrum accompanied by the growth of amplitude of the dominant oscillatory mode (Fig. 4.3). To quantify spectral condensation, we have used spectral measures which are defined as the products of different moments of the power spectrum. They showed that the peaks in the power spectrum follow a power law scaling with these spectral measures (Chapter 4).

In this chapter, we aim to predict the amplitude of TAI using the scaling relation

exhibited by the spectral measures. Therefore, we use the amplitude spectrum instead of the power spectrum, akin to the manner in which we used power spectrum in Chapter 4 to obtain a universal scaling relation. The spectral measures are denoted as $[\mu_m \mu_n]$, where μ_m is the m^{th} moment of the amplitude spectrum, and m & n are integers. Here, we use a representative spectral measure $[\mu_2 \mu_0]$ (the product of 2^{nd} and 0^{th} moments) defined as,

$$[\mu_2 \mu_0] = \left[\int_{-\delta F}^{+\delta F} \frac{A(F)}{A_0} \left| \frac{F}{f_0} \right|^2 dF \right] \times \left[\int_{-\delta F}^{+\delta F} \frac{A(F)}{A_0} dF \right], \quad (5.2)$$

where, $A(F)$ is the amplitude corresponding to the modified frequency $F = f - f_0$. Here, f is the variable indicating the frequency of oscillations, f_0 is the central frequency corresponding to the peak in the spectrum, and A_0 is the maximum amplitude at the center of the peak ($A(f_0)$). We calculate the spectral measure for the peak at f_0 in the neighbourhood of width δF (we use $\delta F \sim f_0/5$).

During the transition to TAI, the broad peak in the amplitude spectrum observed during CN sharpens to a narrow peak, while the amplitude grows. According to Eq. 5.2, the spectral measure $[\mu_2 \mu_0]$ decreases as the peak becomes sharper. We present the variation of $[\mu_2 \mu_0]$ in Fig. 5.5. During CN, the spectral measure does not decrease much and fluctuates near a constant value. Then, it starts to drop to a lower value as we approach TAI. We calculate the spectral measure for all the possible modes that are expected to grow. Thereby, we can track the growth of individual modes of oscillations. The spectral measure follows an inverse power law relation with the corresponding peak amplitude as, $A_0 \propto [\mu_2 \mu_0]^{-0.66 \pm 0.1}$. We use this concept of universal scaling of the peak amplitude and spectral measure to estimate the amplitude of individual modes of oscillations. Note that the power law exponent obtained using the spectral measures defined on the amplitude spectrum with the Hann window is different from the power law exponent for spectral measures from the power spectrum (shown in Chapter 4).

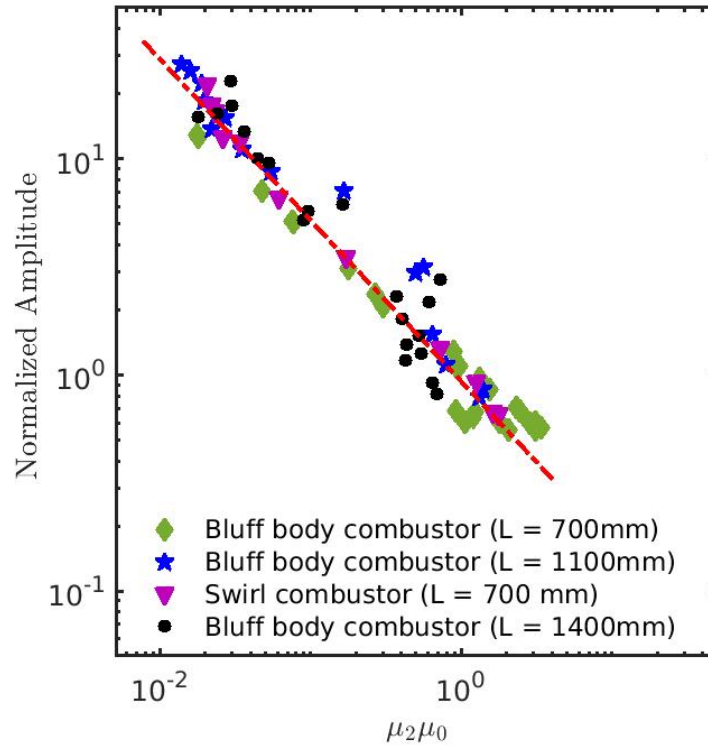


Fig. 5.6: The inverse power law scaling between FFT peak and $[\mu_2\mu_0]$. The data acquired from the bluff body combustor with different lengths and the swirl combustor obey the power law relation with the same exponent. The FFT peak from the amplitude spectrum is normalized to show all these power laws in the same plot (for the sake of visualization). The normalization factor is the estimated value of FFT peak for $[\mu_2\mu_0] = 1$ obtained by extrapolating power law for each system. The average value of the power law exponent across different systems including thermoacoustic, aeroacoustic and aeroelastic systems is found be around -0.66 ± 0.1 .

5.4 PROCEDURE TO ESTIMATE THE AMPLITUDE OF LIMIT CYCLE OSCILLATIONS

These universal scaling relations during the transition to oscillatory instability are observed not just in thermoacoustic systems, but also in other fluid mechanical systems such as aeroacoustic and aeroelastic systems. Commonality among transitions in all these systems is that they exhibit emergence of ordered behavior from a background turbulent flow field following an intermittency route. However, the underlying physical mechanisms involved in these systems are indeed different, suggesting that this scaling

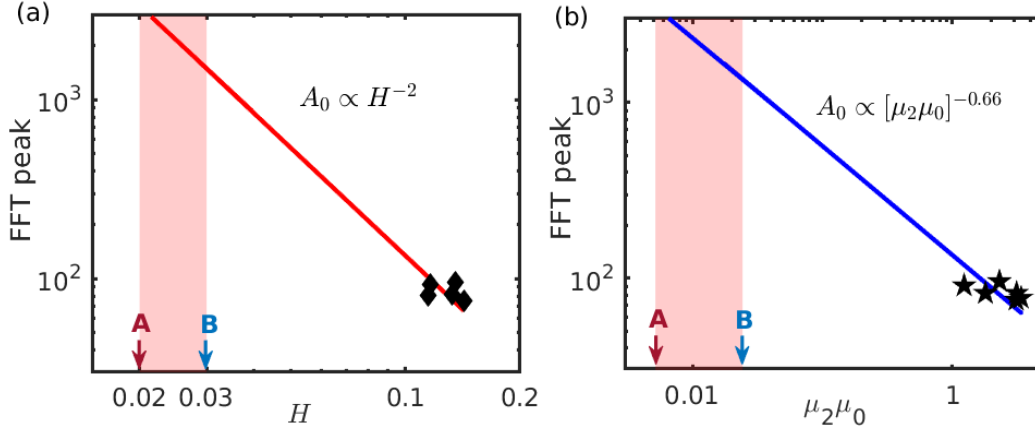


Fig. 5.7: Estimating the amplitude of limit cycle oscillations using (a) the scaling of FFT peak and H and (b) the scaling of FFT peak and the spectral measure $[\mu_2 \mu_0]$. We use a few data points during the state of stable operation (shown as black colour points) and extrapolate the power law behaviour towards TAI, that is towards higher FFT peak. The CN data shown here is obtained from the bluff body stabilized combustor of length 700 mm. The amplitudes in the region between A and B are the estimated amplitude during TAI.

is characteristic of the underlying bifurcation in the system and is not determined by the specific physical processes that govern the system. The current section aims to illustrate the method of amplitude estimation of the limit cycle oscillations using these scaling relations.

We describe the procedure of estimation of the amplitude of TAI using a few input data during stable operation. We plot the power law relations, $A_0 \propto H^{-2.0 \pm 0.2}$ and $A_0 \propto [\mu_2 \mu_0]^{-0.66 \pm 0.1}$ passing through the points corresponding to the input data acquired during stable operation. We extrapolate the power laws towards TAI to find the y-intercept (refer Fig. 5.7). According to the definition of H and $[\mu_2 \mu_0]$, we know that both reduce towards zero as we approach TAI. However, H and $[\mu_2 \mu_0]$ will never attain the value of zero because of the discrete representation of the analog signal. We need the limiting values for H and $[\mu_2 \mu_0]$ to estimate the amplitude of LCO. The theoretical value for H is 0 for a pure sine signal; however, for a limit cycle data acquired for a finite time duration, the lowest possible value would be around 0.02 (marked A in Fig. 5.7a). To fix the lowest limit for $[\mu_2 \mu_0]$, we construct a unit amplitude sine wave with the same

frequency as the natural frequency of the system and with the same sampling frequency as that of the experimental data. The value of $[\mu_2\mu_0]$ for this sine wave is the lower limit A (marked in Fig. 5.7b). The theoretical value of $[\mu_2\mu_0]$ for a sine wave according to Eq. 5.2 is 0. This would happen only if the amplitude spectrum is a Dirac delta function which has a nonzero amplitude only at f_0 . However, the finite time interval for which the data is acquired attributes a nonzero width in the amplitude spectrum at f_0 . This interplay between the localization in the time and frequency domain is in accordance with Heisenberg's uncertainty principle. In addition to this, we use a Hann window of 0.25 s length and the corresponding amplitude spectrum has a reduced resolution of 4 Hz. All these impose a nonzero limit on the value of the $[\mu_2\mu_0]$ for a sine wave.

The estimated amplitude for this limit A corresponds to the maximally "clean" periodic dynamics possible during TAI. For systems that exhibit a smooth transition to TAI via intermittency, this estimate will always be higher than the amplitudes that are practically attainable. A pure sine wave will not be achieved in turbulent systems. The estimated maximum amplitude (limit A) can be considered for designing the combustor. Now, we proceed to set an upper limit B for the threshold values of H and $[\mu_2\mu_0]$. Here, we construct a sine wave with amplitude modulations using the information from the time series of combustion noise. The periodic oscillations during TAI appear to have inter-cycle variability in amplitude, as shown in Fig. 5.1(e). Lieuwen (2002, 2003) discussed the role of noise and system nonlinearities upon the temporal features of the limit-cycle pressure oscillations. Therefore, the limit B corresponds to a sine wave with a noisy amplitude envelope as observed during TAI in practical cases. We extract the envelope (E) of the acoustic pressure fluctuations acquired during CN using Hilbert transform (Panter, 1965). Then, we construct a unit amplitude sine wave and modify its envelope with the extracted amplitude from the experimental data as $x(t) = (1 + E_{normalized})\sin \omega t$. The amplitude envelope is normalized ($E_{normalized} = (E - \text{mean}(E))/\text{max}(E)$), as we consider only its temporal characteristics.

Further, we can continuously improve the prediction by narrowing the range of estimated amplitudes between A & B, as we have more data points during the transition to TAI. When we estimate the amplitude using the data acquired during INT, the envelope of the signal is less noisy compared to that of CN and resembles experimental data more. As a result, the values of H and $[\mu_2\mu_0]$ corresponding to limit B reduce. Using the envelope of INT shifts limit B towards A. Hence, we can narrow the range of estimated amplitudes, as we have more data during intermittency. The shaded region in Fig. 5.7 corresponds to the predicted region of TAI. A more elaborate explanation on the method of selecting the limits A & B is given in Appendix A.

5.5 ILLUSTRATION OF EFFICACY OF THE ESTIMATION PROCEDURE

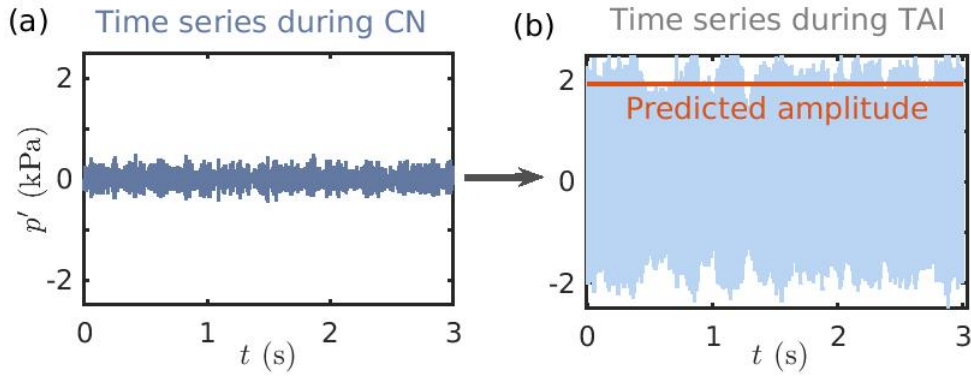


Fig. 5.8: Time series showing aperiodic oscillations during stable operation at $Re = 1.95 \times 10^4$ and the time series with high amplitude limit cycle oscillations during TAI ($Re = 2.78 \times 10^4$). The predicted amplitude (using H), indicated with the red line, reasonably captures the actual limit cycle amplitude. The data presented is for the case of the bluff body stabilized combustor.

We need to test how well the estimation works when applied to experimental data obtained from practical thermoacoustic systems. We use pressure time series obtained from a bluff body and a swirl stabilized combustors having lengths 700 mm to illustrate the efficacy of the devised estimation technique. First, we take only one time series during CN and try to predict the amplitude of TAI. In Fig. 5.2, there are two data points in the region of TAI. In order to compare the predicted amplitude with the actual

value, we find the H and $[\mu_2\mu_0]$ of the data corresponding to TAI, which are available from the experiments. Then, using the power law expression, we predict the amplitude corresponding to that particular values of H and $[\mu_2\mu_0]$, and we calculate the deviation of this predicted values from the actual amplitudes.

Table 5.1: Estimated amplitude of limit-cycle oscillations using the scaling relation of H and FFT peak from the time series acquired during the stable operation. The first row in the table shows the results from only one time series. The second row shows the results using the first and the second time series, and so on.

Re	FFT Peak	H	$A_{predicted}$	$\Delta A, \%$
1) Bluff body (Actual limit cycle amplitude = 1737 Pa)				
2.12×10^4	75.32	0.142	1864	9
2.16×10^4	82.22	0.132	1807	6
2.20×10^4	95.97	0.135	1922	12
2) Swirl (Actual limit cycle amplitude = 1509 Pa)				
1.35×10^4	139.64	0.129	1658	10
1.41×10^4	567.29	0.057	1325	-12
1.46×10^4	1119.97	0.043	1440	-5

Table 5.2: Estimated amplitude of limit-cycle oscillations using the scaling relation of spectral measure and FFT peak from the time series acquired during the stable operation.

Re	FFT Peak	$[\mu_2\mu_0]$	$A_{predicted}$	$\Delta A, \%$
1) Bluff body (Actual limit cycle amplitude = 1737 Pa)				
2.00×10^4	90.84	1.23	1506	-13
2.04×10^4	77.23	3.39	1712	-2
2.08×10^4	82.32	3.12	1865	7
2) Swirl (Actual limit cycle amplitude = 1509 Pa)				
1.35×10^4	139.64	0.37	1007	-33
1.41×10^4	567.29	0.05	1052	-30
1.46×10^4	1119.97	0.02	1212	-20

Subsequently, we try to predict using a higher number of time series data during the CN and INT. Such estimates are in good agreement with the actual values (Fig. 5.8).

The predicted amplitudes and the error in prediction, using H and $[\mu_2\mu_0]$ are listed in Table 5.1 & 5.2. Each row in the table shows the results obtained using all the data in the preceding rows together. The actual amplitudes of LCO for bluff body and swirl stabilized combustors are 1737 Pa and 1509 Pa, respectively. For the bluff body case, the estimate obtained using three input time series is 1922 Pa and 1865 Pa using H and $[\mu_2\mu_0]$, respectively. Note that, these values are within 12% and 7% of the actual amplitude. The estimates using H and $[\mu_2\mu_0]$ for the swirl stabilized combustor have -5% and -20% deviation from the actual value. The accuracy of estimation using a single input time series depends on how well that particular data point fits to the power law scaling. Therefore, we can get significantly low errors in the estimate by using multiple input time series acquired during the transition. An input time series, and the LCO along with the predicted amplitude (indicated with a red line) are shown in Fig. 5.8. The predicted value is indeed close to the actual amplitude of LCO. Note that the methods discussed in this paper are valid for highly turbulent systems which exhibit a steep, albeit smooth transition to TAI via INT. However, it is not clear whether such an approach will work if there is an abrupt jump in the amplitude at the onset of TAI. Further work needs to be done to estimate the amplitude of TAI under such conditions.

5.5.1 Estimating the amplitude of multiple modes of oscillations

We extend the method to predict the amplitude of individual modes of oscillations in thermoacoustics systems, exhibiting multiple modes of oscillations. The experimental setup shown in Fig. 3.1 is observed to have thermoacoustics instability with a single frequency. However, the combustor with a preheater arrangement (to preheat the reactants) is found to excite different frequencies at different temperatures. Refer Pawar *et al.* (2020) for more details of the experiments with preheater setup. We use the pressure data acquired at a preheat temperature of $300^{\circ}C$. Figure 5.9 shows the time series and the amplitude spectra during CN and TAI. At this temperature, the peak at 158 Hz and 456 Hz become sharper during TAI. The dominant mode during TAI is 158

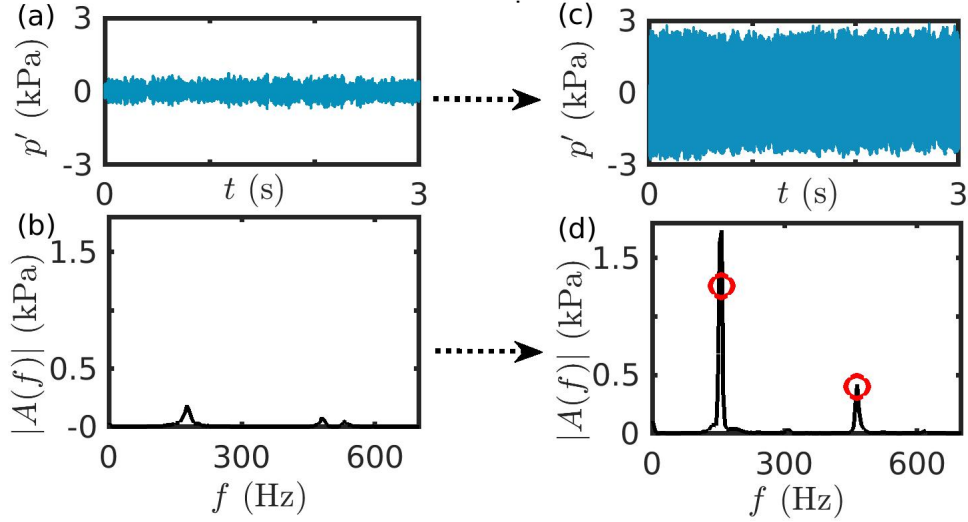


Fig. 5.9: (a) low amplitude aperiodic p' during CN and (b) the corresponding amplitude spectrum with two broad peaks around 160 Hz and 500 Hz. (c-d) Both the modes grow as we reach TAI, and the peak at ~ 158 Hz becomes dominant. The predicted amplitudes of these two modes are marked with red circles in the spectrum.

Hz (amplitude increases from ~ 100 Pa to ~ 1734 Pa). Also, the amplitude of the peak at 456 Hz increases from ~ 80 Pa to ~ 418 Pa, during the transition.

We calculate the $[\mu_2\mu_0]$ in the neighbourhood of both the peaks ($f_1 = 158$ Hz and $f_2 = 456$ Hz) and estimate the amplitude using the scaling relation $A \propto [\mu_2\mu_0]^{-0.66}$. The estimated peak amplitude values using 3 pressure time series data during CN is marked with red colour circles in Fig. 5.9b. Further, the estimated values using a single time series and multiple time series data are listed in Table 5.3. When we compare the predicted and the actual values, the estimates for the first and second peak are within 30% and 10% error, respectively. Thus, the methodology using spectral measure can be applied to predict the amplitude of individual modes during TAI.

For the data from the combustor with preheater (with multiple modes), there is a significant error in the estimated amplitude calculated using the scaling of H . The possible reasons for this inaccuracy could be the low levels of turbulence present in the system and the presence of multiple peaks in the amplitude spectrum. Unlike the scaling of $[\mu_2\mu_0]$, the scaling with H is observed only in turbulent fluid mechanical

Table 5.3: Estimation results for data with multiple modes

Re	FFT peak	$[\mu_2\mu_0]$	$A_{predicted}$	$\Delta A, \%$
1) First mode, $f_1 = 158$ Hz (Actual amplitude = 1734 Pa)				
1.81×10^4	146.45	3.68	1236	-29
1.83×10^4	139.71	4.11	1250	-27
1.84×10^4	113.43	5.84	1261	-27
2) Third mode, $f_2 = 456$ Hz (Actual amplitude = 418 Pa)				
1.81×10^4	88.06	0.36	390	-6
1.83×10^4	105.80	0.26	381	-9
1.84×10^4	96.78	0.41	403	-4

systems. Further, the presence of peaks other than the dominant modes in the amplitude spectrum can effect the value of H since it is calculated over a certain range of time scales. Nevertheless, the variation of H during the transition provides indication of the impending TAI well in advance, and H can be used as a precursor. Further studies need to be done to identify the exact reason for the inaccuracy in amplitude estimation.

In this study, we showed the method of amplitude prediction for longitudinal modes. However, many practical combustors seldom show a single dominant frequency and often exhibit multiple frequencies. Further, the mode of instabilities can also be transverse (or azimuthal) or a combination of transverse and longitudinal modes. In the future, a detailed study for the performance of Hurst exponent and spectral measure towards early warning and amplitude estimation for such modes needs to be done. Further, multiple experiments in different configurations of the experimental setup with changes in different control parameters to approach thermoacoustic instability need to be conducted to establish more accurate error bars for the power law exponent. In the future studies, we aim to derive a theoretical framework for studying spectral condensation.

5.6 SUMMARY

In this study, we present two different methods to predict the amplitude during thermoacoustic instability, by using time series data during the state of stable operation or intermittency. First, we show that the universal scaling relation between the amplitude of the dominant mode and the Hurst exponent in the intermittency regime can be exploited to predict the amplitude during TAI. We demonstrate that this method can predict the amplitude fairly accurately in practical systems, by applying this procedure to the data from a bluff body and a swirl stabilized combustor. However, in the case of a combustor with a preheater that exhibits multiple modes of oscillations, there is a significant error in the predicted amplitude. We speculate that this inaccuracy is due to the low levels of turbulence present and due to the presence of multiple peaks in the amplitude spectrum. Further studies need to be done to pinpoint the exact reason for this inaccuracy.

Along with this, we also show that the amplitude during TAI can be predicted by using the scaling relation between the amplitude of the dominant mode and the spectral measure. For this method as well, we show that the predictions are fairly accurate for the bluff body and swirl combustor. Interestingly, using this method, we are able to predict the amplitude of different modes of oscillations in the case of the combustor with a preheater. To improve the predictions, we need to perform more experiments with combustors exhibiting multiple frequencies.

Both these methods can be used by manufacturers of industrial gas turbines to estimate the amplitude during TAI, even without approaching anywhere close to instability. In other words, the amplitude can be estimated without exposing the combustor to large amplitudes and thereby endangering it. In the future, we would most probably see artificial intelligence based methods or a combination of AI with physics-based methods such as that presented here to predict the amplitude during TAI. AI based models are heavily used for the purpose of forecasting, especially for financial and weather data, currently. Such methods, when applied to thermoacoustics, in combination with physics

based approaches such as that presented here, would hopefully give us more powerful tools to predict the amplitude during thermoacoustic instability.

CHAPTER 6

Effect of rate of change parameter on early warning signals for critical transitions.

¹The dynamics of many natural and human-made systems are controlled by various parameters which evolve in time. A tiny perturbation in a system parameter can qualitatively alter the state of the system when it crosses a critical threshold. This phenomenon is generally known as tipping or critical transition, wherein a small change of a parameter can cause a sudden transition in the state of the system (Lenton *et al.*, 2008). In earth's climate system, a gradual change in local climate can affect ecosystems and can sometimes trigger a drastic switch to a contrasting state (Scheffer *et al.*, 2001; Carpenter *et al.*, 1999). Contagion in financial markets (National-Research-Councils and other, 2007; May *et al.*, 2008), and spontaneous asthma attacks (Venegas *et al.*, 2005) are other instances of tipping.

There are various mechanisms through which tipping occurs such as bifurcation-induced (B), noise-induced (N) or rate-induced (R) tipping (Ashwin *et al.*, 2012). Sometimes, the rate of change of parameter plays a more pivotal role than the actual value of the parameter. When a rate-sensitive parameter is varied as a function of time, at a slow rate, the system dynamics follows the quasi-static attractor. For faster rates of change of the parameter, above a critical rate, the system can be driven outside the basin of attraction of the quasi-static attractor, and can evolve towards a new stable state resulting in rate induced tipping (R-tipping). In such cases, the rate at which the parameter is varied determines the tipping point, not the absolute value of parameter. However, practical systems may exhibit tipping phenomena as a result of a combination of bifurcation, rate and noise.

In the current study, we explore the effects of rates of change of bifurcation parameter on 'bifurcation induced tipping'. When we vary the bifurcation parameter continuously

¹The results presented in this chapter are published in (Pavithran and Sujith, 2021).

at a finite rate, tipping will be delayed considerably from the parameter value predicted by the bifurcation analysis (Baer *et al.*, 1989). Due to the continuous variation of the control parameter, the system stays in the vicinity of the unstable attractor for some time even after the stability is lost. This phenomenon is referred to as ‘rate-delayed tipping’ (Bonciolini *et al.*, 2018). The delay observed in the transition is found to be dependent on the rate of change of parameter and the initial conditions (Park *et al.*, 2011; Berglund, 2000). Later, Majumdar *et al.* (2013) reported that this delay in tipping is independent of the rate of change of control parameter and determined solely by the initial value of the parameter. Recently, Bonciolini *et al.* (2018) showed experimentally that the delay in bifurcation increases with rate of change of parameter. After such contradictory observations in literature, Unni *et al.* (2019a) highlighted the role of interplay between the inherent noise in the system and rate of change of parameter in deciding the tipping point. Even though the delay increases with the rate of change of parameter, noise brings a high variability in the tipping point. Determining the stability margin is difficult for practical systems where stability boundaries are smeared due to this interplay between noise and rate. Devising efficient EWS for abrupt transitions in real systems is of critical importance. For example, predicting earthquakes, climate changes, and catastrophic events in engineering systems are desirable from social and economic viewpoints. However, predicting such tipping before the occurrence of the event is challenging because the system may not show any indication before the tipping point is reached, especially when there is combined effects of rate and noise.

Abundant studies discussing quasi-static bifurcations or B-tipping are available in literature. Despite the inherent characteristics of the systems, the dynamics close to the bifurcation point are found to be the same across different systems (Schroeder, 2009). The transitions through various types of bifurcations are related and generic early warning signals exist for catastrophic bifurcations (Scheffer *et al.*, 2009). The phenomenon known as critical slowing down near the bifurcation point gives information about the impending tipping for many types of bifurcations. The two

commonly used early warning indicators that work based on critical slowing down are the lag-1 autocorrelation and the variance of the fluctuations of a system variable. These measures have been proven to predict B-tipping, wherever the tipping is accompanied by a change of stability of the system (Scheffer *et al.*, 2009; Dakos *et al.*, 2008).

Recently, Wilkat *et al.* (2019) showed that there is no evidence of critical slowing down prior to human epileptic seizures. They conjecture that the tipping mechanisms for the human epileptic brain may be a combination of B-tipping, R-tipping and N-tipping and there may be no easily-identifiable EWS for such cases. Most tipping events occurring in nature involve system parameters changing at a constant, varying or undetermined rate along with considerable intensity of noise in the system (Tsotsis *et al.*, 1988; Kapila, 1981). Then, tipping can be influenced either by noise or by the effect of rate of change of the parameter. Thus, prediction becomes hard with conventional EWS. There are many other issues when dealing with rate dependent phenomena. For example, consider the case where the entire transition happens at a very fast rate such that there is not enough data available. Computing precursors in such conditions will be challenging. Even if we get warning, will there be enough time to perform a control action? The outstanding question is: ‘can we predict transitions in the real systems, considering the combined effects of inherent noise and the rate of change of the parameter?’

In the present study, we choose to work with a prototypical thermoacoustic system (known as a horizontal Rijke tube) exhibiting Hopf bifurcation, because (i) we observe a catastrophic transition similar to that observed in many practical situations, (ii) we can obtain time series data for a long duration with high sampling frequency, (iii) we can vary the control parameter at different rates and, (iv) we can repeat the experiments at same conditions to verify the observations.

The Rijke tube undergoes a subcritical Hopf bifurcation from a non-oscillatory to an oscillatory state (thermoacoustic instability) as we vary the control parameter (Matveev, 2003; Juniper, 2011; Gopalakrishnan and Sujith, 2015). Often, control parameters in

practical systems are changed continuously at a finite non-zero rate. Developing EWS for transition to TAI will help to evade such disastrous events.

In this chapter, we study the effects of rate of change of control parameter on the performance of various EWS, by investigating the variation of warning time provided by EWS with the rate of change of parameter. Further, we present a mathematical model that captures qualitatively, the key features observed in the experiments. Section 6.1 describes the experimental setup. Subsequently, the results and discussions are discussed and the main conclusions are given in Sec. 6.8. We provide the details of the methodologies for calculating different measures in Appendix A. e show the robustness of EWS with the selection of threshold for warning in 6.3 and the analysis to check for false warnings in Appendix C.

6.1 EXPERIMENTS

We perform experiments on a laminar thermoacoustic system known as the horizontal Rijke tube (Fig. 6.1). The setup consists of a horizontal duct with a square cross-section which houses an electrically heated wire mesh. Air enters the duct through a rectangular chamber known as the decoupler, which isolates the duct from the upstream fluctuations. The decoupler ensures that the pressure fluctuations at the end connected to it are negligible. The duct is open to the atmosphere at the end away from decoupler. Thus, the pressure at both the ends becomes equal to the atmospheric pressure. This design helps to maintain an acoustically open boundary condition (i.e., acoustic pressure fluctuations, $p' = 0$) at both the ends. A DC power supply (TDK-Lambda, GEN 8-400, 0-8 V, 0-400 A) is used to provide electric power to heat the wire mesh. The mass flow rate of air through the duct is controlled using an electronic mass flow controller (Alicat Scientific, MCR series) with an uncertainty of $\pm(0.8\%$ of reading + 0.2% of full scale). We measure the acoustic pressure fluctuations inside the duct using a piezoelectric sensor (PCB103B02, sensitivity: 217.5 mV/kPa, resolution: 0.2 Pa and uncertainty: 0.15 Pa) at a sampling rate of 10 kHz. A more detailed description of the setup can be

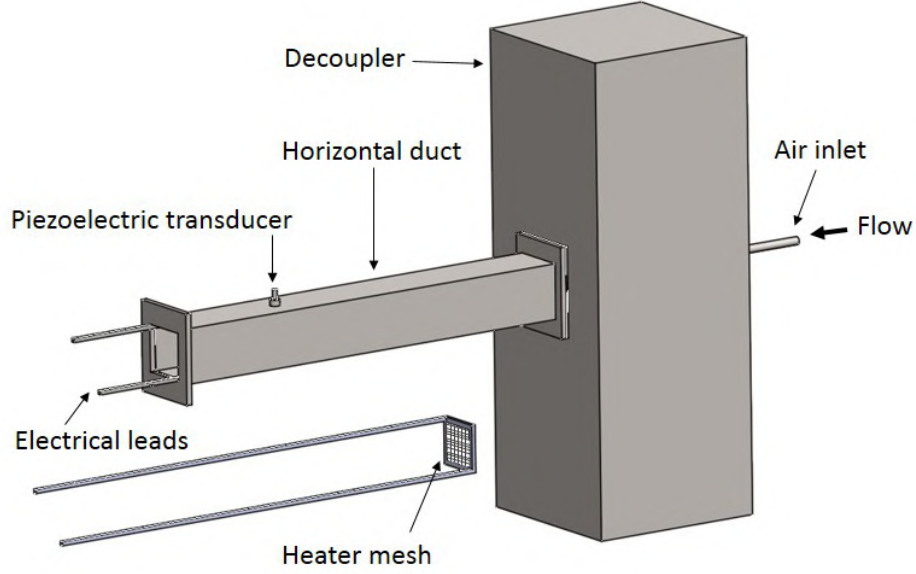


Fig. 6.1: Schematic of the horizontal Rijke tube used for the experiments. It comprises a 1 m long duct, an electrically heated wire mesh and a rectangular chamber called decoupler. The wire mesh is shown separately outside the duct. A piezoelectric transducer is mounted on the duct to acquire the acoustic pressure fluctuations inside the duct.

found in Gopalakrishnan and Sujith (2015). I conducted the experiments for the data used for this study at IIT Madras.

In the present study, we control the voltage (V) applied across the wire mesh and the current through the mesh changes accordingly. Therefore, we estimate the power (P) generated in the wire mesh by measuring both the voltage and current. The uncertainty in the measurement of voltage is $(0.1 V_{rated} + 0.1 V_{measured})\%$ and the uncertainty in the measurement of current is $(0.3 I_{rated} + 0.1 I_{measured})\%$, where $V_{rated} = 8$ V and $I_{rated} = 400$ A. All the other parameters such as the location of the heater mesh (27.5 cm from the decoupler) and the mass flow rate of air (100 SLPM) are kept constant suitably to obtain subcritical Hopf bifurcation.

First, we perform experiments where V is varied in a quasi-steady manner by allowing the system to evolve for a finite time duration at a constant P . We let the system reach its asymptotic state and then measure the acoustic pressure fluctuations at different values of P . We select the maximum heater power to be less than 1152 W for all the experiments, as the wire mesh may melt and get damaged due to overheating at

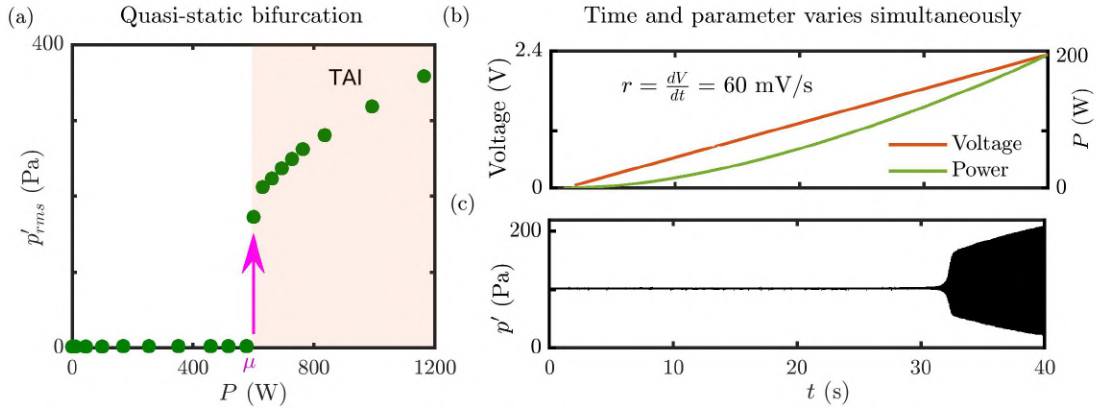


Fig. 6.2: (a) The variation of *rms* of the acoustic pressure fluctuations (p'_{rms}) for the quasi-static experiments. p'_{rms} shows an abrupt jump at the heater power ~ 600 W, denoted as μ . (b) A typical variation of voltage (V) at a constant rate of increase ($dV/dt = 60$ mV/s) and the corresponding variation of heater power (P). (c) The pressure signal (p') acquired continuously as the control parameter is varied in time.

higher powers. Subsequently, we increase V continuously at different rates and record the pressure signals during the ramp. Here, ramp refers to the continuous increase of the heater power in time. In this paper, we report a linear variation of V ; *i.e.*, the rate ($r = dV/dt$) of change of V is constant ($V = V_0 + r t$). As we have programmed V to vary linearly, I changes accordingly and then the corresponding variation of P is quadratic.

6.2 RATE-DEPENDENT TIPPING-DELAY IN A THERMOACOUSTIC SYSTEM

We first conduct quasi-static experiments to identify the range of parameter values required to capture the transition to high amplitude limit cycle oscillations. We calculate the root mean square (*rms*) value of the acoustic pressure fluctuations (p'_{rms}) acquired at different values of heater power (P). Figure 6.2a represents the bifurcation diagram showing the variation of p'_{rms} as a function of P . We observe that $p'_{rms} \approx 0$ for a range of P corresponding to a quiescent state with amplitude levels comparable to the noise floor (~ 5 Pa) of the system. At a particular control parameter value, the system transitions to high amplitude limit cycle oscillations. This transition is reflected in p'_{rms}

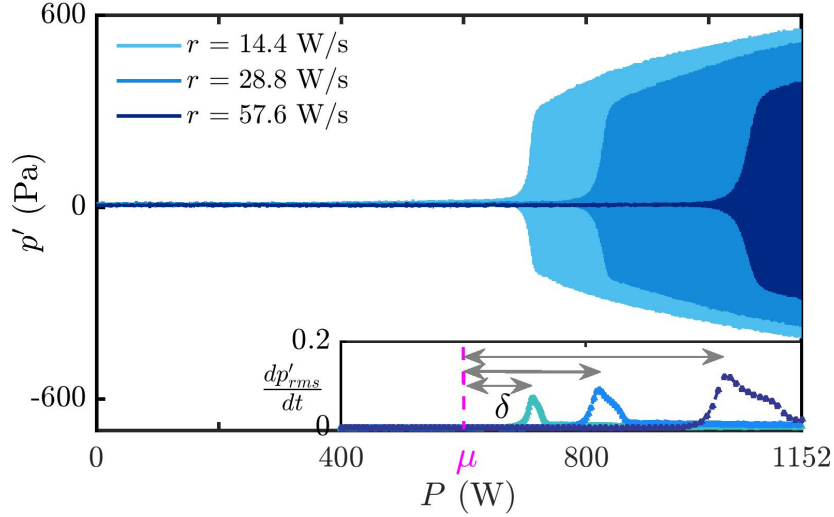


Fig. 6.3: Time evolution of p' as a function of time-varying P for three different rates of change of V . The rate of change of rms of fluctuations is also shown in the inset to identify the onset of TAI. Here, the maximum rate of change of p'_{rms} is considered as the onset of oscillations. The delay in the transition, δ , is found to increase with an increase in r . Here, p'_{rms} is calculated for a moving window of 1 s with an overlap of 0.9 s.

as an abrupt rise and is attributed to subcritical Hopf bifurcation. The parameter value at which this transition occurs, marked as μ in Fig. 6.2a, is known as the Hopf point.

As mentioned earlier, we perform experiments with a linear variation of V . Therefore, P changes continuously starting from a heater power which is far lower than μ and increases through the Hopf point to a high value. Here, the variation of P is from 0 to 1152 W in a nonlinear fashion. Thus, throughout this study, we mention the rate of change of voltage with time ($r = dV/dt$) which is kept constant for each run of the experiment. In Fig. 6.2b-c, we plot the typical variation of V and P and the corresponding acoustic pressure signal ($p' = p - \bar{p}$) depicting the transition from a quiescent state to high amplitude limit cycle oscillations. Here, \bar{p} is the mean of p .

Figure 6.3 provides the evidence for rate-dependent tipping-delay as reported in literature (Baer *et al.*, 1989; Bonciolini *et al.*, 2018; Unni *et al.*, 2019a; Scharpf *et al.*, 1987). We plot the time evolution of p' as a function of time-varying P for three different r (30 mV/s, 60 mV/s, and 120 mV/s) in Fig. 6.3. It is quite challenging to define a tipping point for the onset of oscillations for dynamic bifurcations, unlike

the quasi-static bifurcations. The difficulty in defining a tipping point is because the oscillations take a finite time to grow, and the parameter would have changed to another value by that time. Hence, we adopt the following method to select the tipping point. We calculate the rate of change of p'_{rms} . The sudden increase in the growth rate of oscillations reflects as a maximum in the rate of change of p'_{rms} (shown in the inset of Fig. 6.3). The delay (δ) in the tipping is marked from the Hopf point to the maximum of rate of change of p'_{rms} (Fig. 6.3). Henceforth, we use this method to define the onset of TAI in this study.

According to bifurcation theory, the system loses its stability at the Hopf point, μ . Due to memory effects, the system continues to be in the vicinity of the unstable attractor for a finite time. This phenomenon of rate-dependent tipping-delay occurs during slow passage through Hopf bifurcation as described by Baer *et al.* (1989). On comparing the delay (δ) in the onset of TAI for different r , we observe that δ increases with an increase in r (see Fig. 6.3), congruent with the observations reported in other systems (Baer *et al.*, 1989; Bonciolini *et al.*, 2018; Unni *et al.*, 2019a; Scharpf *et al.*, 1987). In the case of $r = 120$ mV/s (the fastest shown in Fig. 6.3), we observe a delayed onset of ~ 470 W from μ . Furthermore, we vary the control parameter at very fast rates, but limiting the values of P to 1152 W so as to not damage the heated wire mesh. In such cases, we do not observe tipping within the duration during which the power is varied; instead, it occurs when we let the system evolve at the final value of P , allowing more time. Hence, we confirm that the delay in the tipping increases with rate, by performing experiments at various rates. This trend need not be the same for highly turbulent systems where the inherent fluctuations can perturb the unstable fixed point, causing it to tip towards the stable limit cycle.

6.3 EWS FOR CRITICAL TRANSITIONS

We compute several EWS for the pressure signal acquired continuously during the ramp for the experiments performed at different rates of change of control parameter.

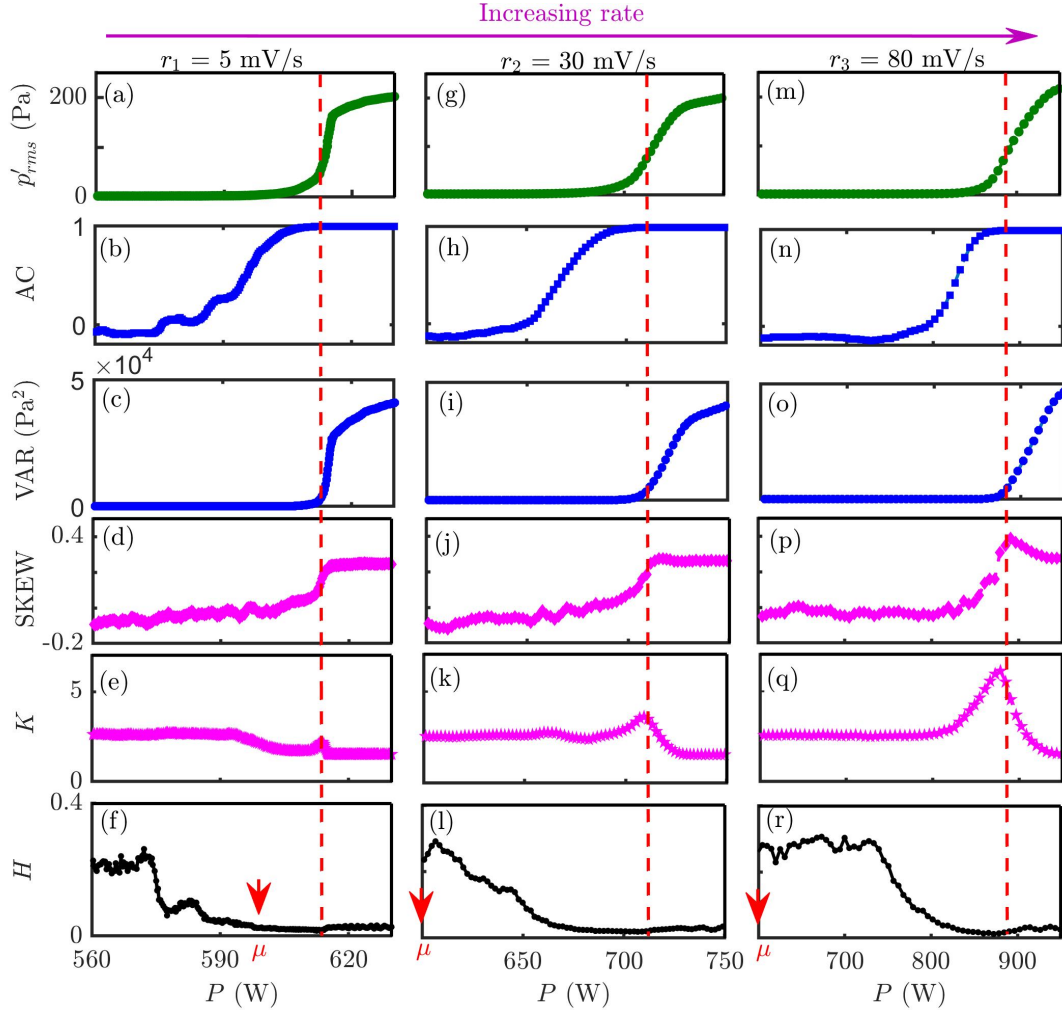


Fig. 6.4: Variation of p'_{rms} , lag-1 autocorrelation (AC), variance (VAR), skewness (SKEW), kurtosis (K) and Hurst exponent (H) during the transition to TAI in Rijke tube. Each column corresponds to the results for a particular rate (r) of change of V ((a)-(f): $r = 5\text{mV/s}$, (g)-(l): $r = 30\text{mV/s}$, (m)-(r): $r = 80\text{mV/s}$). The onset of TAI is marked with a red colour dotted line and quasi-static Hopf point μ is marked on the x -axis. p'_{rms} , and VAR starts to increase almost at the onset of TAI, whereas, K and SKEW detect the tipping slightly before p'_{rms} increases. In contrast, AC and H give early warning well-before the transition to TAI for all the cases shown here.

The following measures are considered in this study: p'_{rms} , lag-1 autocorrelation (AC), variance (VAR), skewness (SKEW), kurtosis (K), and Hurst exponent (H). Here, we provide an overview of the different EWS used in the present study.

The root mean square (rms) of a time series, $p(t)$, is defined as the square root of the mean square or the arithmetic mean of the squares of all the elements in the time series. It is also known as the quadratic mean.

$$p_{rms} = \sqrt{\frac{1}{N} \left(\sum_{i=1}^N p_i^2 \right)} \quad (6.1)$$

where N is the total number of data points. Root mean square value has been widely used in many engineering applications as a first step to check the sudden increase in the amplitude of fluctuations about the mean.

Autocorrelation is the correlation of a signal, $p(t)$, with a delayed copy of itself as a function of delay (τ). It is defined as follows:

$$AC(\tau) = \frac{1}{N} \frac{\sum_{i=1}^N p(i) p(i - \tau)}{\sigma^2} \quad (6.2)$$

In the current study, we consider lag-1 autocorrelation which computes the correlation between values that are one time step apart. In this study, we refer to lag-1 autocorrelation as AC. Variance (VAR) is the expectation of the squared deviation from the mean. VAR measures how the data is spread out from their average value and it is the second moment of the distribution.

$$VAR = \frac{1}{N} \sum_{i=1}^N (p_i - \bar{p})^2 \quad (6.3)$$

where \bar{p} is the mean and N is the number of data points. For critical transitions, both AC and VAR increase based on the phenomenon of critical slowing down. Systems approaching a transition to a new stable state, where the current stable state becomes unstable due to change in the control parameter, show slow response to external

perturbations. The phenomenon of slow recovery rate to the external perturbations close to a critical transition is known as critical slowing down (Strogatz *et al.*, 1994) (CSD). This slowing down leads to an increase in autocorrelation and variance of fluctuations (Scheffer *et al.*, 2009; Dakos *et al.*, 2012).

When a system is driven gradually closer to a critical transition, the increase in the autocorrelation occurs much before the actual transition. Similarly, the impact of perturbations do not decay fast, and their accumulating effect increases the variance of fluctuations. CSD results in increased short term memory of the system, and hence autocorrelation at low lags would increase. CSD is observed in realistic models of spatially complex systems (Lenton *et al.*, 2009) as well as in simple models (Dakos *et al.*, 2008) and has been used as EWS for critical transitions (Scheffer *et al.*, 2009).

Skewness (SKEW) and kurtosis (K) are not directly connected to critical slowing down. SKEW is a measure of the symmetry of the probability distribution of the data about its mean; *i.e.*, whether the distribution is biased towards one side over the other. A distribution is said to be negatively skewed (or left skewed) when a majority of the data falls to the right of the mean. On the other hand, a distribution is positively skewed (or right skewed) when more data is concentrated to the left of the mean. The skewness of a random variable is its third moment.

$$SKEW = \frac{\sum_{i=1}^N (p_i - \bar{p})^3 / N}{\sigma^3} \quad (6.4)$$

where \bar{p} is the mean, σ is the standard deviation, and N is the number of data points. SKEW is zero for a normal distribution. Negative SKEW indicates that the distribution is skewed left and positive SKEW indicates that the distribution is skewed right. Skewed left means that the left tail is longer than the right tail and vice versa. Generally, asymmetry of fluctuations may increase (SKEW increases) on approaching a catastrophic bifurcation, as the potential landscape near the transition would be less steep on one side of the equilibrium than the other (Guttal and Jayaprakash, 2008; Scheffer *et al.*, 2009). Kurtosis (K) gives information about whether the distribution has

heavy tails, or is more centred. The kurtosis of a normal distribution is 3, and a higher K indicates more outliers in the data. Very close to the tipping point, a comparatively longer distribution with fatter tails results in a high value of kurtosis, $K > 3$. If Kurtosis is less than 3, it means that the distribution has lesser outliers compared to the normal distribution. The kurtosis is the fourth standardized moment and is defined as follows:

$$K = \frac{\sum_{i=1}^N (p_i - \bar{p})^4 / N}{\sigma^4} \quad (6.5)$$

where \bar{p} is the mean, σ is the standard deviation and N is the number of data points.

Apart from these conventional measures, we investigate the fractal characteristics of the data close to tipping (Nair and Sujith, 2014; Sujith and Unni, 2020). We use the Hurst exponent (H), which is related to the fractal dimension (D) of the time series (Mandelbrot, 1983; Hurst, 1951) as $H = 2 - D$. For a fractal time series, the scaling of the rms of the standard deviation of fluctuations with the length of the data segment gives H . We calculate H following the algorithm of Multifractal Detrended Fluctuation Analysis (MFDFA)(Kantelhardt *et al.*, 2002), which is described in detail in sec. 3.4.1. H is a measure of persistence or correlation of a signal. If an increase in the value is more likely to be followed by another increase in value, then the signal is called persistent. A persistent or a positively correlated signal has $H > 0.5$, an anti-persistent or negatively correlated signal (an increase in value is mostly followed by a decrease in value, or vice versa) have $H < 0.5$ and uncorrelated white noise has $H = 0.5$. Fractal analysis has found a variety of applications in life sciences, engineering, econophysics, and geophysics (Ivanov *et al.*, 1999; Hu *et al.*, 2004; Grech and Mazur, 2004; Vandewalle and Ausloos, 1997; Grech and Pamuła, 2008; Alvarez-Ramirez *et al.*, 2008; Matos *et al.*, 2008; Domino, 2011; Suyal *et al.*, 2009; Kilcik *et al.*, 2009; Nair and Sujith, 2014; Unni and Sujith, 2015; Gotoda *et al.*, 2012). For instance, it has been used to distinguish healthy patients from patients with heart failures (Ivanov *et al.*, 1999; Havlin *et al.*, 1999). Similarly, the variations in the H of geoelectric and seismic fluctuations provide indicators for earthquakes (Telesca *et al.*, 2001). In econophysics,

Qian and Rasheed (2004) used H as a measure of financial market predictability. In the present study, we use H to predict critical transitions in a thermoacoustic system.

To study the effect of rate of change of parameter on the performance of the aforementioned EWS, we plot the variation of these measures as a function of P for three representative cases of r : 5 mV/s, 30 mV/s and 80 mV/s in the first, second and third column, respectively (Fig. 6.4). We compute the measures for a moving window of size 1 s with an overlap of 0.9 s. The choice of this particular window size is to ensure that at least 100 cycles of oscillations are covered in a window. The Hopf point (μ) is marked at 600 W with a red coloured arrow for reference, even though the tipping occurs after a delay. p'_{rms} indicates the growth in the amplitude of oscillations during the transition. VAR detects the transition almost at the same P where the amplitude rises which is reflected as a steep increase in the p'_{rms} at the onset of TAI, while SKEW and K seem to perform slightly better than p'_{rms} and VAR. Initially, we observe small negative SKEW values indicating a slightly left/negatively skewed distribution, and during the transition, it shifts to a slightly right/positively skewed distribution. Nevertheless, there is no significant change in SKEW during the transition, since $-0.5 < \text{SKEW} < 0.5$ is generally considered as symmetric distribution. Thus, the distribution has not changed in terms of skewness, and we cannot consider the change in SKEW as a precursor for the tipping. Besides, kurtosis has a value ~ 3 pertaining to a normal distribution during the quiescent state. After the transition to TAI, kurtosis reduces to a value lower than 3. It appears that in all the cases, there is a local maxima for the kurtosis at the onset of TAI. However, we observe a drop in the kurtosis for the first case (Fig. 6.4e), prior to the tipping point. Close to the tipping, the variation of kurtosis is not consistent for different rates: it reduces for the first case (Fig. 6.4e) and increases for the other cases (Fig. 6.4k,q). Hence, we do not recommend K as a good EWS for critical transitions in practical systems.

Among these conventional measures, lag-1 autocorrelation (AC) appears to be the best EWS for this type of transition. An initial quiescent state results in near zero AC

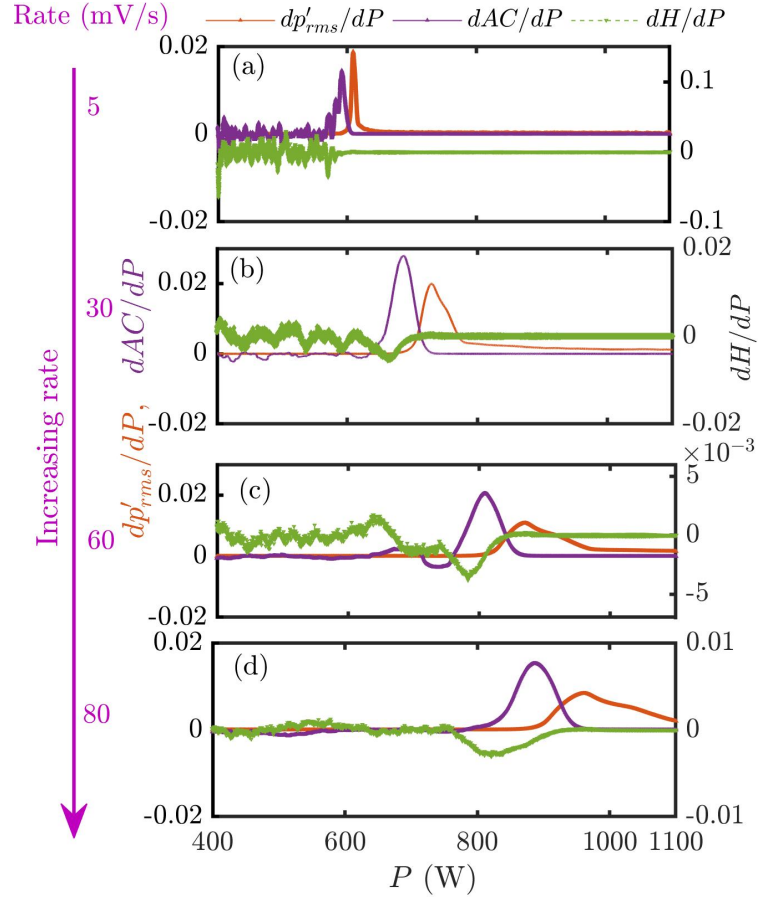


Fig. 6.5: Rate of change of p'_{rms} , lag-1 autocorrelation (AC), and Hurst exponent (H) with P is plotted for different rates of change of V . The maximum rate of change of AC and H occurs much before the maximum growth of p'_{rms} . As the rate of change of input voltage with time (dV/dt) increases (from (a)-(d)), the delay (in terms of P) in growth of amplitude increases.

due to the low amplitude uncorrelated noise. AC increases as periodicity increases and approaches 1 for limit cycle oscillations. It is clear from these experiments that AC is a more robust early warning measure compared to p'_{rms} , VAR, SKEW and K . Earlier studies (Gopalakrishnan *et al.*, 2016a; Ghanavati *et al.*, 2014) have reported that autocorrelation in the presence of fluctuations is a less effective precursor compared to variance. Actually, variance starts to build up gradually long before the transition, but it increases rapidly only at the tipping point. In fact, variance is the square of p'_{rms} . As we do not know the amplitude of oscillations in the final state, it is difficult to rely on variance to determine when the transition will take place. In contrast, the value of AC is bounded between 0 and 1, and we know how close we are to the tipping from the value

of AC.

The fractal based measure, H fluctuates between the values 0.2 to 0.5 for the fixed point state. Even though the flow field is laminar, there is noise present in the fixed point state originating from different sources such as the compressor or electronic noises. Therefore, the fixed point state with low amplitude aperiodic noisy fluctuations would give H values between 0.2 and 0.5. During the transition to the state of limit cycle oscillations, H approaches zero. H captures the periodicity (or the loss of fractal nature) in the data even if the amplitudes are very low. We start observing an emergence of periodicity as we approach the tipping point. The inherent noisy fluctuations perturb the system from the stable fixed point. These noise-induced oscillations occur at frequencies centred around the natural frequency of the system and the oscillations decay in time. These fluctuations contain very low amplitude bursts of periodicity which has oscillations around the natural frequency of the system (Wiesenfeld, 1985). Capturing this slight periodicity in the system variables close to the transition, H starts to decrease towards 0 well-before the rms of fluctuations grows. For very slow rates, H tends to decrease before μ (Fig. 6.4f). For relatively faster rates, the tipping is delayed significantly from μ ; nevertheless, H forewarns the tipping well-before the rise in p'_{rms} (Fig. 6.4l,r).

We repeat the computations of all EWS for data acquired at many different rates of change of V . The results shown in Fig. 6.4 are for three representative cases from this collection of data. A similar inference is obtained for even faster rates of change of voltage up to 240 mV/s. In all the cases, AC and H prove to be the better measures to forewarn an impending TAI compared to other measures such as VAR, SKEW and K , and both AC and H have comparable effectiveness.

In summary, there are two things happening on approaching the transition; one is the growth of the amplitude of oscillations due to Hopf bifurcation, and the second is the increase in temporal correlation. Out of all the EWS discussed here, rms and variance capture the growth of amplitude of oscillations; skewness and kurtosis detect

the changing distribution of data during the transition; lag-1 autocorrelation determines the increasing correlation between consecutive time instants; H looks at the increasing correlation as well as the emergence of periodicity. AC and H are capturing features that are different from the features captured by p'_{rms} , VAR, SKEW and K . Variance, skewness and kurtosis do not change if we were to shuffle the data randomly. However, AC and H will change upon shuffling the data. Hence, AC and H are capturing the temporal correlations present in the data more than just the statistical characteristics of the data. From Fig. 6.5, it is clear that the increase in correlation occurs prior to the growth of amplitude. Therefore, AC and H are able to predict the tipping well in advance. For faster rates of change of control parameter, growth of correlation occurs at a much lower parameter value than the growth of amplitude in the signal.

6.4 VARIATION OF WARNING TIME WITH RATE

Our analysis shows that AC and H are effective EWS for critical transitions in the considered thermoacoustic system. Next, we compare the early warning time for different rates using AC and H . Till now, we were focused on the warning in the parameter space, *i.e.*, at what parameter value we can predict, compared to the tipping point. Ultimately, EWS need to be compared across both temporal domain and parameter space.

Figure 6.6-6.7 show the variation of H and AC as a function of the control parameter (left column) and time (right column), for different values of r . Variation of p'_{rms} is plotted on the right axis for comparison. A window of 20 s time interval is shown (right column) for all the plots, for the sake of comparison. The time t' is selected as a time instant before the tipping point within a window of 20 s. The warning time is marked as τ (blue shaded region in Figs. 6.6-6.7). We calculate τ by selecting a threshold in AC and H so that, when it crosses the threshold we are warned of an impending tipping. In the present case, we select $AC = 0.4$ and $H = 0.1$ as the threshold, because H never reduces to 0.1 unless the system is proceeding towards an impending tipping. Similarly,

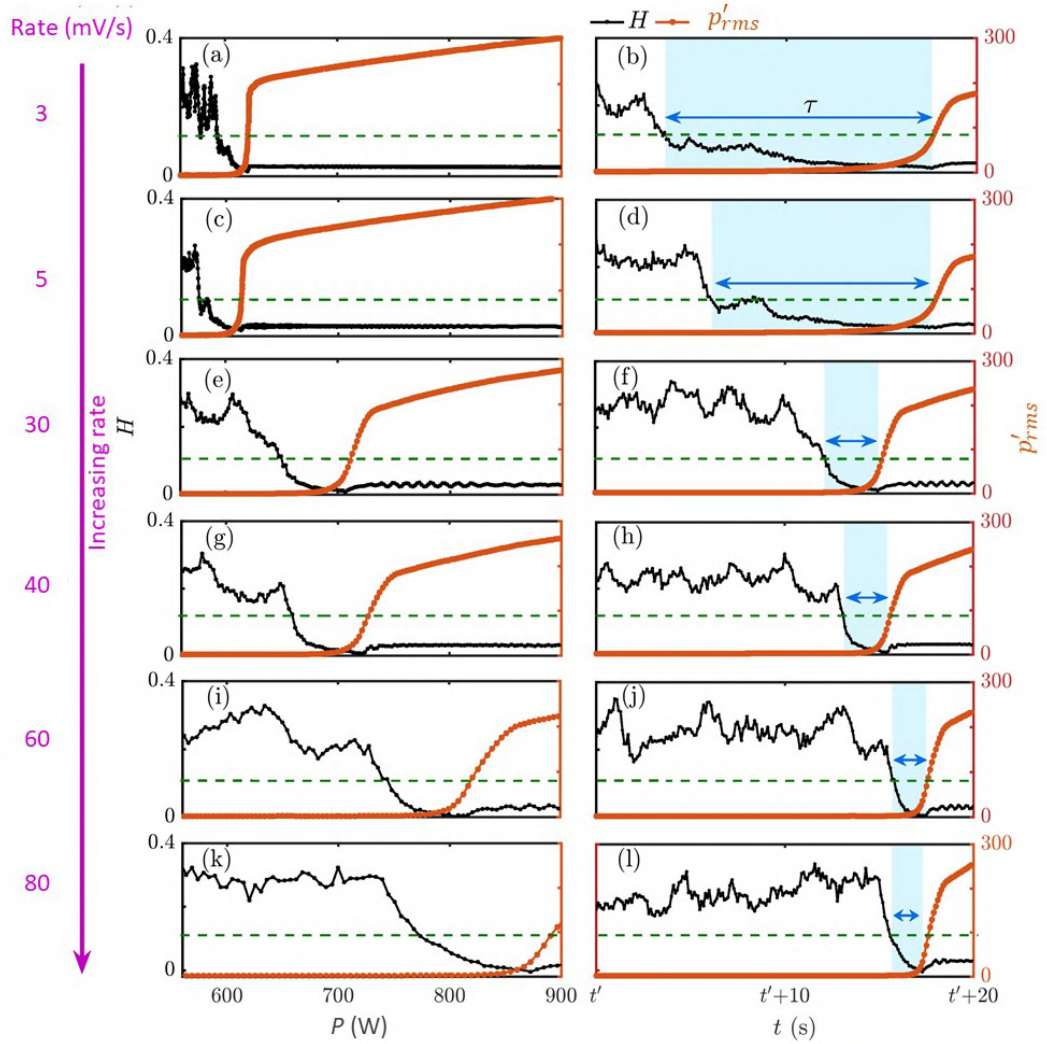


Fig. 6.6: Variation of p'_{rms} and H evaluated for data acquired at different rates of change of V is plotted as a function of the P (left column - a,c,e,g,i,k) and time (right column - b,d,f,h,j,l). Rate of change of parameter increases from top to bottom. For all these rates, we are able to predict the tipping using H , before p'_{rms} starts to increase. The green dotted line represents to the threshold value of $H = 0.1$. The warning time before the tipping (marked with blue colour) is the difference between the time at which H crosses the threshold and the time at which maximum rate of change of p'_{rms} is observed.

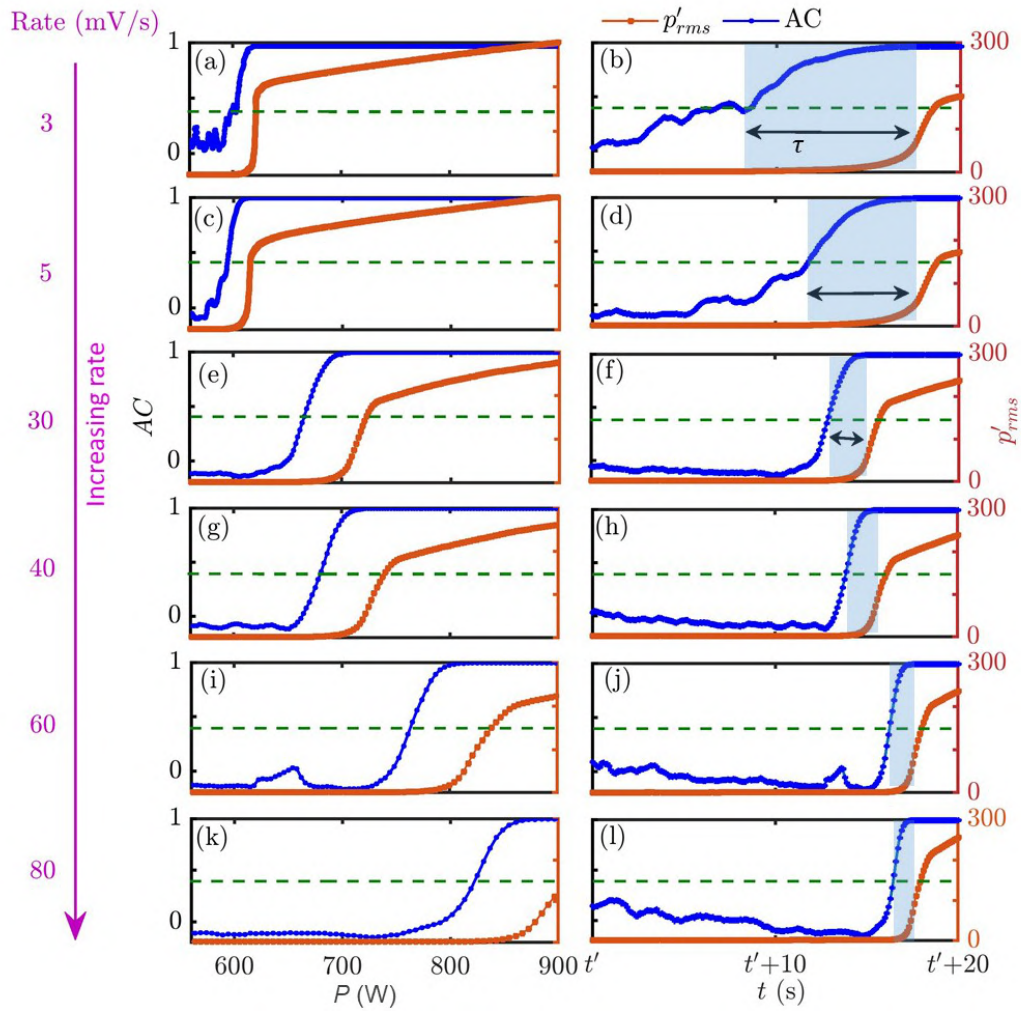


Fig. 6.7: Variation of p'_{rms} and AC is plotted as a function of control parameter, P , (left column - a,c,e,g,i,k) and time, t , (right column - b,d,f,h,j,l) evaluated for data acquired at different rates of change of P . Rate of change of control parameter increases from top to bottom. For all the transitions shown, AC provides an early warning before p'_{rms} starts to rise. The green dotted line represents to the threshold value of AC. The warning time, τ , (marked with blue colour) is the difference between the time at which AC crosses the threshold and the time at which maximum rate of change of p'_{rms} is observed.

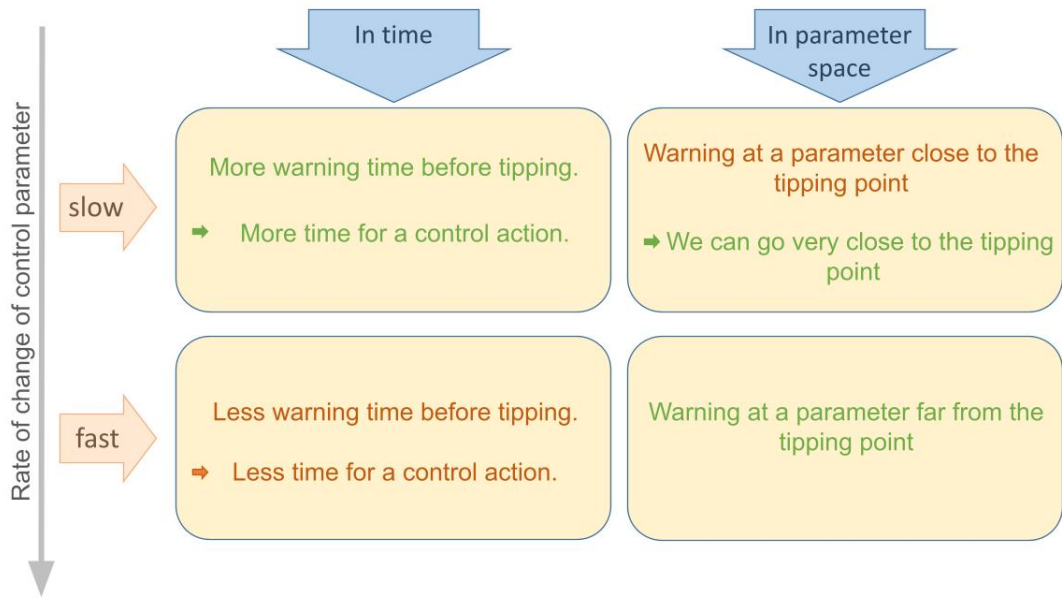


Fig. 6.8: The effect of rate of change of control parameter on EWS for critical transitions

AC also has fluctuations, but, $AC = 0.4$ is out of bounds for the quiescent state. The green dotted line in Figs. 6.6-6.7 corresponds to the selected threshold value of $H = 0.1$ or $AC = 0.4$. The time between $H = 0.1$ or $AC = 0.4$ and the onset of TAI (corresponds to the maximum rate of change of p'_{rms}) is considered as τ . This choice of threshold for AC and H are not unique, and any other slightly different threshold also will work equally well. Before the amplitude rises steeply, we have more warning time (τ) in the case of a relatively slower rates shown in Fig. 6.6b,d.

In terms of the parameter, we get warning at a parameter value well ahead of the tipping point for faster rates (Figs. 6.6k,l and 6.7k,l). However, the time needed to reach the tipping point is really short, as the rate of change of P is fast. Hence, we have relatively lesser time to implement control actions for faster rates (Figs. 6.6k,l and 6.7k,l). For slower rates, we have more time for control, but we are close to the tipping point in the parameter space (Fig. 6.6a,b and 6.7a,b). As we are going closer to the tipping point in case of slower rates, there is a possibility of N-tipping if external noise or inherent fluctuations of significant magnitude are present. The analysis of warning time using

AC provides a similar inference, wherein slower rates result in more warning time and faster rates give more early warning in terms of the control parameter (Fig. 6.7). These findings are summarized in Fig. 6.8.

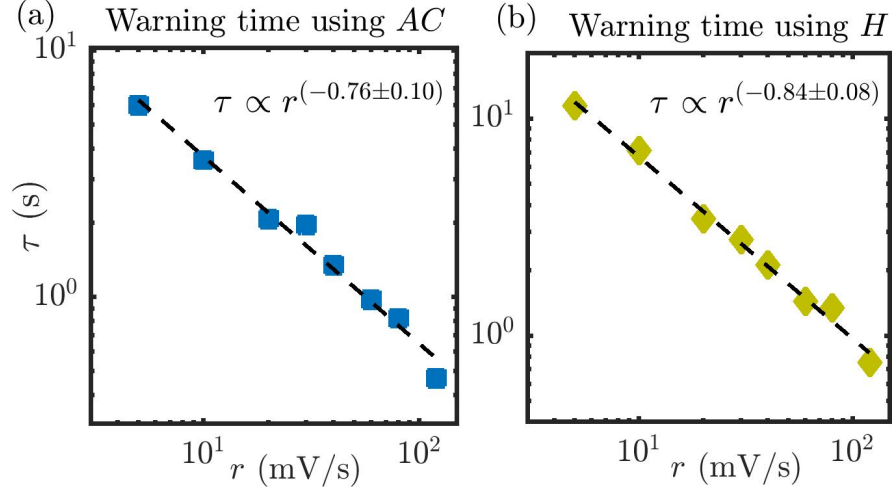


Fig. 6.9: Warning time (τ) obtained from (a) AC and (b) H are plotted as a function of r in logarithmic scale. (b) The value of τ decreases with r following an inverse power law relation as $\tau \propto r^n$ with $n = -0.76 \pm 0.10$ and $n = -0.84 \pm 0.08$ for AC and H , respectively. The threshold for obtaining warning is 0.4 for AC and 0.1 for H .

Next, we examine how the warning time (τ) varies with the rate of change of voltage with time ($r = dV/dt$). We calculate τ by selecting a threshold, as mentioned in the preceding paragraph. As we increase the rate, τ decreases drastically (see Fig. 6.9). We observe an inverse power law relation between the warning time and the rate of change of parameter as $\tau \propto r^n$ with $n = -0.76 \pm 0.10$ and $n = -0.84 \pm 0.08$ for AC and H , respectively. The uncertainty in fitting is estimated with 95% confidence. The scaling with a constant exponent holds for a range thresholds for AC (threshold: 0.2-0.8) and H (threshold: 0.15-0.06). The scaling using different thresholds are shown in Appendix B.

6.5 QUANTIFICATION OF THE PERFORMANCE OF EARLY WARNING SIGNALS

We quantify how reliable an early warning measure is in avoiding false alarms, and how sensitive it is to missing subtle warning signs. We use a method known as ‘Receiver Operating Characteristic (ROC)’ to quantify this trade-off between reliability and sensitivity of EWS. In other words, ROC illustrates the trade-off between false alarms and failed detection.

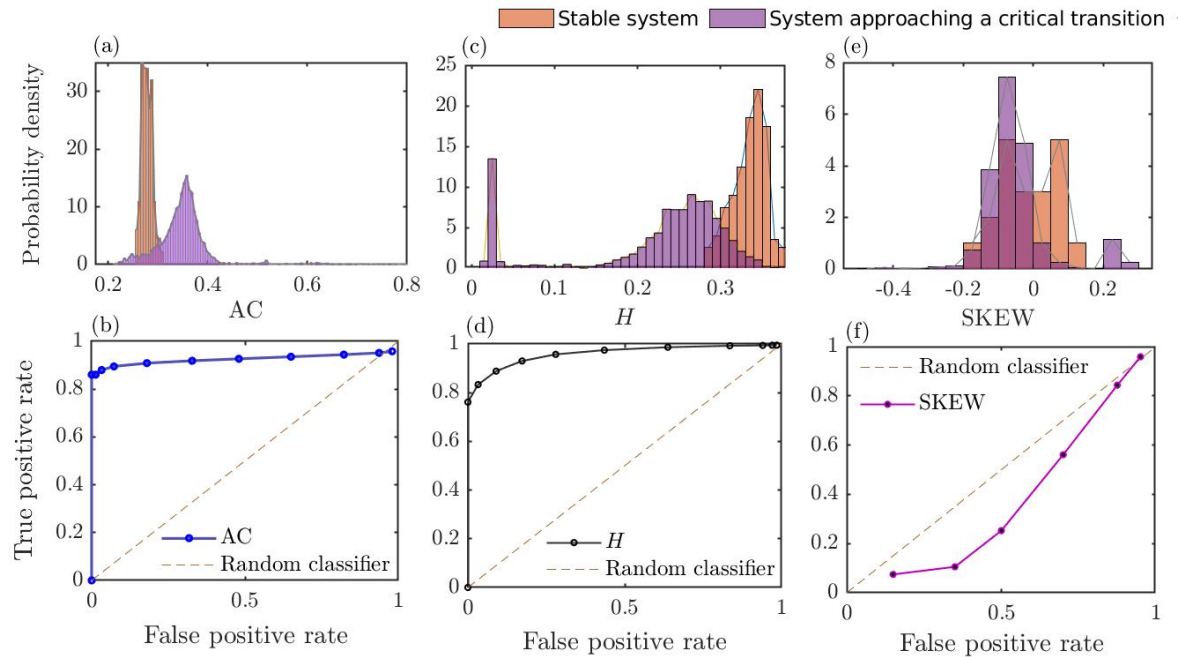


Fig. 6.10: The distributions of three different early warning signals (Auto correlation at lag-1 (AC), Hurst exponent (H), and skewness (SKEW)) are shown for the case of the stable system (orange) and the system approaching a critical transition (violet). The corresponding ROC are shown in the bottom row. The dotted diagonal line representing a random classifier such as a coin toss is shown for a comparison. Here, AC and H show better performance than SKEW.

The top row of Fig. 6.10 shows the distribution of different EWS under the case of the stable system and the system approaching a critical transition. The closer these distributions are to each other, the more severe the problems of false alarms and failed detection. If they overlap exactly, then it is difficult to tell apart. From these distributions, following Boettiger and Hastings (Boettiger and Hastings, 2012b),

we estimate ROC which represents the true positive rate and the corresponding false positive rate at any detection sensitivity. Suppose the EWS measure is increasing during the critical transition, the false positive rate is the integral of the distribution of the measure for the stable system right side of a selected threshold. The integral of the distribution under the right side of the threshold for the system approaching a transition gives the true positive rate. The sensitivity and accuracy of an EWS depend on both the indicator and the data available. Here, in Fig. 6.10, I show representative cases of indicators and datasets.

6.6 MODEL FOR NOISY HOPF BIFURCATION WITH CONTINUOUS VARIATION OF PARAMETER

In the present study, we use the model of a nonlinear oscillator with additive noise exhibiting subcritical Hopf bifurcation (Noiray, 2017).

$$\ddot{\eta} + \alpha\dot{\eta} + \omega^2\eta = \dot{\eta}(\beta + K\eta^2 - \gamma\eta^4) + \mathcal{N}_1, \quad (6.6)$$

$$\frac{d\alpha}{dt} = 2rt,$$

where η and $\dot{\eta}$ are the state variables, α and β are linear damping and driving respectively and ω is the natural frequency. We use additive Gaussian white noise \mathcal{N}_1 of intensity Γ_1 with an autocorrelation $\langle \mathcal{N}_1 \mathcal{N}_1 \tau \rangle = \Gamma_1^2 \delta(\tau)$. Following Noiray (2017), the values of the parameters ω , β , γ and K are kept constant as follows: $\omega = 2\pi \times 120$ rad/s, $\beta = 50$ rad/s, $\gamma = 0.7$, and $K = 9$. We select a low value of $\Gamma_1 = \sqrt{10^{-1}}$ as we are modelling a laminar system. Here, the linear damping (α) can be considered as the bifurcation parameter analogous to the control parameter in the experiment. α is reduced from 200 rad/s to -50 rad/s to capture the subcritical Hopf bifurcation from a state of stable fixed point to limit cycle oscillations.

In order to study the effect of rate of change of parameter in the model, we vary α continuously. In experiments, the heater power is changing nonlinearly even though we

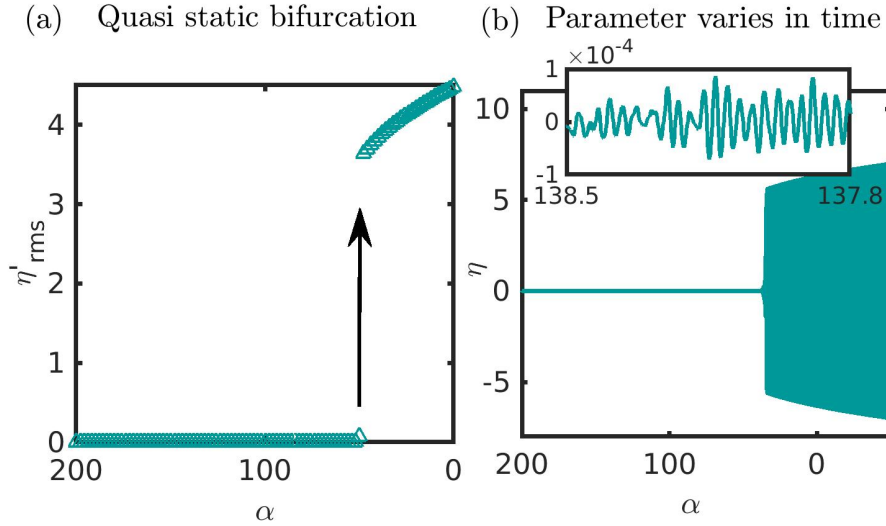


Fig. 6.11: (a) Bifurcation diagram showing the variation of η'_{rms} as a function of linear damping, α . The Hopf point (μ) is at $\alpha = 50$ rad/s, where $\alpha = \beta$. (b) The time series of η obtained by solving Eq. 6.6 for a continuous variation of α is shown along with a zoomed view of the bursts occurring during the fixed point state.

vary V linearly. To replicate a similar variation of the control parameter, we change α as $\alpha = \alpha_0 + r t^2$ in the model. Initially, the linear damping α is high (200 rad/s) to obtain a fixed point. Upon decreasing α , once $\alpha = \beta$, the fixed point becomes unstable. However, there has to be a non-zero perturbation for the system to escape from the fixed point. The additive white noise term (\mathcal{N}_1) in Eq. 6.6 constantly perturbs the system from the fixed point and helps to jump to the limit cycle state. In experiments, even though the system is laminar, low amplitude noisy fluctuations are always present in the flow field.

Although the above model captures the dynamic transitions qualitatively, the initial fixed point state appears to have bursts with a high level of periodicity (Fig. 6.11b), unlike the noisy aperiodic fluctuations observed in the experiments. Notably, the fixed point in Hopf bifurcation under the influence of noise contains fluctuations with bursts of periodicity with shallow peaks near the fundamental frequency of the system (Wiesenfeld, 1985; Fujisaka and Inoue, 1989). However, the experimental data appears to be more aperiodic. In experiments, the base state with constant airflow and zero

heater power itself generates low amplitude aperiodic pressure fluctuations which will also get measured along with the system dynamics. This inherent fluctuations and the measurement noise involved in the dynamics could be modelled by adding Gaussian white noise (\mathcal{N}_2) with intensity Γ_2 to the time series of $\eta(t)$ obtained by solving the model.

$$\eta(t) = \eta(t) + \mathcal{N}_2(t). \quad (6.7)$$

We choose a noise intensity ratio, $\Gamma_2/\Gamma_1 = 0.03$, to replicate the experimental data qualitatively. A very low value of Γ_2/Γ_1 would result in high values of AC and low values of H due to the presence of low amplitude bursty oscillations during the noisy fixed point state. As we gradually increase the intensity of external noise (*i.e.*, increasing Γ_2/Γ_1), the values of H increases and AC decreases. Then, the values during the transition also matches with those obtained from experiments. However, if we add external noise more than necessary, it would suppress all the underlying dynamics and produce $AC = 0$ and $H = 0.5$ due to the white noise characteristics. The addition of external noise to the output with a particular ratio of intensity makes the signal more aperiodic and match the characteristics of experimental data.

Now, with this model, all the previously discussed EWS are computed for data generated with different rates of change of α is shown in Fig. 6.12. For all the measures, we observe a similar performance as that observed for the experiments. Again, AC and H provide a better warning for an impending TAI compared to the other measures. For faster rates of change of parameter, SKEW and K predict the tipping slightly better for the model when compared to the experiments. For slower rates of change of parameter, the transition is more abrupt in terms of the control parameter and all measures except AC and H detect this very close to the tipping point. In contrast, the growth of amplitude of fluctuations is more gradual for faster rates of change of parameter, and the other measures (SKEW and K) are also able to predict the tipping before η'_{rms} and VAR increases.

Next, we analyze the warning time obtained using AC and H for different rates of

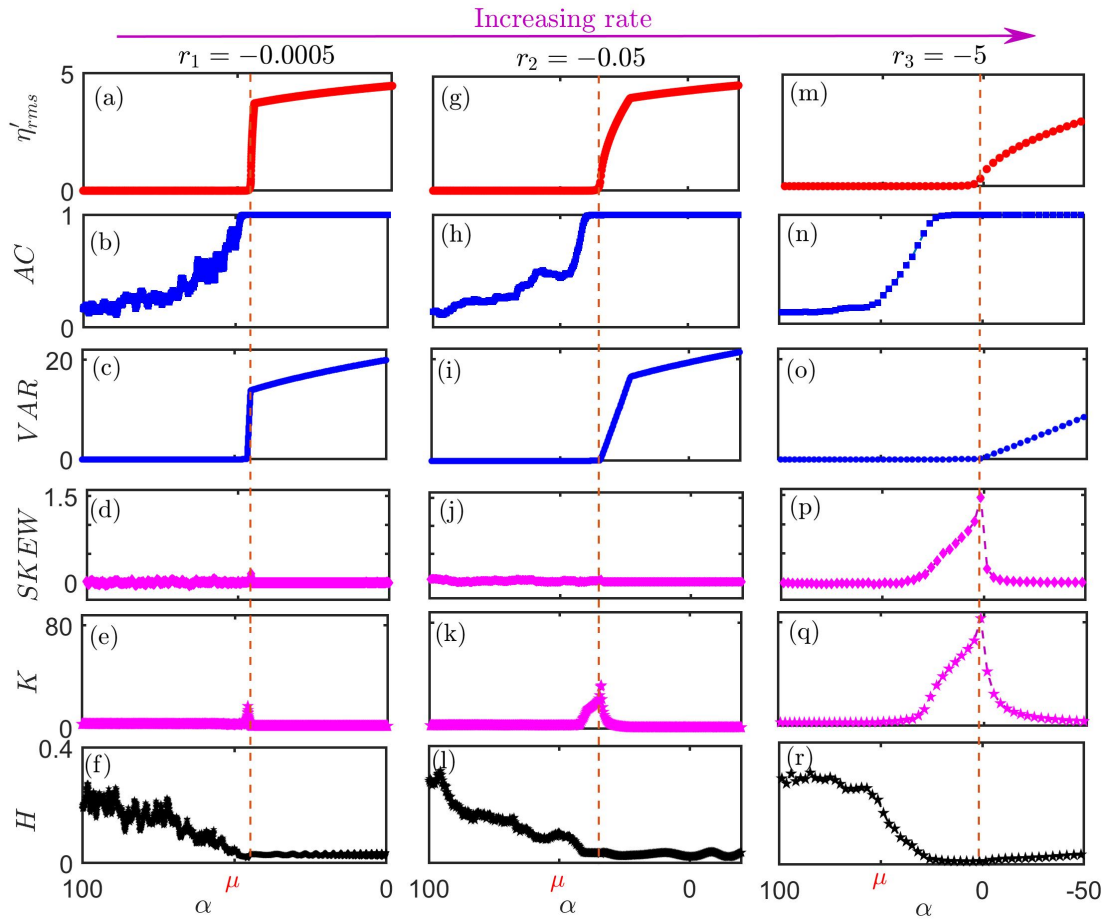


Fig. 6.12: Variation of η'_{rms} , lag-1 autocorrelation (AC), variance (VAR), skewness (SKEW), kurtosis (K) and Hurst exponent (H) with the parameter α during the transition to limit cycle oscillations in the model. Each column corresponds to the results for a particular rate of change of α ((a)-(f): $r = -0.0005$, (g)-(l): $r = -0.05$, (m)-(r): $r = -5$). The point of the maximum rate of change of η'_{rms} is marked with a red dotted line. For higher values of r , kurtosis and skewness detect the tipping before η'_{rms} and VAR. Here, AC and H consistently give early warning well-before the transition to limit cycle oscillations for all the rates.

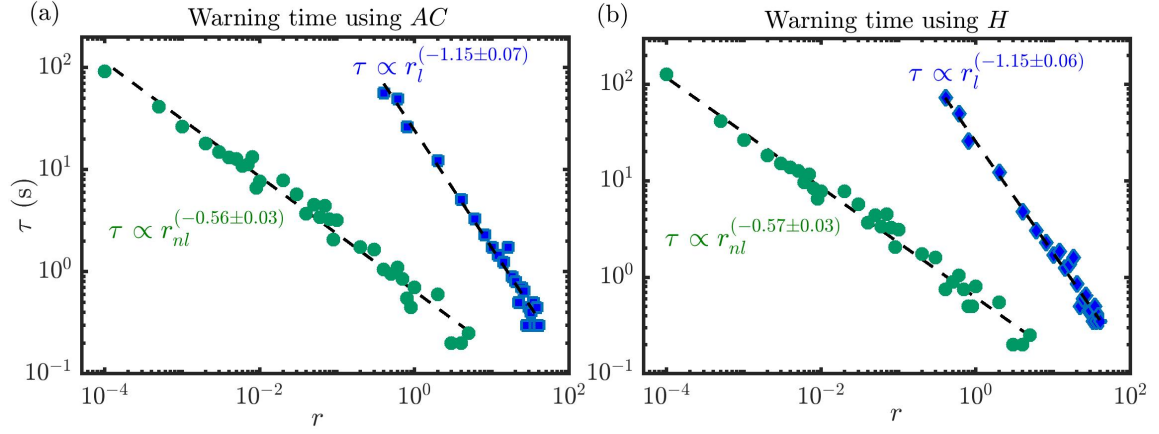


Fig. 6.13: Warning time (τ) obtained from (a) AC and (b) H are plotted as a function of r in a double logarithmic plot for both linear (blue colour) and quadratic (green colour) variation of α . We observe a power law relation between τ and AC and τ and H . The threshold chosen for obtaining warning is 0.4 for AC and 0.1 for H .

change of α . The warning time reduces with the rate of change of parameter following an inverse power law relation. We show the scaling for linear and nonlinear variation of the parameter as $\alpha = \alpha_0 + r_l t$ and $\alpha = \alpha_0 + r_{nl} t^2$ (Fig. 6.13). The trends are qualitatively the same, even though the obtained exponents are different from those of experiments. This difference in the exponent could be because of multiple reasons. The transition depends on the rate of change of parameter, the initial value of the parameter and the type and intensity of noise present in the system. Also, the other parameters such as the β , κ and γ can be varied to adjust the model to represent the experimental system better. In the current study, we vary V linearly; ideally, P has to vary as $P = V(t)^2/R$, where R is the resistance. However, R can change slightly with temperature as V increases. In real systems, as we vary one parameter in the system, there can be multiple parameters changing simultaneously. Hence, the actual control parameter in practical systems can be a combination of multiple parameters. We do not attempt to obtain the exact parameters and condition, but only aim for a qualitative match between the experiment and the model.

6.7 RELATION BETWEEN LAG-1 AUTOCORRELATION AND VARIANCE CLOSE TO THE TIPPING POINT

Critical slowing down leads to an increased autocorrelation and variance of fluctuations in a stochastically perturbed system approaching a bifurcation (Scheffer *et al.*, 2009). Near the critical point, AC tends to one, and VAR tends to infinity. Here, we examine the variation of lag-1 autocorrelation (AC) with the variance of fluctuations close to the tipping where the AC grows and saturates to 1. VAR stays nearly zero almost till the onset of TAI and then shoots up to really high values. At the same time, AC increases gradually during the transition. Here, we observe that AC scales with VAR following a hyperexponential relation (Varfolomeyev and Gurevich, 2001),

$$\frac{d(VAR)}{d(AC)} = k(VAR)^a. \quad (6.8)$$

Refer to Fig. 6.14a for the scaling obtained from experiments and Fig. 6.14b for data from the model. The most common growth principle is exponential, where $a = 1$ in the above equation. To determine the exponent a , we fit $\frac{d(VAR)}{d(AC)}$ with VAR in a double logarithmic plot (Figs. 6.14c-d). The fitting is performed only for the data points in the middle of the curve in Fig. 6.14a. The scaling shown in Fig. 6.14c is a representative case of one experiment with a rate of 3 mV/s. The exponent is found to be $a = 1.94 \pm 0.02$ for the experiments and $a = 1.99 \pm 0.01$ for the model. On integrating Eq. 6.8, we get $VAR = [a_1(k AC + constant)]^{(1/a_1)}$, where $a_1 = -a + 1$ and $a \sim 2$ from the Fig. 6.14. Finally, we have empirically found a relation between AC and VAR for dynamic Hopf bifurcation as follows $VAR \propto \frac{-1}{k AC + constant}$. If we apply the limits approaching the tipping point: VAR tends to infinity as AC tends to one, we get the constant as $-k$ and the final expression as,

$$VAR \propto \frac{1}{1 - AC}. \quad (6.9)$$

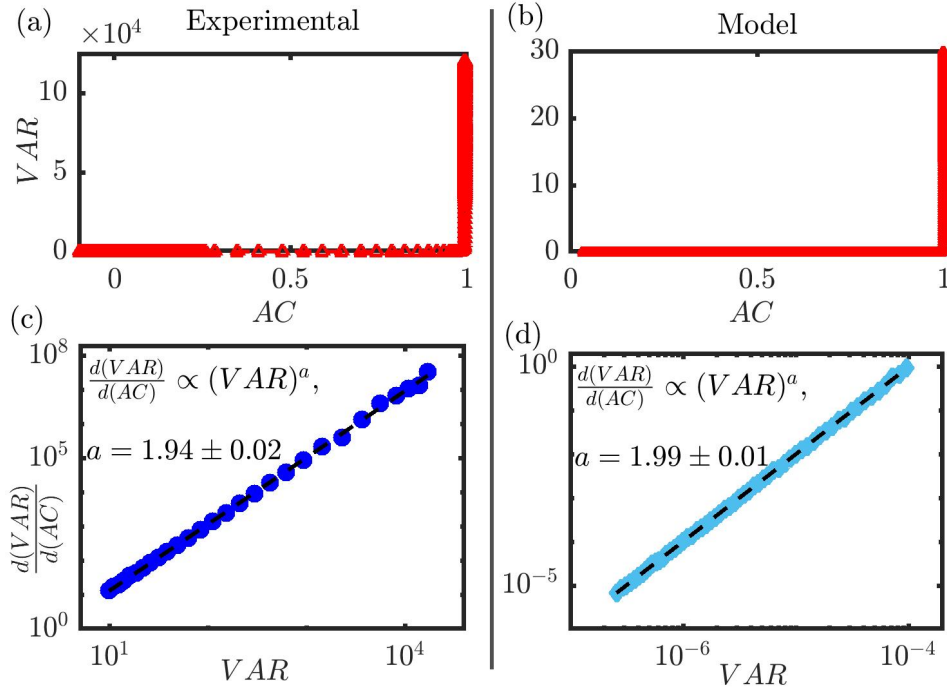


Fig. 6.14: (a-b) Increase in the variance of fluctuations as a function of AC shows a curve increasing faster than exponential (hyperexponential). (c-d) To find the exponent of the hyperexponential function, a linear fit is done on the double logarithmic plot of $\frac{d(VAR)}{d(AC)}$ vs. VAR.

We observe the same scaling exponent for linear and nonlinear variation of the control parameter in the model. The scaling relation seems to be independent of the functional form of the parameter. This hyperexponential scaling observed in experiments and model irrespective of the rate of change of parameter and the functional form of control parameter suggests that this can be a scaling during the occurrence of dynamic Hopf bifurcation.

6.7.1 Autocorrelation for turbulent systems

Generally, the increase in lag-1 autocorrelation on approaching critical transitions is used as a measure of CSD. However, obtaining a significant increase in lag-1 AC to warrant early warning is not so straightforward. Lag-1 AC can be high even before the CSD, due to the presence of correlated dynamics in the system. In such cases, one must be careful in using lag-1 AC as an indicator of CSD. Autocorrelation for a time series can be evaluated at different lags. AC_τ , the autocorrelation estimated

at lag τ , may increase or decrease as we approach the critical transition. CSD accompanies many types of bifurcations. However, the variation of AC_τ is different for the transition to non-oscillatory state (e.g., transcritical and fold bifurcations) and transitions to oscillatory state (e.g., Hopf bifurcations). For non-oscillatory bifurcations, AC_τ decreases with lag. Whereas, for oscillatory bifurcations, the variation of AC_τ is periodic with lag, having a time scale depending on the dominant time scale during the oscillatory state (Bury *et al.*, 2020).

Conventionally, EWS using AC is computed for a particular lag throughout the transition. Autocorrelation for all lags will increase on approaching the transition to a non-oscillatory state (Fig. 6.15a). On the other hand, during the transitions associated with an oscillatory state, autocorrelation may show an increasing or decreasing trend, depending on the chosen lag (Fig. 6.15b). Selecting the most suitable lag is not trivial; at lags lower than $1/4^{\text{th}}$ of the time period, autocorrelation increases closer to the transition, but it decreases for higher lags near half the time period. Bury *et al.* (2020) explained this as a possible reason for the previously reported contradictory trends of autocorrelation. We need prior knowledge of the time scales in the system to select the appropriate lag. Relying on lag-1 AC for EWS, as generally followed, may not be the correct method to capture such transitions in practical systems.

Nevertheless, lag-1 AC is shown to provide EWS in a laminar thermoacoustic system, where the transition is a subcritical Hopf bifurcation from fixed point to limit cycle oscillations (Pavithran and Sujith, 2021). Autocorrelation is almost zero for the noisy fixed point state and 1 for LCO. In contrast, in a turbulent system, the stable operating state is not a fixed point with noise; rather, it is characterised by deterministic fluctuations arising from the turbulent flow (Tony *et al.*, 2015). These turbulent fluctuations possess a high correlation between each time instant, resulting in a very high value for AC at lag-1 (Fig. 6.16b). In general, AC at lag-1 may not work for any given deterministic system. Thus, we need to explore the performance of AC for several lags to capture the transition.

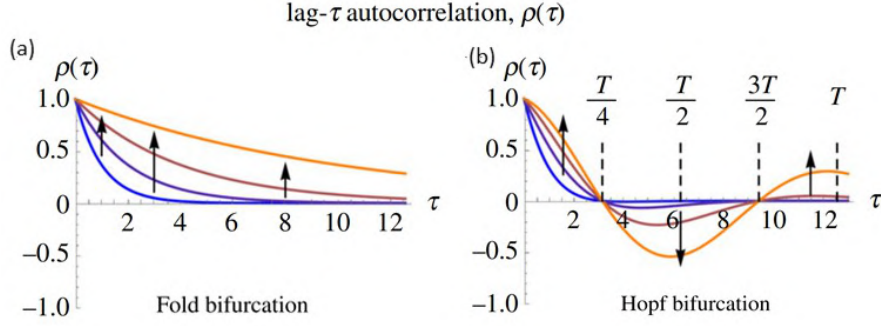


Fig. 6.15: Autocorrelation as a function of lag for (a) fold bifurcation and (b) Hopf bifurcation. Autocorrelation function is plotted at various parameter values on approaching the bifurcation and are plotted in different colours ranging from blue to orange. As we approach the transition, this autocorrelation function changes as indicated by the arrows. For fold bifurcation, AC increases at all lags. In contrast, the trend of AC depends on the lag for Hopf bifurcation. During the transition, AC increases for lags less than $T/4$ and decreases for lags near $T/2$. Reproduced with permission from Bury *et al.* (2020).

Towards this purpose, we use acoustic pressure data during the transition to thermoacoustic instability in a turbulent combustor. Refer Sec. 3.2.1 for more details on the experimental setup and the measurements. We vary the control parameter (Reynolds number) continuously towards thermoacoustic instability. We calculate AC for several lags up to a maximum lag corresponding to 2 cycles of oscillations. AC at low lags have high values for stable operation as well as for thermoacoustic instability, because of the correlated nature of the fluctuations. Instead of AC at lag-1, we can plot the variation of AC at different lags to find the most sensitive lag to capture the transition. Using only the data before transition, finding the optimum lag for each system may be difficult for real systems. We define a general AC vector with many different lags, and the variance of such a vector can be used as EWS for turbulent complex systems. The variance of autocorrelation over τ ($\text{VAR}(\text{AC})$) for the data acquired for a constant change of airflow rate of 10 SLPM/s shows better performance as EWS compared to rms, lag-1 AC, and variance (see Fig. 6.16). $\text{VAR}(\text{AC})$ captures the transition well before the amplitude grows. Further, it is a bounded measure wherein values change between 0 to 0.5, unlike the variance of the signal. In the presented case, we observe that the performance of

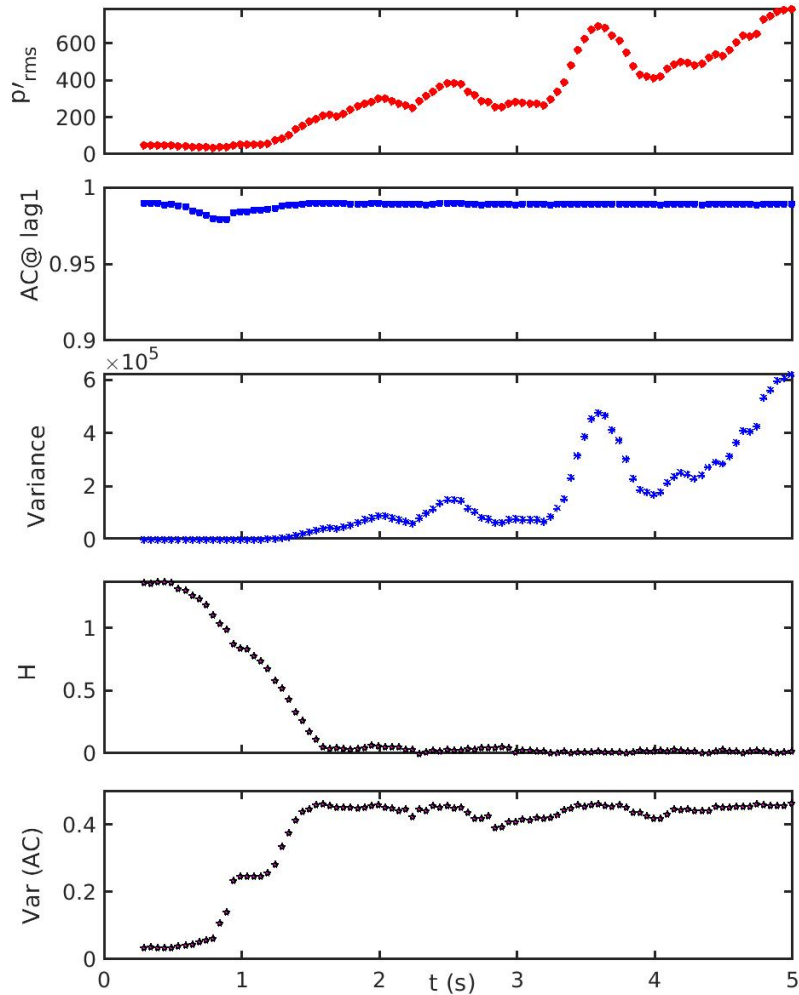


Fig. 6.16: The variation of EWS calculated for pressure fluctuations obtained from a turbulent combustor where the control parameter is varied continuously. Here, the rms and variance increase gradually with increase in the control parameter, whereas AC at lag 1 hardly changes during the transition. However, the Hurst exponent and the variance of AC detects the transition much before p'_{rms} rises. The variance of AC for multiple lags increases and approaches a maximum of 0.5. The autocorrelation is a periodic function of lag for a periodic signal and the variance of AC over two cycles would be 0.5.

VAR(AC) in detecting the transition is as good as the Hurst exponent.

6.8 SUMMARY

We study several early warning signals for critical transitions in a thermoacoustic system. Compared to the quasi-static bifurcation, the onset of tipping is delayed when the control parameter is varied continuously at a finite rate. We confirm the observation of increased delay with increase in the rate of change of control parameter. By analyzing the performance of various early warning signals, we observe that the variance, kurtosis and skewness do not provide adequate warning; they change only when p'_{rms} rises. The lag-1 autocorrelation and the Hurst exponent are able to predict the transition well-before the tipping point. We confirmed this observation by performing experiments at different rates of change of control parameter. For slower rates, AC and H give more warning time compared to faster rates, even though we are relatively close to the transition in terms of the parameter. On the other hand, for faster rates where we have relatively lesser time to initiate control measures, AC and H capture the tipping at a parameter value which is well ahead of the tipping point. Furthermore, we notice that the warning time reduces with the rate of change of parameter following an inverse power law relation. Then, we perform a similar analysis for a noisy Hopf bifurcation model. The qualitative features of the EWS using the lag-1 autocorrelation and the Hurst exponent are captured using the model. Finally, we empirically obtained a relation between lag-1 autocorrelation and the variance of fluctuations for dynamic Hopf bifurcation. This hyperexponential scaling is found to be independent of the functional form of variation of the control parameter.

CHAPTER 7

Rate-dependent transitions in complex systems

Critical points are often related to bifurcations, wherein the system undergoes a transition from one state to another upon varying a system parameter past a critical value (May, 1977; Scheffer *et al.*, 2009). However, in some scenarios, if the parameter is varied faster than a critical rate, unexpected transitions occur, which are absent for slow rates and quasi-steady variations. Such transitions are called rate-induced tipping (R-tipping) (Ashwin *et al.*, 2012). In engineering practice, the stability margins are usually estimated by varying control parameters either in a quasi-steady manner or at a very slow rate. However, in reality, the control parameters change continuously and even exhibit sudden variations. An unexpected R-tipping during a rapid variation of a parameter would be catastrophic. In this chapter, we demonstrate R-tipping experimentally in a real-world complex system, namely a turbulent thermoacoustic system. To investigate the mechanism of R-tipping, we perform experiments by varying the control parameter at constant rates. Motivated by the experiments, we use a nonlinear oscillator model exhibiting Hopf bifurcation to illustrate R-tipping and generalize the mechanism of tipping to complex systems with competing slow and fast parameters involved.

7.1 INTRODUCTION

Rising carbon dioxide levels in the atmosphere continue to heat our planet, which is rapidly approaching a critical climate change leading to unanticipated catastrophic consequences (Lenton *et al.*, 2019; Lovejoy and Nobre, 2019). Climate change can affect ecosystems and trigger abrupt transitions. Natural systems such as the earth's climate, wildlife populations, and ecosystems exhibit sudden changes in their state (Carpenter *et al.*, 1999; Scheffer *et al.*, 2001). Such transitions include epileptic seizures, asthma attacks, migraines, algae blooms in lake ecosystems, extinction of

species in ecosystems and desertification (Venegas *et al.*, 2005; Litt *et al.*, 2001; Ortiz *et al.*, 2020). A sudden transition to a contrasting state due to a gradual change in the system parameter is generally known as ‘tipping’ (Lenton *et al.*, 2008). In real-world complex systems, these transitions are often ‘not easily reversible’ and have prolonged consequences or result in the collapse of the entire system. Here, complex systems refers to systems comprising many interacting subsystems whose interactions can lead to emergent phenomena. The positive feedback mechanisms in complex systems are found to be the basic ingredients of tipping (Scheffer *et al.*, 2012; Angeli *et al.*, 2004). The use of bifurcation theory helped understand the problem of unexpected tipping in many systems (Kuznetsov *et al.*, 1998; Thompson and Sieber, 2011). Whenever the tipping is induced by a bifurcation, the stability margin can be identified by estimating the stability of the equilibrium states. In such cases, the tipping point is nearly the same as the bifurcation point. However, the tipping point can deviate from the bifurcation point due to the presence of random fluctuations (noise) in the system or time-dependent variation of the parameters (Baer *et al.*, 1989; Unni *et al.*, 2019a). The system relaxes back to the stable equilibrium for small perturbations due to noise. For sufficiently high noise intensity, there is a possibility of escaping from the basin of attraction, before reaching the expected tipping point (N-tipping) (Ashwin *et al.*, 2012; Ritchie and Sieber, 2017; Ditlevsen and Johnsen, 2010). Further, parameters varying continuously at a finite rate can delay tipping; this is commonly known as rate-delayed tipping or slow passage through bifurcation (Baer *et al.*, 1989). On the other hand, instances of advanced tipping are also reported (Suchithra *et al.*, 2020; Manikandan and Sujith, 2020).

Many real-world systems are non-autonomous. In natural systems, the parameters often vary continuously on their own, whereas we vary them intentionally in engineering systems. Throttling in aircraft engines is an example of a situation where we change the parameter continuously. In contrast, parameters in the climate system such as global temperature or planetary albedo vary on their own. Therefore, one should consider the

rate at which the parameter varies while studying critical transitions in real systems. Fast rates of change of parameters introduce interesting effects on tipping, including unexpected tipping even without having an underlying bifurcation.

Ashwin *et al.* (2012) classified this category of tipping as rate induced tipping (R-tipping), where a slow variation of a parameter does not show any tipping. Only fast variations of the parameter (faster than a critical rate) lead to tipping; such tipping does not need any change in the stability of equilibrium states. They defined R-tipping as a condition where the system fails to track the continuously changing quasi-steady attractors and tips to an alternative stable state. While the quasi-steady or sufficiently slow variation of parameter does not result in any bifurcation, a continuous variation at a rate faster than the critical rate results in tipping. In other words, the dynamical system, $\dot{x} = f(x, a)$, does not exhibit bifurcation upon varying the parameter a ; however, it can undergo transition upon changing r , where $\dot{a} = r$. Recently, a different mechanism of R-tipping called preconditioned R-tipping was discovered by Tony *et al.* (2017) and illustrated in an experimental thermoacoustic system and in a model exhibiting subcritical Hopf bifurcation. Here, the bifurcation parameter itself is continuously varied at different rates within a bistable region. They achieved R-tipping by preconditioning the system with a high initial perturbation and then by variation of the parameter at a fast rate. The high amplitude initial perturbation alone is not sufficient to induce tipping. Fast rates of change of parameter above a critical rate results in tipping; the system directly approaches a stable limit cycle instead of decaying to a fixed point.

In all the above scenarios, the variation of a system parameter has to exceed a threshold rate for a runaway change to occur, wherein the system abruptly leaves an attractor. The resulting change can be reversible as well, as described by Wicczorek *et al.* (2011). Their work on excitable slow-fast systems showed the possibility of rate dependency and a new mechanism of tipping in a climate system model. A reversible type of R-tipping was observed, where the system can be excited, with a ramped parameter, from

the existing attractor and return to it repeatedly. They used the climate-carbon cycle model with global warming to explain a potential climate tipping point known as the compost-bomb instability (an explosive release of soil carbon into the atmosphere).

This dangerous sudden tipping may come with no early warning. Most of the generic early warning signals work by capturing the signatures of the underlying bifurcation (Carpenter and Brock, 2006; van Nes and Scheffer, 2007). However, R-tipping need not be accompanied by a change of stability of the system (bifurcation); as a result, the occurrence of R-tipping is challenging to predict. Therefore, we need to understand the mechanisms behind them to predict such transitions, especially in real-world complex systems.

The theoretical studies explaining the mechanism of R-tipping are shown with models and do not have any experimental evidence. At the same time, experimental observations of R-tipping as reported by Manikandan and Sujith (2020) lack the understanding of the underlying mechanism. Due to the limited accessibility to the system variables in experiments, the existing theories do not explain these results. To address this issue, we perform experiments in a real-world complex system, a turbulent thermoacoustic system, by measuring other slow varying parameters to identify the mechanism. We experimentally show a mechanism of R-tipping in complex systems with positive feedback. We describe experiments in the following section.

7.2 EXPERIMENTS

Turbulent combustors are used in rockets and aircrafts for propulsion, and power-producing gas turbines. A turbulent thermoacoustic system is a complex system that exhibits rich dynamical transitions originating from the nonlinear interactions between the sound waves, the hydrodynamic field, and the flame inside the combustor. Under certain operating conditions, the interactions between these subsystems establish a positive feedback mechanism (Sujith and Unni, 2020). This positive feedback mechanism drives the system towards a self-organized state known as thermoacoustic

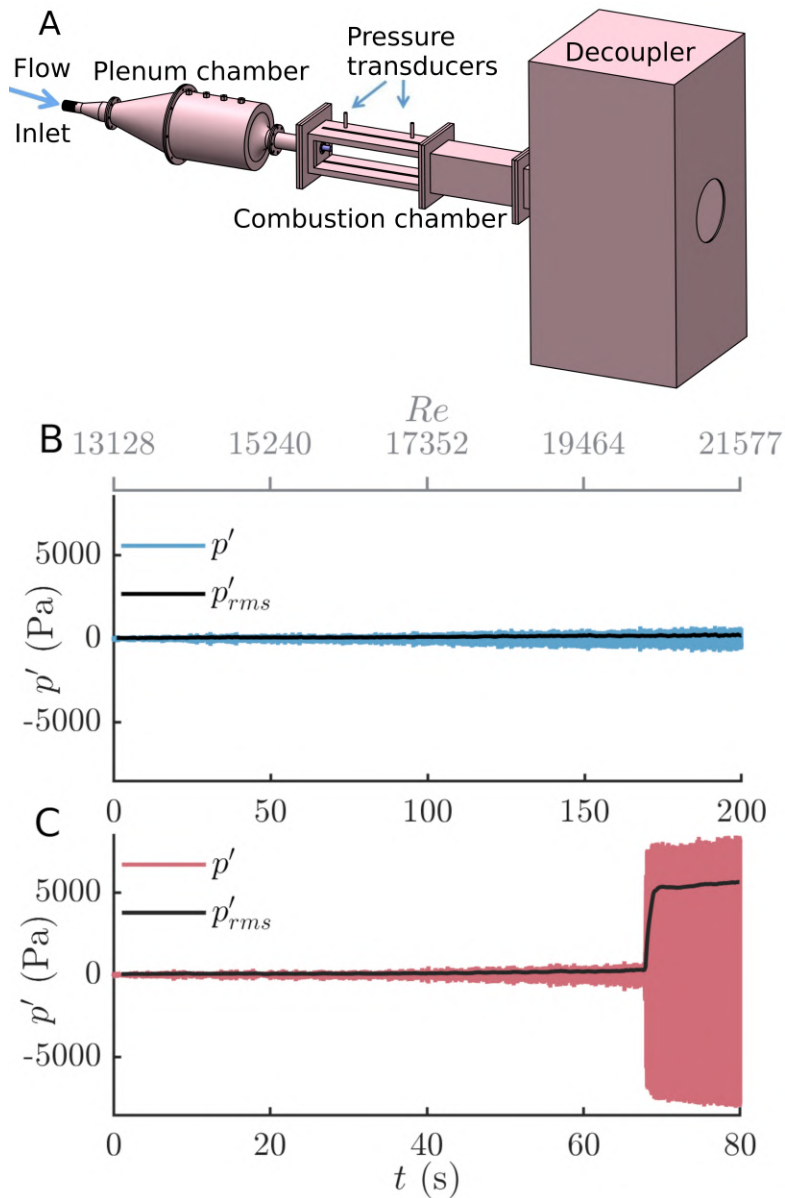


Fig. 7.1: (A) Schematic of the laboratory-scale turbulent combustor used for this study. A backward-facing step combustor with a combustion chamber having a cross-section of $90 \text{ mm} \times 90 \text{ mm}$ and a length of 800 mm is used. The air flow enters through the inlet to the plenum chamber. We vary the Re of the flow continuously. Time series of pressure oscillations acquired for (B) a slow variation ($dRe/dt = 42 \text{ s}^{-1}$) and (C) a fast variation of Reynolds number ($dRe/dt = 106 \text{ s}^{-1}$). Initially, we observe a state of low amplitude aperiodic fluctuations for low values of Re in both cases. Then, the system transitions to a state of periodic oscillations with very high amplitude ($\sim 8000 \text{ Pa}$) for the fast variation of Re . Even though we are varying Re in the same range, we do not observe a high amplitude limit cycle for the slow variation of Re .

instability. Transition to thermoacoustic instability is accompanied by a growth of ruinously high amplitude pressure oscillations and is a catastrophic critical transition that is undesirable.

The spontaneous emergence of high amplitude pressure oscillations in gas turbine engines and rocket motors is a persistent challenge faced by the propulsion and power industry (Juniper and Sujith, 2018; Sujith and Pawar, 2021). The phenomenon of thermoacoustic instability can cause catastrophic damage to the system through severe vibrations leading to structural failure, fatigue, failure of thermal protection systems, failure of navigation and control systems, and reduced life span of the engine (Lieuwen and Yang, 2005). The problems of thermoacoustic instability have even led to the failure of space missions (Fisher and Rahman, 2009). Moreover, rate induced transitions resulting in the unexpected occurrence of thermoacoustic instability are even more dangerous as it is hard to detect the transition during quasi-steady experiments. In this work, we investigate the possibility of rate induced transition to thermoacoustic instability and elucidate the mechanism of R-tipping in a turbulent combustor.

We explain the experiments briefly here; for a detailed description of the experimental setup, we refer the reader to George *et al.* (2018a). The turbulent thermoacoustic system comprises a backward facing step combustor, a plenum chamber, and a decoupler (Fig. 7.1A). The combustion chamber is 800 mm long. The air flow enters through the inlet to the plenum chamber. The fuel (liquefied petroleum gas (LPG): 60% butane and 40% propane) is injected upstream of the combustion chamber. We ignite the partially premixed reactant mixture using a spark plug. We use a fixed vane swirler of diameter $d = 40$ mm for flame holding. The swirler has 8 vanes, with a vane angle of 40° with respect to the longitudinal axis. Once the flame is stabilized in the combustor, we vary the mass flow rate of air, which, in turn, varies the Reynolds number (Re). Re is considered as the control parameter in this study and is calculated as $Re = 4\dot{m}/\pi\mu D_0$, where $\dot{m} = \dot{m}_a + \dot{m}_f$ is the total mass flow rate of the air-fuel mixture, μ is the dynamic viscosity of the mixture and D_0 is the diameter of the circular duct just before the

combustion chamber.

In the present study, we vary Re continuously by controlling the mass flow rate of air, \dot{m}_a , as a linearly increasing function of time. The mass flow rate of fuel, \dot{m}_f is kept constant at 0.76 g/s, and \dot{m}_a is increased from 7.76 g/s to 13.07 g/s at different rates, and Re varies from 1.3×10^4 to 2.2×10^4 . The corresponding variation in equivalence ratio is from 0.99 to 0.59. The equivalence ratio is defined as $\phi = \frac{(\dot{m}_f/\dot{m}_a)_{actual}}{(\dot{m}_f/\dot{m}_a)_{stoichiometry}}$, where \dot{m}_f and \dot{m}_a are the mass flow rates of fuel and air, respectively. The flow rates of air and fuel are controlled using mass flow controllers (Alicat, MCR series) with an uncertainty of $\pm(0.8\% \text{ of reading} + 0.2\% \text{ of full scale})$. The corresponding maximum uncertainty in Re is $\pm 2.5\%$. To study the dynamical transitions in the system, we measure the pressure fluctuations inside the combustor (at a sampling rate of 4 kHz) using piezoelectric pressure transducer (PCB103B02) mounted at a distance of 360 mm from the swirler. The sensitivity of the transducers is 217.5 mV/kPa, and the maximum uncertainty is ± 0.15 Pa. A K-type thermocouple is used to measure the wall temperature of the combustion chamber close to the swirler at a distance of 90 mm from the backward facing step. The pressure signals are acquired using a 16-bit A/D card (NI-6343), and the temperature data are acquired by a 24-bit A/D card (NI-9211) at a sampling rate of 4 Hz.

We perform experiments by varying Re at different rates (from $dRe/dt = 35.2 \text{ s}^{-1}$ to 140.8 s^{-1}). We keep all the operating conditions the same, except for the rate of variation of the control parameter. The rate of change of the Reynolds number, dRe/dt , is kept constant for a particular experiment. First, we present an analysis of the data acquired from two trials of experiments with two different values of dRe/dt . One experiment is performed at a relatively slow rate ($dRe/dt = 42 \text{ s}^{-1}$), and the total duration of the experiment is 200 s (Fig. 7.1B). The system remains in a state of low amplitude aperiodic fluctuations throughout the entire range of Reynolds numbers. Next, we present another data for an experiment conducted at a faster rate ($dRe/dt = 106 \text{ s}^{-1}$) where the Reynolds number is varied in the same range, but for a

duration of 80 s (Fig. 7.1C). Here, as the Reynolds number varies, the system exhibits a transition from low amplitude aperiodic fluctuations to high amplitude limit cycle oscillations. We observe a sudden jump from a low amplitude state to a high amplitude periodic oscillatory state. During the state of low-amplitude fluctuations, the amplitude spectrum shows a wide band of frequencies, and after the transition it becomes a narrow peak centered around 190 Hz. I have performed the experiments for this study at IIT Madras.

7.3 R-TIPPING IN A TURBULENT THERMOACOUSTIC SYSTEM

To analyze the experiments performed at different dRe/dt , the root mean square (rms) of acoustic pressure fluctuations, calculated for a moving window of 1 s and overlap of 0.9 s, is plotted as a function of Re for different values of dRe/dt (Fig. 7.2). We do not observe tipping for slow rates of variation of Re ($dRe/dt \leq 60.3 \text{ s}^{-1}$), whereas, fast rates of variation of Re ($dRe/dt > 60.3 \text{ s}^{-1}$) result in a transition to thermoacoustic instability. We observe two different dynamics at rates lower and higher than a critical rate, for the same range of control parameter values. $dRe/dt \sim 60.3 \text{ s}^{-1}$ is the ‘experimentally observed’ critical rate in this case. This idea of the critical rate will be clearer when we discuss the model.

The inset in Fig. 7.2 shows the rate of change of p'_{rms} which helps to identify the point of maximum growth in the amplitude of pressure fluctuations. Such a point of maximum change in p'_{rms} is identified as the tipping point (Pavithran and Sujith, 2021). This plot is drawn considering only the cases where there is tipping (i.e., for rates faster than the critical rate, $dRe/dt > 60.3 \text{ s}^{-1}$). An interesting observation is that there is an advancement in the tipping point with the increase in the rate change of parameter, contrary to the rate-dependent tipping-delay observed in earlier studies (Baer *et al.*, 1989; Pavithran and Sujith, 2021; Tandon *et al.*, 2020). The peak in the plot shifts towards lower values of Re with an increase in the rate of change of parameter; i.e., the tipping point advances for faster rates. Although advanced tipping has been

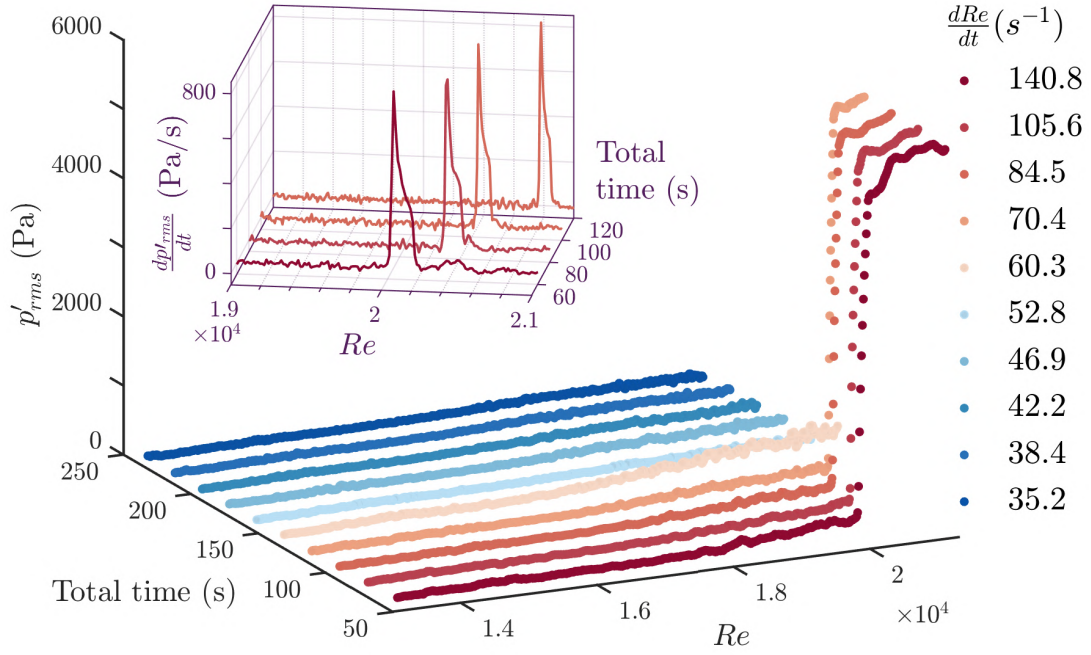


Fig. 7.2: Bifurcation diagram for experiments performed at different dRe/dt . We vary Re in the same range at different rates, thereby having different duration for the experiments. For each experiment, we plot the rms of pressure oscillations as a function of Re . We observe rate-induced tipping to high amplitude limit cycle oscillations for faster variations of the parameter ($dRe/dt > 60.3$). Slower rates of variation below a critical rate do not lead to a jump in p'_{rms} . The inset figure shows the rate of change of p'_{rms} , wherein the maximum increase in amplitude appears as a peak. This helps to define a tipping point when control parameters vary continuously. The advanced onset of thermoacoustic instability with fast rates of change of parameter can be clearly observed here.

reported earlier in various complex systems (Suchithra *et al.*, 2020; Manikandan and Sujith, 2020), to date, there is no physical explanation for such advancement of tipping with fast rates of variation of parameters. To identify when to expect advanced tipping (contrary to delayed tipping) in non-autonomous systems, we proceed to investigate the mechanism behind the rate induced tipping observed in this thermoacoustic system and then generalize it by illustrating it in a mathematical model.

To analyze the experiments performed at different dRe/dt , the root mean square (rms) of acoustic pressure fluctuations, calculated for a moving window of 1 s and overlap of 0.9 s, is plotted as a function of Re for different values of dRe/dt (Fig. 7.2). We do not observe tipping for slow rates of variation of Re ($dRe/dt \leq 60.3 \text{ s}^{-1}$), whereas, fast

rates of variation of Re ($dRe/dt > 60.3 \text{ s}^{-1}$) result in a transition to thermoacoustic instability. We observe two different dynamics at rates lower and higher than a critical rate, for the same range of control parameter values. $dRe/dt \sim 60.3 \text{ s}^{-1}$ is the ‘experimentally observed’ critical rate in this case. This idea of critical rate will be more clearer when we discuss the model. The inset figure in Fig. 7.2 shows the rate of change of p'_{rms} which helps to identify the point of maximum growth in the amplitude of pressure fluctuations. Such a point of maximum change in p'_{rms} is identified as the tipping point (Pavithran and Sujith, 2021). This plot is drawn considering only the cases where there is tipping (rates faster than the critical rate, $dRe/dt > 60.3 \text{ s}^{-1}$). An interesting observation is that there is an advancement in the tipping point with the increase in the rate change of parameter, contrary to rate-dependent tipping-delay observed in earlier studies (Baer *et al.*, 1989; Pavithran and Sujith, 2021; Tandon *et al.*, 2020). The peak in the inset plot of Fig. 7.2 shifts towards lower values of Re with an increase in the rate of change of parameter, i.e., the tipping point advances for faster rates. Although advanced tipping has been reported earlier in various systems (Suchithra *et al.*, 2020; Manikandan and Sujith, 2020), to date, there is no explanation for such advancement of tipping with fast rates of variation of parameters. To identify when to expect advanced tipping (contrary to delayed tipping) in non-autonomous systems, we proceed to investigate the mechanism behind the rate induced tipping observed in this thermoacoustic system and then generalize it by illustrating it in a mathematical model.

7.4 THE MECHANISM OF R-TIPPING

We investigate the mechanism behind rate-induced tipping to high amplitude limit cycle oscillations observed in our thermoacoustic system. We examine the evolution of the wall temperature of the combustor to understand the dynamics during the transition. The walls of the combustor get heated up gradually during the experiment, and therefore the wall temperature varies continuously at a finite rate. Therefore, the wall

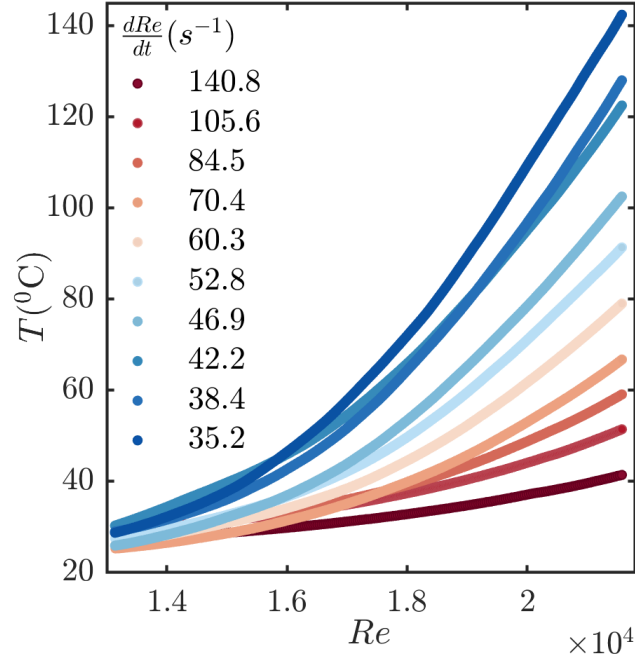


Fig. 7.3: Variation of wall temperature in time as a function of the control parameter. The dark blue curves, which are increasing up to high temperatures, represent slow rates. In contrast, the faster variations of Re result in comparatively lower values of wall temperature at a given value of Re (dark red). Even though the increase in wall temperature is gradual in time, due to the difference in the duration of the experiments, we obtain significantly different wall temperatures for a given Re for experiments at different dRe/dt . Hence, different paths are obtained in the (Re, T) parameter plane. Note that each curve in the figure corresponds to experiments of different duration.

temperature is another variable that varies simultaneously with the control parameter at a different rate. Thus, we have a non-autonomous dynamical system. Figure 7.3 shows the variation of wall temperature with change in Re . Note that we start all the experiments at room temperature ($25^{\circ}C \pm 1^{\circ}C$), then ramp (parameter variation) after a constant delay after ignition. Each of the curves in Fig. 7.3 corresponds to different duration of experiments; therefore, higher values of wall temperatures are attained in the experiments having longer duration corresponding to slow variations in Re . On the other hand, the increase in wall temperature is relatively small for fast variations in Re . Thus, the wall temperatures for a given Re are different for slow and fast rates; it is relatively higher for slower rates of change of Re compared to that of faster rates. Therefore, in this 2-parameter plot, the system tracks different directions depending

on the rate of change of Re and reaches a different set of parameters. Thus, different dynamics can be expected for these cases, as each set of parameters can drive the system towards different attractors. Note that we do not discuss quasi-static variation in the experiments; we have to wait asymptotically keeping the parameters constant, which is not possible in this case as the wall temperature is changing continuously.

Most importantly, the system did not undergo any transition to limit cycle oscillations for slow rates with relatively high wall temperatures. As tipping is not observed for higher wall temperatures, we examine the effect of wall temperature on acoustic damping. Towards this purpose, we measure the decay rate (ζ) of acoustic pressure oscillations, which is a measure of the acoustic damping, at different wall temperatures.

7.4.1 Measuring damping at high temperatures

To understand the role of wall temperature in R-tipping, we have to determine how a change in wall temperature contributes to the damping/driving in the system. At room temperatures, without any inlet flow, we can measure damping by exciting the natural modes of the combustor duct using an externally driven speaker. A sinusoidal pressure perturbation is generated, the speaker is abruptly switched off, and the decay rate of periodic oscillations is estimated. We extract the envelope of amplitude and fit a line in the semi-logarithmic plot of the envelope to estimate the decay rate. The decay of amplitude of the signal is fitted with an exponential ($e^{-\zeta t}$) function.

It is hard to measure damping at high temperatures by using externally driven speakers, as done for room temperature measurements. Therefore, we use a different method, where we establish the system in the state of thermoacoustic instability and abruptly cut off the fuel supply and stop the combustion. We start the experiments by keeping all the operating conditions but the wall temperature the same, and then vary Re to reach the state of thermoacoustic instability. The wall temperature is recorded throughout the experiment, and the specific value is noted at the instant when the flow of fuel is cut.

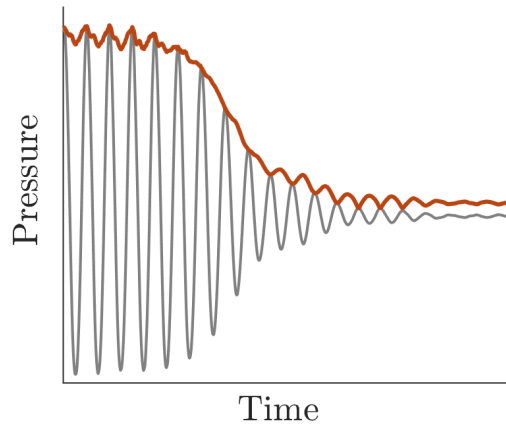


Fig. 7.4: A representative acoustic pressure signal showing the decay of oscillations when the fuel is cut abruptly. We extract the amplitude envelope of oscillations and fit a line in the semi-log plot to calculate the decay rate.

7.4.2 The effect of wall temperature on acoustic damping

The plot of the decay rate as a function of the wall temperature (Fig. 7.5) shows that the acoustic damping increases with increasing wall temperature depicting a clear linear relation between them. Interestingly, this type of a relation between wall temperature and acoustic damping has not been reported till now in turbulent thermoacoustic systems to the best of our knowledge, and the physical mechanisms behind such a dependency of acoustic damping on temperature needs further investigation. An increase in Re corresponds to an increase in acoustic driving) in time, and the acoustic damping increases simultaneously at a rate that we do not have any control over.

Although we are varying a single parameter during the experiment, there is another "hidden" parameter continuously changing on its own, at a different rate. We vary Re continuously to drive the system towards thermoacoustic instability. Concurrently, the continuously increasing wall temperature increases the acoustic damping in the system. The transition to thermoacoustic instability occurs when the thermoacoustic driving overcomes the acoustic damping in the system. As the walls of the combustor are heated only for a shorter duration for experiments corresponding to fast variation of Re ,

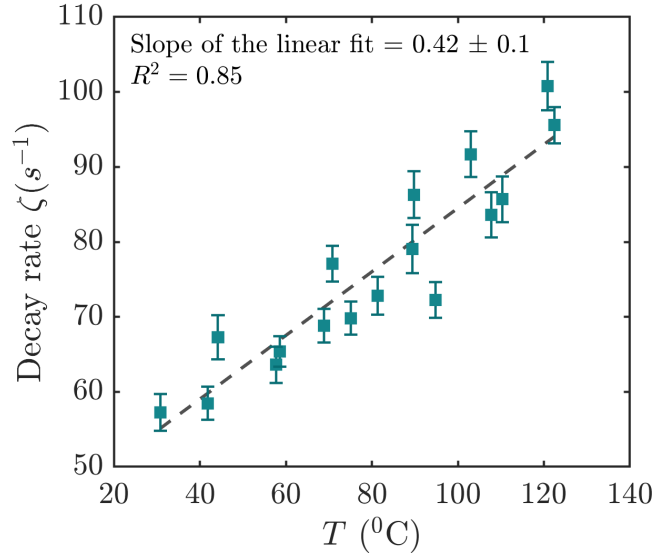


Fig. 7.5: To explore the dependency of acoustic damping on the wall temperature, we measure the decay rate of the envelope of acoustic pressure oscillations, ζ , as a function of the wall temperature. We conduct a set of experiments wherein the combustion is stopped abruptly by cutting off the fuel supply during the state of periodic oscillations. We fit an exponential function to the envelope of oscillations (Culick and Kuentzmann, 2006; Perry, 1970) to measure the rate of decay of oscillations at different wall temperatures. We observe that the decay rate (a measure of acoustic damping) increases with increasing wall temperature. We fit a straight line to obtain an empirical relation between the decay rate and the wall temperature.

the wall temperatures attained are relatively lower, leading to lower levels of acoustic damping. Therefore, it is easy to overcome acoustic damping at a comparatively lower level of thermoacoustic driving, resulting in an advanced onset of tipping for faster variations of Re .

The applicability of this mechanism of R-tipping is not restricted to thermoacoustic systems. In fact, it can be observed in any system where two parameters vary simultaneously, given that each has the opposite effect on the driving mechanism of a critical transition. Then, the competition between the two variables determines whether and when the tipping will occur. For instance, this mechanism can explain the potential climate tipping point, the ‘compost bomb instability’ (Luke and Cox, 2011). The compost bomb instability occurs above a specific rate of global warming when heat is generated in the soil faster than it can escape to the atmosphere. This can, in

turn, significantly accelerate global warming. Wieczorek *et al.* (2011) have studied R-tipping to compost bomb instability in an analytical framework and derived conditions for the critical rate and excitability threshold. However, they have viewed it from a different perspective of excitable systems. Here, we illustrate the mechanism of R-tipping discussed and generalize its occurrence to various systems using a system independent nonlinear oscillator model with two time varying parameters.

7.5 R-TIPPING IN A NOISY HOPF BIFURCATION MODEL

A simple model of a nonlinear oscillator (a Van der Pol oscillator with higher order terms) exhibits subcritical Hopf bifurcation.

$$\ddot{\eta} + \alpha\dot{\eta} + \omega^2\eta = \dot{\eta} (\beta + \kappa\eta^2 - \gamma\eta^4) + \xi \quad (5)$$

Here, α and β are the linear damping and driving terms, respectively. The variations in α and β can be considered analogous to varying wall temperature and Re in the experiments. The additive white noise ξ with intensity Γ and autocorrelation $\langle \xi\xi_\tau \rangle = \Gamma\delta(\tau)$ is added to represent the inherent fluctuations in the system variables. The values of the parameters ω , γ , κ and Γ are kept constant ($\omega = 2\pi \times 120$ rad/s, $\beta = 50$ rad/s, $\gamma = 0.7$, $\kappa = 9$, $\Gamma = 10^5$), following Noiray (2017). The linear damping (α) and driving (β) are varied. Whenever the damping (α) is greater than driving (β), any perturbations decay to the fixed point state ($\eta = 0$) and for $\beta > \alpha$ the system exhibits limit cycle oscillations. The fixed point state appears as low-amplitude oscillations in η due the presence of noise. The transition from the state of low-amplitude fluctuations to high amplitude limit cycle oscillations occurs when the value of β exceeds α . The deterministic bifurcation curve is shown for $\alpha = 60$ and β as the control parameter.

The nonlinear oscillator discussed in above exhibits a subcritical Hopf bifurcation from a state of low amplitude aperiodic fluctuations to a high amplitude limit cycle oscillations when the linear driving and damping are equal ($\beta = \alpha$). Generally, the

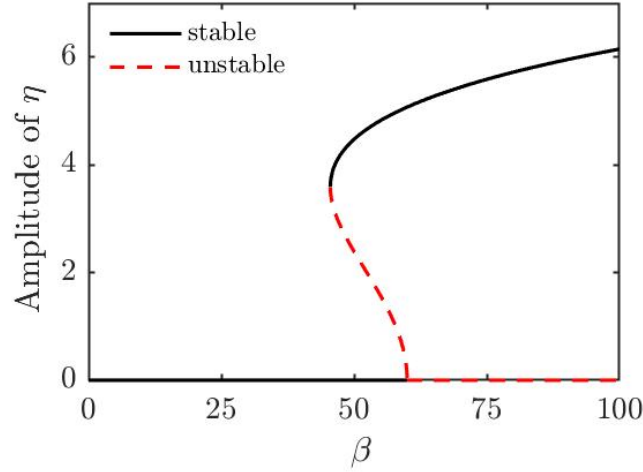


Fig. 7.6: Deterministic bifurcation diagram showing stable and unstable attractors.

effective driving, i.e., $\beta - \alpha$, is considered as the control parameter in such models. However, in reality, various processes contribute to driving and damping, and those processes occur independently at different rates. Hence, we consider such a scenario where β and α vary at different rates.

$$\beta = \beta_0 + \dot{\beta}t \quad (7.1)$$

$$\alpha = \alpha_0 + \dot{\alpha}t. \quad (7.2)$$

Here, we choose α as a monotonically increasing function of time, varying at a constant rate ($\dot{\alpha}$) and β is our control parameter. We vary β at different rates ($\dot{\beta}$) - slower and faster compared to the rate of variation of α . Figure 7.7 shows two cases with faster and slower rates of β compared to α . When β is varied at a rate faster than $\dot{\alpha}$, the transition to limit cycle is observed for $\beta > \alpha$ (Fig. 7.7A). In the second case, wherein β is varied at a relatively slower rate, the driving never exceeds damping, and the system does not transition to limit cycle oscillations (Fig. 7.7B).

For the driving to match the damping, the variation of α and β must intersect at some point, as shown in Fig. 7.7A. This happens only when β varies faster than α , as we start the system from a state of $\alpha > \beta$ (noisy fixed point state). When α is varying in time starting from a high value, β has to vary at a rate faster than α , for tipping to occur in

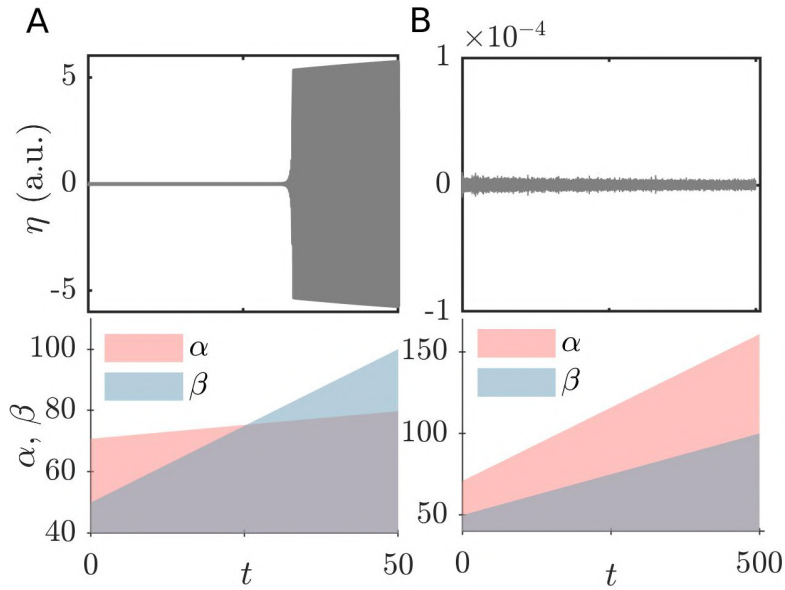


Fig. 7.7: Time series of η obtained by solving the model with continuously varying α and β . We vary α at a constant rate and β at different rates: (A) fast ($\dot{\beta} = 1$) and (B) slow ($\dot{\beta} = 0.1$) rates. Here, a constant variation of α corresponds to a linearly increasing damping. Whenever the rate of change of driving is faster than the rate of variation of α , we observe tipping ($\dot{\beta} > \dot{\alpha}$). The high amplitude limit cycle oscillations occur when driving exceeds damping (A). Driving never exceeds damping for $\dot{\beta} < \dot{\alpha}$ (B).

the system ($\dot{\beta} > \dot{\alpha}$). When $\dot{\beta} = \dot{\alpha}$, the trajectories of α and β do not intersect. If $\dot{\beta} > \dot{\alpha}$ and they meet in a finite time within the duration of experiments, tipping occurs. Thus, there exists a critical rate of change of β above which tipping occurs. However, it is difficult to find out such critical rate in experiments where $\dot{\beta} = \dot{\alpha}$. For $\dot{\beta}$ slightly greater than $\dot{\alpha}$, the driving intersects damping at very high value of driving (at a very large t), thereby making it hard to detect the correct critical rate in experiments.

Next, we examine the dynamics for two different rates of change of β , i.e., $\dot{\beta} > \dot{\alpha}$. One important aspect to remember here is the rate-dependent tipping delay, well studied in the literature. Baer *et al.* (1989) have discovered bifurcation delay when the control parameter is swept through the bifurcation point, and the same has been confirmed later by many others (Bonciolini *et al.*, 2018; Park *et al.*, 2011; Berglund, 2000; Majumdar *et al.*, 2013). Such rate-dependent delay due to memory effects is commonly observed and is more prominent for fast rates. Hence tipping gets delayed from the bifurcation

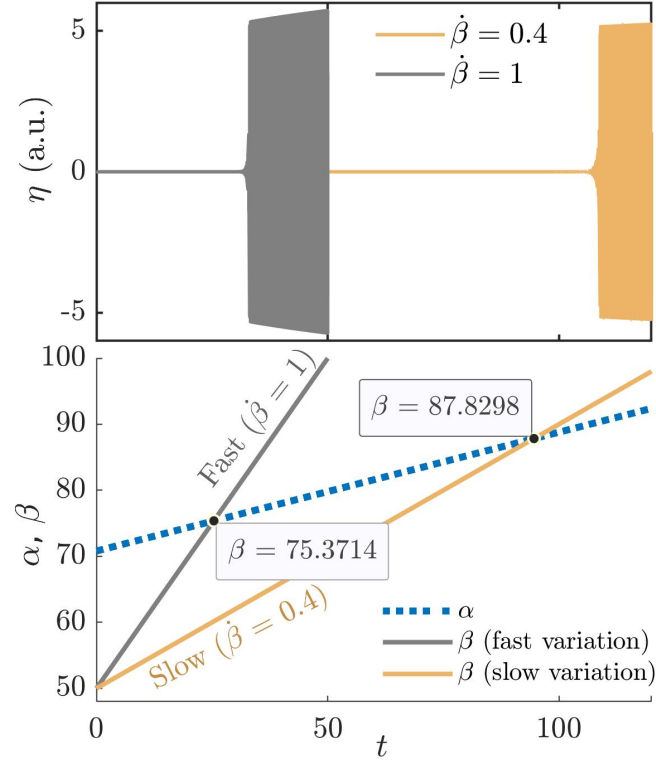


Fig. 7.8: Time series of η and the corresponding variation of α and β are shown for two different rates change of β . In both the cases, $\dot{\beta} > \dot{\alpha}$, i.e., β is faster than α . The onset of tipping is when driving crosses damping. However, as damping varies in time, we need more driving to overcome damping for slow variation of driving.

point for fast rates. However, we do not observe rate-dependent delay; in contrast, we observe advanced tipping for faster rates of variation of the control parameter (β). Figure 7.8 shows the dynamics corresponding to $\dot{\beta} = 1$ and $\dot{\beta} = 0.4$. For $\dot{\beta} = 1$, the variation of β is fast enough to cross α earlier before it grows to high magnitudes, whereas β crosses α at a large value (analogous to higher Re in experiments) for the slow rate ($\dot{\beta} = 0.4$). Thus, we observe tipping at lower values of β as we vary β faster. The Hopf bifurcation model discussed here is a representative case where competing parameters vary continuously at finite rates.

7.6 SUMMARY

In this work, we show the possibility of rate-induced tipping in a turbulent thermoacoustic system. When we vary the Reynolds number continuously at a slow

rate, the system remains in the same dynamical state and does not exhibit any tipping. In contrast, if the Reynolds number is varied fast enough, we observe a transition to a state of thermoacoustic instability with high amplitude limit cycle oscillations. In order to understand the mechanism behind this rate induced tipping in the context of transition to thermoacoustic instability, we explore the variations of other system parameters such as the wall temperature and damping.

We discover that the wall temperature varies continuously at a slow rate. In other words, another parameter, which is not in our control, varies simultaneously at a different rate. Experiments conducted at faster rates of change of Re last for shorter duration and the increase in wall temperature is smaller. In contrast, the wall temperature increases gradually to very high values for experiments conducted at slower rates of change of Re , which last for a longer duration. Then, we measure the acoustic damping rate by estimating the decay rate of oscillations in the system for different wall temperatures and discover that the damping increases linearly with increasing temperature. Thus, we infer that the fast variation of parameters could take the system to a different set of parameters where the damping is very low and can be excited to a high amplitude limit cycle that was otherwise inaccessible.

The increase in Re drives the system towards thermoacoustic instability, whereas the increasing wall temperature increases damping and, in turn, reduces the effective driving. Here, we find a mechanism of R-tipping, where two parameters that have the opposite effect on tipping compete to determine the dynamics. Motivated from the experimental observations, we use a simple system-independent model of Hopf bifurcation to illustrate this phenomenon. When we vary a control parameter which drives the system towards tipping and there exists another parameter that has negative effect on transitions, the control parameter has to be varied at very high rates to achieve tipping. This mechanism and explanation for R-tipping is very general and system independent. To date, such a type of R-tipping has not been explained in any experimental systems. As R-tipping in real-world systems is extremely dangerous,

understanding the mechanism of R-tipping would enable better predictions of R-tipping.

CHAPTER 8

Conclusions and future prospects

In this thesis, we explore the dynamics during critical transitions in diverse physical systems. Specifically, in the first part of the thesis, we focus on finding universal features of critical transitions in disparate systems. Then, early warning signals and amplitude prediction methods are developed based on the obtained universal features close to critical transitions. In the last two chapters, we study critical transitions in non-autonomous systems with control parameters varying at different rates. The main findings of the thesis are summarized here.

Firstly, experiments were performed in three different fluid mechanical systems to study the critical transition to oscillatory instabilities. From the analysis of time series of fluctuating system variables, the oscillatory instabilities in turbulent flows are found to emerge following a universal route. The amplitude of the dominant mode of oscillations scales as inverse power law with the Hurst exponent of the time series of the appropriate state variable. The scaling exponent is invariant across the three systems considered, namely aeroacoustic, aeroelastic and thermoacoustic systems. Here, we report the experimental observation of an inverse square law ($A \propto H^{-2}$) for a class of non-equilibrium systems. In literature, such power law scaling have been discovered for various critical transitions.

Then, we extend our search of universal features during critical transitions to various systems such as optical and electronic systems (a random laser and a Chua's circuit). A much more general behaviour during the self-organization to ordered dynamics in fluid mechanical, optical or electronic systems is discovered. We observed spectral condensation in the power spectrum of the appropriate system variables (in the emission spectrum in the case of the optical system), where the energy distributed in broadband of frequencies gets condensed into a dominant mode. A set of spectral measures are defined to compare and quantify spectral condensation in different systems.

Quantifying the sharpening of the peak in the power spectrum revealed a universal route through which spectral condensation occurs in fluid mechanical, optical and electronic systems. The dominant peak in the power spectrum sharpens with an increase in peak power following inverse power law relations with the spectral measures. Such an inverse power law scaling is observed for all the systems studied, and, interestingly, the scaling exponents are within a small range across the systems.

The discovery of these unique scaling relations has an immediate practical application; it enables a priori estimation of the amplitude of oscillations at the onset of oscillatory instability. This information of the amplitude can be critical in devising counter-measures needed to limit the possible damages from oscillatory instabilities. We present two different methods, based on the two scaling relations, to predict the amplitude during oscillatory instability using time series data well before the critical transition. Using the universal scaling relations between the amplitude of the dominant mode of pressure oscillations and both the Hurst exponent and spectral measure, we show that the amplitude of limit cycle oscillations during thermoacoustic instability can be predicted. We demonstrate that this method can accurately predict the amplitude in practical systems by applying this procedure to data from different combustors. Manufacturers of industrial gas turbines can use both these methods to estimate the amplitude during thermoacoustic instability, even without approaching anywhere close to it. In other words, the amplitude can be estimated without endangering the combustor by exposing it to large amplitudes.

In the last two chapters, critical transitions in non-autonomous systems are studied. Delayed transitions are observed for continuous variation of the control parameter. The delay increases with the rate of change of parameters for the experiments performed in a laminar thermoacoustic system. By analyzing the performance of various early warning signals, the lag-1 autocorrelation and the Hurst exponent are found to predict the transition well before the onset. Here, we find that the warning time reduces with the rate of change of parameter following an inverse power law relation. Then, we

empirically obtained a hyperexponential relation between lag-1 autocorrelation and the variance of fluctuations for dynamic Hopf bifurcation, which is found to be independent of the functional form of the variation of the control parameter. All these results are captured and illustrated using a Hopf bifurcation model.

Finally, a possibility of rate induced tipping for fast variations of control parameters in complex systems is experimentally demonstrated in a thermoacoustic system. Such rate induced tipping can occur unexpectedly, which will not be identified during the stability analysis by quasi-steady experiments. Slow variations of control parameter did not exhibit any critical transitions, whereas fast enough variation of parameter cause transition to high amplitude thermoacoustic instability. We explore the mechanism behind this rate induced tipping and discover that another parameter, which is not in our control, varies continuously at a slow rate. This mechanism of critical transition is not restricted to a thermoacoustic system, but it can occur in any other system where two competing parameters vary simultaneously. We demonstrate this phenomenon in a simple system-independent model of Hopf bifurcation.

Scope for future work

As an extension to the works on universality during critical transitions, an analytical investigation to explain the empirically obtained scaling relations can be done. The well-developed framework of equilibrium phase transitions can be extended to understand the physical reasons behind the power law scaling observed during the critical transitions. Further analysis can be performed to find the corresponding universality classes using the much studied concepts such as percolation. Further, the transition to oscillatory instabilities in turbulent systems is found to follow an intermittency route. The known types of intermittencies in the literature do not follow the scaling relations presented in this thesis. Therefore, the specific route of the emergence of oscillatory instabilities might have a different type of intermittency. More detailed work is needed to identify the type of intermittency. We have mainly focused

on universality during the emergence of oscillatory phenomena or Hopf bifurcation. Extending the analysis to other types of bifurcations is a possible direction in the future. Apart from understanding the physics behind the universal features of critical transitions, we can also extend the research on early warning signals and the amplitude predictions methods based on the generic features close to the transition. In the future, we would most probably see artificial intelligence (AI) based methods or a combination of AI with physics-based methods such as that presented in this thesis to forewarn impending critical transitions and predict the amplitude of oscillatory instabilities. AI based models are currently heavily used for the purpose of forecasting, especially for financial and weather data. Such methods, when applied to engineering systems, in combination with physics based approaches, offer the promise of giving us more powerful tools to predict the amplitude of catastrophic critical transitions to oscillatory instabilities.

Further, in the current work, we have analysed the effect of continuous variation of system parameters on early warning signals. Experimental studies considering the continuous variation of system parameters during the critical transitions are limited. We have performed these experiments on a laminar thermoacoustic system where inherent flow fluctuations are not significant compared to turbulent systems. This is done to study the effect of rate on critical transitions independently, keeping the effects of noise apart. However, in reality, the presence of different levels of noise is unavoidable. Hence, we should study the interplay of noise and rate of change of parameter on early warning signals together, perhaps in turbulent systems, which are closer to the scenario in practical systems. Another possible idea is to derive the hyperexponential relation between autocorrelation and variance presented in Chapter 6 for Hopf bifurcation and other types of bifurcations.

Explanation of the mechanism of R-tipping in real-world systems was lacking, and we found a possible mechanism in a complex system where two parameters vary continuously. Such an attempt can be made for other systems as well, where unexpected

transitions could be dangerous. Understanding the mechanism of R-tipping can help devise control strategies. As of now, there exist no early warning signals for R-tipping. Developing early warning signals for R-tipping and a combination of rate and noise induced tipping will be of great practical relevance since such transitions are dangerous and observed very common.

APPENDIX A

Test for scaling during transitions from chaos to limit cycle via other types of intermittency

We discuss the results obtained from mathematical models that show the transition from chaos to periodic oscillations via different types of intermittency.

A.1 TYPE I INTERMITTENCY

To study the transition from chaos to periodic oscillations through type I intermittency, we consider the example of a three-dimensional Lorenz system Manneville and Pomeau (1979). The system is described as,

$$\begin{aligned}\dot{x} &= \sigma(y - x) \\ \dot{y} &= \rho x - y - xz \\ \dot{z} &= -\beta z + xy\end{aligned}\tag{A.1}$$

We choose $\sigma = 10$, $\beta = 83$ and ρ as the control parameter which is varied from 175 to 165 in steps of 0.05. In these range of values of the control parameter, the system shows a gradual transition from a chaotic state to a state with finite intervals of regular oscillations amidst intermittent bursts of irregular oscillations and finally to a periodic attractor. The oscillations in the state z are shown in Fig. A1. There is no particular scaling relation observed when we plot the amplitude corresponding to the dominant frequency versus Hurst exponent in a logarithmic scale (Fig. A2a).

We use another example of a generalized Lorenz model Macek and Strumik (2014) to

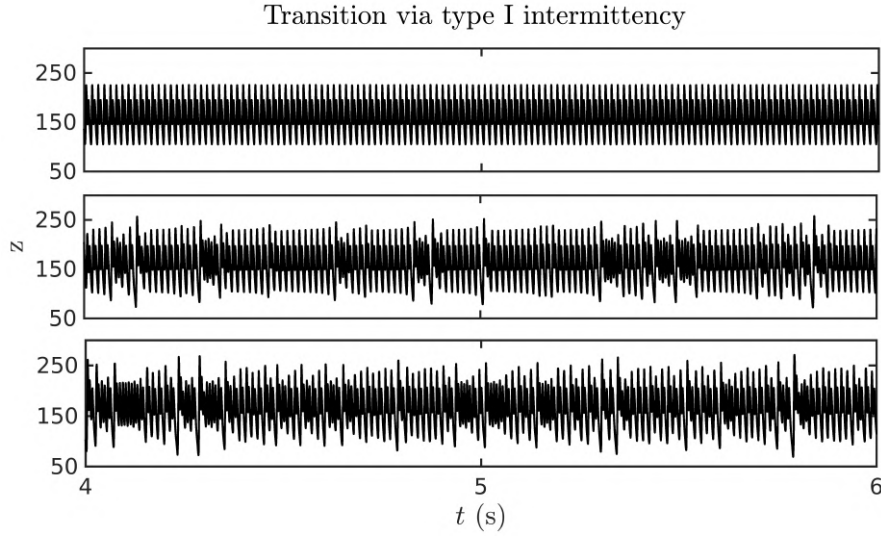


Fig. A1: The oscillations in the state z for selected values of ρ of the Lorenz system. The top figure corresponds to the state of periodic oscillations at $\rho = 165$. We observe type I intermittency (middle figure) around $\rho = 166.5$. The fully chaotic state ($\rho = 172$) is shown in the bottom figure.

confirm the results for type I intermittency.

$$\begin{aligned}
 \dot{X} &= \sigma(Y - X) - \omega_0 W \\
 \dot{Y} &= rX - Y - XZ \\
 \dot{Z} &= -bZ + XY \\
 \dot{W} &= \omega_0 - \sigma_m W
 \end{aligned} \tag{A.2}$$

This model shows Type I intermittency Macek and Strumik (2014) for the following set of parameters: $r = 256$, $\sigma = 10$, $\sigma_m = 1$, $b = 8/3$. Here ω_0 is the control parameter and is varied between 3.65 and 3.85 in steps of 0.005. The variation of amplitude with Hurst exponent is plotted in Fig. A2b. No particular scaling behaviour is observed during the transition in both Fig. A2a & b.

A.2 TYPE II INTERMITTENCY

The model used to obtain the transition from chaos to limit cycle with type II intermittency is a periodically driven third-order nonlinear oscillator Richetti *et al.*

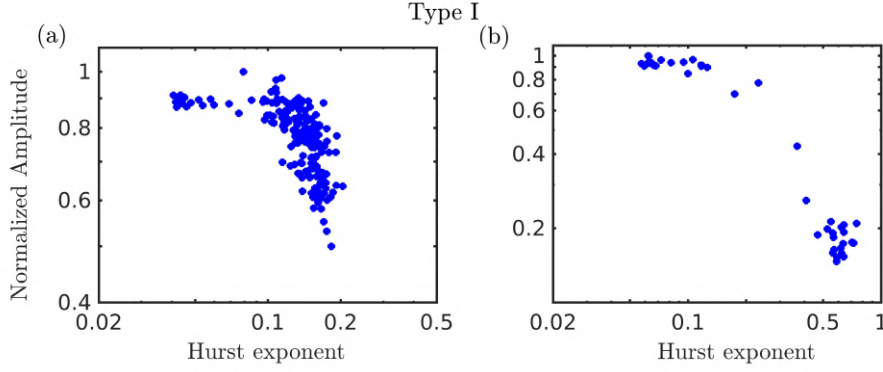


Fig. A2: Variation of the amplitude of the dominant mode with Hurst exponent is plotted in a logarithmic scale for the data generated from models showing type I intermittency. (a), (b) correspond the three dimensional Lorenz model and the generalized Lorenz model respectively. There is no particular scaling observed during the transition in both a & b.

(1986). The following ODE describes the system.

$$\ddot{x} + \eta\dot{x} + \nu x + \mu x + k_1 x^2 + k_2 \dot{x}^2 + k_3 x \dot{x} + k_4 x \ddot{x} + k_5 x^2 \ddot{x} = F \cos(\omega t) \quad (\text{A.3})$$

Figure A3 represents the results after solving the equation (Eq. A.3) for the parameter values $F = 0.5$, $\omega = 15$, $\eta = 1$, $\nu = 1.2$, $k_1 = -100$, $k_2 = 120$, $k_3 = 0$, $k_4 = -20$ and $k_5 = 100$. Richetti *et al.* Richetti *et al.* (1986) reported this model results showing type II intermittency. They stated that there have been no examples identifying type-II intermittency in either real experiments or in simulation studies. Later, an experimental observation of type II intermittency in a coupled nonlinear oscillator has been reported Huang and Kim (1987). So, we show only one example for this case.

The parameter is varied to observe the transition from a periodic signal ($\mu = 1.1$) to chaos ($\mu = 1.22$). Further, we observe type II intermittency ($\mu = 1.16$). The amplitude of the dominant mode is plotted with Hurst exponent and shown in Fig. A4. No particular scaling behaviour is observed during the transition via Type II intermittency.

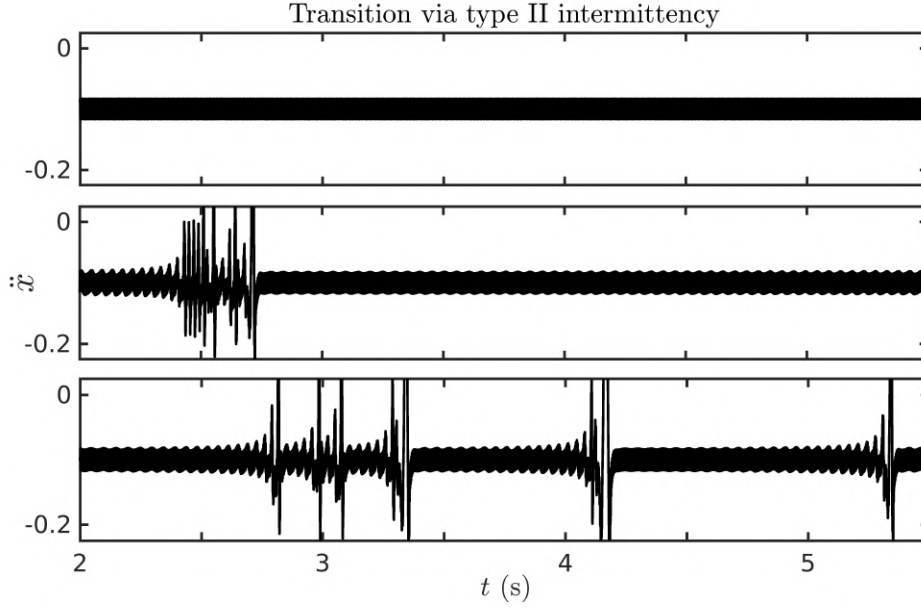


Fig. A3: Time series obtained from a model that shows type II intermittency. The top figure represents periodic oscillations corresponds to $\mu = 1.1$. We observe intermittent transitions to chaos at $\mu = 1.16$ and to a fully chaotic state around $\mu = 1.22$.

A.3 TYPE III INTERMITTENCY

We study the transition from periodic to chaos through type III intermittency, following the work done by Malasoma *et al.* Malasoma *et al.* (1994), considering the parametrically excited nonlinear system.

$$\ddot{x}(t) + c\dot{x}(t) + (\omega_0^2 + f\cos(\omega t))x(t) + ax^2(t) + bx^3(t) = 0 \quad (\text{A.4})$$

where, c is the damping coefficient, a and b are quadratic and cubic nonlinearity coefficients, and ω_0 is the natural frequency of the system. Here, f and ω are the amplitude and the frequency of the sinusoidal parametric excitation. The system is solved for the parameters $c = 0.2$, $\omega_0 = 1$, $a = 1.5$, $b = 0.5$ and $F = 0.85$. We observe periodic oscillations, intermittency and chaos (Fig. A5) at 1.6886, 1.7086 and 1.1682 values of ω respectively.

Type III intermittency can also be seen in the generalized Lorenz model Macek and

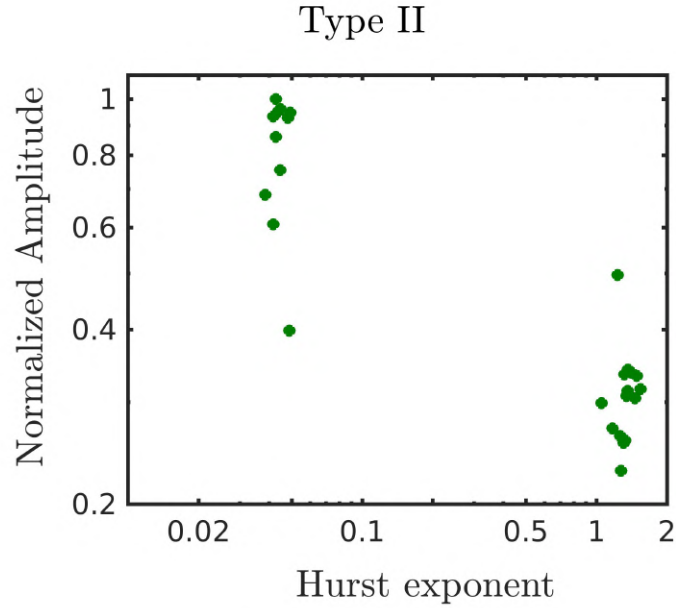


Fig. A4: Variation of the amplitude of the dominant mode with Hurst exponent is plotted in a logarithmic scale for the data generated from model showing type II intermittency. There is no particular scaling observed during the transition.

Strumik (2014) which is described earlier in the case of type I intermittency. The same model for the following set of values show type III intermittency: $r = 28$, $\sigma = 10$, $\sigma_m = 1$, $b = 8/3$. Here ω_0 is the control parameter and is varied between 2.8 and 5.8 in steps of 0.1. Figure A6 shows the corresponding variation of the amplitude with Hurst exponent for the two models with type III intermittency. We observe that there is no particular scaling relation.

In summary, the models discussed here which exhibit transition from chaos to limit cycle through type I, II & III intermittencies do not seem to follow the scaling behavior observed in the experiments reported in this paper. We note that in general, turbulence may not fit into universality classes.

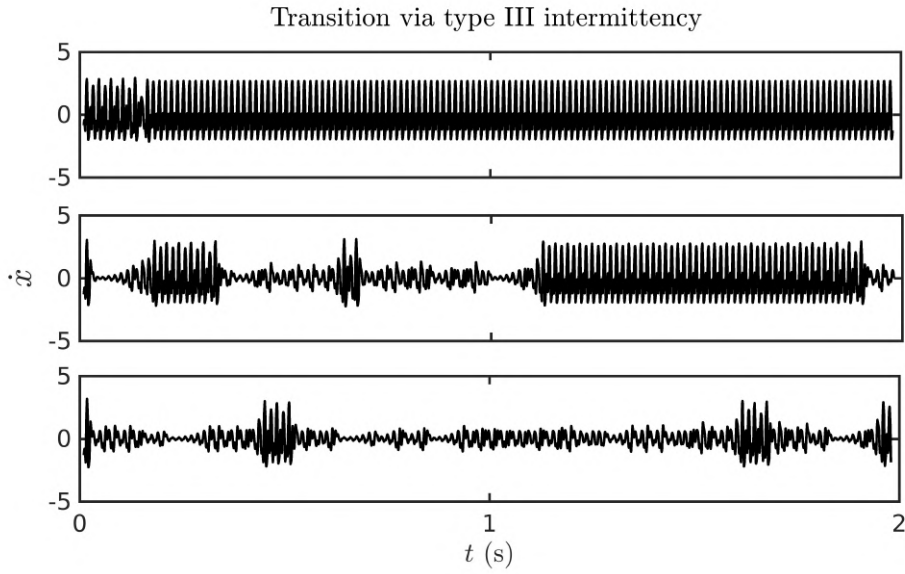


Fig. A5: Time series obtained from a model of a parametrically excited nonlinear system that shows type III intermittency. The figure represents periodic oscillations (top figure) intermittency (middle figure) and a fully chaotic state (bottom figure). We observe a bifurcation happening from periodic oscillations to chaos through type III intermittency.

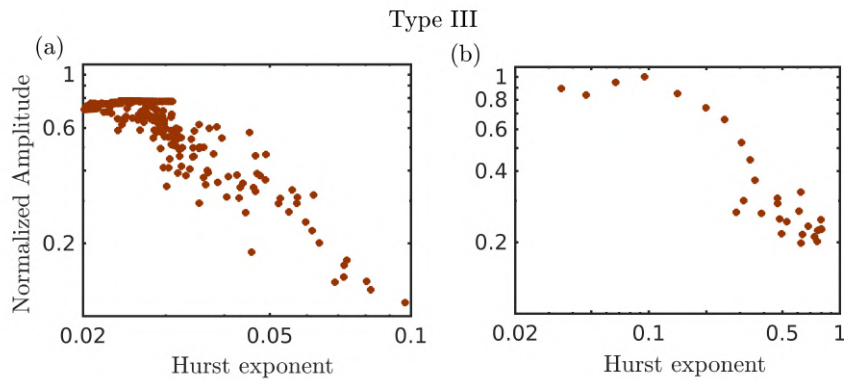


Fig. A6: Variation of the amplitude of the dominant mode with Hurst exponent is plotted in a logarithmic scale for the data generated from models showing type III intermittency. (a) plot of A vs. H for a parametrically excited nonlinear system. (b) plot of A vs. H for generalized Lorenz model with particular values of the parameter. There is no power law scaling observed during the transition in both the cases.

APPENDIX B

Selection of threshold for Hurst exponent and spectral measures

B.1 LOWER LIMIT FOR THE MEASURES

By definition, both H and the spectral measure $[\mu_2\mu_0]$ reduce towards zero as we approach TAI. However, H and $[\mu_2\mu_0]$ will never attain the value of zero because of the discrete representation of the analog signal. To estimate the lower limit of H and $[\mu_2\mu_0]$ in practical scenarios, we construct a unit amplitude sinusoidal signal with the same frequency as the natural frequency of the system and with the same sampling frequency as that of the experimental data. Such a constant amplitude sine wave is representative of the maximally “clean” periodic dynamics possible during thermoacoustic instability. The H and spectral measure for this sinusoidal signal are considered as limit A in Fig. 5.7. Thus, the estimated amplitude corresponding to limit A is the maximum possible amplitude for a given system configuration.

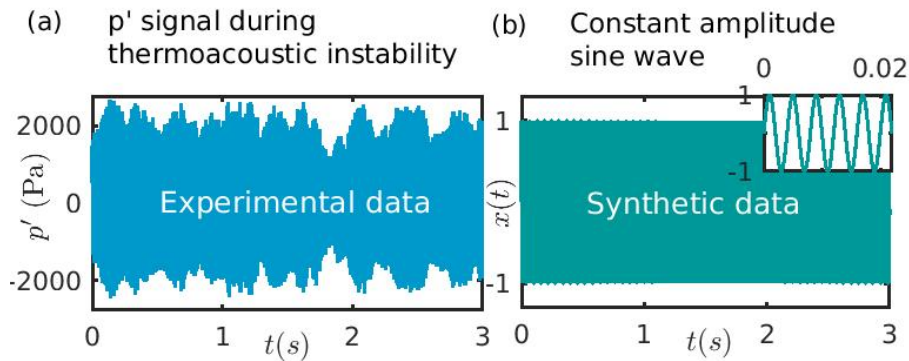


Fig. B.1: (a) A typical time series representing pressure fluctuations acquired from experiments during TAI and (b) a synthetic sine wave signal. The zoomed view shows the periodic nature of the signal.

Figure B.1(a)-(b) shows the time series of pressure fluctuations acquired from the experiments during TAI and a synthetic sine wave signal with the same frequency, respectively. In contrast to the regularity in a clean sinusoidal signal, experimental data of pressure fluctuations during TAI have inter-cycle variability in the amplitude. The

values of H and $[\mu_2\mu_0]$ for a clean sine wave will be close to zero, and the estimated amplitude will be higher than practically attainable amplitudes in highly turbulent systems exhibiting smooth transition via intermittency.

B.2 UPPER LIMIT FOR THE MEASURES

To avoid such an over-estimation of amplitude using limit A, we construct a sine wave with amplitude modulations to define limit B. We do not add any noise to get the envelope fluctuations; rather we use characteristics of time series data during stable operation. We extract the envelope (E) of the pressure fluctuations during CN using the Hilbert transform. Then, we construct a unit amplitude sine wave ($\sin \omega t$) and multiply it with $(1 + E_{normalized})$ as follows, $x(t) = (1 + E_{normalized})\sin \omega t$. Here, $E_{normalized} = (E \sim mean(E))/max(E)$.

Figure B.2(a) shows three representative time series (I, II & III) acquired from the experiments (before the onset of TAI). The extracted envelope (E) is shown with a violet color. These envelopes are normalized as mentioned before and used to modify the sine waves. The time series in each row I, II, & III of Fig. B.2(b) corresponds to the sine waves multiplied with the extracted envelopes from Fig. B.2(a). The zoomed plot (Fig. B.2(c)) shows that the signal is sinusoidal with amplitude modulations.

In Fig. B.2(a), the time series I & II represents CN, and III corresponds to INT. From Fig. B.2(b)I-III, we observe that the signal's envelope becomes less noisy (see the black curves indicating the envelopes of the sine waves). The signal in III b resembles the experimental data more than I b. The values of H and $[\mu_2\mu_0]$ for the sine waves with the envelope extracted from the three representative time series I, II & III are shown in Fig. B.2(d). As expected, the values of H and $[\mu_2\mu_0]$ for the sine wave with the envelope of INT (Fig. B.2(b)-III) are slightly lower than that of the case with combustion noise. Using the signal with the lower H and $[\mu_2\mu_0]$ shifts the limit B towards limit A (i.e., the difference between the two limits is reduced). Hence, we can narrow the range of estimated amplitudes (between A and B) by using the data for intermittency instead of

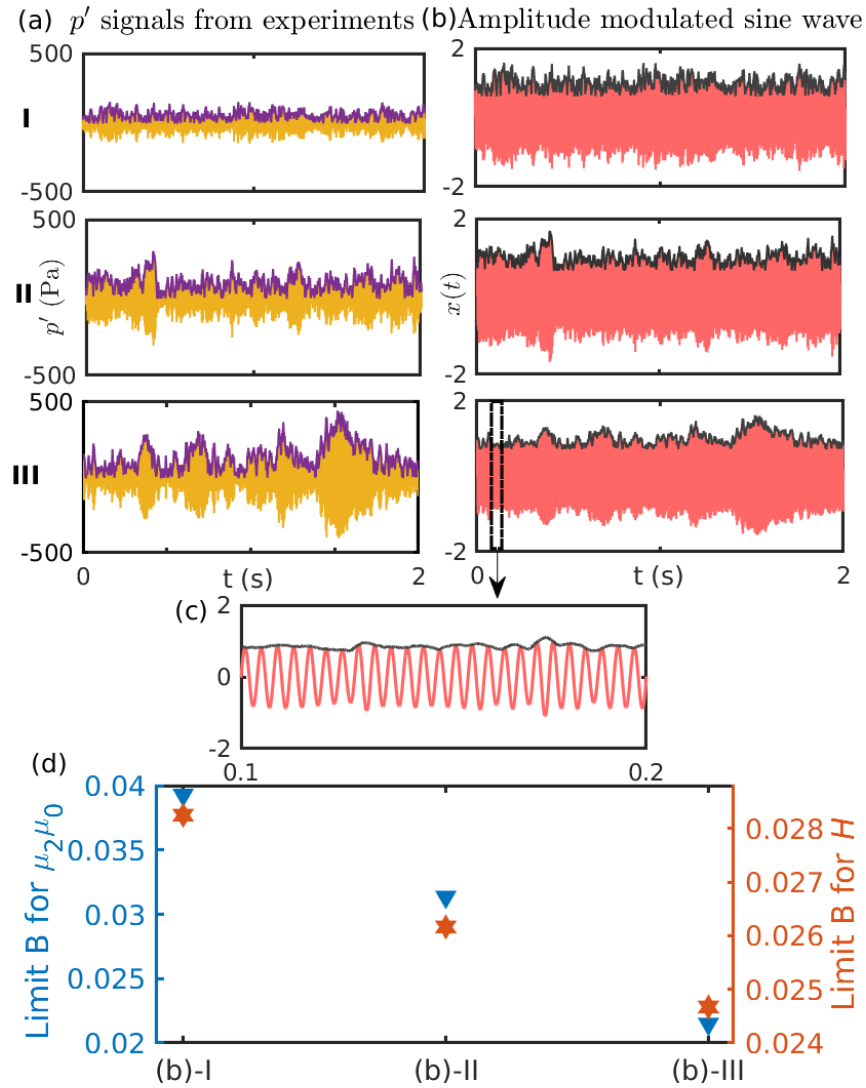


Fig. B.2: (a) Time series showing acoustic pressure signals during the states of stable operation. Three representative signals I, II & III are shown along with the extracted amplitude envelope. (b) Amplitude modulated sinusoidal signals with the envelope of experimental data shown in (a). The time series I - III are acquired during the transition towards TAI; I & II represent CN, and III corresponds to INT. From I - III (b), we observe that the envelope of the signal becomes less noisy. The zoomed plot (c) shows that the signal is sinusoidal with slight amplitude variations. The limit B evaluated for H and $[\mu_2 \mu_0]$ for the signals in (b) are shown in (d).

combustion noise to extract the amplitude envelope.

APPENDIX C

Robustness of EWS with the threshold and test for false warnings

C.1 ROBUSTNESS OF EWS WITH THE THRESHOLD

We observe that the inverse power law scaling between the warning time and rate of change of parameter is consistent with almost the same exponents for different values of thresholds of EWS as shown in Fig. C.1.

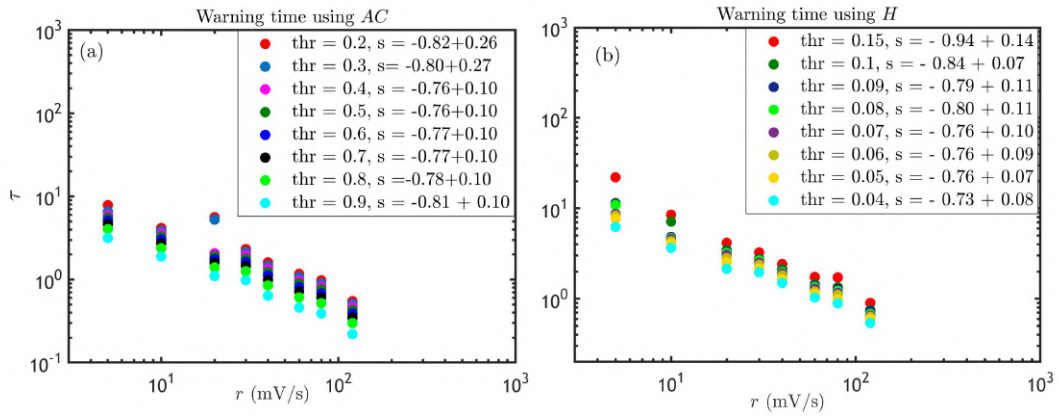


Fig. C.1: The inverse power law scaling between the warning time and rate of change of parameter is plotted for different values of thresholds for (a) AC and (b) H .

C.2 ANALYSIS TO CHECK FALSE WARNINGS

To check for false warnings, we calculate EWS for data for cases where transition to thermoacoustic instability does not occur. Here, we have the time series data acquired for constant values of voltage (quasi-static experiments). Figure C.2 shows one such data and the corresponding variation of all the EWS. This is a representative case of data for voltage = 1.6 V and heater power = 253.7 W, and we have confirmed these observations by analysing many data sets which are taken for quasi-static experiments. We wait at a particular value of control parameter far below the Hopf point, and there is no transition to limit cycle oscillations as expected. All the EWS calculated for a moving window show constant values indicative of a low amplitude aperiodic state, for

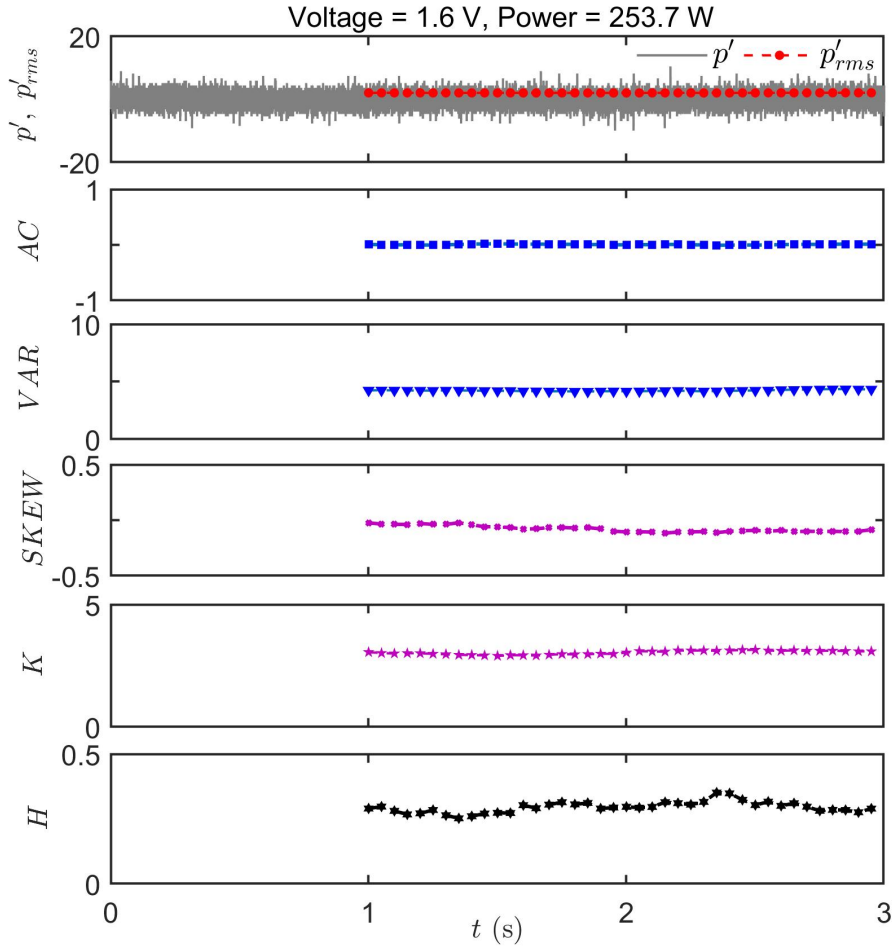


Fig. C.2: Acoustic pressure fluctuations (p') acquired for a constant value of control parameter (voltage = 1.6 V and heater power = 253.7 W), lower than the Hopf point. The time series contains only low amplitude aperiodic fluctuations, and there is no transition to limit cycle oscillations. The *rms* of pressure fluctuations is plotted along with the signal in the top plot. The corresponding variation of all the EWS is shown as subplots. We calculate the EWS for a moving window of 1 s with an overlap of 0.98 s. p'_{rms} , AC, VAR, SKEW, K and H stay nearly constant for the total duration of the experiment, and we do not observe any significant change in the values of EWS.

the entire length of the data. Hence, we do not observe any false warnings for these EWS.

REFERENCES

1. **Alvarez-Ramirez, J., J. Alvarez, E. Rodriguez, and G. Fernandez-Anaya** (2008). Time-varying Hurst exponent for us stock markets. *Physica A: Statistical Mechanics and its Applications*, **387**(24), 6159–6169.
2. **An, Q., A. M. Steinberg, S. Jella, G. Bourque, and M. Furi** (2019). Early warning signs of imminent thermoacoustic oscillations through critical slowing down. *Journal of Engineering for Gas Turbines and Power*, **141**(5).
3. **Ananthkrishnan, N., S. Deo, and F. E. Culick** (2005). Reduced-order modeling and dynamics of nonlinear acoustic waves in a combustion chamber. *Combustion Science and Technology*, **177**(2), 221–248.
4. **Ananthkrishnan, N., K. Sudhakar, S. Sudershan, and A. Agarwal** (1998). Application of secondary bifurcations to large-amplitude limit cycles in mechanical systems. *Journal of sound and Vibration*, **1**(215), 183–188.
5. **Angeli, D., J. E. Ferrell, and E. D. Sontag** (2004). Detection of multistability, bifurcations, and hysteresis in a large class of biological positive-feedback systems. *Proceedings of the National Academy of Sciences*, **101**(7), 1822–1827.
6. **Ashwin, P., C. Perryman, and S. Wieczorek** (2017). Parameter shifts for nonautonomous systems in low dimension: bifurcation-and rate-induced tipping. *Nonlinearity*, **30**(6), 2185.
7. **Ashwin, P., S. Wieczorek, R. Vitolo, and P. Cox** (2012). Tipping points in open systems: bifurcation, noise-induced and rate-dependent examples in the climate system. *Philosophical Transactions of the Royal Society A: Mathematical, Physical and Engineering Sciences*, **370**(1962), 1166–1184.
8. **Baer, S. M., T. Erneux, and J. Rinzel** (1989). The slow passage through a hopf bifurcation: delay, memory effects, and resonance. *SIAM Journal on Applied mathematics*, **49**(1), 55–71.
9. **Bak, P.** (1996). *How Nature Works: The Science of Self-Organized Criticality*. Copernicus, New York.
10. **Bak, P.** (2013). *How nature works: the science of self-organized criticality*. Springer Science & Business Media.
11. **Bak, P., C. Tang, and K. Wiesenfeld** (1987). Self-organized criticality: An explanation of the $1/f$ noise. *Physical review letters*, **59**(4), 381.
12. **Berglund, N.** (2000). Dynamic bifurcations: Hysteresis, scaling laws and feedback control. *Progress of Theoretical Physics Supplement*, **139**, 325–336.
13. **Bhattacharya, C., J. O'Connor, and A. Ray** (2020). Data-driven detection and early prediction of thermoacoustic instability in a multi-nozzle combustor. *Combustion Science and Technology*, 1–32. DOI:10.1080/00102202.2020.1820495.

14. **Bhattacharya, C.** and **A. Ray** (2020). Online discovery and classification of operational regimes from an ensemble of time series data. *Journal of Dynamic Systems, Measurement, and Control*, **142**(11).
15. **Bianconi, G.** and **A.-L. Barabási** (2001). Bose-Einstein condensation in complex networks. *Physical review letters*, **86**(24), 5632.
16. **Bilinsky, L. M.** and **S. M. Baer** (2018). Slow passage through a hopf bifurcation in excitable nerve cables: Spatial delays and spatial memory effects. *Bulletin of mathematical biology*, **80**(1), 130–150.
17. **Boettiger, C.** and **A. Hastings** (2012a). Early warning signals and the prosecutor’s fallacy. *Proceedings of the Royal Society B: Biological Sciences*, **279**(1748), 4734–4739.
18. **Boettiger, C.** and **A. Hastings** (2012b). Quantifying limits to detection of early warning for critical transitions. *Journal of the Royal Society Interface*, **9**(75), 2527–2539.
19. **Bonciolini, G., D. Ebi, E. Boujo,** and **N. Noiray** (2018). Experiments and modelling of rate-dependent transition delay in a stochastic subcritical bifurcation. *Royal Society open science*, **5**(3), 172078.
20. **Bonciolini, G., A. Faure-Beaulieu, C. Bourquard,** and **N. Noiray** (2021). Low order modelling of thermoacoustic instabilities and intermittency: Flame response delay and nonlinearity. *Combustion and Flame*, **226**, 396–411.
21. **Bonciolini, G.** and **N. Noiray** (2019). Bifurcation dodge: avoidance of a thermoacoustic instability under transient operation. *Nonlinear Dynamics*, **96**(1), 703–716.
22. **Bountis, T. C.** (1981). Period doubling bifurcations and universality in conservative systems. *Physica D: Nonlinear Phenomena*, **3**(3), 577–589.
23. **Braun, T., V. R. Unni, R. I. Sujith, J. Kurths,** and **N. Marwan** (2021). Detection of dynamical regime transitions with lacunarity as a multiscale recurrence quantification measure. *Nonlinear Dynamics*, 1–19.
24. **Bressloff, P. C.** (2010). Metastable states and quasicycles in a stochastic wilson-cowan model of neuronal population dynamics. *Physical Review E*, **82**(5), 051903.
25. **Bury, T. M., C. T. Bauch,** and **M. Anand** (2020). Detecting and distinguishing tipping points using spectral early warning signals. *Journal of the Royal Society Interface*, **17**(170), 20200482.
26. **Bury, T. M., R. I. Sujith, I. Pavithran, M. Scheffer, T. M. Lenton, M. Anand,** and **C. T. Bauch** (2021). Deep learning for early warning signals of tipping points. *Proceedings of the National Academy of Sciences*, **118**(39).
27. **Cao, H.** (2003). Lasing in random media. *Waves in random media*, **13**(3), R1–R39.

28. **Carbone, A., G. Castelli, and H. Stanley** (2004). Analysis of clusters formed by the moving average of a long-range correlated time series. *Physical Review E*, **69**(2), 026105.
29. **Carpenter, S. R. and W. A. Brock** (2006). Rising variance: a leading indicator of ecological transition. *Ecology letters*, **9**(3), 311–318.
30. **Carpenter, S. R., J. J. Cole, M. L. Pace, R. Batt, W. Brock, T. Cline, J. Coloso, J. R. Hodgson, J. F. Kitchell, D. A. Seekell, et al.** (2011). Early warnings of regime shifts: a whole-ecosystem experiment. *Science*, **332**(6033), 1079–1082.
31. **Carpenter, S. R., D. Ludwig, and W. A. Brock** (1999). Management of eutrophication for lakes subject to potentially irreversible change. *Ecological applications*, **9**(3), 751–771.
32. **Chakraborty, S., S. Gupta, A. Ray, and A. Mukhopadhyay** (2008). Data-driven fault detection and estimation in thermal pulse combustors. *Proceedings of the Institution of Mechanical Engineers, Part G: Journal of Aerospace Engineering*, **222**(8), 1097–1108.
33. **Chattopadhyay, P., S. Mondal, C. Bhattacharya, A. Mukhopadhyay, and A. Ray** (2017). Dynamic data-driven design of lean premixed combustors for thermoacoustically stable operations. *Journal of Mechanical Design*, **139**(11).
34. **Chiocchini, S., T. Pagliaroli, R. Camussi, and E. Giacomazzi** (2018). Chaotic and linear statistics analysis in thermoacoustic instability detection. *Journal of Propulsion and Power*, **34**(1), 15–26.
35. **Chua, L. O., C. A. Desoer, and E. S. Kuh** (1987). *Linear and nonlinear circuits*.
36. **Clements, C. F., J. M. Drake, J. I. Griffiths, and A. Ozgul** (2015). Factors influencing the detectability of early warning signals of population collapse. *The American Naturalist*, **186**(1), 50–58.
37. **Conti, C., M. Leonetti, A. Fratolocchi, L. Angelani, and G. Ruocco** (2008). Condensation in disordered lasers: Theory, 3 d+ 1 simulations, and experiments. *Physical review letters*, **101**(14), 143901.
38. **Ćosić, B., J. P. Moeck, and C. O. Paschereit** (2013). Prediction of pressure amplitudes of self-excited thermoacoustic instabilities for a partially premixed swirl-flame. *In Turbo Expo: Power for Land, Sea, and Air*, volume 55102. American Society of Mechanical Engineers. DOI:10.1115/GT2013-94160.
39. **Costa, L. d. F., O. N. Oliveira Jr, G. Travieso, F. A. Rodrigues, P. R. Villas Boas, L. Antiquera, M. P. Viana, and L. E. Correa Rocha** (2011). Analyzing and modeling real-world phenomena with complex networks: a survey of applications. *Advances in Physics*, **60**(3), 329–412.
40. **Croquette, V.** (1989). Convective pattern dynamics at low prandtl number: Part 1. *Contemporary Physics*, **30**(2), 113–133.

41. **Cross, M. C.** and **P. C. Hohenberg** (1993). Pattern formation outside of equilibrium. *Reviews of modern physics*, **65**(3), 851.
42. **Culick, F.** and **P. Kuentzmann** (2006). *Unsteady motions in combustion chambers for propulsion systems*. Technical report, NATO Research and Technology Organization Neuilly-Sur-Seine (France).
43. **Dakos, V.** and **J. Bascompte** (2014). Critical slowing down as early warning for the onset of collapse in mutualistic communities. *Proceedings of the National Academy of Sciences*, **111**(49), 17546–17551.
44. **Dakos, V., M. Scheffer, E. H. van Nes, V. Brovkin, V. Petoukhov, and H. Held** (2008). Slowing down as an early warning signal for abrupt climate change. *Proceedings of the National Academy of Sciences*, **105**(38), 14308–14312.
45. **Dakos, V., E. H. Van Nes, P. D’Odorico, and M. Scheffer** (2012). Robustness of variance and autocorrelation as indicators of critical slowing down. *Ecology*, **93**(2), 264–271.
46. **Datta, S., A. Mukhopadhyay, and D. Sanyal** (2006). Use of temporal irreversibility of symbolic time series for early detection of extinction in thermal pulse combustors. *In ASME International Mechanical Engineering Congress and Exposition*, volume 47853.
47. **Davis, K. B., M.-O. Mewes, M. R. Andrews, N. J. van Druten, D. S. Durfee, D. Kurn, and W. Ketterle** (1995). Bose-Einstein condensation in a gas of sodium atoms. *Physical review letters*, **75**(22), 3969.
48. **Daw, C. S., C. E. A. Finney, and E. R. Tracy** (2003). A review of symbolic analysis of experimental data. *Review of Scientific instruments*, **74**(2), 915–930.
49. **Dhadphale, J. M., V. R. Unni, A. Saha, and R. I. Sujith** (2022). Neural ode to model and prognose thermoacoustic instability. *Chaos: An Interdisciplinary Journal of Nonlinear Science*, **32**(1), 013131.
50. **Ditlevsen, P. D.** and **S. J. Johnsen** (2010). Tipping points: early warning and wishful thinking. *Geophysical Research Letters*, **37**(19).
51. **Domen, S., H. Gotoda, T. Kuriyama, Y. Okuno, and S. Tachibana** (2015). Detection and prevention of blowout in a lean premixed gas-turbine model combustor using the concept of dynamical system theory. *Proc. Combust. Inst.*, **35**(3), 3245–3253.
52. **Domino, K.** (2011). The use of the Hurst exponent to predict changes in trends on the warsaw stock exchange. *Physica A: Statistical Mechanics and its Applications*, **390**(1), 98–109.
53. **Dutta, A. K., G. Ramachandran, and S. Chaudhuri** (2019). Investigating thermoacoustic instability mitigation dynamics with a kuramoto model for flamelet oscillators. *Physical Review E*, **99**(3), 032215.
54. **Dutta, P. S., Y. Sharma, and K. C. Abbott** (2018). Robustness of early warning signals for catastrophic and non-catastrophic transitions. *Oikos*, **127**(9), 1251–1263.

55. **Eckmann, J., S. O. Kamphorst, D. Ruelle, et al.** (1995). Recurrence plots of dynamical systems. *World Scientific Series on Nonlinear Science Series A*, **16**, 441–446.
56. **Eckmann, J.-P.** (1981). Roads to turbulence in dissipative dynamical systems. *Reviews of Modern Physics*, **53**(4), 643.
57. **Eisenman, I. and J. Wettlaufer** (2009). Nonlinear threshold behavior during the loss of arctic sea ice. *Proceedings of the National Academy of Sciences*, **106**(1), 28–32.
58. **Etikyala, S. and R. I. Sujith** (2017). Change of criticality in a prototypical thermoacoustic system. *Chaos: An Interdisciplinary Journal of Nonlinear Science*, **27**(2), 023106.
59. **Feigenbaum, M. J.** (1978). Quantitative universality for a class of nonlinear transformations. *Journal of statistical physics*, **19**(1), 25–52.
60. **Feigenbaum, M. J.** (1979). The universal metric properties of nonlinear transformations. *Journal of Statistical Physics*, **21**(6), 669–706.
61. **Feigenbaum, M. J.** (1983). Universal behavior in nonlinear systems. *Physica D: Nonlinear Phenomena*, **7**(1-3), 16–39.
62. **Feudel, U., A. N. Pisarchik, and K. Showalter** (2018). Multistability and tipping: From mathematics and physics to climate and brain—minireview and preface to the focus issue. *Chaos: An Interdisciplinary Journal of Nonlinear Science*, **28**(3), 033501.
63. **Fischer, B. and A. Bekker** (2013). Many-body photonics. *Optics and Photonics News*, **24**(9), 40–47.
64. **Fischer, B. and R. Weill** (2012). When does single-mode lasing become a condensation phenomenon? *Optics express*, **20**(24), 26704–26713.
65. **Fisher, S. C. and S. A. Rahman** (2009). *Remembering the giants: Apollo rocket propulsion development*. NASA Monographs in Aerospace History series.
66. **Flandro, G. A. and J. Majdalani** (2003). Aeroacoustic instability in rockets. *AIAA journal*, **41**(3), 485–497.
67. **Fleming, C.** (Feb 13, 1998). Turbine makers are caught in innovation trap. *Wall Street Journal*.
68. **Fujisaka, H. and M. Inoue** (1989). Correlation functions of temporal fluctuations. *Physical Review A*, **39**(9), 4778.
69. **George, N. B., V. R. Unni, M. Raghunathan, and R. Sujith** (2018a). Spatiotemporal dynamics during the transition to thermoacoustic instability: effect of varying turbulence intensities. *International Journal of Spray and Combustion Dynamics*, **10**(4), 337–350.

70. **George, N. B., V. R. Unni, M. Raghunathan, and R. I. Sujith** (2018b). Pattern formation during transition from combustion noise to thermoacoustic instability via intermittency. *Journal of Fluid Mechanics*, **849**, 615–644.
71. **Ghalyan, N. F., S. Mondal, D. J. Miller, and A. Ray** (2019). Hidden markov modeling-based decision-making using short-length sensor time series. *Journal of Dynamic Systems, Measurement, and Control*, **141**(10).
72. **Ghanavati, G., P. D. H. Hines, T. I. Lakoba, and E. Cotilla-Sanchez** (2014). Understanding early indicators of critical transitions in power systems from autocorrelation functions. *IEEE Transactions on Circuits and Systems I: Regular Papers*, **61**(9), 2747–2760.
73. **Ghoniem, A. F., S. Park, A. Wachsman, A. Annaswamy, D. Wee, and H. M. Altay** (2005). Mechanism of combustion dynamics in a backward-facing step stabilized premixed flame. *Proceedings of the Combustion Institute*, **30**(2), 1783–1790.
74. **Godavarthi, V., P. Kasthuri, S. Mondal, R. I. Sujith, N. Marwan, and J. Kurths** (2020). Synchronization transition from chaos to limit cycle oscillations when a locally coupled chaotic oscillator grid is coupled globally to another chaotic oscillator. *Chaos: An Interdisciplinary Journal of Nonlinear Science*, **30**(3), 033121.
75. **Godavarthi, V., S. A. Pawar, V. R. Unni, R. I. Sujith, N. Marwan, and J. Kurths** (2018). Coupled interaction between unsteady flame dynamics and acoustic field in a turbulent combustor. *Chaos*, **28**, 113111.
76. **Godavarthi, V., V. R. Unni, E. A. Gopalakrishnan, and R. I. Sujith** (2017). Recurrence networks to study dynamical transitions in a turbulent combustor. *Chaos*, **27**(6), 063113.
77. **Gopalakrishnan, E. A., Y. Sharma, T. John, P. S. Dutta, and R. I. Sujith** (2016a). Early warning signals for critical transitions in a thermoacoustic system. *Scientific reports*, **6**, 35310.
78. **Gopalakrishnan, E. A. and R. I. Sujith** (2014). Influence of system parameters on the hysteresis characteristics of a horizontal rijke tube. *International Journal of Spray and Combustion Dynamics*, **6**(3), 293–316.
79. **Gopalakrishnan, E. A. and R. I. Sujith** (2015). Effect of external noise on the hysteresis characteristics of a thermoacoustic system. *Journal of Fluid Mechanics*, **776**, 334–353.
80. **Gopalakrishnan, E. A., J. Tony, E. Sreelekha, and R. I. Sujith** (2016b). Stochastic bifurcations in a prototypical thermoacoustic system. *Physical Review E*, **94**(2), 022203.
81. **Gotoda, H., M. Amano, T. Miyano, T. Ikawa, K. Maki, and S. Tachibana** (2012). Characterization of complexities in combustion instability in a lean premixed gas-turbine model combustor. *Chaos: An Interdisciplinary Journal of Nonlinear Science*, **22**(4), 043128. DOI:10.1063/1.4766589.

82. **Gotoda, H., H. Kinugawa, R. Tsujimoto, S. Domen, and Y. Okuno** (2017). Characterization of combustion dynamics, detection, and prevention of an unstable combustion state based on a complex-network theory. *Physical Review Applied*, **7**(4), 044027.
83. **Gotoda, H., Y. Shinoda, M. Kobayashi, Y. Okuno, and S. Tachibana** (2014). Detection and control of combustion instability based on the concept of dynamical system theory. *Physical Review E*, **89**, 022910.
84. **Grech, D. and Z. Mazur** (2004). Can one make any crash prediction in finance using the local Hurst exponent idea? *Physica A: Statistical Mechanics and its Applications*, **336**(1-2), 133–145.
85. **Grech, D. and G. Pamuła** (2008). The local Hurst exponent of the financial time series in the vicinity of crashes on the polish stock exchange market. *Physica A: statistical mechanics and its applications*, **387**(16-17), 4299–4308.
86. **Guan, Y., V. Gupta, and L. K. Li** (2020). Intermittency route to self-excited chaotic thermoacoustic oscillations. *Journal of Fluid Mechanics*, **894**.
87. **Gummaluri, V. S., S. Krishnan, and C. Vijayan** (2018). Stokes mode Raman random lasing in a fully biocompatible medium. *Optics letters*, **43**(23), 5865–5868.
88. **Gupta, S., A. Ray, and A. Mukhopadhyay** (2006). Anomaly detection in thermal pulse combustors using symbolic time series analysis. *Proceedings of the Institution of Mechanical Engineers, Part I: Journal of Systems and Control Engineering*, **220**(5), 339–351.
89. **Güthe, F. and B. Schuermans** (2007). Phase-locking in post-processing for pulsating flames. *Measurement Science and Technology*, **18**(9), 3036.
90. **Guttal, V. and C. Jayaprakash** (2008). Changing skewness: an early warning signal of regime shifts in ecosystems. *Ecology letters*, **11**(5), 450–460.
91. **Guttal, V. and C. Jayaprakash** (2009). Spatial variance and spatial skewness: leading indicators of regime shifts in spatial ecological systems. *Theoretical Ecology*, **2**(1), 3–12.
92. **Hachijo, T., S. Masuda, T. Kurosaka, and H. Gotoda** (2019). Early detection of thermoacoustic combustion oscillations using a methodology combining statistical complexity and machine learning. *Chaos: An Interdisciplinary Journal of Nonlinear Science*, **29**(10), 103123.
93. **Haken, H.** (1984). *The Science of Structure : Synergetics*. Van Nostrand Reinhold, C1984.
94. **Halperin, B. and P. Hohenberg** (1969). Scaling laws for dynamic critical phenomena. *Physical Review*, **177**(2), 952.
95. **Halperin, B. I. and P. Hohenberg** (1967). Generalization of scaling laws to dynamical properties of a system near its critical point. *Physical Review Letters*, **19**(12), 700.

96. **Hansen, M. H.** (2007). Aeroelastic instability problems for wind turbines. *Wind Energy: An International Journal for Progress and Applications in Wind Power Conversion Technology*, **10**(6), 551–577.
97. **Hashimoto, T., H. Shibuya, H. Gotoda, Y. Ohmichi, and S. Matsuyama** (2019). Spatiotemporal dynamics and early detection of thermoacoustic combustion instability in a model rocket combustor. *Physical Review E*, **99**(3), 032208.
98. **Havlin, S., L. A. N. Amaral, Y. Ashkenazy, A. L. Goldberger, P. C. Ivanov, C.-K. Peng, and H. E. Stanley** (1999). Application of statistical physics to heartbeat diagnosis. *Physica A: Statistical Mechanics and its Applications*, **274**(1-2), 99–110.
99. **Heagy, J., N. Platt, and S. Hammel** (1994). Characterization of on-off intermittency. *Physical Review E*, **49**(2), 1140.
100. **Hu, K., P. C. Ivanov, M. F. Hilton, Z. Chen, R. T. Ayers, H. E. Stanley, and S. A. Shea** (2004). Endogenous circadian rhythm in an index of cardiac vulnerability independent of changes in behavior. *Proceedings of the National Academy of Sciences*, **101**(52), 18223–18227.
101. **Huang, J.-Y. and J.-J. Kim** (1987). Type-ii intermittency in a coupled nonlinear oscillator: Experimental observation. *Physical Review A*, **36**(3), 1495.
102. **Huberman, B. and J. Rudnick** (1980). Scaling behavior of chaotic flows. *Physical review letters*, **45**(3), 154.
103. **Huerta-Cuellar, G., A. N. Pisarchik, and Y. O. Barmenkov** (2008). Experimental characterization of hopping dynamics in a multistable fiber laser. *Physical Review E*, **78**(3), 035202.
104. **Hurst, H. E.** (1951). Long-term storage capacity of reservoirs. *Trans. Amer. Soc. Civil Eng.*, **116**, 770–799.
105. **Ihlen, E. A. F. E.** (2012). Introduction to multifractal detrended fluctuation analysis in matlab. *Frontiers in physiology*, **3**, 141.
106. **Ivanov, P. C., L. A. N. Amaral, A. L. Goldberger, S. Havlin, M. G. Rosenblum, Z. R. Struzik, and H. E. Stanley** (1999). Multifractality in human heartbeat dynamics. *Nature*, **399**(6735), 461.
107. **Ives, A. R.** (1995). Measuring resilience in stochastic systems. *Ecological Monographs*, **65**(2), 217–233.
108. **Jacob, R., K. Harikrishnan, R. Misra, and G. Ambika** (2016). Uniform framework for the recurrence-network analysis of chaotic time series. *Physical Review E*, **93**(1), 012202.
109. **Jahnke, C. C. and F. E. Culick** (1994). Application of dynamical systems theory to nonlinear combustion instabilities. *Journal of propulsion and power*, **10**(4), 508–517.

110. **Johnson, C. E., Y. Neumeier, T. C. Lieuwen, and B. T. Zinn** (2000). Experimental determination of the stability margin of a combustor using exhaust flow and fuel injection rate modulations. *Proceedings of the Combustion Institute*, **28**(1), 757–763. DOI:10.1016/S0082-0784(00)80278-7.
111. **Juniper, M. P.** (2011). Triggering in the horizontal rijke tube: non-normality, transient growth and bypass transition. *Journal of Fluid Mechanics*, **667**, 272–308.
112. **Juniper, M. P. and R. I. Sujith** (2018). Sensitivity and nonlinearity of thermoacoustic oscillations. *Annual Review of Fluid Mechanics*, **50**, 661–689.
113. **Kabiraj, L., A. Saurabh, P. Wahi, and R. I. Sujith** (2012). Route to chaos for combustion instability in ducted laminar premixed flames. *Chaos: An Interdisciplinary Journal of Nonlinear Science*, **22**(2), 023129.
114. **Kabiraj, L. and R. I. Sujith** (2012). Nonlinear self-excited thermoacoustic oscillations: intermittency and flame blowout. *Journal of Fluid Mechanics*, **713**, 376–397.
115. **Kadanoff, L. P.** (1966). Scaling laws for ising models near t c. *Physics Physique Fizika*, **2**(6), 263.
116. **Kadanoff, L. P.** (1990). Scaling and universality in statistical physics. *Physica A: Statistical Mechanics and its Applications*, **163**(1), 1–14.
117. **Kadanoff, L. P., W. Götze, D. Hamblen, R. Hecht, E. Lewis, V. V. Palciauskas, M. Rayl, J. Swift, D. Aspnes, and J. Kane** (1967). Static phenomena near critical points: theory and experiment. *Reviews of Modern Physics*, **39**(2), 395.
118. **Kantelhardt, J. W., S. A. Zschiegner, E. Koscielny-Bunde, S. Havlin, A. Bunde, and H. E. Stanley** (2002). Multifractal detrended fluctuation analysis of nonstationary time series. *Physica A: Statistical Mechanics and its Applications*, **316**(1-4), 87–114.
119. **Kapila, A. K.** (1981). Arrhenius systems: dynamics of jump due to slow passage through criticality. *SIAM Journal on Applied Mathematics*, **41**(1), 29–42.
120. **Kashinath, K., I. C. Waugh, and M. P. Juniper** (2014). Nonlinear self-excited thermoacoustic oscillations of a ducted premixed flame: bifurcations and routes to chaos. *J FLUID MECH*, **761**, 399–430.
121. **Kasthuri, P., I. Pavithran, S. A. Pawar, R. I. Sujith, R. Gejji, and W. E. Anderson** (2019). Dynamical systems approach to study thermoacoustic transitions in a liquid rocket combustor. *Chaos*, **29**, 103115.
122. **Kelso, J. S.** (1995). *Dynamic patterns: The self-organization of brain and behavior*. MIT press.
123. **Kennedy, M. P.** (1992). Robust op amp realization of Chua’s circuit. *Frequenz.*, **46**(3), 66–80.
124. **Kerres, B., V. Nair, A. Cronhjort, and M. Mihaescu** (2016). Analysis of the turbocharger compressor surge margin using a hurst-exponent-based criterion. *SAE International Journal of Engines*, **9**(3), 1795–1806.

125. **Ketterle, W.** (1999). Experimental studies of Bose-Einstein condensation. *Phys. Today*, **52**(12), 30–35.
126. **Kilcik, A., C. N. K. Anderson, J. P. Rozelot, H. Ye, G. Sugihara, and A. Ozguc** (2009). Nonlinear prediction of solar cycle 24. *The Astrophysical Journal*, **693**(2), 1173.
127. **Klaers, J., J. Schmitt, F. Vewinger, and M. Weitz** (2010). Bose-Einstein condensation of photons in an optical microcavity. *Nature*, **468**(7323), 545–548.
128. **Kobayashi, T., S. Murayama, T. Hachijo, and H. Gotoda** (2019). Early detection of thermoacoustic combustion instability using a methodology combining complex networks and machine learning. *Physical Review Applied*, **11**(6), 064034.
129. **Kraemer, K. H., R. V. Donner, J. Heitzig, and N. Marwan** (2018). Recurrence threshold selection for obtaining robust recurrence characteristics in different embedding dimensions. *Chaos: An Interdisciplinary Journal of Nonlinear Science*, **28**(8), 085720.
130. **Kraichnan, R. H.** (1967). Inertial ranges in two-dimensional turbulence. *The Physics of Fluids*, **10**(7), 1417–1423.
131. **Krediet, H., W. Krebs, J. E. Portillo, and J. Kok** (2010). Prediction of thermoacoustic limit cycles during premixed combustion using the modified galerkin approach. In *46th AIAA/ASME/SAE/ASEE Joint Propulsion Conference & Exhibit*. DOI:10.2514/6.2010-7150.
132. **Kriesels, P. C., M. Peters, A. Hirschberg, A. Wijnands, A. Iafrati, G. Riccardi, R. Piva, and J. C. Bruggeman** (1995). High amplitude vortex-induced pulsations in a gas transport system. *Journal of Sound and Vibration*, **184**(2), 343–368.
133. **Krishnan, A., R. Manikandan, P. Midhun, K. Reeja, V. Unni, R. I. Sujith, N. Marwan, and J. Kurths** (2019). Mitigation of oscillatory instability in turbulent reactive flows: A novel approach using complex networks. *EPL (Europhysics Letters)*, **128**(1), 14003.
134. **Krishnan, A., R. I. Sujith, N. Marwan, and J. Kurths** (2021). Suppression of thermoacoustic instability by targeting the hubs of the turbulent networks in a bluff body stabilized combustor. *Journal of Fluid Mechanics*, **916**.
135. **Kuznetsov, Y. A., I. A. Kuznetsov, and Y. Kuznetsov** (1998). *Elements of applied bifurcation theory*, volume 112. Springer.
136. **Lakshmanan, M. and K. Murali** (1996). *Chaos in nonlinear oscillators: controlling and synchronization*, volume 13. World scientific.
137. **Lakshmanan, M. and S. Rajaseekar** (2012). *Nonlinear dynamics: integrability, chaos and patterns*. Springer Science & Business Media.

138. **Larsen, A.** and **J. H. Walther** (1997). Aeroelastic analysis of bridge girder sections based on discrete vortex simulations. *Journal of Wind Engineering and Industrial Aerodynamics*, **67**, 253–265.
139. **Lee, J.** and **D. Santavicca** (2003). Experimental diagnostics for the study of combustion instabilities in lean premixed combustors. *Journal of Propulsion and Power*, **19**(5), 735–750.
140. **Lee, M., K. T. Kim, V. Gupta,** and **L. K. B. Li** (2020). System identification and early warning detection of thermoacoustic oscillations in a turbulent combustor using its noise-induced dynamics. *Proceedings of the Combustion Institute*.
141. **Lei, S.** and **A. Turan** (2009). Nonlinear/chaotic behaviour in thermo-acoustic instability. *Combustion Theory and Modelling*, **13**(3), 541–557.
142. **Lenton, T. M., H. Held, E. Kriegler, J. W. Hall, W. Lucht, S. Rahmstorf,** and **H. J. Schellnhuber** (2008). Tipping elements in the earth’s climate system. *Proceedings of the national Academy of Sciences*, **105**(6), 1786–1793.
143. **Lenton, T. M., V. N. Livina, V. Dakos, E. H. van Nes,** and **M. Scheffer** (2012). Early warning of climate tipping points from critical slowing down: comparing methods to improve robustness. *Philosophical Transactions of the Royal Society A: Mathematical, Physical and Engineering Sciences*, **370**(1962), 1185–1204.
144. **Lenton, T. M., R. J. Myerscough, R. Marsh, V. N. Livina, A. R. Price, S. J. Cox,** and **GENIE-team** (2009). Using GENIE to study a tipping point in the climate system. *Philosophical Transactions of the Royal Society A: Mathematical, Physical and Engineering Sciences*, **367**(1890), 871–884.
145. **Lenton, T. M., J. Rockström, O. Gaffney, S. Rahmstorf, K. Richardson, W. Steffen,** and **H. J. Schellnhuber** (2019). Climate tipping points—too risky to bet against.
146. **Lieuwen, T.** (2005). Online combustor stability margin assessment using dynamic pressure data. *J. Eng. Gas Turbines Power*, **127**(3), 478–482. DOI:10.1115/1.1850493.
147. **Lieuwen, T. C.** (2002). Experimental investigation of limit-cycle oscillations in an unstable gas turbine combustor. *Journal of Propulsion and Power*, **18**(1), 61–67.
148. **Lieuwen, T. C.** (2003). Statistical characteristics of pressure oscillations in a premixed combustor. *Journal of Sound and Vibration*, **260**(1), 3–17.
149. **Lieuwen, T. C.** and **V. Yang** (2005). *Combustion instabilities in gas turbine engines: operational experience, fundamental mechanisms, and modeling*. American Institute of Aeronautics and Astronautics.
150. **Litt, B., R. Esteller, J. Echauz, M. D’Alessandro, R. Shor, T. Henry, P. Pennell, C. Epstein, R. Bakay, M. Dichter,** *et al.* (2001). Epileptic seizures may begin hours in advance of clinical onset: a report of five patients. *Neuron*, **30**(1), 51–64.

151. **Livina, V., P. Ditlevsen, and T. Lenton** (2012). An independent test of methods of detecting system states and bifurcations in time-series data. *Physica A: Statistical Mechanics and its Applications*, **391**(3), 485–496.
152. **Lovejoy, T. E. and C. Nobre** (2019). Amazon tipping point: Last chance for action.
153. **Lucarini, V. and T. Bódai** (2017). Edge states in the climate system: exploring global instabilities and critical transitions. *Nonlinearity*, **30**(7), R32.
154. **Luke, C. and P. Cox** (2011). Soil carbon and climate change: from the jenkinson effect to the compost-bomb instability. *European Journal of Soil Science*, **62**(1), 5–12.
155. **Macek, W. M. and M. Strumik** (2014). Hyperchaotic intermittent convection in a magnetized viscous fluid. *Physical review letters*, **112**(7), 074502.
156. **Majumdar, A., J. Ockendon, P. Howell, and E. Surovyatkina** (2013). Transitions through critical temperatures in nematic liquid crystals. *Physical Review E*, **88**(2), 022501.
157. **Malasoma, J.-M., C.-H. Lamarque, and L. Jezequel** (1994). Chaotic behavior of a parametrically excited nonlinear mechanical system. *Nonlinear Dynamics*, **5**(2), 153–160.
158. **Mandelbrot, B. B.** (1982). *The fractal geometry of nature*, volume 1. WH freeman New York.
159. **Mandelbrot, B. B.** (1983). *The fractal geometry of nature*, volume 173. WH freeman New York.
160. **Mandelbrot, B. B. and J. R. Wallis** (1969). Robustness of the rescaled range r/s in the measurement of noncyclic long run statistical dependence. *Water Resources Research*, **5**(5), 967–988.
161. **Manikandan, S. and R. I. Sujith** (2020). Rate dependent transition to thermoacoustic instability via intermittency in a turbulent afterburner. *Experimental Thermal and Fluid Science*, **114**, 110046.
162. **Manneville, P. and Y. Pomeau** (1979). Intermittency and the lorenz model. *Physics Letters A*, **75**(1-2), 1–2.
163. **Marwan, N., M. C. Romano, M. Thiel, and J. Kurths** (2007). Recurrence plots for the analysis of complex systems. *PHYS REP*, **438**, 237–329.
164. **Matos, J. A., S. M. Gama, H. J. Ruskin, A. Al Sharkasi, and M. Crane** (2008). Time and scale Hurst exponent analysis for financial markets. *Physica A: Statistical Mechanics and its Applications*, **387**(15), 3910–3915.
165. **Matveev, K. I.** (2003). *Thermoacoustic instabilities in the Rijke tube: experiments and modeling*. Doctoral thesis, California Institute of Technology.
166. **May, R. M.** (1977). Thresholds and breakpoints in ecosystems with a multiplicity of stable states. *Nature*, **269**(5628), 471–477.

167. **May, R. M., S. A. Levin, and G. Sugihara** (2008). Ecology for bankers. *Nature*, **451**(7181), 893–894.
168. **McManus, K., T. Poinso, and S. M. Candel** (1993). A review of active control of combustion instabilities. *Progress in energy and combustion science*, **19**(1), 1–29.
169. **Mondal, S., A. Chattopadhyay, A. Mukhopadhyay, and A. Ray** (2021). Transfer learning of deep neural networks for predicting thermoacoustic instabilities in combustion systems. *Energy and AI*, 100085.
170. **Mondal, S., S. De, A. Mukhopadhyay, S. Sen, and A. Ray** (2020). Early prediction of lean blowout from chemiluminescence time series data. *Combustion Science and Technology*, 1–28.
171. **Mondal, S., N. F. Ghalyan, A. Ray, and A. Mukhopadhyay** (2018). Early detection of thermoacoustic instabilities using hidden markov models. *Combustion Science and Technology*.
172. **Mondal, S., V. R. Unni, and R. I. Sujith** (2017). Onset of thermoacoustic instability in turbulent combustors: an emergence of synchronized periodicity through formation of chimera-like states. *J FLUID MECH*, **811**, 659–681.
173. **Mukherjee, N., M. Heckl, A. Bigongiari, R. Vishnu, S. A. Pawar, and R. I. Sujith** (2015). Nonlinear dynamics of a laminar V flame in a combustor. *In Proceedings of the 22nd International Congress on Sound and Vibration*.
174. **Mukhopadhyay, A., R. R. Chaudhari, T. Paul, S. Sen, and A. Ray** (2013). Lean blow-out prediction in gas turbine combustors using symbolic time series analysis. *Journal of Propulsion and Power*, **29**(4), 950–960.
175. **Murugesan, M. and R. I. Sujith** (2015). Combustion noise is scale-free: transition from scale-free to order at the onset of thermoacoustic instability. *Journal of Fluid Mechanics*, **772**, 225–245.
176. **Murugesan, M. and R. I. Sujith** (2016). Detecting the onset of an impending thermoacoustic instability using complex networks. *Journal of Propulsion and Power*, **32**(1), 707–712.
177. **Murugesan, M., R. U. Vishnu, V. N. VINOD, and S. R. P. I. Nair** (2019). Devices and methods for early prediction of impending instabilities of a system. US Patent 10,337,414.
178. **Nair, V. and R. I. Sujith** (2014). Multifractality in combustion noise: predicting an impending combustion instability. *J FLUID MECH*, **747**, 635–655.
179. **Nair, V. and R. I. Sujith** (2015). A reduced-order model for the onset of combustion instability: physical mechanisms for intermittency and precursors. *Proceedings of the Combustion Institute*, **35**(3), 3193–3200.
180. **Nair, V. and R. I. Sujith** (2016). Precursors to self-sustained oscillations in aeroacoustic systems. *International Journal of Aeroacoustics*, **15**(3), 312–323.

181. **Nair, V., G. Thampi, S. Karuppusamy, S. Gopalan, and S. R. P. I. Nair** (2017). System and method for predetermining the onset of impending oscillatory instabilities in practical devices. US Patent 9,804,054.
182. **Nair, V., G. Thampi, S. Karuppusamy, S. Gopalan, and R. I. Sujith** (2013). Loss of chaos in combustion noise as a precursor of impending combustion instability. *International journal of spray and combustion dynamics*, **5**(4), 273–290.
183. **Nair, V., G. Thampi, and R. Sujith** (2014a). Intermittency route to thermoacoustic instability in turbulent combustors. *Journal of Fluid Mechanics*, **756**, 470–487, doi:10.1017/jfm.2014.468. DOI: 10.1017/jfm.2014.468.
184. **Nair, V., G. Thampi, and R. I. Sujith** (2014b). Engineering precursors to forewarn the onset of an impending combustion instability. *In Turbo Expo: Power for Land, Sea, and Air*, volume 45691. American Society of Mechanical Engineers. DOI:10.1115/GT2014-26020.
185. **Nair, V., G. Thampi, and R. I. Sujith** (2014c). Intermittency route to thermoacoustic instability in turbulent combustors. *J FLUID MECH*, **756**, 470–487.
186. **National-Research-Councils and other** (2007). *New directions for understanding systemic risk: a report on a conference cosponsored by the Federal Reserve Bank of New York and the National Academy of Sciences*. National Academies Press.
187. **Nayfeh, A. H. and B. Balachandran** (2008a). *Applied nonlinear dynamics: analytical, computational, and experimental methods*. John Wiley & Sons.
188. **Nayfeh, A. H. and B. Balachandran** (2008b). *Applied nonlinear dynamics*,(1995). WileyInterscience, New York.
189. **Noiray, N.** (2017). Linear growth rate estimation from dynamics and statistics of acoustic signal envelope in turbulent combustors. *Journal of Engineering for Gas Turbines and Power*, **139**(4), 041503.
190. **Noiray, N. and B. Schuermans** (2013). Deterministic quantities characterizing noise driven hopf bifurcations in gas turbine combustors. *International Journal of Non-Linear Mechanics*, **50**, 152–163.
191. **Ortiz, D., J. Palmer, and G. Wilkinson** (2020). Detecting changes in statistical indicators of resilience prior to algal blooms in shallow eutrophic lakes. *Ecosphere*, **11**(10), e03200.
192. **Panter, P. F.** (1965). *Modulation, noise and spectral analysis: applied to information transmission*.
193. **Park, Y., Y. Do, and J. M. Lopez** (2011). Slow passage through resonance. *Physical Review E*, **84**(5), 056604.
194. **Pavithran, I. and R. I. Sujith** (2021). Effect of rate of change of parameter on early warning signals for critical transitions. *Chaos: An Interdisciplinary Journal of Nonlinear Science*, **31**(1), 013116.

195. **Pavithran, I., V. R. Unni, A. Saha, A. J. Varghese, R. I. Sujith, N. Marwan, and J. Kurths** (2021a). Predicting the amplitude of thermoacoustic instability using universal scaling behavior. *Journal of Engineering for Gas Turbines and Power*, **143**(12).
196. **Pavithran, I., V. R. Unni, and R. I. Sujith** (2018a). Patent of addition to the patent, system and method for predetermining the onset of impending oscillatory instabilities in practical devices - US20210131663A1.
197. **Pavithran, I., V. R. Unni, and R. I. Sujith** (2021b). Critical transitions and their early warning signals in thermoacoustic systems. *The European Physical Journal Special Topics*, 1–22, doi:10.1140/epjs/s11734-021-00214-w.
198. **Pavithran, I., V. R. Unni, A. J. Varghese, P. Kasthuri, and R. I. Sujith** (2018b). System and method for determining oscillatory instabilities in fluid mechanical devices - WO2020021565A1. India Provisional Patent Reference Number: 201841027977.
199. **Pavithran, I., V. R. Unni, A. J. Varghese, D. Premraj, R. I. Sujith, C. Vijayan, A. Saha, N. Marwan, and J. Kurths** (2020a). Universality in spectral condensation. *Sci Rep* 10, 17405. DOI:10.1038/s41598-020-73956-7.
200. **Pavithran, I., V. R. Unni, A. J. Varghese, R. I. Sujith, A. Saha, N. Marwan, and J. Kurths** (2020b). Universality in the emergence of oscillatory instabilities in turbulent flows. *EPL (Europhysics Letters)*, **129**(2), 24004. DOI:10.1209/0295-5075/129/24004.
201. **Pawar, S. A., M. Raghunathan, K. V. Reeja, P. R. Midhun, and R. I. Sujith** (2020). Effect of preheating of the reactants on the transition to thermoacoustic instability in a bluff-body stabilized dump combustor. *Proceedings of the Combustion Institute*. DOI:10.1016/j.proci.2020.06.370.
202. **Pawar, S. A., A. Seshadri, V. R. Unni, and R. I. Sujith** (2017). Thermoacoustic instability as mutual synchronization between the acoustic field of the confinement and turbulent reactive flow. *J FLUID MECH*, **827**, 664–693.
203. **Pawar, S. A. and R. I. Sujith** (2018). Intermittency: A state that precedes thermoacoustic instability. *In Droplets and Sprays*, 403–430. Springer.
204. **Perry, E. H.** (1970). *Investigations of the T-burner and its Role in Combustion Instability Studies*. California Institute of Technology.
205. **Pisarchik, A. N., R. Jaimes-Reátegui, C. A. Magallón-García, and C. O. Castillo-Morales** (2014). Critical slowing down and noise-induced intermittency in bistable perception: bifurcation analysis. *Biological Cybernetics*, **108**(4), 397–404.
206. **Poinsot, T. J., A. C. Trounev, D. P. Veynante, S. M. Candel, and E. J. Esposito** (1987). Vortex-driven acoustically coupled combustion instabilities. *Journal of fluid mechanics*, **177**, 265–292.
207. **Pomeau, Y. and P. Manneville** (1980). Intermittent transition to turbulence in dissipative dynamical systems. *Communications in Mathematical Physics*, **74**(2), 189–197.

208. **Prebianca, F., H. A. Albuquerque, and M. W. Beims** (2018). Describing intrinsic noise in Chua's circuit. *Physics Letters A*, **382**(35), 2420–2423.
209. **Premraj, D., S. Kumarasamy, S. A. Pawar, L. Kabiraj, A. Prasad, and R. I. Sujith** (2021). Dragon-king extreme events as precursors for catastrophic transition. *Accepted for publication in EPL (Europhysics Letters)*.
210. **Premraj, D., S. A. Pawar, L. Kabiraj, and R. I. Sujith** (2020). Strange nonchaos in self-excited singing flames. *EPL (Europhysics Letters)*, **128**(5), 54005.
211. **Qian, B. and K. Rasheed** (2004). Hurst exponent and financial market predictability. *In IASTED conference on Financial Engineering and Applications*.
212. **Raghunathan, M., N. B. George, V. R. Unni, P. Midhun, K. V. Reeja, and R. I. Sujith** (2020). Multifractal analysis of flame dynamics during transition to thermoacoustic instability in a turbulent combustor. *Journal of Fluid Mechanics*, **888**.
213. **Raghunathan, M., N. B. B. George, V. R. Unni, R. Sujith, J. Kurths, and E. Surovyatkina** (2022). Seeds of phase transition to thermoacoustic instability. *New Journal of Physics*.
214. **Ray, A.** (2004). Symbolic dynamic analysis of complex systems for anomaly detection. *Signal processing*, **84**(7), 1115–1130.
215. **Rayleigh, J. W. S.** (1878). The explanation of certain acoustical phenomena. *Nature*, **18**, 319–321.
216. **Richards, G. A., D. L. Straub, and E. H. Robey** (2003). Passive control of combustion dynamics in stationary gas turbines. *Journal of Propulsion and Power*, **19**(5), 795–810.
217. **Richardson, L. F.** (1926). Atmospheric diffusion shown on a distance-neighbour graph. *Proceedings of the Royal Society of London. Series A, Containing Papers of a Mathematical and Physical Character*, **110**(756), 709–737.
218. **Richetti, P., F. Argoul, and A. Arneodo** (1986). Type-ii intermittency in a periodically driven nonlinear oscillator. *Physical Review A*, **34**(1), 726.
219. **Ritchie, P. and J. Sieber** (2016). Early-warning indicators for rate-induced tipping. *Chaos: An Interdisciplinary Journal of Nonlinear Science*, **26**(9), 093116.
220. **Ritchie, P. and J. Sieber** (2017). Probability of noise-and rate-induced tipping. *Physical Review E*, **95**(5), 052209.
221. **Rouwenhorst, D., J. Hermann, and W. Polifke** (2017). Online monitoring of thermoacoustic eigenmodes in annular combustion systems based on a state-space model. *Journal of Engineering for Gas Turbines and Power*, **139**(2).
222. **Roy, A., C. Premchand, M. Raghunathan, A. Krishnan, V. Nair, and R. I. Sujith** (2021). Critical region in the spatiotemporal dynamics of a turbulent thermoacoustic system and smart passive control. *Combustion and Flame*, **226**, 274–284.

223. **Ruelle, D.** and **F. Takens** (1971). On the nature of turbulence. *Communications in mathematical physics*, **20**(3), 167–192.
224. **Ruiz, E. A., V. R. Unni, I. Pavithran, R. I. Sujith,** and **A. Saha** (2021). Convolutional neural networks to predict the onset of oscillatory instabilities in turbulent systems. *Chaos: An Interdisciplinary Journal of Nonlinear Science*, **31**(9), 093131.
225. **Sarkar, S., K. G. Lore,** and **S. Sarkar** (2015a). Early detection of combustion instability by neural-symbolic analysis on hi-speed video. *In CoCo@ NIPS*.
226. **Sarkar, S., K. G. Lore, S. Sarkar, V. Ramanan, S. R. Chakravarthy, S. Phoha,** and **A. Ray** (2015b). Early detection of combustion instability from hi-speed flame images via deep learning and symbolic time series analysis. *In Annual Conf. of the Prognostics and Health Management*.
227. **Schadow, K.** and **E. Gutmark** (1992). Combustion instability related to vortex shedding in dump combustors and their passive control. *Progress in Energy and Combustion Science*, **18**(2), 117–132.
228. **Scharpf, W., M. Squicciarini, D. Bromley, C. Green, J. Tredicce,** and **L. Narducci** (1987). Experimental observation of a delayed bifurcation at the threshold of an argon laser. *Optics communications*, **63**(5), 344–348.
229. **Scheffer, M., J. Bascompte, W. A. Brock, V. Brovkin, S. R. Carpenter, V. Dakos, H. Held, E. H. van Nes, M. Rietkerk,** and **G. Sugihara** (2009). Early-warning signals for critical transitions. *Nature*, **461**(7260), 53.
230. **Scheffer, M., S. Carpenter, J. A. Foley, C. Folke,** and **B. Walker** (2001). Catastrophic shifts in ecosystems. *Nature*, **413**(6856), 591–596.
231. **Scheffer, M., S. R. Carpenter, T. M. Lenton, J. Bascompte, W. Brock, V. Dakos, J. van de Koppel, I. A. van de Leemput, S. A. Levin, E. H. van Nes,** *et al.* (2012). Anticipating critical transitions. *Science*, **338**(6105), 344–348.
232. **Schroeder, M.** (2009). *Fractals, chaos, power laws: Minutes from an infinite paradise*. Courier Corporation.
233. **Schuster, H. G.** and **W. Just** (2006). *Deterministic chaos: an introduction*. John Wiley & Sons.
234. **Seekell, D. A., S. R. Carpenter,** and **M. L. Pace** (2011). Conditional heteroscedasticity as a leading indicator of ecological regime shifts. *The American Naturalist*, **178**(4), 442–451.
235. **Sengupta, U., C. Rasmussen,** and **M. Juniper** (2020). Bayesian machine learning for the prognosis of combustion instabilities from noise.
236. **Sengupta, U., C. E. Rasmussen,** and **M. P. Juniper** (2021). Bayesian machine learning for the prognosis of combustion instabilities from noise. *Journal of Engineering for Gas Turbines and Power*, **143**(7), 071001.

237. **Seshadri, A., V. Nair, and R. I. Sujith** (2016). A reduced-order deterministic model describing an intermittency route to combustion instability. *Combustion Theory and Modelling*, **20**(3), 441–456.
238. **Seshadri, A., I. Pavithran, V. R. Unni, and R. I. Sujith** (2018a). Predicting the amplitude of limit-cycle oscillations in thermoacoustic systems with vortex shedding. *AIAA Journal*, **56**(9), 3507–3514.
239. **Seshadri, A., I. Pavithran, V. R. Unni, and R. I. Sujith** (2018b). Predicting the amplitude of limit-cycle oscillations in thermoacoustic systems with vortex shedding. *AIAA Journal*, **56**(9), 3507–3514. DOI:10.2514/1.J056926.
240. **Shanbhogue, S. J., S. Husain, and T. Lieuwen** (2009). Lean blowoff of bluff body stabilized flames: Scaling and dynamics. *Progress in Energy and Combustion Science*, **35**(1), 98–120.
241. **Shats, M., H. Xia, and H. Punzmann** (2006). Self-organization in plasma and 2d fluid turbulence: similarities and analogies. In *33rd EPS Conference on Plasma Phys. Rome, ECA*, volume 30.
242. **Singh, S., A. Roy, K. V. Reeja, A. Nair, S. Chaudhuri, and R. I. Sujith** (2020). Intermittency, secondary bifurcation and mixed-mode oscillations in a swirl-stabilized annular combustor: Experiments and modeling. *Journal of Engineering for Gas Turbines and Power*.
243. **Stanley, H. E.** (1999). Scaling, universality, and renormalization: Three pillars of modern critical phenomena. *Reviews of modern physics*, **71**(2), S358.
244. **Steinberg, A. M., I. Boxx, M. Stöhr, C. D. Carter, and W. Meier** (2010). Flow-flame interactions causing acoustically coupled heat release fluctuations in a thermoacoustically unstable gas turbine model combustor. *Combustion and Flame*, **157**(12), 2250–2266.
245. **Sterling, J. D.** (1993). Nonlinear analysis and modelling of combustion instabilities in a laboratory combustor. *Combustion Science and Technology*, **89**(1-4), 167–179.
246. **Stolbova, V., P. Martin, B. Bookhagen, N. Marwan, and J. Kurths** (2014). Topology and seasonal evolution of the network of extreme precipitation over the indian subcontinent and sri lanka. *Nonlinear Processes in Geophysics*, **21**(4), 901–917.
247. **Stolbova, V., E. Surovyatkina, B. Bookhagen, and J. Kurths** (2016). Tipping elements of the indian monsoon: Prediction of onset and withdrawal. *Geophysical Research Letters*, **43**(8), 3982–3990.
248. **Stow, S. R. and A. P. Dowling** (2004). Low-order modelling of thermoacoustic limit cycles. In *Turbo Expo: Power for Land, Sea, and Air*, volume 41669. DOI:10.1115/GT2004-54245.
249. **Strogatz, S. H., M. Friedman, A. J. Mallinckrodt, S. McKay, et al.** (1994). Nonlinear dynamics and chaos: With applications to physics, biology, chemistry, and engineering. *Computers in Physics*, **8**(5), 532–532.

250. **Subramanian, P., S. Mariappan, R. I. Sujith, and P. Wahi** (2010). Bifurcation analysis of thermoacoustic instability in a horizontal rijke tube. *International journal of spray and combustion dynamics*, **2**(4), 325–355.
251. **Subramanian, P., R. I. Sujith, and P. Wahi** (2013). Subcritical bifurcation and bistability in thermoacoustic systems. *Journal of Fluid Mechanics*, **715**, 210.
252. **Suchithra, K., E. A. Gopalakrishnan, E. Surovyatkina, and J. Kurths** (2020). Rate-induced transitions and advanced takeoff in power systems. *Chaos: An Interdisciplinary Journal of Nonlinear Science*, **30**(6), 061103.
253. **Sujith, R. I. and S. A. Pawar** (2021). *Thermoacoustic instability: A complex systems perspective*. Springer Nature.
254. **Sujith, R. I., A. Seshadri, and I. Pavithran** (2021). Apparatus to estimate the root means square value or the amplitude of limit cycle oscillations in systems that encounter oscillatory instabilities and methods thereof. US Patent App. 16/605,054.
255. **Sujith, R. I. and V. R. Unni** (2020). Complex system approach to investigate and mitigate thermoacoustic instability in turbulent combustors. *Physics of Fluids*, **32**(6), 061401, doi:10.1063/5.0003702.
256. **Sujith, R. I. and V. R. Unni** (2021). Dynamical systems and complex systems theory to study unsteady combustion. *Proceedings of the Combustion Institute*, **38**(3), 3445–3462, doi:10.1016/j.proci.2020.07.081.
257. **Sun, C., S. Jia, C. Barsi, S. Rica, A. Picozzi, and J. W. Fleischer** (2012). Observation of the kinetic condensation of classical waves. *Nature Physics*, **8**(6), 470–474.
258. **Suyal, V., A. Prasad, and H. P. Singh** (2009). Nonlinear time series analysis of sunspot data. *Solar Physics*, **260**(2), 441–449.
259. **Takens, F.** (1981). Detecting strange attractors in turbulence. *In Dynamical systems and turbulence*, 366–381. Springer.
260. **Tandon, S., S. A. Pawar, S. Banerjee, A. J. Varghese, P. Durairaj, and R. I. Sujith** (2020). Bursting during intermittency route to thermoacoustic instability: Effects of slow–fast dynamics. *Chaos: An Interdisciplinary Journal of Nonlinear Science*, **30**(10), 103112.
261. **Tandon, S. and R. I. Sujith** (2021). Condensation in the phase space and network topology during transition from chaos to order in turbulent thermoacoustic systems. *Chaos: An Interdisciplinary Journal of Nonlinear Science*, **31**(4), 043126.
262. **Täuber, U. C.** (2017). Phase transitions and scaling in systems far from equilibrium. *Annual Review of Condensed Matter Physics*, **8**, 185–210.
263. **Telesca, L., V. Cuomo, V. Lapenna, and M. Macchiato** (2001). A new approach to investigate the correlation between geoelectrical time fluctuations and earthquakes in a seismic area of southern italy. *Geophysical Research Letters*, **28**(23), 4375–4378.

264. **Tham, P.** and **A. K. Sen** (1994). Scaling behavior and self-organization in plasma turbulence. *Physical review letters*, **72**(7), 1020.
265. **Thompson, J. M. T.** and **J. Sieber** (2011). Predicting climate tipping as a noisy bifurcation: a review. *International Journal of Bifurcation and Chaos*, **21**(02), 399–423.
266. **Tilman, D., J. Fargione, B. Wolff, C. D’antonio, A. Dobson, R. Howarth, D. Schindler, W. H. Schlesinger, D. Simberloff, and D. Swackhamer** (2001). Forecasting agriculturally driven global environmental change. *science*, **292**(5515), 281–284.
267. **Tony, J., E. A. Gopalakrishnan, E. Sreelekha, and R. I. Sujith** (2015). Detecting deterministic nature of pressure measurements from a turbulent combustor. *Physical Review E*, **92**(6), 062902.
268. **Tony, J., S. Subarna, K. S. Syamkumar, G. Sudha, S. Akshay, E. A. Gopalakrishnan, E. Surovyatkina, and R. I. Sujith** (2017). Experimental investigation on preconditioned rate induced tipping in a thermoacoustic system. *Scientific reports*, **7**(1), 1–7.
269. **Tsotsis, T. T., R. C. Sane, and T. H. Lindstrom** (1988). Bifurcation behavior of a catalytic reaction due to a slowly varying parameter. *AIChE journal*, **34**(3), 383–388.
270. **Unni, V. R., E. A. Gopalakrishnan, K. S. Syamkumar, R. I. Sujith, E. Surovyatkina, and J. Kurths** (2019a). Interplay between random fluctuations and rate dependent phenomena at slow passage to limit-cycle oscillations in a bistable thermoacoustic system. *Chaos: An Interdisciplinary Journal of Nonlinear Science*, **29**(3), 031102.
271. **Unni, V. R., A. Krishnan, R. Manikandan, N. B. George, R. I. Sujith, N. Marwan, and J. Kurths** (2018a). On the emergence of critical regions at the onset of thermoacoustic instability in a turbulent combustor. *Chaos: An Interdisciplinary Journal of Nonlinear Science*, **28**(6), 063125.
272. **Unni, V. R., A. Mukhopadhyay, and R. I. Sujith** (2015). Online detection of impending instability in a combustion system using tools from symbolic time series analysis. *International Journal of Spray and Combustion Dynamics*, **7**(3), 243–255.
273. **Unni, V. R. and R. I. Sujith** (2015). Multifractal characteristics of combustor dynamics close to lean blowout. *J FLUID MECH*, **784**, 30–50.
274. **Unni, V. R. and R. I. Sujith** (2016). Precursors to blowout in a turbulent combustor based on recurrence quantification. *In 52nd AIAA/SAE/ASEE Joint Propulsion Conference*.
275. **Unni, V. R. and R. I. Sujith** (2017). Flame dynamics during intermittency in a turbulent combustor. *Proc. Combust. Inst.*, **36**(3), 3791–3798.
276. **Unni, V. R., V. N. Vinod, and S. R. P. I. Nair** (2019b). System and method for detecting precursors to control blowout in combustion systems. US Patent 10,267,519.

277. **Unni, V. R., V. N. Vinod, S. R. P. I. Nair, and A. Mukhopadhyay** (2018b). System and method for controlling oscillatory instabilities in a device. US Patent 10,095,247.
278. **Van Nes, E. H., T. Amaro, M. Scheffer, and G. C. Duineveld** (2007). Possible mechanisms for a marine benthic regime shift in the north sea. *Marine Ecology Progress Series*, **330**, 39–47.
279. **van Nes, E. H. and M. Scheffer** (2007). Slow recovery from perturbations as a generic indicator of a nearby catastrophic shift. *The American Naturalist*, **169**(6), 738–747.
280. **Vandewalle, N. and M. Ausloos** (1997). Coherent and random sequences in financial fluctuations. *Physica A: Statistical Mechanics and its Applications*, **246**(3-4), 454–459.
281. **Vapnik, V. N.** (1999). An overview of statistical learning theory. *IEEE Transactions on Neural Networks*, **10**(5), 988–999.
282. **Varfolomeyev, S. D. and K. G. Gurevich** (2001). The hyperexponential growth of the human population on a macrohistorical scale. *Journal of Theoretical Biology*, **212**(3), 367–372.
283. **Varghese, A. J., A. Chechkin, R. Metzler, and R. I. Sujith** (2021). Capturing multifractality of pressure fluctuations in thermoacoustic systems using fractional-order derivatives. *Chaos: An Interdisciplinary Journal of Nonlinear Science*, **31**(3), 033108.
284. **Venegas, J. G., T. Winkler, G. Musch, M. F. V. Melo, D. Layfield, N. Tgavalekos, A. J. Fischman, R. J. Callahan, G. Bellani, and R. S. Harris** (2005). Self-organized patchiness in asthma as a prelude to catastrophic shifts. *Nature*, **434**(7034), 777.
285. **Venkatramani, J., V. Nair, R. I. Sujith, S. Gupta, and S. Sarkar** (2016). Precursors to flutter instability by an intermittency route: a model free approach. *Journal of Fluids and Structures*, **61**, 376–391.
286. **Venkatramani, J., V. Nair, R. I. Sujith, S. Gupta, and S. Sarkar** (2017). Multifractality in aeroelastic response as a precursor to flutter. *Journal of Sound and Vibration*, **386**, 390–406.
287. **Veraart, A. J., E. J. Faassen, V. Dakos, E. H. van Nes, M. Lürling, and M. Scheffer** (2012). Recovery rates reflect distance to a tipping point in a living system. *Nature*, **481**(7381), 357–359.
288. **Watkins, N. W., G. Pruessner, S. C. Chapman, N. B. Crosby, and H. J. Jensen** (2016). 25 years of self-organized criticality: Concepts and controversies. *Space Science Reviews*, **198**(1-4), 3–44.
289. **Waxenegger-Wilfing, G., U. Sengupta, J. Martin, W. Armbruster, J. Hardi, M. Juniper, and M. Oswald** (2021). Early detection of thermoacoustic instabilities in a cryogenic rocket thrust chamber using combustion noise features and machine learning. *Chaos: An Interdisciplinary Journal of Nonlinear Science*, **31**(6), 063128.
290. **Webber Jr, C. L. and N. Marwan** (2015). *Recurrence quantification analysis*. Springer.

291. **Weng, Y., V. R. Unni, R. I. Sujith, and A. Saha** (2020). Synchronization framework for modeling transition to thermoacoustic instability in laminar combustors. *Nonlinear Dynamics*, 1–12.
292. **West, B. J., M. Latka, M. Glaubic-Latka, and D. Latka** (2003). Multifractality of cerebral blood flow. *Physica A: Statistical Mechanics and its Applications*, **318**(3-4), 453–460.
293. **Wieczorek, S., P. Ashwin, C. M. Luke, and P. M. Cox** (2011). Excitability in ramped systems: the compost-bomb instability. *Proceedings of the Royal Society A: Mathematical, Physical and Engineering Sciences*, **467**(2129), 1243–1269.
294. **Wiesenfeld, K.** (1985). Noisy precursors of nonlinear instabilities. *Journal of Statistical Physics*, **38**(5-6), 1071–1097.
295. **Wilkat, T., T. Rings, and K. Lehnertz** (2019). No evidence for critical slowing down prior to human epileptic seizures. *Chaos: An Interdisciplinary Journal of Nonlinear Science*, **29**(9), 091104.
296. **Wilson, K. G.** (1971a). Renormalization group and critical phenomena. i. renormalization group and the kadanoff scaling picture. *Physical review B*, **4**(9), 3174.
297. **Wilson, K. G.** (1971b). Renormalization group and critical phenomena. ii. phase-space cell analysis of critical behavior. *Physical Review B*, **4**(9), 3184.
298. **Xie, X.-q., W.-p. He, B. Gu, Y. Mei, and S.-s. Zhao** (2019). Can kurtosis be an early warning signal for abrupt climate change? *Climate dynamics*, **52**(11), 6863–6876.
299. **Xiong, S., S. Mondal, and A. Ray** (2018). Detection of thermoacoustic instabilities via nonparametric bayesian markov modeling of time-series data. *Journal of Dynamic Systems, Measurement, and Control*, **140**(2).
300. **Zanette, D. and A. Mikhailov** (1998). Condensation in globally coupled populations of chaotic dynamical systems. *Physical Review E*, **57**(1), 276.
301. **Zbilut, J. P., J.-M. Zaldivar-Comenges, and F. Strozzi** (2002). Recurrence quantification based liapunov exponents for monitoring divergence in experimental data. *Physics Letters A*, **297**(3-4), 173–181.
302. **Zhang, X., Y. Xu, Q. Liu, and J. Kurths** (2020). Rate-dependent tipping-delay phenomenon in a thermoacoustic system with colored noise. *Science China Technological Sciences*, **63**(11), 2315–2327.
303. **Zhang, X., Y. Xu, Q. Liu, J. Kurths, and C. Grebogi** (2021). Rate-dependent bifurcation dodging in a thermoacoustic system driven by colored noise. *Nonlinear Dynamics*, **104**(3), 2733–2743.
304. **Zickfeld, K., B. Knopf, V. u. Petoukhov, and H. Schellnhuber** (2005). Is the indian summer monsoon stable against global change? *Geophysical Research Letters*, **32**(15).
305. **Zou, Y., R. V. Donner, N. Marwan, J. F. Donges, and J. Kurths** (2019). Complex network approaches to nonlinear time series analysis. *Physics Reports*, **787**, 1–97.

CURRICULUM VITAE

1. **NAME** : Induja P
2. **DATE OF BIRTH** : 15 March 1994

3. **EDUCATIONAL QUALIFICATIONS**

2014 Bachelor of Science (B. Sc.)

Institution : Kannur University, Kerala

Specialization : physics

2016 Master of Science (M. Sc.)

Institution : National Institute of Technology Calicut

Specialization : Physics

Doctor of Philosophy

Institution : Indian Institute of Technology Madras

Specialization : Physics + Aerospace Engineering

Registration Date : 10 July 2017